



Metal-Ligand Multiple Bonds in High-Spin Complexes

Citation

King, Evan. 2012. Metal-Ligand Multiple Bonds in High-Spin Complexes. Doctoral dissertation, Harvard University.

Permanent link

<http://nrs.harvard.edu/urn-3:HUL.InstRepos:9282601>

Terms of Use

This article was downloaded from Harvard University's DASH repository, and is made available under the terms and conditions applicable to Other Posted Material, as set forth at <http://nrs.harvard.edu/urn-3:HUL.InstRepos:dash.current.terms-of-use#LAA>

Share Your Story

The Harvard community has made this article openly available.
Please share how this access benefits you. [Submit a story](#).

[Accessibility](#)

©2012 – Evan Robert King
All rights reserved.

Metal-Ligand Multiple Bonds in High-Spin Complexes

Abstract

The chemistry of late first row transition metals supported by dipyrromethane and dipyrromethene ligands bearing sterically bulky substituents was explored. Transition metal complexes (Mn, Fe, Co, Ni, Zn) of the dipyrromethane ligand 1,9-dimesityl-5,5-dimethyldipyrromethane (dpma) were prepared. Structural and magnetic characterization (SQUID, EPR) of the bis-pyridine adducts (dpma)Mn(py)₂, (dpma)Fe(py)₂, and (dpma)Co(py)₂ showed each tetrahedral divalent ion to be high-spin, while square planar (dpma)Ni^{II}(py)₂ and tetrahedral (dpma)Zn(py)₂ were shown to be diamagnetic. Electrochemical experiments revealed oxidative events at common potentials independent of metal identity or spin state, consistent with ligand-based oxidation.

Dipyrromethene ligand scaffolds were synthesized bearing large aryl (Ar = 2,4,6-Ph₃C₆H₂, Mes = 2,4,6-Me₃C₆H₂) or alkyl (tBu = CMe₃, Ad = 1-adamantyl) flanking groups to afford three new disubstituted ligands (^Rdpme, 1,9-R₂-5-mesityldipyrromethene, R = Ar, Mes, tBu, Ad). While high-spin (*S* = 2), four-coordinate iron complexes of the type (^Rdpme)FeCl(sol_v) were obtained when R was Mes, tBu, or Ad, use of the sterically encumbered aryl-substituted ligand gave a three-coordinate high-spin (*S* = 2) complex (^{Ar}dpme)FeCl. Intramolecular C–H amination was discovered in the reaction of organic azides with (^{Mes}dpme)FeCl(thf), though no intermediate was observed by UV/Vis, IR, or ¹H VT-NMR experiments. Reaction of (^{Ad}dpme)FeCl(OEt₂) with alkyl azides resulted in the catalytic amination of C–H bonds or aziridination of olefins at room temperature. Reaction of *p*-tBuC₆H₄N₃ with (^{Ar}dpme)FeCl permitted isolation of a high-spin (*S* = 2) iron complex (^{Ar}dpme)FeCl(N(*p*-tBuC₆H₄)),

featuring a terminal imidyl radical antiferromagnetically coupled to high-spin Fe^{III}, as determined by ¹H NMR, X-ray crystallography, and ⁵⁷Fe Mössbauer.

A three-coordinate Co^I complex (^{Ar}dpme)Co(py) was synthesized and characterized by ¹H NMR, SQUID magnetometry, and X-ray crystallography. Reaction of (^{Ar}dpme)Co(py) with ^tBuN₃ afforded an isolable three-coordinate Co imide complex (^{Ar}dpme)Co(N^tBu) that exhibits spin crossover from a singlet to a quintet. Reaction of (^{Ar}dpme)Co(py) with mesityl azide produces a spectroscopically observed intermediate, consistent with an S = 1 terminal imide complex, that converted via benzylic C–H activation into the metallacycloindoline (^{Ar}dpme)Co(κ^2 -NHC₆H₂-2,4-Me₂-6-CH₂).

Table of Contents

<i>Abstract</i>	<i>iii</i>
<i>Acknowledgements</i>	<i>viii</i>
<i>List of Schemes</i>	<i>xi</i>
<i>List of Figures</i>	<i>xii</i>
<i>List of Tables</i>	<i>xv</i>
<i>List of Chemical Abbreviations</i>	<i>xvi</i>
<i>List of Acronyms, Symbols, and Units</i>	<i>xvii</i>
Chapter 1: Multiple Bonds, Electronic Structure and Reactivity	1
1-1. Introduction.	1
1-2. Electronic Structure.	2
1-3. Biological and Synthetic Iron Oxos.	4
1-4. Late Metal Imides.	7
1-5. Iron Imides.	8
1-6. Cobalt Imides.	12
1-7. Dipyrrole Ligand Architectures.	14
1-8. Chapter Summaries	16
Chapter 2: The Electronic Structure of First Row Dipyrromethane Complexes	19
2-1. Introduction.	19
2-2. Synthesis and Characterization of dpmaH and Its Metal Complexes.	21
2-3. Structural Characterization of Dipyrromethane Complexes.	23
2-4. Electronic and Magnetic Characterization of Dipyrromethane Complexes.	24
2-5. Electrochemical Behavior of Dipyrromethane Complexes.	30
2-6. Computational Analysis.	32
2-7. Chemical Oxidation.	34
2-8. Understanding the Electronic Structure of Dipyrromethane Complexes.	36
2-9. Conclusions.	38

2-10. Experimental Methods.	39
Chapter 3: Intramolecular C–H Amination from an Iron Dipyrrromethene Complex	55
3-1. Introduction.	55
3-2. Synthesis and Characterization of Dipyrrromethene Complexes.	57
3-3. Intramolecular C–H Amination.	60
3-4. Conclusions.	63
3-5. Experimental Methods.	64
Chapter 4: Catalytic C–H Bond Amination from High-Spin Iron Imide Complexes	80
4-1. Introduction.	80
4-2. Development of New Dipyrrromethene Platforms.	82
4-3. Synthesis and Characterization of Potential Catalysts.	84
4-4. Catalytic C–H Amination.	85
4-5. Isolation and Characterization of an Intermediate.	88
4-6. Reactivity of the Imide Radical.	93
4-7. Conclusions.	96
4-8. Experimental Methods.	96
Chapter 5: Cobalt Imides Exhibiting Spin Crossover and C–H bond Activation	123
5-1. Introduction.	123
5-2. Synthesis and Characterization of Dipyrrromethene Cobalt Complexes.	125
5-3. Isolation of an Alkyl Cobalt Imide.	128
5-4. Reactivity of (^{Ar} dpme)Co(py) with Aryl Azides.	131
5-5. Understanding the Electronic Structure of Open Shell Cobalt Imides.	132
5-6. Conclusions.	135
5-7. Experimental Methods.	136
<i>Appendix A: Crystallographically Characterized Compounds</i>	156
<i>Curriculum Vitae</i>	171

to Annie

Acknowledgements

A Brief History of the Group that Goes by Betley

The Betley Lab got its first member on July 4th, 2007. I worked a half-day looking up glassware and equipment numbers at a table in the only room not under construction, 306E. Since Independence Day, the routine gradually expanded to include unpacking frits, organizing chemicals, and occasionally conversing about the local sports teams with a quiet and well-mannered undergraduate volunteer from Brockton, Massachusetts. On a quiet Saturday in August the right-hand hood in 306M was christened by the somewhat successful condensation of acetone and 2-mesitylpyrrole. Shortly thereafter Kin arrived, her coming heralded by shipments of rare earth elements from her former lab. And soon Emily joined as the first member of the lab to actually be enrolled at Harvard University. Ted, Evan, Guy, Kin and Emily, comprised the proto-Betley Lab. The golden age of the Betley Lab was soon to dawn.

From across the globe came the recruiting class of 2008, Libby, Tamara, Austin, and Graham, swelling the ranks of our offices to nearly double digits. Joining the core four would be postdocs Mat, a man with as little need for a two t's as he has for chairs or carbohydrates, and Alison, whose legendary meanness is quite possibly the only reason the lab has not been crushed under the weight of a thousand discarded flasks, as well as a veritable battalion of talented undergraduates. They included Barrett who would be the first to take what little training I offered him and turn it into many colorful compounds, before becoming the first graduate to have departed our lab. And so things went on through many other milestones: the ACS conference in Philadelphia, our first submitted paper, several iterations of group meeting format, the evolution of Chem 40, our first accepted paper, at least two group members having babies, more undergraduate graduations, Kin beginning her career, the expansion to Suite 303, our first Rhino cup season, Guy and Dianne's launch into the west, etc. Any voids in the group's collective personality were quickly filled by the impassioned boisterousness of Dave, and the unmitigated charisma of Raul. Although with latest G1 crop of Denise, Benji, and Matt they are now overflowing in vast excess. So closes the first golden age of Mallinckrodt, as only Theodore shall remain to remember our humble beginnings and witness the continuing adventures of the Betset.

And now some actual acknowledgements. It's hard not to like chemistry when your high school teacher is Paul McCartney, or at least looks enough like him and is a huge Beatles fan, so thank you Mr. McCready. Thanks also to my Prof. Tyler McQuade for making me legitimately excited to go to 9 am organic lecture and 8 pm review/problem sessions, and for getting me into the Chirik lab. Thank you to Pete Wolczanski for teaching me in two semesters about as much inorganic chemistry as I have learned since, though I could only pick up about a quarter of it at the time. Thank you to Paul Chirik for genuinely incorporating me into your lab despite the fact that I barely knew what I was doing, and thanks to Wes Bernskoetter for helping me enough to cover up the fact that I barely knew what I was doing, and for encouraging me to go to graduate school while declaring almost every member of the field a hack at one point or another.

Thanks to John Curley, Nick Piro, Alex Fox, and Glen Alliger for being my compatriots in the Cummins group. Special thanks to Alex who had to live with me in lab and at home, and through an eviction from the later, and to Glen for sharing the bay and bearing the brunt of all the cryptand project had to offer. Thanks to Kit for being Kit and for giving me an opportunity to learn in his lab. Thanks to Ted for offering me a chance to build something from the ground up, and for being a tremendously encouraging advisor. Anytime I went to him intending to just vent unproductively, I never got the chance. He would start going on about the 'metal and ligand orbitals being matched in energy' or 'the accessibility of radical density along the bond vector', somewhere along the way acknowledging that he understood my frustrations, but quickly bring it back to the realm of scientific possibilities. I usually learned enough in those interactions that I had something new to contemplate rather than my previous consternation.

Thanks to the past and present inhabitants of the best office, 306M, especially Alison, Dianne, Emily, Benji, Max, and Guy for all the random and entertaining musings. Thanks all those who have at one point or another made compounds that have contributed, knowingly or otherwise, to my efforts. We downplay the importance of making things like ligands once they are not new, but I could not have run all the experiments I did without multi-day ligand syntheses being carried out largely on my behalf by Barrett, Guy, Sam, and Matt. Thank you to the residents of box Haiti, who have kept it running so smoothly, none more so than Libby. There is so much chemistry I could not have done, and so much about our project that would not have been figured out without the countless reactions you have run and continue to run so expertly.

Thanks to Graham for the countless discussions we have had which have oscillated between the scientific, the serious, and the absurd, from fantasy team strategy, to origins of the Mössbauer effect, to the global economy, to solar energy, to why Ron Swanson is hilarious. We even talked about the NFL once or twice. Thanks to Guy for keeping it real real right now right now, and for some epic non-stories, I hope he finally got paid. Matt, I finally figure out that since we are only going to overlap for one year, more than half of what you say is just an effort to fit four more years into that window, so thank you for your accelerated friendship.

I could not have started any of this without the love and support of my parents and the aspects of my thinking they have helped to shape. Thank you mom for the genuine wonder for learning that you have always expressed. Thank you dad for the perceptive sense of logic and reason with which you have always answered my questions. Thank you both for supporting me wherever I have gone and in the choices I have made. Thank you to the Maryann, Richard, and David Calnan for their encouraging belief in me for many years. There are a lot of people with whom this accomplishment would not be possible, but the most literal, is my wife Annie, without whom I would not have started let alone completed this work. If being a loving wife was not enough she's helped me as a chemist and as a student who has already been down this path. She is a source of inspiration, comfort, and strength, but mostly I have to thank her for keeping me happy and sane, well, sane enough at least.

List of Schemes

Chapter 1	
Scheme 1.1. The electronic structure of P450 compound I and ‘radical rebound’ mechanism.	2
Scheme 1.2. Examples of high-spin non-heme iron oxos.	6
Scheme 1.3. Crystallographically characterized iron imides.	11
Scheme 1.4. Isolated cobalt imides.	13
Scheme 1.5. Dipyrrrole ligands referred to throughout this thesis.	15
Chapter 2	
Scheme 2.1. Synthesis of dipyrromethane transition metal complexes.	21
Scheme 2.2. Ligand centered oxidation in (dpma)M(py) ₂ complexes.	34
Scheme 2.3. Chemical oxidation of (dpma) ²⁻ .	36
Chapter 3	
Scheme 3.1. Synthesis of (^{Mes} dpme)FeCl(thf).	57
Scheme 3.2. Intramolecular C–H amination.	61
Chapter 4	
Scheme 4.1. Synthesis of the dpme ligands and their metal complexes.	83
Scheme 4.2. Proposed catalytic cycle for the amination of C–H bonds by reaction of (^{Ad} dpme)FeCl(OEt ₂) with organic azides.	88
Scheme 4.3. Synthesis of the bimolecularly coupled Fe ^{III} imide precursor [Fe ^{III}] ₂ and the terminal imide complex (^{Ar} dpme)FeCl(NAr ^{tBu})	94
Chapter 5	
Scheme 5.1. Synthesis of (^{Ar} dpme)Co(py), (^{Ar} dpme)Co(N ^t Bu), and (^{Ar} dpme)Co(indoline).	125

List of Figures

Chapter 2

Figure 2.1. Structures of the Mn, Fe, Co, and Zn bis-pyridine complexes.	22
Figure 2.2. Structures of the Ni bis-pyridine, Co ate complex, and Fe(bpy) complexes.	23
Figure 2.3. Absorption spectra of transition metal bis-pyridine complexes.	26
Figure 2.4. Magnetometry of paramagnetic dpma bis-pyridine complexes.	28
Figure 2.5. 77 K X-band EPR of Co and Mn dpma bis-pyridine complexes.	28
Figure 2.6. Room Temperature EPR of dpma Co and Mn bis-pyridine complexes.	29
Figure 2.7. Mössbauer spectra of Fe dpma complexes.	29
Figure 2.8. Differential Pulse Voltammograms of dpma complexes in ACN.	30
Figure 2.9. Differential Pulse Voltammograms of dpma complexes in ACN and THF.	32
Figure 2.10. Computed molecular orbital energy levels for dpma bis-pyridine complexes.	33
Figure 2.11. Calculated molecular orbitals of (dpma)Co(py) ₂ .	34
Figure 2.12. Calculated spin densities for paramagnetic dpma bis-pyridine complexes.	34
Figure 2.13. Structure of the diazapentalene.	36
Figure 2.14. Cyclic voltammogram of the diazapentalene.	36

Chapter 3

Figure 3.1. Structure of (^{Mes} dpme)FeCl(thf).	58
Figure 3.2. Absorption spectra and cyclic voltammogram of (^{Mes} dpme)FeCl(thf).	59
Figure 3.3. Comparison of Fe and Zn cyclic voltammograms.	60
Figure 3.4. Structure of intramolecular C–H amination product (^{Mes} dpme–NAd)FeCl.	62
Figure 3.5. Changes in the electronic absorption spectrum during conversion of (^{Mes} dpme)FeCl(thf) to (^{Mes} dpme–NAd)FeCl.	63
Figure 3.6. Absorption spectra of ^{Mes} dpmeH and its metal complexes.	66

Figure 3.7. Structure of $(^{\text{Mes}}\text{dpme})\text{FeCl}(\text{py})$.	70
Figure 3.8. Structure of $(^{\text{Mes}}\text{dpme})\text{ZnCl}(\text{py})$.	72
Figure 3.9. Variable temperature ^1H NMR of $(^{\text{Mes}}\text{dpme})\text{FeCl}(\text{thf}) + \text{N}_3\text{Ad}$ in DCM.	75
Figure 3.10. ^1H NMR of $(^{\text{Mes}}\text{dpme})\text{FeCl}(\text{thf}) + \text{N}_3^t\text{Bu}$ in DCM.	76
Figure 3.11. Variable temperature ^1H NMR of $(^{\text{Mes}}\text{dpme})\text{FeCl}(\text{thf})$ DCM.	77
Figure 3.12. Variable temperature ^1H NMR of $(^{\text{Mes}}\text{dpme}-\text{NAd})\text{FeCl}$ in DCM.	77

Chapter 4

Figure 4.1. Solid-state molecular structures of Fe^{II} dpme complexes.	83
Figure 4.2. Mössbauer of $^{\text{Ar}}\text{dpme}$ complexes and calculated model for the imide radical.	89
Figure 4.3. Truncated solid-state molecular structures of isolated $^{\text{Ar}}\text{dpme}$ Fe^{III} complexes.	90
Figure 4.4. Molecular orbitals and energy levels for $(^{\text{Ar}}\text{dpme})\text{Fe}(\text{NAr}^t\text{Bu})$.	95
Figure 4.5. Structure of $^{\text{Ar}}\text{dpmeH}$.	105
Figure 4.6. Structure of $(^{\text{Ad}}\text{dpme})\text{FeCl}(\text{OEt}_2)$.	108
Figure 4.7. Mössbauer of $(^{\text{Ad}}\text{dpme})\text{FeCl}(\text{OEt}_2)$.	108
Figure 4.8. Structure of $(^t\text{Bu}\text{dpme})\text{FeCl}(\text{THF})$.	110
Figure 4.9. Structure of $(^{\text{Ar}}\text{dpme})\text{FeCl}$.	111
Figure 4.10. Mössbauer of $(^{\text{Ar}}\text{dpme})\text{FeCl}$.	111
Figure 4.11. Structure of $[\text{Fe}^{\text{III}}]_2$.	112
Figure 4.12. Mössbauer spectrum of $[\text{Fe}^{\text{III}}]_2$.	112
Figure 4.13. Structure of $(^{\text{Ar}}\text{dpme})\text{FeCl}(\text{NAr}^t\text{Bu})$.	113
Figure 4.14. Mössbauer spectrum of $(^{\text{Ar}}\text{dpme})\text{FeCl}(\text{NAr}^t\text{Bu})$.	113

Chapter 5

Figure 5.1. Solid-state structures for cobalt dipyrromethene complexes.	127
Figure 5.2. Variable temperature magnetic susceptibility data for $(^{\text{Ar}}\text{dpme})\text{Co}(\text{N}^t\text{Bu})$.	129
Figure 5.3. Frontier molecular orbital description for trigonal $\text{Co}^{\text{III}}(\text{NR})$.	134

Figure 5.4. Structure of (^{Ar} dpme)CoCl(py).	139
Figure 5.5. Structure of (^{Ar} dpme)Co(py).	140
Figure 5.6. Structure of (^{Ar} dpme)Co(N ₄ Ar ^{NMe₂}).	141
Figure 5.7. Structure of (^{Ar} dpme)Co(N ^t Bu ₂).	142
Figure 5.8. Structure of (^{Ar} dpme)Co(N ^t Bu).	144
Figure 5.9. Structure for (^{Ar} dpme)Co(indoline).	145
Figure 5.10. Variable temperature ¹ H NMR of (^{Ar} dpme)Co(py) in toluene- <i>d</i> ₈ at 400 MHz.	147
Figure 5.11. Variable temperature ¹ H NMR of (^{Ar} dpme)Co(N ^t Bu) in toluene- <i>d</i> ₈ at 400 MHz.	148
Figure 5.12. Variable temperature ¹ H NMR of (^{Ar} dpme)Co(indoline) in toluene- <i>d</i> ₈ at 400 MHz.	149
Figure 5.13. Variable temperature ¹ H NMR of (^{Ar} dpme)Co(NMes)- <i>d</i> ₁₁ in toluene- <i>d</i> ₈ at 400 MHz.	150
Figure 5.14. Magnetic susceptibility data for (^{Ar} dpme)Co(py) and (^{Ar} dpme)Co(N ^t Bu).	151
Figure 5.15. Reduced magnetization data (<i>M</i> vs. <i>H/T</i>) for (^{Ar} dpme)Co(N ^t Bu).	152

List of Tables

Chapter 2

Table 2.1. Dipyrromethane and metal-ligand bond length comparisons.	23
Table 2.2. Magnetic and spectral properties of the transition metal dpma complexes.	24
Table 2.3. Equations for magnetic measurements.	41
Table 2.4. X-ray diffraction experimental details.	54

Chapter 4

Table 4.1. Spectral and magnetic properties of (dpme)Fe complexes.	85
Table 4.2. LC/MS (¹ H NMR) yields at various temperatures of products generated in catalytic amination reaction with (^{Ad} dpme)FeCl(OEt ₂).	87
Table 4.3. Metal–ligand bond lengths of dpme complexes.	91
Table 4.4. Bond Lengths and Angles of [Fe ^{III}] ₂ and (^{Ar} dpme)FeCl(NAr ^{tBu}).	92
Table 4.5. Equations for computationally determined Mössbauer parameters.	118
Table 4.6. Equations for calculation of Broken Symmetry Energies and Couplings.	119
Table 4.7. X-ray diffraction experimental details.	122

Chapter 5

Table 5.1. Equations used to model the susceptibility and magnetization data.	130
Table 5.2. Equations for susceptibility of triplet and quintet states with zero field splitting.	137
Table 5.3. Metal-Ligand Bond Lengths of Dipyrromethene Complexes.	154
Table 5.4. X-ray diffraction experimental details.	155

Appendix A

Table A.1. List of crystallographically characterized compounds.	156
---	-----

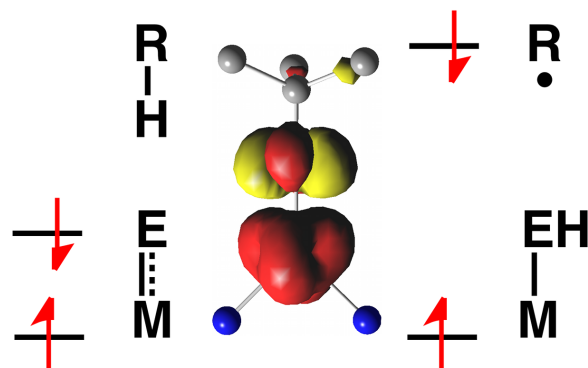
List of Chemical Abbreviations

ACN	acetonitrile
Ad or ¹ Ad	1-adamantyl (unless specified ² Ad for 2-admantyl)
Ar	2,4,6-triphenylphenyl
Ar ^{NMe₂}	4-(<i>N,N</i> -dimethylamino)phenyl
Ar ^{tBu}	4- <i>tert</i> -butylphenyl
Bn	benzyl
bpy	2,2'-bipyridine
CHD	cyclohexadiene
Cp	cyclopentadienyl
Cy	cyclohexyl
CyPhos	2-dicyclohexylphosphinobiphenyl
dba	dibenzylideneacetone
DCM	dichloromethane
DDQ	2,3-dichoro-5,6-dicyano-1,4-benzoquinone
dipp	2,6-diisopropylphenyl
dmep	2,6-dimethylphenyl
DMP	2,2-dimethoxypropane
dpma	dipyrromethane
dpme	dipyrromethene or dipyririn
Et	ethyl
Fc	ferrocene
Fc ⁺	ferrocenium
indoline	κ^2 -NHC ₆ H ₂ -2,4-Me ₂ -6-CH ₂
ⁱ Pr or iPr	isopropyl
JohnPhos	2-di- <i>tert</i> -butylphosphinobiphenyl
Me	methyl
Mes	mesityl or 2,4,6-trimethylphenyl
OTf	trifluoromethylsulfonate or triflate
PDI	pyridine diimine, 2,6-bis[1-(2,6-diisopropylphenylimino)ethyl]pyridine
Ph	phenyl
PPTS	pyridinium <i>para</i> -toluenesulfonate
py	pyridine
SPhos	2-dicyclohexylphosphino-2',6'-dimethoxybiphenyl
TBA	tetrabutylammonium
^t Bu or tBu	<i>tert</i> -butyl
TEA	triethylamine
TFA	trifluoroacetic acid
thf or THF	tetrahydrofuran
TMS	trimethylsilyl
tol	toluene
trip	2,4,6-triisopropylphenyl
Ts	<i>para</i> -toluenesulfonyl or tosyl

List of Acronyms, Symbols, and Units

•	radical
{ ¹ H}	proton decoupled
¹³ C	carbon-13
¹ H	proton
<i>A</i>	hyperfine coupling constant
Å	angstrom, 10 ⁻¹⁰ meters
avg	average
br	broad
CHN%	combustion or elemental analysis percentages for carbon, hydrogen, and nitrogen
cm ⁻¹	wavenumbers or inverse centimeters
CV	cyclic voltammetry or cyclic voltammogram
<i>D</i>	axial zero field splitting parameter
d	doublet in NMR
D or ² H	deuterium
dc	direct current
<i>d_n</i>	deuterated (<i>n</i> is the number of positions where ² H replaces ¹ H)
DPV	differential pulse voltammetry or differential pulse voltammogram
<i>e</i>	elementary charge, charge of a single proton or electron, 1.602 × 10 ⁻¹⁹ coulombs
<i>E</i>	rhombic zero field splitting parameter
e ⁻	electron
EPR	electron paramagnetic resonance
ESI ⁺	positive ion electron spray ionization
G	gauss
<i>g</i>	Landé <i>g</i> -factor (but may also refer to the anomalous gyromagnetic ratio, 2.0023)
GHz	gigahertz, 10 ⁹ Hertz or 10 ⁹ s ⁻¹
<i>H</i>	Hamiltonian operator
<i>H</i>	magnetic field
HAT	hydrogen atom transfer
HOMO	highest occupied molecular orbital
HRMS	high-resolution mass spectrometry
<i>I</i>	current in microamperes
IR	infrared spectroscopy (NIR denotes near infrared spectroscopy)
<i>J</i>	coupling constant
<i>J_{HH}</i>	proton–proton coupling constant
<i>k</i>	Boltzmann constant, 0.695 cm ⁻¹ /K
K	kelvin
KIE	kinetic isotope effect
LC/MS	liquid chromatography/mass spectrometry
LUMO	lowest unoccupied molecular orbital
M	molar, moles per liter
m	multiplet in NMR

<i>m</i> -	<i>meta</i> position on an aryl ring, indicating a 1,3 relationship
<i>m/z</i>	mass to charge ratio
MHz	megahertz, 10^6 Hertz or 10^6 s ⁻¹
MLMB	metal-ligand multiple bond
mmol	millimole, 10^{-3} moles
MO	molecular orbital
mV	millivolt, 10^{-3} volts
<i>N</i>	Avogadro constant, 6.022×10^{23} mol ⁻¹
nm	nanometer, 10^{-9} meters
NMR	nuclear magnetic resonance
<i>o</i> -	<i>ortho</i> position on an aryl ring, indicating a 1,2 relationship
Oe	oersted
<i>p</i> -	<i>para</i> position on an aryl ring, indicating a 1,4 relationship
ppm	parts per million
q	quartet in NMR
rt	room temperature
s	singlet in NMR or second
<i>S</i>	spin
S	spin operator
sh	shoulder
SOMO	singly-occupied molecular orbital
SQUID	superconducting quantum interference device
T	tesla
t	triplet in NMR
<i>T</i> or T	temperature
<i>T_c</i>	crossover temperature
UV/Vis	ultraviolet-visible absorption spectroscopy
V	potential in mV or V
V	volt
<i>w/w</i>	mass fraction or percentage weight solute per weight solution
δ	delta, chemical shift in ppm
δ	isomer shift for ⁵⁷ Fe Mössbauer in mm/s
ΔE_Q	quadrupole splitting for ⁵⁷ Fe Mössbauer in mm/s
ΔH	enthalpy
ϵ	epsilon, extinction coefficient or molar absorptivity in M ⁻¹ cm ⁻¹
η^n	eta, hapticity or the number, <i>n</i> , of contiguous atoms in a ligand bound to a metal
κ^n	kappa, denticity or the number, <i>n</i> , of atoms in a polydentate ligand bound to the metal
λ	lambda, wavelength in nm
μA	microampere, 10^{-6} ampere
μ_B	Bohr magneton, 9.274×10^{-21} erg/G
μ_{eff}	mu effective, effective magnetic moment in Bohr magnetons
μ^n	mu, the number, <i>n</i> , of metal atoms to which a bridging ligand is bound (default <i>n</i> = 2)
ν	frequency
χ	magnetic susceptibility
χ_M or χ_m	molar magnetic susceptibility in cm ³ /mol



Chapter 1: Multiple Bonds, Electronic Structure and Reactivity

1-1. Introduction.

Transition metal centers featuring metal-ligand multiple bonds (MLMBs) have been implicated in the key intermediates of many important functionalizing enzymes. Numerous heme¹ and non-heme² hydroxylases have been well studied due to their ability to introduce oxygen into various substrates including completely unactivated substrates such as methane.³ The critical intermediate in most hydroxylase mechanisms in which a C–H bond is functionalized is the species that will initiate hydrogen atom transfer (HAT), the first step of the ‘radical rebound’ mechanism⁴ prior to carbon oxygen bond formation. This reactivity has most frequently been ascribed to a terminal iron oxo, such as the (Cys–S)(porphyrin)Fe=O proposed for cytochrome P450.¹ The electronic structure of the iron oxo has

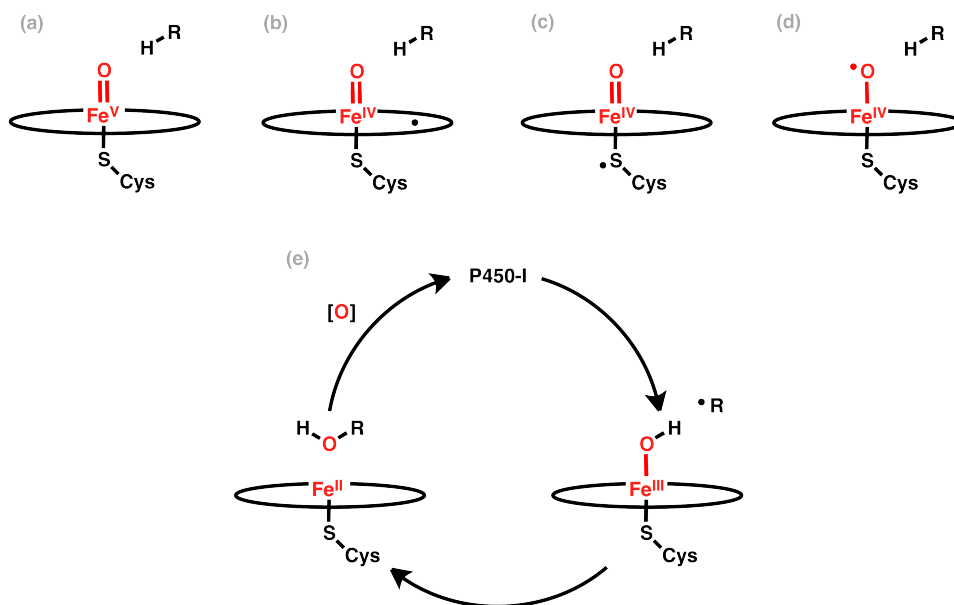
(1) (a) *Cytochrome P450 : Structure, Mechanism, and Biochemistry*; 4th ed.; Ortiz de Montellano, P. R., Ed.; Kluwer Academic/Plenum Publishers: New York, 2005. (b) Sono, M.; Roach, M. P.; Coulter, E. D.; Dawson, J. H. *Chem. Rev.* **1996**, *96*, 2841-2887. (c) Meunier, B.; de Visser, S. P.; Shaik, S. *Chem. Rev.* **2004**, *104*, 3947-3980. (d) Denisov, I. G.; Makris, T. M.; Sligar, S. G.; Schlichting, I. *Chem. Rev.* **2005**, *105*, 2253-2277. (e) Makris, T. M.; von Koenig, K.; Schlichting, I.; Sligar, S. G. *J. Inorg. Biochem.* **2006**, *100*, 507-518.

(2) (a) Krebs, C.; Fujimori, D. G.; Walsh, C. T.; Bollinger, J. M. *Acc. Chem. Res.* **2007**, *40*, 484-492. (b) Wallar, B. J.; Lipscomb, J. D. *Chem. Rev.* **1996**, *96*, 2625-2657. (c) Solomon, E. I.; Brunold, T. C.; Davis, M. I.; Kemsley, J. N.; Lee, S. K.; Lehnert, N.; Neese, F.; Skulan, A. J.; Yang, Y. S.; Zhou, J. *Chem. Rev.* **2000**, *100*, 235-349. (d) Costas, M.; Mehn, M. P.; Jensen, M. P.; Que, L. *Chem. Rev.* **2004**, *104*, 939-986. (e) Abu-Omar, M. M.; Loaiza, A.; Hontzeas, N. *Chem. Rev.* **2005**, *105*, 2227-2252. (f) Kovaleva, E. G.; Lipscomb, J. D. *Nat. Chem. Biol.* **2008**, *4*, 186-193.

(3) (a) Ragsdale, S. W. *Chem. Rev.* **2006**, *106*, 3317-3337. (b) Baik, M. H.; Newcomb, M.; Friesner, R. A.; Lippard, S. J. *Chem. Rev.* **2003**, *103*, 2385-2419.

(4) Groves, J. T. *J. Chem. Educ.* **1985**, *62*, 928-931.

been linked to the reactivity,⁵ though the precise connection between electronic structure and function remains unclear. Further development of the relationship between electronic structure and function of the class of paramagnetic transition metal complexes with MLMBs would assist in understanding how these enzymes work and how catalysts can be better designed to capture similar efficiency and selectivity in the synthetic setting.



Scheme 1.1. The electronic structure of P450 compound I and ‘radical rebound’ mechanism. Four descriptions for the iron oxo intermediate P450-I: (a) Fe^V oxo; (b) Fe^{IV} oxo with porphyrin π radical; (c) Fe^{IV} oxo with sulfide radical; and (d) Fe^{IV} oxyl radical. The radical rebound mechanism (e) shows hydrogen atom abstraction and Fe–C radical coupling. [O] represents dioxygen driven re-oxidation of the Fe^{II} state to compound I.

1-2. Electronic Structure.

There are three descriptors necessary to codify the electronic structure of such species, in simplest form they are (1) the oxidation state, (2) the spin state, and (3) the nature of the M–E bond. For some molecules these three factors can be straightforwardly assigned through a combination of spectroscopy,

(s) (a) Decker, A.; Rohde, J. U.; Klinker, E. J.; Wong, S. D.; Que, L., Jr.; Solomon, E. I. *J. Am. Chem. Soc.* **2007**, *129*, 15983-15996. (b) Bernasconi, L.; Louwse, M. J.; Baerends, E. J. *Eur. J. Inorg. Chem.* **2007**, 3023-3033. (c) Ye, S. F.; Neese, F. *Curr. Opin. Chem. Biol.* **2009**, *13*, 89-98.

theory, and/or structure determination. However amongst active heme and non-heme intermediates and their analogs these descriptors become ambiguous to assign due to a variety of factors. Often the ligands supporting the metal center are redox active, which creates a complication in assigning a formal oxidation state or spin state to the metal since unpaired electrons may be localized in ligand-based orbitals, metal-based orbitals, or both. This is the case for cytochrome P450, where the formal iron(V) oxidation state depiction (Cys-S)(porphyrin)Fe^V(O), is better described with a ligand centered radical on either the porphyrin or cysteine sulfide, as (Cys-S)(porphyrin[•])Fe^{IV}(O) or (Cys-S[•])(porphyrin)Fe^{IV}(O), respectively. The oxidation state must thus be described in terms of a *molecular oxidation state* which accounts for the oxidation levels of both the metal and ligands. Likewise, the spin state must be described as a *molecular spin state*, in which both the metal and ligands may bear unpaired electron density. The interaction between these localized spins (i.e. ferromagnetic and antiferromagnetic coupling) must also be taken into account.

The nature of the M-E bond then must be described with the molecular oxidation and spin states in mind. High-spin species are likely to have partially populated M-E σ^* and π^* orbitals, resulting in formal bond orders less than that for true double or triple bonds. The E ligand itself may also be non-innocent, with radicals being localized on E; for the cytochrome P450 this might look like (Cys-S)(porphyrin)Fe^{IV}(O[•]) where an oxyl radical bears an unpaired spin in place of the porphyrin or sulfide. Part of the energetic interaction between M and E may therefore be derived from an interaction of spins (i.e. antiferromagnetic coupling) rather than from a traditional π bond.

The electronic structure of paramagnetic metal complexes with MLMBs can therefore only be appropriately described by the following modified descriptors: (1) a *molecular oxidation state* that takes into account the oxidation state of the metal and the oxidation states of redox active ligands; (2) a

molecular spin state that combines the spin states of the metals and ligands in their respective oxidation states, and describes the interaction or coupling of the spins between the localized fragments; and (3) *an orbital understanding of the M–E bond* that accounts for unpaired electrons within the σ and π framework and for the possible presence and interaction of unpaired electrons on the E ligand itself. These factors may be further complicated by spin state tautomerism⁶ or spin crossover,⁷ and by the fact that the covalent nature of the metal-ligand bonding interactions may blur the localization of electrons, oxidation states, and spin states on particular atoms and fragments.

1-3. Biological and Synthetic Iron Oxos.

Porphyrin iron(IV) oxos have been synthesized and characterized by spectroscopic methods,⁸ though they have yet to be crystallographically characterized. Radical character within the iron oxo bond has been postulated as a key factor in engendering hydroxylase like activity. Although the properties of the ferryl bond are unaffected by the presence of a porphyrin π cation radical in model studies, they are sensitive to the nature of the axial ligand *trans* to the oxo.⁹ The electronic structure of the P450 enzyme has been determined by Mössbauer and EPR studies to be an intermediate-spin $S = 1$ iron(IV) center exchange coupled with a ligand-based radical $S = 1/2$ with significant density at the axial sulfur of the cysteine ligand.¹⁰

(6) Storr, T.; Verma, P.; Pratt, R. C.; Wasinger, E. C.; Shimazaki, Y.; Stack, T. D. P. *J. Am. Chem. Soc.* **2008**, *130*, 15448-15459.

(7) Gütlich, P.; Garcia, Y.; Goodwin, H. A. *Chem. Soc. Rev.* **2000**, *29*, 419-427.

(8) (a) Groves, J. T. *J. Inorg. Biochem.* **2006**, *100*, 434-447. (b) Groves, J. T.; Haushalter, R. C.; Nakamura, M.; Nemo, T. E.; Evans, B. J. *J. Am. Chem. Soc.* **1981**, *103*, 2884-2886.

(9) Fujii, H. *Coord. Chem. Rev.* **2002**, *226*, 51-60.

(10) Rittle, J.; Green, M. T. *Science* **2010**, *330*, 933-937.

A very different electronic structure has been determined for non-heme systems,^{2a, 11} where characterization of taurine α -ketoglutarate dioxygenase (TauD),¹² prolyl 4-hydroxylase (P4H),¹³ tyrosine hydroxylase (TyrH),¹⁴ halogenase CytC3,¹⁵ and halogenase SyrB2,¹⁶ has in each case revealed a high-spin $S = 2$ iron(IV) oxo. Synthetic non-heme analogs are less amenable to spectroscopic detection than those with porphyrin chromophores,¹⁷ but a mononuclear model complex supported by a pentadentate cyclam acetate ligand was first directly observed by Wieghardt utilizing Mössbauer spectroscopy to assign the oxidation state as iron (IV).¹⁸ Since then a veritable battalion of iron oxos have been prepared and characterized primarily with polydentate pyridine and amine ligands, led by the laboratories of Que¹⁷ and Nam.¹⁹ Until recently all of the spectroscopically and structurally characterized²⁰ mononuclear non-heme iron oxos were observed to possess an $S = 1$ spin state.^{17,19} The lone exception is the transiently observed pentaquoferryl, $[(\text{H}_2\text{O})_5\text{Fe}^{\text{IV}}(\text{O})]^{2+}$, shown by Bakac to be high-spin iron(IV) by applied field Mössbauer.²¹

Non-heme iron oxo complexes have been shown to perform HAT, aliphatic and aromatic hydroxylation, alkene epoxidation, sulfide oxidation, phosphine oxidation, and nitrogen dealkylation.¹⁹ However, HAT and hydroxylation reactivity is only observed for substrates with weak C–H bonds, and

(11) Bollinger, J. M.; Krebs, C. J. *Inorg. Biochem.* **2006**, *100*, 586-605.

(12) (a) Price, J. C.; Barr, E. W.; Tirupati, B.; Bollinger, J. M.; Krebs, C. *Biochemistry* **2003**, *42*, 7497-7508. (b) Bollinger, J. M.; Price, J. C.; Hoffart, L. M.; Barr, E. W.; Krebs, C. *Eur. J. Inorg. Chem.* **2005**, 4245-4254. (c) Krebs, C.; Price, J. C.; Baldwin, J.; Saleh, L.; Green, M. T.; Bollinger, J. M. *Inorg. Chem.* **2005**, *44*, 742-757.

(13) Hoffart, L. M.; Barr, E. W.; Guyer, R. B.; Bollinger, J. M.; Krebs, C. *Proc. Natl. Acad. Sci. U. S. A.* **2006**, *103*, 14738-14743.

(14) Eser, B. E.; Barr, E. W.; Frantom, P. A.; Saleh, L.; Bollinger, J. M.; Krebs, C.; Fitzpatrick, P. F. *J. Am. Chem. Soc.* **2007**, *129*, 11334-11335.

(15) Galonic, D. P.; Barr, E. W.; Walsh, C. T.; Bollinger, J. M.; Krebs, C. *Nat. Chem. Biol.* **2007**, *3*, 113-116.

(16) Matthews, M. L.; Krest, C. M.; Barr, E. W.; Vaillancourt, F. H.; Walsh, C. T.; Green, M. T.; Krebs, C.; Bollinger, J. M. *Biochemistry* **2009**, *48*, 4331-4343.

(17) Que, L., Jr. *Acc. Chem. Res.* **2007**, *40*, 493-500. and references contained therein.

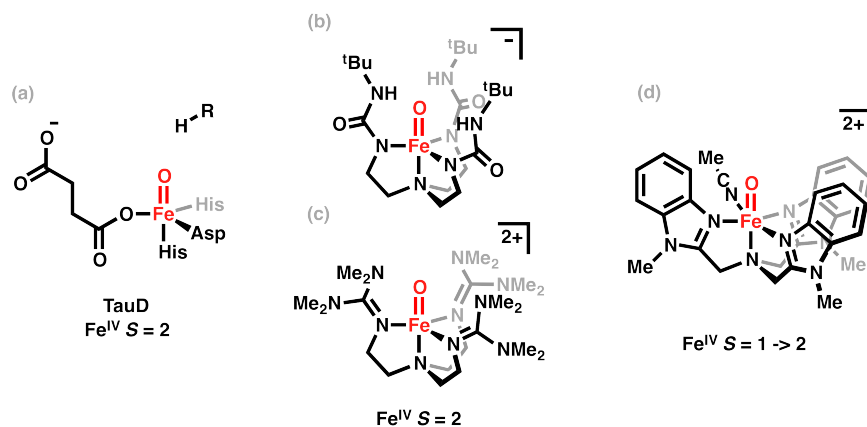
(18) Grapperhaus, C. A.; Mienert, B.; Bill, E.; Weyhermuller, T.; Wieghardt, K. *Inorg. Chem.* **2000**, *39*, 5306-5317.

(19) Nam, W. *Acc. Chem. Res.* **2007**, *40*, 522-531. and references contained therein.

(20) Rohde, J. U.; In, J. H.; Lim, M. H.; Brennessel, W. W.; Bukowski, M. R.; Stubna, A.; Münck, E.; Nam, W.; Que, L., Jr. *Science* **2003**, *299*, 1037-1039.

(21) (a) Pestovsky, O.; Bakac, A. *J. Am. Chem. Soc.* **2004**, *126*, 13757-13764. (b) Pestovsky, O.; Stoian, S.; Bominaar, E. L.; Shan, X. P.; Münck, E.; Que, L., Jr.; Bakac, A. *Angew. Chem., Int. Ed.* **2005**, *44*, 6871-6874.

yields and efficiencies are greatly limited compared to enzymatic systems. Theoretical studies have predicted the $S = 2$ state to be significantly more reactive than the $S = 1$ state.⁵ The reactivity that has been observed for systems with an $S = 1$ ground state may in fact rely on the accessibility of the $S = 2$ state via two-state reactivity.²²



Scheme 1.2. Examples of high-spin non-heme iron oxos. The hydrogen abstracting intermediate of TauD (a),¹² crystallographically characterized quintet iron oxos reported by Borovik (b)²⁴ and Que (c),²⁵ and a highly reactive triplet ground state triplet iron oxo observed by Nam (c).²⁷

Recently, a move away from pseudo-octahedral ligand fields allowed for the isolation of high-spin iron(IV) oxos in trigonal bipyramidal frameworks.²³ Crystallographic and spectroscopic characterization of a trianionic tris(urea)amine supported iron oxo anion by Borovik,²⁴ and a tris(guanidine)amine iron oxo dication by Que,²⁵ confirmed the presence of iron(IV) and an $S = 2$ ground state. Disappointingly, the quintet iron oxos did not display enhanced rates in HAT or oxo transfer reactions, a result attributed

(22) (a) Hirao, H.; Kumar, D.; Que, L.; Shaik, S. *J. Am. Chem. Soc.* **2006**, *128*, 8590-8606. (b) Dhuri, S. N.; Seo, M. S.; Lee, Y. M.; Hirao, H.; Wang, Y.; Nam, W.; Shaik, S. *Angew. Chem., Int. Ed.* **2008**, *47*, 3356-3359. (c) Klinker, E. J.; Shaik, S.; Hirao, H.; Que, L., Jr. *Angew. Chem., Int. Ed.* **2009**, *48*, 1291-1295.

(23) England, J.; Martinho, M.; Farquhar, E. R.; Frisch, J. R.; Bominaar, E. L.; Münck, E.; Que, L., Jr. *Angew. Chem., Int. Ed.* **2009**, *48*, 3622-3626.

(24) Lacy, D. C.; Gupta, R.; Stone, K. L.; Greaves, J.; Ziller, J. W.; Hendrich, M. P.; Borovik, A. S. *J. Am. Chem. Soc.* **2010**, *132*, 12188-12190.

(25) England, J.; Guo, Y. S.; Farquhar, E. R.; Young, V. G.; Münck, E.; Que, L., Jr. *J. Am. Chem. Soc.* **2010**, *132*, 8635-8644.

to the bulky nature of the ligands necessary to afford isolation.²⁶ Synthesis of an analogous $S = 2$ iron oxo with only two guanidine arms did lead to a species more active than most of the lower spin examples.²⁶ Surprisingly, the most reactive species among non-heme iron(IV) oxos is not a high-spin system. Nam, Shaik, and Latour have proposed that this tris(benzimidazole)amine complex features a stable $S = 1$ ground state and a highly reactive low-lying $S = 2$ state;²⁷ a reminder that knowing only the electronic structure of the ground state may be insufficient towards explaining reactivity.

1-4. Late Metal Imides.

Metal imides do not have a biological counterpart, however gaining understanding about their electronic structure is important in developing methods for C–H amination and nitrene transfer.²⁸ An increasing number of late metal imides have been synthesized; examples have been isolated on iron,²⁹ cobalt,³⁰ nickel,³¹ ruthenium,³² osmium,⁶⁹ and iridium.³³ Terminal imides have yet to be isolated on copper, though they have been implicated as intermediates in nitrene transfer and HAT.³⁴ Many of the

(26) England, J.; Guo, Y. S.; Van Heuvelen, K. M.; Cranswick, M. A.; Rohde, G. T.; Bominaar, E. L.; Münck, E.; Que, L. J. *Am. Chem. Soc.* **2011**, *133*, 11880-11883.

(27) Seo, M. S.; Kim, N. H.; Cho, K. B.; So, J. E.; Park, S. K.; Clémancey, M.; Garcia-Serres, R.; Latour, J. M.; Shaik, S.; Nam, W. *Chem. Sci.* **2011**, *2*, 1039-1045.

(28) (a) Bergman, R. G. *Nature* **2007**, *446*, 391-393. (b) Labinger, J. A.; Bercaw, J. E. *Nature* **2002**, *417*, 507-514.

(29) Iron imides: See references 36, 37, 38, 39, 40, and 42 and Section 1-5. Iron Imides for details.

(30) Cobalt imides: See references 49, 37a, 37b, 50, 51, 52, 53 and Section 1-6. Cobalt Imides. for details.

(31) Nickel imides: (a) Mendiola, D. J.; Hillhouse, G. L. *J. Am. Chem. Soc.* **2001**, *123*, 4623-4624. (b) Waterman, R.; Hillhouse, G. L. *J. Am. Chem. Soc.* **2008**, *130*, 12628-12629. (c) Kogut, E.; Wiencko, H. L.; Zhang, L. B.; Cordeau, D. E.; Warren, T. H. *J. Am. Chem. Soc.* **2005**, *127*, 11248-11249. (d) Iluc, V. M.; Hillhouse, G. L. *J. Am. Chem. Soc.* **2010**, *132*, 15148-15150. (e) Laskowski, C. A.; Miller, A. J. M.; Hillhouse, G. L.; Cundari, T. R. *J. Am. Chem. Soc.* **2011**, *133*, 771-773.

(32) Ruthenium imides: (a) Danopoulos, A. A.; Wilkinson, G.; Hussainbates, B.; Hursthouse, M. B. *Polyhedron* **1992**, *11*, 2961-2964. (b) Burrell, A. K.; Steedman, A. J. *J. Chem. Soc., Chem. Commun.* **1995**, 2109-2110. (c) Burrell, A. K.; Steedman, A. J. *Organometallics* **1997**, *16*, 1203-1208. (d) Leung, S. K. Y.; Tsui, W. M.; Huang, J. S.; Che, C. M.; Liang, J. L.; Zhu, N. Y. *J. Am. Chem. Soc.* **2005**, *127*, 16629-16640. (e) Walstrom, A. N.; Fullmer, B. C.; Fan, H. J.; Pink, M.; Buschhorn, D. T.; Caulton, K. G. *Inorg. Chem.* **2008**, *47*, 9002-9009. (f) Fantauzzi, S.; Gallo, E.; Caselli, A.; Ragaini, F.; Casati, N.; Macchi, P.; Cenini, S. *Chem. Commun.* **2009**, 3952-3954. (g) Takaoka, A.; Gerber, L. C. H.; Peters, J. C. *Angew. Chem., Int. Ed.* **2010**, *49*, 4088-4091.

(33) Iridium imides: (a) Glueck, D. S.; Hollander, F. J.; Bergman, R. G. *J. Am. Chem. Soc.* **1989**, *111*, 2719-2721. (b) Glueck, D. S.; Wu, J. X.; Hollander, F. J.; Bergman, R. G. *J. Am. Chem. Soc.* **1991**, *113*, 2041-2054.

(34) Badiei, Y. M.; Dinescu, A.; Dai, X.; Palomino, R. M.; Heinemann, F. W.; Cundari, T. R.; Warren, T. H. *Angew. Chem., Int. Ed.* **2008**, *47*, 9961-9964.

isolated late metal imides are surprisingly stable, in fact only a handful exhibit HAT. In addition to the iron and cobalt examples which will be discussed below, Warren has shown HAT to a nickel(III) imide,³⁵ and Gallo and Che have shown C–H amination from ruthenium(VI) diimides.

In analogy to oxo chemistry, a specific electronic structure may be necessary to achieve more facile reactivity. Many early examples of iron and cobalt imides, for instance, were low- or intermediate-spin complexes with strong field ligands, a sharp contrast to the analogous enzymatic iron oxos which are high-spin ($S = 2$ for non-heme Fe^{IV} oxos) and are supported by much weaker donors. Since that work metal imides have been made in a greater variety of ligand environments and consequently with a range of spin states and electronic structures, which in some cases has resulted in enhanced reactivity.

1-5. Iron Imides.

A terminal iron imide was first isolated by Lee in a tetranuclear iron cubane, in which one unique iron was ligated by a terminal imide and by 3 bridging imides.³⁶ Mossbauer spectroscopy was used to assign the unique site as iron(IV); EPR revealed the cluster's spin state to be $S = 1/2$.³⁶ Peters and coworkers have made a series of mononuclear terminal iron imides starting with the first mononuclear example on a tris(phosphino)borate platform^{37a} and building off of this tripodal motif with a variety of modified^{37b,c,d,e} or related ligands.^{37f,g} These complexes span a range of oxidation and spin states: $\text{Fe}^{\text{II}} S = 0$,^{37c,g} $\text{Fe}^{\text{III}} S = 1/2$,^{37a,b,d,e} and $\text{Fe}^{\text{IV}} S = 1$.^{37f} The reactivity of these complexes has thus far been limited to nitrene transfer

(35) Kogut, E.; Wiencko, H. L.; Zhang, L. B.; Cordeau, D. E.; Warren, T. H. *J. Am. Chem. Soc.* **2005**, *127*, 11248-11249.

(36) Verma, A. K.; Nazif, T. N.; Achim, C.; Lee, S. C. *J. Am. Chem. Soc.* **2000**, *122*, 11013-11014.

(37) (a) Brown, S. D.; Betley, T. A.; Peters, J. C. *J. Am. Chem. Soc.* **2003**, *125*, 322-323. (b) Betley, T. A.; Peters, J. C. *J. Am. Chem. Soc.* **2003**, *125*, 10782-10783. (c) Brown, S. D.; Peters, J. C. *J. Am. Chem. Soc.* **2005**, *127*, 1913-1923. (d) Mehn, M. P.; Brown, S. D.; Jenkins, D. M.; Peters, J. C.; Que, L., Jr. *Inorg. Chem.* **2006**, *45*, 7417-7427. (e) Lu, C. C.; Saouma, C. T.; Day, M. W.; Peters, J. C. *J. Am. Chem. Soc.* **2007**, *129*, 4-5. (f) Thomas, C. M.; Mankad, N. P.; Peters, J. C. *J. Am. Chem. Soc.* **2006**, *128*, 4956-4957. (g) Moret, M. E.; Peters, J. C. *Angew. Chem., Int. Ed.* **2011**, *50*, 2063-2067.

to carbon monoxide to make isocyanates.^{37a} Tris(carbene)borates have also been used to stabilize iron imides, as shown by Smith for both Fe^{III} $S = 1/2$,^{38a} and Fe^{IV} $S = 1$.^{38b}

Iron imides can also be isolated in geometries that are not pseudo-tetrahedral at iron. With a terphenyl ligand designed to stabilize extremely low-coordinate complexes Power has isolated a formally iron(V) diimide with one very short Fe–N bond (1.619(2) Å); the spin state was determined by magnetometry to be $S = 1/2$.³⁹ Holland has synthesized several stable intermediate-spin ($S = 3/2$) trigonal iron(III) imides within a β -diketiminato framework.^{40a,b} This quartet spin state makes the β -diketiminato system unique from the other iron(III) examples, and may be a factor in the additional reactivity that was observed. These reactions included carbodiimide and isocyanate formation via group transfer to isocyanides and CO^{40c} and more notably the first examples of intermolecular HAT to an isolated iron imide.^{40a,d,e} Que isolated a short-lived pseudo-octahedral tosyl imido supported by a tetrapyrrolineamine ligand, and characterized its structure via extended X-ray absorption fine structure (EXAFS) and its electronic structure, iron(IV) $S = 1$, by X-ray absorption spectroscopy (XAS) and applied-field Mössbauer.⁴¹

Square planar iron imides have been isolated by Chirik which evince rather complex electronic structures in part due to the non-innocent nature of the supporting bis(imino)pyridine ligand.⁴² In the case of aryl substituted imides they have been assigned as iron(III) by Mössbauer with an overall spin

(38) (a) Scepianiak, J. J.; Young, J. A.; Bontchev, R. P.; Smith, J. M. *Angew. Chem., Int. Ed.* **2009**, *48*, 3158-3160. (b) Nieto, I.; Ding, F.; Bontchev, R. P.; Wang, H. B.; Smith, J. M. *J. Am. Chem. Soc.* **2008**, *130*, 2716-2717.

(39) Ni, C. B.; Fettingner, J. C.; Long, G. J.; Brynda, M.; Power, P. P. *Chem. Commun.* **2008**, 6045-6047.

(40) (a) Eckert, N. A.; Vaddadi, S.; Stoian, S.; Lachicotte, R. J.; Cundari, T. R.; Holland, P. L. *Angew. Chem., Int. Ed.* **2006**, *45*, 6868-6871. (b) Cowley, R. E.; DeYonker, N. J.; Eckert, N. A.; Cundari, T. R.; DeBeer, S.; Bill, E.; Ottenwaelder, X.; Flaschenriem, C.; Holland, P. L. *Inorg. Chem.* **2010**, *49*, 6172-6187. (c) Cowley, R. E.; Eckert, N. A.; Elhaik, J.; Holland, P. L. *Chem. Commun.* **2009**, 1760-1762. (d) Cowley, R. E.; Holland, P. L. *Inorg. Chim. Acta* **2011**, *369*, 40-44. (e) Cowley, R. E.; Eckert, N. A.; Vaddadi, S.; Figg, T. M.; Cundari, T. R.; Holland, P. L. *J. Am. Chem. Soc.* **2011**, *133*, 9796-9811.

(41) Klinker, E. J.; Jackson, T. A.; Jensen, M. P.; Stubna, A.; Juhasz, G.; Bominaar, E. L.; Münck, E.; Que, L., Jr. *Angew. Chem., Int. Ed.* **2006**, *45*, 7394-7397.

(42) (a) Bart, S. C.; Lobkovsky, E.; Bill, E.; Chirik, P. J. *J. Am. Chem. Soc.* **2006**, *128*, 5302-5303. (b) Bowman, A. C.; Milsmann, C.; Bill, E.; Turner, Z. R.; Lobkovsky, E.; DeBeer, S.; Wieghardt, K.; Chirik, P. J. *J. Am. Chem. Soc.* **2011**, *133*, 17353-17369.

state of $S = 1$ comprised of an intermediate-spin ($S = 3/2$) iron(III) antiferromagnetically coupled to a bis(imino)pyridine centered radical $S = 1/2$ (the ligand oxidation state was established by analysis of C–C and C–N bond lengths from the X-ray structure).^{42a} The aryl imides were also shown to undergo hydrogenation to produce anilines, a process that could also be carried out catalytically.^{42a} In the case of alkyl imides the X-ray data shows the bis(imino)pyridine ligand is likely a closed shell dianion,^{42b} which leads to three possible descriptions for the iron imide fragment: a diamagnetic iron(II) with a coordinated neutral nitrene, a diamagnetic iron (IV) with a dianionic imide, or a low-spin ($S = 1/2$) iron (III) antiferromagnetically coupled to an imidyl radical. The latter description is favored in the case of a 2-adamantyl imide, while a resonance combination of the former two descriptions is most consistent for data from other alkyl imides, including a 1-adamantyl imide. The discrepancy between adamantly isomers highlights the sensitivity of electronic structure to very minor structural changes.^{42b}

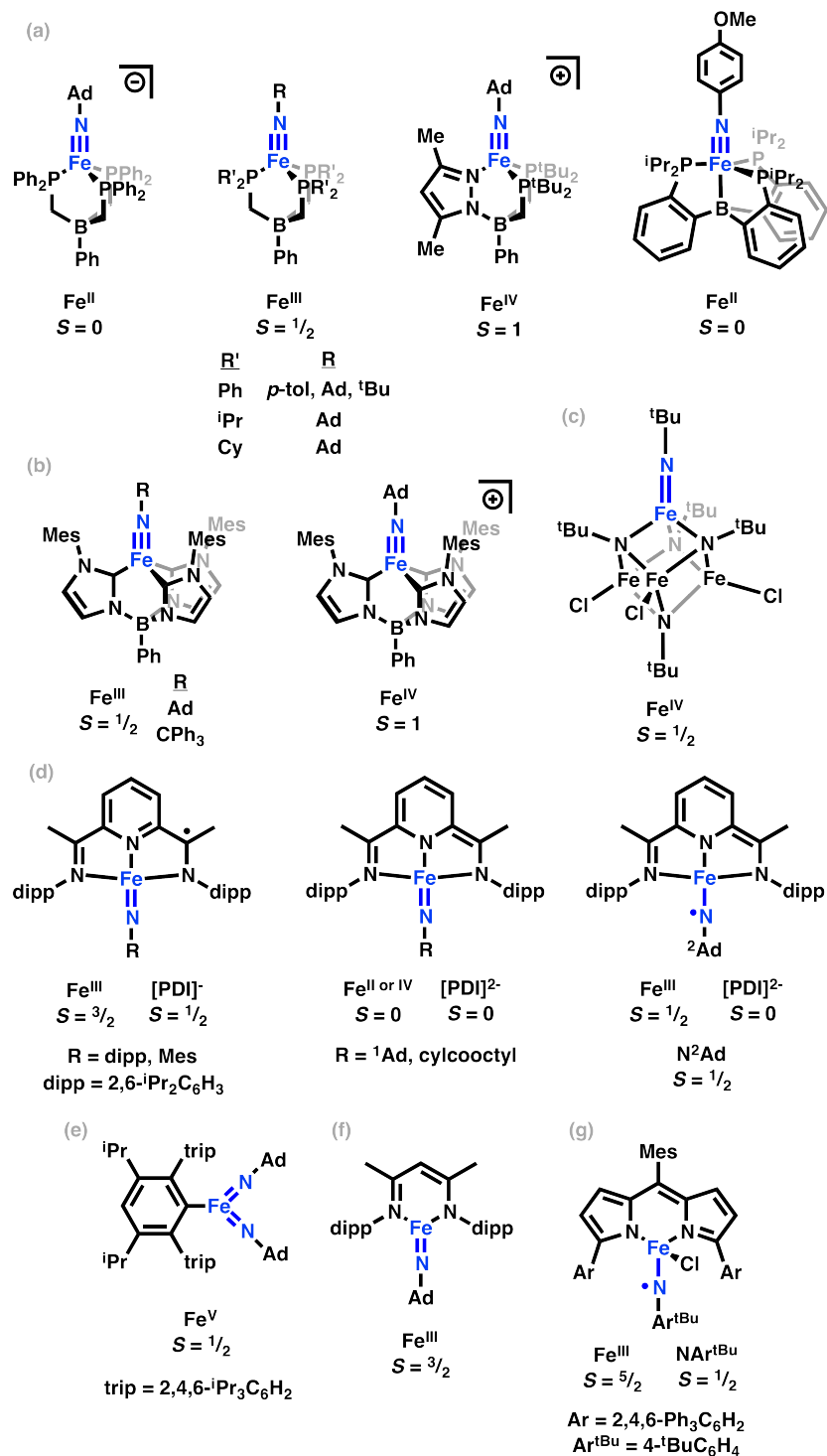
Iron imides have also been implicated as the key intermediates in several systems that have eluded isolation. Examples of the reactivity observed include intramolecular aryl C–H amination from Que⁴³ and Latour,⁴⁴ intramolecular HAT from Power,³⁹ and intermolecular HAT from Borovik⁴⁵ and Peters.⁴⁶ In the example from Peters, with a tris(phosphino)silyl ligand, the intermediate *para*-tolyl imide was observed to be low-spin iron(III) by EPR.⁴⁶ Nitrene transfer to isocyanide to form carbodiimides and to azide to give diazenes were observed in addition to HAT from dihydroanthracene.⁴⁶ The expanded scope of reactivity relative to the many other low-spin ($S = 1/2$) iron(III) imides was attributed to the possible accessibility of two-state reactivity²² via a low-lying intermediate-spin ($S = 3/2$) state.

(43) Jensen, M. P.; Mehn, M. P.; Que, L., Jr. *Angew. Chem., Int. Ed.* **2003**, *42*, 4357-4360.

(44) Avenier, F.; Gouré, E.; Dubourdeaux, P.; Sénèque, O.; Oddou, J. L.; Pécaut, J.; Chardon-Noblat, S.; Deronzier, A.; Latour, J. M. *Angew. Chem., Int. Ed.* **2008**, *47*, 715-717.

(45) Lucas, R. L.; Powell, D. R.; Borovik, A. S. *J. Am. Chem. Soc.* **2005**, *127*, 11596-11597.

(46) Mankad, N. P.; Müller, P.; Peters, J. C. *J. Am. Chem. Soc.* **2010**, *132*, 4083-4084.



Scheme 1.3. Crystallographically characterized iron imides. Reported by: Peters (a),³⁷ Smith (b),³⁸ Lee (c),³⁶ Chirik (d),⁴² Power (e),³⁹ Holland (f),^{40b} and Betley (g).⁴⁸

An iron(IV) imide was suspected as an intermediate after observation of intramolecular C–H amination upon addition of organic azides to dipyrin iron(II) complexes as described by Betley⁴⁷ and herein. Modification of the ligand to prevent intramolecular activation led to isolation of a dipyrin iron imide chloride, featuring a very long iron imide bond (1.768(2) Å).⁴⁸ Further elucidation of the electronic structure revealed a high-spin $S = 5/2$ iron(III) center antiferromagnetically coupled to an imidyl radical $S = 1/2$ to give an overall $S = 2$ spin state. The isolated ferric imidyl radical which features very bulky aryl substituents on the dipyrin performed C–H amination and olefin aziridination stoichiometrically, while an alkyl substituted dipyrin carried out both reactions catalytically and likely proceeds through a fully analogous iron(III) imidyl radical intermediate.⁴⁸

1-6. Cobalt Imides.

Several examples of cobalt imides have been isolated, though unlike the diversity seen with iron, they are all cobalt(III) and all have singlet ground states. The first terminal cobalt imide was isolated within a tris(phosphino)borate framework by Peters and coworkers;^{49,37b,37d} nitrene transfer to CO to form an isocyanate was observed.⁴⁹ Tris(carbene)amine supported cobalt imides were made by Meyer, but at room temperature they decomposed via insertion of the imide into one of the cobalt–carbene bonds.⁵⁰ Another tripodally-coordinated example came from Theopold, featuring a tris(pyrazolyl)borate ligand and an adamantyl imide.⁵¹ Upon heating C–H amination of a *tert*-butyl group of the ligand was observed, a result that was initially ascribed to the complex having an $S = 1$ spin state.^{51a} Although it was

(47) King, E. R.; Betley, T. A. *Inorg. Chem.* **2009**, *48*, 2361-2363.

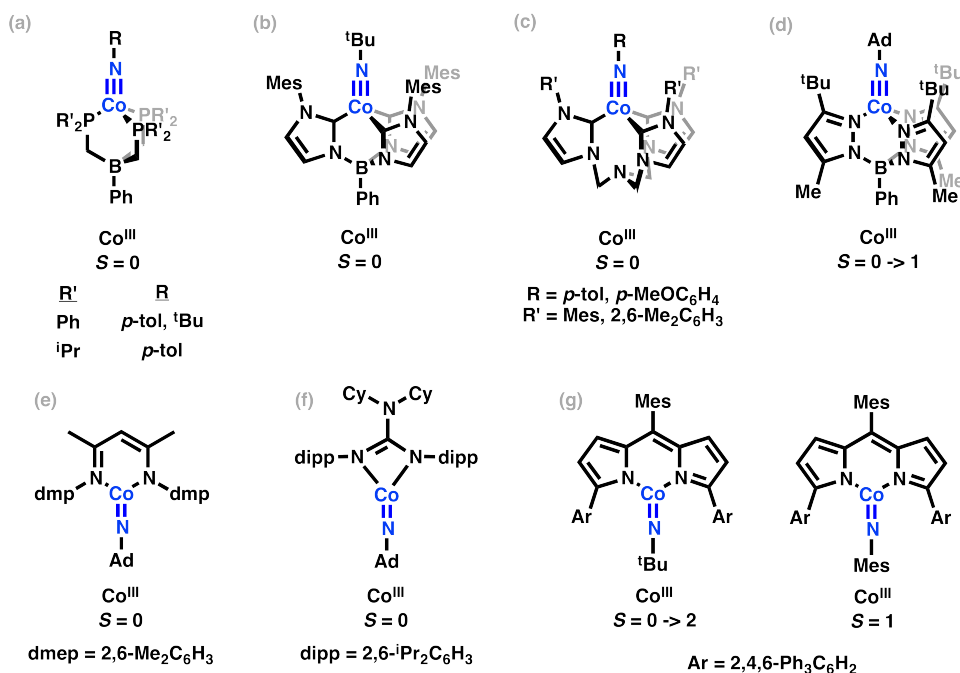
(48) King, E. R.; Hennessy, E. T.; Betley, T. A. *J. Am. Chem. Soc.* **2011**, *133*, 4917-4923.

(49) Jenkins, D. M.; Betley, T. A.; Peters, J. C. *J. Am. Chem. Soc.* **2002**, *124*, 11238-11239.

(50) Hu, X. L.; Meyer, K. *J. Am. Chem. Soc.* **2004**, *126*, 16322-16323.

(51) (a) Shay, D. T.; Yap, G. P. A.; Zakharov, L. N.; Rheingold, A. L.; Theopold, K. H. *Angew. Chem., Int. Ed.* **2005**, *44*, 1508-1510. (b) Shay, D. T.; Yap, G. P. A.; Zakharov, L. N.; Rheingold, A. L.; Theopold, K. H. *Angew. Chem., Int. Ed.* **2006**, *45*, 7870.

later discovered that spin ground state is $S = 0$, the accessibility of a triplet state near room temperature likely factors into the capability for C–H activation.^{51b} A tris(carbene)borane supported cobalt imide was made by Smith by abstraction of a hydrogen atom from a cobalt(II) amide with an aryloxy radical.⁵² Three-coordinate cobalt imides have been isolated by Warren with a β -diketiminato ligand,⁵³ and by Jones supported by a bulky guanidinate.⁵⁴



Scheme 1.4. Isolated cobalt imides. Reported by: Peters (a),^{49,37b,37d} Smith (b),⁵² Meyer (c),⁵⁰ Theopold (d),⁵¹ Warren (e),⁵³ Jones (f),⁵⁴ and Betley (g).⁵⁷

Non-isolable imides have also been suggested in systems where HAT was observed. Theopold has observed (via isolation of the resulting amide species) intramolecular hydrogen atom abstraction followed by either C–C or Co–C bond formation in a tris(pyrazolyl)borate system similar to the

(52) Cowley, R. E.; Bontchev, R. P.; Sorrell, J.; Sarracino, O.; Feng, Y. H.; Wang, H. B.; Smith, J. M. *J. Am. Chem. Soc.* **2007**, *129*, 2424-2425.

(53) Dai, X. L.; Kapoor, P.; Warren, T. H. *J. Am. Chem. Soc.* **2004**, *126*, 4798-4799.

(54) Jones, C.; Schulten, C.; Rose, R. P.; Stasch, A.; Aldridge, S.; Woodul, W. D.; Murray, K. S.; Moubaraki, B.; Brynda, M.; La Macchia, G.; Gagliardi, L. *Angew. Chem., Int. Ed.* **2009**, *48*, 7406-7410.

adamantyl case described above, but instead using trimethylsilyl azide as the nitrene source.⁵⁵ A transient intermediate capable of forming isocyanates with CO, and capable of intermolecular HAT from 1,2-diphenylhydrazine to form the resulting amide, has been described as a cobalt imide by Arnold.⁵⁶

The isolation of two three-coordinate cobalt imides is described herein for a dipyrin ligand with bulky aryl substituents.⁵⁷ The first an alkyl cobalt imide that partially populates a quintet state at room temperature carried out nitrene transfer to phosphine, and a triplet aryl cobalt imide underwent intramolecular hydrogen atom abstraction.

1-7. Dipyrrole Ligand Architectures.

Metals in metalloproteins are frequently ligated by prototypical weak field ligands: carboxylates and imidazoles of amino acid side chains as in soluble methane monooxygenase (sMMO)³ and taurine α -ketoglutarate dioxygenase (TauD),¹² and unique cofactors such as porphyrins as in cytochrome P450.¹ Structural mimics of complex active sites such as sMMO have been made,⁵⁸ though this ligand framework cannot easily be mimicked by one simple modular ligand design. Many synthetic porphyrin models have been studied,⁸ although the tetrachelating nature of porphyrin restricts the available geometries (and electronic structures) that can be accessed, such as those of non-heme systems. It is also non-trivial to introduce appropriately oriented sterically demanding substituents near the metal or M–E vector within a porphyrin construct. The pyrrole subunit of a porphyrin is a weak σ donor, and the pyrrole π system attenuates the nitrogen atom's ability to be a π base. This lessened basicity makes

(55) Thyagarajan, S.; Shay, D. T.; Incarvito, C. D.; Rheingold, A. L.; Theopold, K. H. *J. Am. Chem. Soc.* **2003**, *125*, 4440-4441.

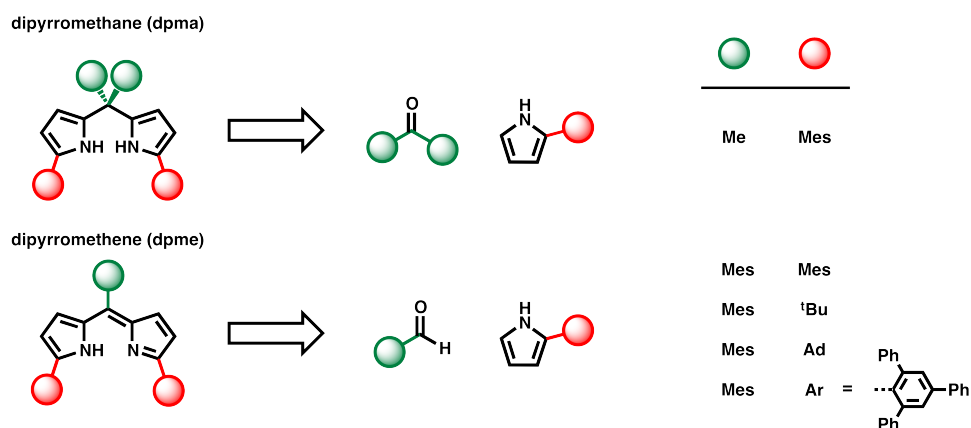
(56) Chomitz, W. A.; Arnold, J. *Chem. Commun.* **2008**, 3648-3650.

(57) Chapter 4: Catalytic C–H Bond Amination from High-Spin Iron Imide Complexes

(58) Yoon, S.; Lippard, S. J. *J. Am. Chem. Soc.* **2004**, *126*, 2666-2667.

pyrrole less reducing than most anionic N donors, and may be why porphyrin is stable to high metal oxidation states.

Dipyrromethanes, **dpma**,⁵⁹ and dipyrromethenes (or dipyrins), **dpme**,⁶⁰ are pyrrole-based chelates that can support transition metals in a variety of geometries and coordination modes. Initial efforts into dipyrromethane coordination chemistry focused on *f*-block elements⁶¹ or featured the ligand in the η^5, η^1 coordination mode on early metals⁶² or with both rings coordinating η^5, η^5 in ferrocene analogs.⁶³



Scheme 1.5. Dipyrrole ligands referred to throughout this thesis.

Dipyrromethenes are perhaps most recognized as a ligand for boron in fluorescent dye chemistry,⁶⁴ but their homoleptic coordination chemistry with late metals was explored early on in large part due to

(59) (a) Raines, S.; Kovacs, C. A. *J Heterocyclic Chem* **1970**, *7*, 223-224. (b) Bellut, H.; Miller, C. D.; Koester, R. In *Synthesis in Inorganic and Metal-Organic Chemistry*; M. Dekker: New York, 1971; Vol. 1, pp 83-91. (c) Lee, C. H.; Lindsey, J. S. *Tetrahedron* **1994**, *50*, 11427-11440.

(60) (a) In *Die Chemie des Pyrrols*; Fischer, H., Orth, H., Eds.; Akademische Verlagsgesellschaft: Leipzig, 1940; Vol. IX, pp 1-151. (b) Falk, H. *The Chemistry of Linear Oligopyrroles and Bile Pigments*; Springer-Verlag: Vienna, 1989. (c) Wagner, R. W.; Lindsey, J. S. *Pure Appl. Chem.* **1996**, *68*, 1373-1380.

(61) Dube, T.; Conoci, S.; Gambarotta, S.; Yap, G. P. A.; Vasapollo, G. *Angew. Chem., Int. Ed.* **1999**, *38*, 3657-3659.

(62) (a) Harris, S. A.; Ciszewski, J. T.; Odom, A. L. *Inorg. Chem.* **2001**, *40*, 1987-1988. (b) Novak, A.; Blake, A. J.; Wilson, C.; Love, J. B. *Chem. Commun.* **2002**, 2796-2797.

(63) Lo, M. M.-C.; Fu, G. C. *J. Am. Chem. Soc.* **1998**, *120*, 10270-10271.

(64) (a) Loudet, A.; Burgess, K. *Chem. Rev.* **2007**, *107*, 4891-4932. (b) Benniston, A. C.; Copley, G. *Phys. Chem. Chem. Phys.* **2009**, *11*, 4124-4131.

structural and photophysical similarities to porphyrins.⁶⁵ The inclusion of bulky substituents at the 1 and 9 (or α) positions can be used to favor η^1, η^1 coordination in dipyrromethanes⁶⁶ and for both ligands to promote a low coordination number and encapsulate reactive intermediates. Formation of both constructs involves condensation of two pyrrole fragments with an aldehyde or ketone (or the corresponding acetals), making for a highly modular framework, especially with regards to disubstitution at the 1 and 9 positions and the substituent(s) at the 5 (or *meso*) position. The structural similarity of dipyrromethanes and dipyrromethenes to porphyrinogens⁶⁷ and porphyrins, respectively, suggests they may also share similar electronic properties and are likely to be redox active ligands. Anionic pyrrole ligands have been shown to be both poor σ donors and poor π donors, a factor that as shown in this thesis makes them ideal ancillary ligands for favoring high-spin configurations. Specifically, their ligand donor strength has been estimated through a combination of calculation and experiment to more closely match that of fluorinated alkoxides, carboxylates, and halides, than that of simple amides and alkoxides.⁶⁸

1-8. Chapter Summaries

Chapter 2 describes the synthesis of a series of first row transition metal complexes (M = Mn, Fe, Co, Ni, and Zn) supported by a dimesityl substituted dipyrromethane ligand. The complexes were characterized by NMR, UV/Visible spectroscopy, EPR, Mössbauer, differential pulse voltammetry, and single crystal X-ray diffraction. Electrochemical experiments revealed the onset of oxidation for each of the complexes to occur at the same potential, regardless of metal ion and spin state. The

(65) (a) Dolphin, D.; Harris, R. L. N.; Huppatz, J. L.; Johnson, A. W.; Kay, I. T.; Leng, J. J. *Chem. Soc. C* **1966**, 98-106. (b) Chierici, L.; Gardini, G. P. *Tetrahedron* **1966**, 22, 53-56. (c) Ferguson, J.; West, B. O. *J. Chem. Soc. A* **1966**, 1565-1568. (d) Murakami, Y.; Matsuda, Y.; Sakata, K. *Inorg. Chem.* **1971**, 10, 1728-1738. (e) Bruckner, C.; Karunaratne, V.; Rettig, S. J.; Dolphin, D. *Can. J. Chem.* **1996**, 74, 2182-2193. (f) Bruckner, C.; Zhang, Y. J.; Rettig, S. J.; Dolphin, D. *Inorg. Chim. Acta* **1997**, 263, 279-286.

(66) Swartz, D. L.; Odom, A. L. *Organometallics* **2006**, 25, 6125-6133.

(67) Floriani, C.; Floriani-Moro, R. In *The Porphyrin Handbook*; Kadish, K. M., Smith, K. M., Guillard, R., Eds.; Academic Press: San Diego, 2000; Vol. 3, pp 405-420.

(68) DiFranco, S. A.; Maciulis, N. A.; Staples, R. J.; Batrice, R. J.; Odom, A. L. *Inorg. Chem.* **2012**, 51, 1187-1200.

electrochemistry gave strong evidence for a ligand-based oxidation and confirmed that the ligand non-innocence that was known for porphyrinogens was also present in the smaller dipyrromethane unit. Computations suggested a unique electronic structure for the paramagnetic complexes, in which the filled dipyrromethane orbitals lie higher in energy than the partially filled orbitals of Mn, Fe, or Co. Electrochemical or chemical oxidation removed electrons from the ligand-based HOMOs and not the metal-based SOMOs.

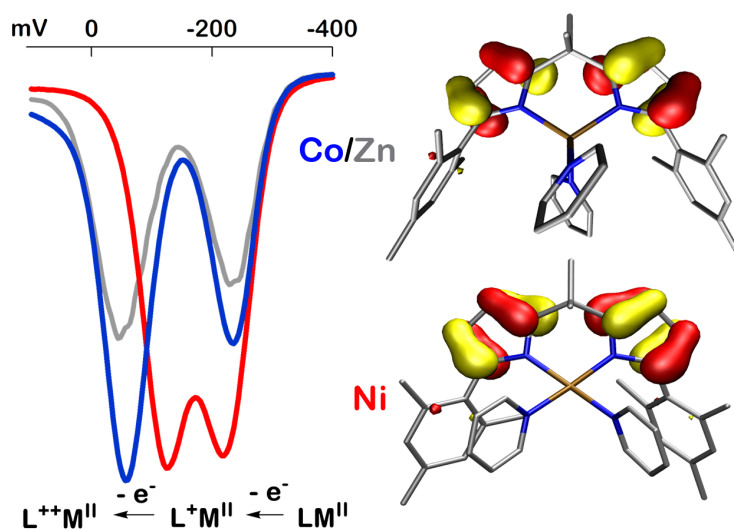
Based on the observed decomposition of the dipyrromethane complexes and the ligand itself, pursuit of high-valent oxos or imides in this framework would have required significant ligand modification. Instead an entirely new ligand was pursued, namely dipyrromethene, which is the product of two-electron oxidation of a dipyrromethane and thus should be more oxidatively stable. **Chapter 3** describes the synthesis and reactivity of an iron(II) dipyrromethene complex. Cyclic voltammetry revealed reversible and quasi-reversible oxidation waves for the (dpme)FeCl(thf) complex, an indication of the capacity for 2 e⁻ oxidation that was not present for any of the dipyrromethane complexes, (dpma)M(py)₂. Reactions with organic azides showed intramolecular C–H amination at the benzylic positions of the mesityl substituents on the ligand. The process was proposed to involve an iron(IV) imide, although an equivalent molecular oxidation state involving 1 e⁻ of the dpme ligand was also possible. Encouragingly the starting material and product of the amination reaction were both iron(II) complexes, (dpme)Fe^{II}Cl(L), an indication that catalysis may be possible if the amination could be directed towards substrate rather than the ligand.

Utilizing the modularity of the dpme synthesis, several ligands with more inert flanking substituents (*tert*-butyl, 1-adamantyl, 2,4,6-triphenylphenyl) were synthesized and complexed to iron. **Chapter 4** describes the reactivity of compounds that became accessible with the new ligands. Catalytic C–H amination and olefin aziridination with organic azides were observed for the *tert*-butyl and adamantyl

cases. Complexes of the very bulky 2,4,6-triphenylphenyl also exhibited intermolecular amination and aziridination, though only stoichiometrically. The enhanced steric protection did allow for the isolation of an intermediate iron imide capable of H-atom abstraction and nitrene transfer, which was structurally and spectroscopically characterized. This complex was assigned as an overall $S = 2$ species with a high-spin Fe^{III} ($S = 5/2$) antiferromagnetically coupled to an imide radical ($S = 1/2$).

In **Chapter 5** the chemistry of cobalt complexes of the 2,4,6-triphenylphenyl dipyrromethene ligand is explored. Reaction of a cobalt(I) starting material with organic azides led to either cobalt(III) tetrazenes, imides, or metallacycles, dependent on the identity of the azide. Although less reactive than the iron imide radical, the cobalt imide complexes did display some potential for C–H activation. The electronic structure of the cobalt imides varies with the imide R substituent, but all cases appear to be paramagnetic (either $S = 1$ or $S = 2$) at room temperature. The results of Chapters 4 and 5 highlight the extent to which dipyrromethenes are very weak field donors and favor the formation of high-spin complexes in all but a few cases.

(69) Osmium imides: (a) Nugent, W. A.; Harlow, R. L.; McKinney, R. J. *J. Am. Chem. Soc.* **1979**, *101*, 7265-7268. (b) Griffith, W. P.; McManus, N. T.; Skapski, A. C.; White, A. D. *Inorg. Chim. Acta Lett.* **1985**, *105*, L11. (c) Shapley, P. A. B.; Own, Z. Y.; Huffman, J. C. *Organometallics* **1986**, *5*, 1269-1271. (d) Anhaus, J. T.; Kee, T. P.; Schofield, M. H.; Schrock, R. R. *J. Am. Chem. Soc.* **1990**, *112*, 1642-1643. (e) McGilligan, B. S.; Arnold, J.; Wilkinson, G.; Hussain-Bates, B.; Hursthouse, M. B. *J. Chem. Soc., Dalton Trans.* **1990**, 2465-2475. (f) Danopoulos, A. A.; Wilkinson, G.; Hussain-Bates, B.; Hursthouse, M. B. *J. Chem. Soc., Dalton Trans.* **1991**, 269-275. (g) Danopoulos, A. A.; Wilkinson, G.; Hussainbates, B.; Hursthouse, M. B. *J. Chem. Soc., Dalton Trans.* **1991**, 1855-1860. (h) Schofield, M. H.; Kee, T. P.; Anhaus, J. T.; Schrock, R. R.; Johnson, K. H.; Davis, W. M. *Inorg. Chem.* **1991**, *30*, 3595-3604. (i) Michelman, R. I.; Andersen, R. A.; Bergman, R. G. *J. Am. Chem. Soc.* **1991**, *113*, 5100-5102. (j) Michelman, R. I.; Bergman, R. G.; Andersen, R. A. *Organometallics* **1993**, *12*, 2741-2751. (k) Smieja, J. A.; Omberg, K. M.; Breneman, G. L. *Inorg. Chem.* **1994**, *33*, 614-616. (l) Lapointe, A. M.; Schrock, R. R.; Davis, W. M. *Organometallics* **1995**, *14*, 2699-2703. (m) Sellmann, D.; Wemple, M. W.; Donaubaauer, W.; Heinemann, F. W. *Inorg. Chem.* **1997**, *36*, 1397-1402. (n) Li, Z.-Y.; Huang, J.-S.; Chan, M. C.-W.; Cheung, K.-K.; Che, C.-M. *Inorg. Chem.* **1997**, *36*, 3064-3071. (o) Smieja, J. A.; Shirzad, K.; Roy, M.; Kittilstved, K.; Twamley, B. *Inorg. Chim. Acta* **2002**, *335*, 141-146. (p) Muñiz, K.; Nieger, M.; Mansikkamäki, H. *Angew. Chem., Int. Ed.* **2003**, *42*, 5958-5961. (q) Muñiz, K.; Iesato, A.; Nieger, M. *Chem.-Eur. J.* **2003**, *9*, 5581-5596. (r) Lutz, C. M.; Wilson, S. R.; Shapley, P. A. *Organometallics* **2005**, *24*, 3350-3353.



Chapter 2: The Electronic Structure of First Row Dipyrrromethane Complexes¹

2-1. Introduction.

Multi-electron redox activity has long been associated with transition metal complexes with two or more accessible oxidation state changes (e.g., $M^n \rightarrow M^{n+1} \rightarrow M^{n+2}$). When the ligands that bind the transition metal ions can themselves operate as electron (or hole) reservoirs, the notion of accessible *molecular* redox states expands beyond that dictated by the metal's *d* orbital electron configuration.² Redox activity has been attributed to a variety of ligand platforms (e.g., catechols,³ dithiolates,⁴ phenolates,⁵ porphyrins,⁶ bis(imino)pyridines,⁷ amido-phenolates,⁸ etc.) via their observed coordination

(1) This chapter was adapted with permission from King, E. R.; Betley, T. A. *J. Am. Chem. Soc.* **2009**, *131*, 14374-14380. Copyright 2009 American Chemical Society.

(2) Chaudhuri, P.; Verani, C. N.; Bill, E.; Bothe, E.; Weyhermüller, T.; Wieghardt, K. *J. Am. Chem. Soc.* **2001**, *123*, 2213-2223.

(3) Masui, H.; Lever, A. B. P.; Auburn, P. R. *Inorg. Chem.* **1991**, *30*, 2402-2410.

(4) (a) Schrauzer, G. N.; Mayweg, V. *J. Am. Chem. Soc.* **1962**, *84*, 3221. (b) Stiefel, E. I.; Waters, J. H.; Billig, E.; Gray, H. B. *J. Am. Chem. Soc.* **1965**, *87*, 3016-3017.

(5) (a) Hockertz, J.; Steenken, S.; Wieghardt, K.; Hildebrandt, P. *J. Am. Chem. Soc.* **1993**, *115*, 11222-11230. (b) Chaudhuri, P.; Hess, M.; Müller, J.; Hildenbrand, K.; Bill, E.; Weyhermüller, T.; Wieghardt, K. *J. Am. Chem. Soc.* **1999**, *121*, 9599-9610.

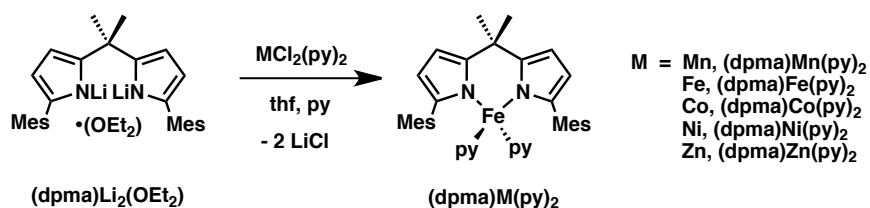
(6) *The Porphyrin Handbook*; Kadish, K. M.; Smith, K. M.; Guilard, R., Eds.; Academic Press: San Diego, 2000; Vol. 15-20.

chemistry and spectrochemical properties. The redox properties of the ligand platforms are being increasingly parlayed into driving new stoichiometric and catalytic reaction sequences. Redox-active ligands have most notably enriched the field of organometallic research with impacts ranging from bestowing multi-electron reactivity to d^0 metals,⁸ facilitating electronic interplay between metal and ligand during catalytic transformations,⁷ as well as enabling dual-site reactivity during reaction sequences.⁹

Our own studies have focused on the coordination chemistry of dipyrromethane^{10, 11} and dipyrromethene¹² ligand frameworks as analogs to porphyrinogen and porphyrin scaffolds, respectively. The pyrrole aromaticity both attenuates the binding N π basicity and makes them good candidates for ligand-centered redox activity by virtue of the high-lying π orbitals.^{13,14} This contribution reports the synthesis and characterization of a series of divalent metal complexes of a dipyrromethane ligand. The complexes display surprisingly uniform electrochemical behavior despite differences in metal valence electron configuration as assessed by magnetic and spectroscopic methods, suggesting an interesting electronic structure which may involve intramolecular redox between the ligand and metal. Specifically,

-
- (7) (a) Bouwkamp, M. W.; Bowman, A. C.; Lobkovsky, E.; Chirik, P. J. *J. Am. Chem. Soc.* **2006**, *128*, 13340-13341. (b) Bart, S. C.; Chlopek, K.; Bill, E.; Bouwkamp, M. W.; Lobkovsky, E.; Neese, F.; Wieghardt, K.; Chirik, P. J. *J. Am. Chem. Soc.* **2006**, *128*, 13901-13912. (c) Bart, S. C.; Lobkovsky, E.; Bill, E.; Wieghardt, K.; Chirik, P. J. *Inorg. Chem.* **2007**, *46*, 7055-7063.
- (8) (a) Herebian, D.; Bothe, E.; Bill, E.; Weyhermüller, T.; Wieghardt, K. *J. Am. Chem. Soc.* **2001**, *123*, 10012-10023. (b) Blackmore, K. J.; Ziller, J. W.; Heyduk, A. F. *Inorg. Chem.* **2005**, *44*, 5559-5561. (c) Haneline, M. R.; Heyduk, A. F. *J. Am. Chem. Soc.* **2006**, *128*, 8410-8411. (d) Blackmore, K. J.; Lal, N.; Ziller, J. W.; Heyduk, A. F. *J. Am. Chem. Soc.* **2008**, *130*, 2728-2730.
- (9) (a) Gunanathan, C.; Milstein, D. *Angew. Chem., Int. Ed.* **2008**, *47*, 8661-8664. (b) Gunanathan, C.; Shimon, L. J. W.; Milstein, D. *J. Am. Chem. Soc.* **2009**, *131*, 3146-3147. (c) Kohl, S. W.; Weiner, L.; Schwartsburd, L.; Konstantinovski, L.; Shimon, L. J. W.; Ben-David, Y.; Iron, M. A.; Milstein, D. *Science* **2009**, *324*, 74-77.
- (10) (a) Jones, D. J.; Gibson, V. C. *Heterocycles* **2006**, *68*, 1121-1127. (b) Swartz, D. L.; Odom, A. L. *Organometallics* **2006**, *25*, 6125-6133.
- (11) (a) Novak, A.; Blake, A. J.; Wilson, C.; Love, J. B. *Chem. Commun.* **2002**, 2796-2797. (b) Love, J. B.; Salyer, P. A.; Bailey, A. S.; Wilson, C.; Blake, A. J.; Davies, E. S.; Evans, D. J. *Chem. Commun.* **2003**, 1390-1391.
- (12) See Chapter 3: Intramolecular C–H Amination from an Iron Dipyrromethene Complex or King, E. R.; Betley, T. A. *Inorg. Chem.* **2009**, *48*, 2361-2363.
- (13) Floriani, C.; Floriani-Moro, R. In *The Porphyrin Handbook*; Kadish, K. M., Smith, K. M., Guilard, R., Eds.; Academic Press: San Diego, 2000; Vol. 3, pp 405-420.
- (14) (a) Bachmann, J.; Nocera, D. G. *J. Am. Chem. Soc.* **2004**, *126*, 2829-2837. (b) Bachmann, J.; Nocera, D. G. *J. Am. Chem. Soc.* **2005**, *127*, 4730-4743.

we consider three possible scenarios: (1) high energy pyrrole-based electrons could reduce the bound metal ion filling the n partially filled $3d$ orbitals with $n e^-$, leaving n holes on the ligand platform; (2) the ligand and metal-based orbitals are close enough in energy such that spin state tautomerism is possible;¹⁵ (3) no intramolecular redox occurs, leaving each metal in the divalent state with the ligand fully reduced. Our data lead us to favor the third scenario, wherein several fully populated ligand-based orbitals reside higher in energy than partially filled metal $3d$ orbitals, giving rise to a *non-Aufbau* electronic arrangement.



Scheme 2.1. Synthesis of dipyrromethane transition metal complexes.

2-2. Synthesis and Characterization of dpmaH and Its Metal Complexes.

To assess the steric and electronic properties the 1,9-dimesityl-5,5-dimethyldipyrromethane (**dpmaH₂**) ligand imparts, transition metal complexes were prepared in the following manner: Reaction of (**dpma**)Li₂(OEt₂) (prepared by deprotonation of **dpmaH₂** with two equivalents of PhLi) with a stoichiometric amount of a divalent metal precursor (i.e., MCl₂(py)₂; M = Mn, Co, Fe, Ni, Zn; py = pyridine) in thawing THF solutions afforded the metallated species of the type (dpma)M(py)₂ upon isolation via crystallization (M = Mn, pale yellow (**dpma**)Mn(py)₂; Fe, bright orange (**dpma**)Fe(py)₂; Co, maroon (**dpma**)Co(py)₂; Ni, crimson (**dpma**)Ni(py)₂; and Zn, yellow (**dpma**)Zn(py)₂). In the absence of strongly coordinating solvents, the formation of ate-complexes was observed (e.g.,

(15) Storr, T.; Verma, P.; Pratt, R. C.; Wasinger, E. C.; Shimazaki, Y.; Stack, T. D. P. *J. Am. Chem. Soc.* **2008**, *130*, 15448-15459.

$[(\text{dpma})\text{CoCl}(\text{thf})][\text{Li}(\text{thf})_2]$. Substitution of the two pyridine ligands in $(\text{dpma})\text{Fe}(\text{py})_2$ for 2,2'-bipyridine (bpy) results in the clean formation of $(\text{dpma})\text{Fe}(\text{bpy})$. The dpma ligand was found to uniformly coordinate in an η^1, η^1 -coordination mode, accommodating both tetrahedral (observed for $(\text{dpma})\text{Mn}(\text{py})_2$, $(\text{dpma})\text{Fe}(\text{py})_2$, $(\text{dpma})\text{Co}(\text{py})_2$, $(\text{dpma})\text{Zn}(\text{py})_2$, and $[(\text{dpma})\text{CoCl}(\text{thf})][\text{Li}(\text{thf})_2]$) and square planar coordination modes at the metal ion (observed for the diamagnetic $(\text{dpma})\text{Ni}(\text{py})_2$) as confirmed by X-ray diffraction studies. The solid state molecular structures for $(\text{dpma})\text{Mn}(\text{py})_2$, $(\text{dpma})\text{Fe}(\text{py})_2$, $(\text{dpma})\text{Fe}(\text{bpy})$, $(\text{dpma})\text{Co}(\text{py})_2$, $[(\text{dpma})\text{CoCl}(\text{thf})][\text{Li}(\text{thf})_2]$, $(\text{dpma})\text{Ni}(\text{py})_2$, and $(\text{dpma})\text{Zn}(\text{py})_2$ are shown in **Figure 2.1** and **Figure 2.2**.

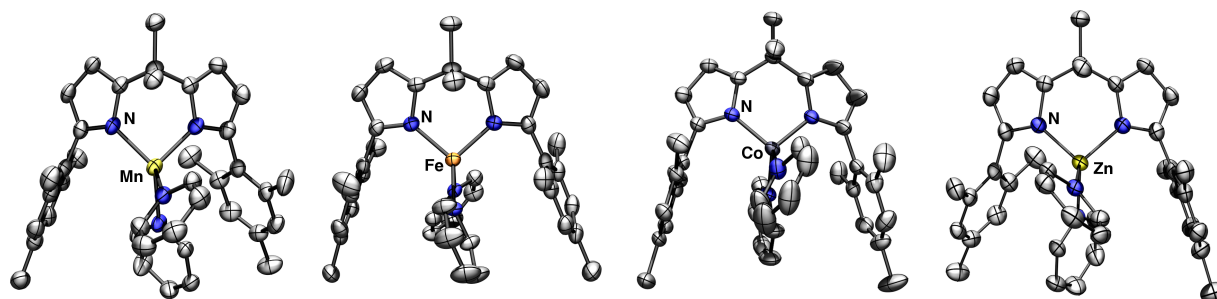


Figure 2.1. Structures of the Mn, Fe, Co, and Zn bis-pyridine complexes. Solid-state molecular structure for the complexes $(\text{dpma})\text{Mn}(\text{py})_2$, $(\text{dpma})\text{Fe}(\text{py})_2$, $(\text{dpma})\text{Co}(\text{bpy})$, and $(\text{dpma})\text{Zn}(\text{py})_2$ with the thermal ellipsoids set at the 50% probability level (hydrogen atoms and minor structural disorder in $(\text{dpma})\text{Mn}(\text{py})_2$ and $(\text{dpma})\text{Fe}(\text{py})_2$ are omitted for clarity).

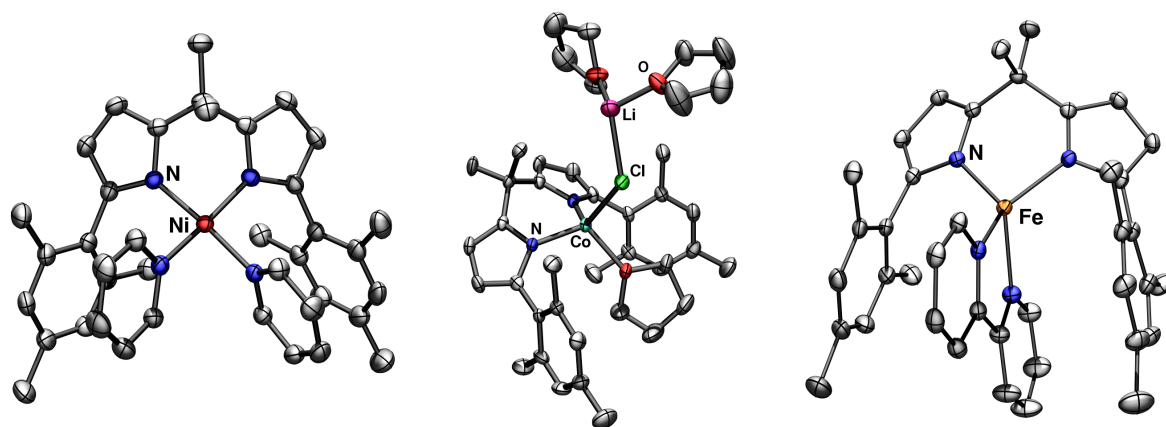


Figure 2.2. Structures of the Ni bis-pyridine, Co ate complex, and Fe(bpy) complexes. Solid-state molecular structure for the complexes $(\text{dpma})\text{Ni}(\text{py})_2$, $[(\text{dpma})\text{CoCl}(\text{thf})][\text{Li}(\text{thf})_2]$, and $(\text{dpma})\text{Fe}(\text{bpy})$ with the thermal ellipsoids set at the 50% probability level (hydrogen atoms, one solvent molecule for $(\text{dpma})\text{Ni}(\text{py})_2$, and two solvent molecules for $(\text{dpma})\text{Fe}(\text{bpy})$ are omitted for clarity). The Li^+ in $[(\text{dpma})\text{CoCl}(\text{thf})][\text{Li}(\text{thf})_2]$ is coordinated to an adjacent molecule's pyrrole ring.

Table 2.1. Dipyrromethane and metal-ligand bond length comparisons.

complex	Bond lengths (Å)													
	1	2	3	4	5	6	7	8	9	10	11	12	13	14
$(\text{dpma})\text{Mn}(\text{py})_2^a$	2.058 (1)	2.048 (1)	2.166 (1)	2.228 (1)	1.386 (3)	1.376 (3)	1.405 (3)	1.373 (3)	1.389 (3)	1.383 (3)	1.372 (3)	1.413 (3)	1.368 (3)	1.386 (3)
$(\text{dpma})\text{Fe}(\text{py})_2$	1.979 (2)	1.985 (2)	2.112 (2)	2.128 (3)	1.388 (3)	1.371 (3)	1.408 (3)	1.377 (3)	1.389 (3)	1.389 (2)	1.369 (3)	1.403 (2)	1.377 (3)	1.391 (3)
$(\text{dpma})\text{Fe}(\text{bpy})$	1.964 (1)	1.964 (1)	2.087 (1)	2.128 (1)	1.385 (2)	1.377 (2)	1.421 (2)	1.382 (2)	1.383 (2)	1.384 (2)	1.379 (2)	1.419 (2)	1.379 (2)	1.384 (2)
$(\text{dpma})\text{Co}(\text{py})_2$	1.964 (2)	1.958 (2)	2.041 (2)	2.049 (2)	1.382 (2)	1.375 (2)	1.420 (3)	1.378 (3)	1.383 (2)	1.383 (2)	1.369 (3)	1.413 (3)	1.376 (3)	1.376 (2)
$(\text{dpma})\text{Ni}(\text{py})_2$	1.878 (2)	1.915 (2)	1.942 (2)	1.910 (2)	1.395 (3)	1.379 (3)	1.406 (3)	1.379 (3)	1.372 (3)	1.379 (3)	1.374 (3)	1.399 (3)	1.378 (3)	1.401 (3)
$(\text{dpma})\text{Zn}(\text{py})_2^a$	1.963 (1)	1.966 (1)	2.115 (1)	2.062 (1)	1.386 (2)	1.378 (3)	1.408 (3)	1.376 (3)	1.388 (2)	1.388 (2)	1.379 (3)	1.414 (3)	1.377 (3)	1.384 (2)

^a Averaged values from two molecules in the asymmetric unit.

2-3. Structural Characterization of Dipyrromethane Complexes.

Complexes $(\text{dpma})\text{Mn}(\text{py})_2$, $(\text{dpma})\text{Fe}(\text{py})_2$, $(\text{dpma})\text{Co}(\text{bpy})$, and $(\text{dpma})\text{Zn}(\text{py})_2$ are isostructural featuring a pseudo-tetrahedral geometry at the metal center. The Ni complex

(**dpma**)Ni(**py**)₂ is distinct from this series, featuring a square planar geometry at Ni. The metal pyrrolide nitrogen bond lengths decrease across the series of pseudo-tetrahedral complexes (d_{avg} (Å): Mn–N_{dpma} = 2.053(1), Fe–N_{dpma} = 1.982(1), Co–N_{dpma} = 1.961(1), Zn–N_{dpma} = 1.965(1); see **Table 2.1** for a more comprehensive comparison of bond lengths). A similar trend is found comparing the metal pyridine nitrogen bond lengths (d_{avg} (Å): Mn–N_{py} = 2.197(1), Fe–N_{py} = 2.120(2), Co–N_{py} = 2.045(2), Zn–N_{py} = 2.090(2)). In order to adopt the square planar geometry in (**dpma**)Ni(**py**)₂, the Ni(**py**)₂ unit is brought out of the ligand plane (dihedral angle of 33.96(12)° with respect to the dipyrrolide subunits), further evidenced by the splaying of the two flanking mesityl aryl groups. The mesityl units of the dpma ligand carve a cleft about the Ni of 80.52(5)°, defined as the angle formed by the two mesityl *ipso*-C atoms and the dpma bridgehead carbon atom ($\angle C_{ipso}-C_{Me2}-C_{ipso}$). This angle is consistent throughout the series, where angles of 78.46(4)° for Mn, 86.61(4)° for Fe, 81.58(3)° for Fe(**bpy**), 81.88(4)° for Co, and 79.15(4)° for Zn are observed.

Table 2.2. Magnetic and spectral properties of the transition metal dpma complexes.

complex	S	μ_{eff} / μ_B	λ / nm ($\epsilon / M^{-1}cm^{-1}$)	$\delta / mm/s$	$ \Delta E_Q / mm/s$
(dpma)Mn(py) ₂	⁵ / ₂	5.97 ^a , 6.1(1) ^b	–	–	–
(dpma)Fe(py) ₂	2	5.00 ^a , 5.2(1) ^b	420 (1500), 1359 (70), 1675 (50) (sh)	0.80, 0.86	3.46, 2.63
(dpma)Fe(bpy)	2	5.1(1) ^b	535 (410), 585 (620), 613 (870), 1125 (110), 1260 (105) (sh)	0.72	3.00
(dpma)Co(py) ₂	³ / ₂	4.20 ^a , 4.5(1) ^b	395 (1100)	–	–
(dpma)Ni(py) ₂	0	–	503 (190)	–	–

^a Average moment over T range of 200–300 K from SQUID.

^b Room temperature (295 K) moment in solution by Evans's method.

2-4. Electronic and Magnetic Characterization of Dipyrromethane Complexes.

The magnetic and spectral data for (**dpma**)Mn(**py**)₂, (**dpma**)Fe(**py**)₂, (**dpma**)Co(**py**)₂, and (**dpma**)Ni(**py**)₂, (**dpma**)Fe(**bpy**) and are provided in **Table 2.2**. The nearly colorless (**dpma**)Mn(**py**)₂ has no transitions in the visible or near IR (NIR) regions (**Figure 2.3**) as expected for the ¹H NMR

silent, high-spin d^5 ($S = 5/2$) Mn^{II} center (solution magnetic moment, $\mu_{\text{eff}}(295 \text{ K}) = 6.1(1) \mu_{\text{B}}$). Based on the magnitude of their molar absorptivities, the visible absorptions for orange **(dpma)Fe(py)₂** ($\lambda_{\text{max}} = 420 \text{ nm}$, $\epsilon = 1500 \text{ M}^{-1}\text{cm}^{-1}$) and maroon **(dpma)Co(py)₂** ($\lambda_{\text{max}} = 613 \text{ nm}$, $\epsilon = 870 \text{ M}^{-1}\text{cm}^{-1}$) are of the appropriate magnitude for spin-allowed $d \rightarrow d$ transitions for the high-spin Fe^{II} ($S = 2$, $\mu_{\text{eff}}(295 \text{ K}) = 5.2(1) \mu_{\text{B}}$) and Co^{II} ($S = 3/2$, $\mu_{\text{eff}}(295 \text{ K}) = 4.5(1) \mu_{\text{B}}$) centers in pseudo-tetrahedral ligand fields, respectively. Only very weak transitions are found for **(dpma)Fe(py)₂** ($\lambda_{\text{max}}/\text{nm}$ ($\epsilon/\text{M}^{-1}\text{cm}^{-1}$): 1359 (70), 1675 (50)) and **(dpma)Co(py)₂** ($\lambda_{\text{max}}/\text{nm}$ ($\epsilon/\text{M}^{-1}\text{cm}^{-1}$): 1125 (110), 1260 (105)) in the near-infrared region, which are too low in intensity to correspond to charge transfer bands (e.g. LMCT). Despite the paramagnetism of **(dpma)Fe(py)₂** and **(dpma)Co(py)₂**, all nine proton resonances are discernable by ^1H NMR at 295 K ranging from δ 148 to -15 ppm. ^1H NMR analysis of **(dpma)Ni(py)₂** reveals several significantly broadened ($\Delta\delta = 1 - 2$ ppm) resonances, yet no solution magnetic moment was measurable at room temperature – thus signifying the square planar geometry observed in the low temperature solid state structure is preserved in solution. The observed broadening of the ^1H resonances can then be attributed to the limited motion of the mesityl aryl groups when accommodating the square planar geometry. The relatively weak electronic transition observed for **(dpma)Ni(py)₂** ($\lambda_{\text{max}} = 503 \text{ nm}$, $\epsilon = 190 \text{ M}^{-1}\text{cm}^{-1}$) is consistent with a Laporte forbidden $d \rightarrow d$ transition.

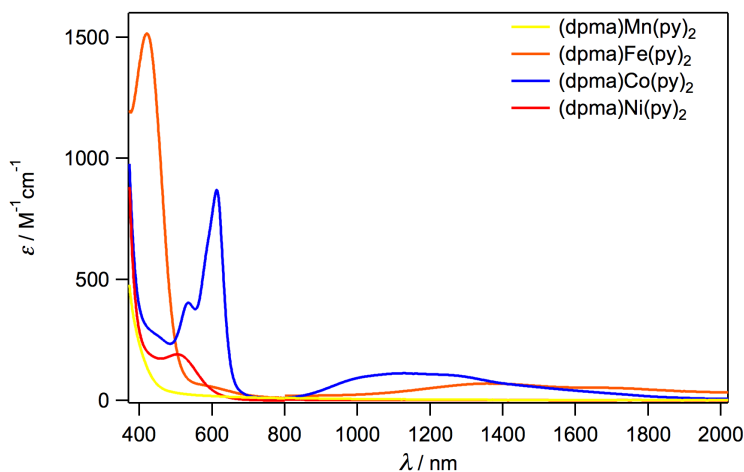


Figure 2.3. Absorption spectra of transition metal bis-pyridine complexes. UV/Vis/NIR molar absorptivity spectra of **(dpma)Mn(py)₂**, **(dpma)Fe(py)₂**, **(dpma)Co(py)₂**, and **(dpma)Ni(py)₂**. Spectra were taken in DCM, molar absorptivities are based on measurements at 4 concentrations.

To confirm the high-spin character of complexes **(dpma)Mn(py)₂**, **(dpma)Fe(py)₂**, and **(dpma)Co(py)₂** at low temperatures, each complex was also characterized by SQUID magnetometry from 4.2–300 K and simulated with the *julX* package.¹⁶ As can be seen from **Figure 2.4**, the Mn, Fe, and Co complexes maintain their sextet, **(dpma)Mn(py)₂**, quintet, **(dpma)Fe(py)₂**, and quartet, **(dpma)Co(py)₂** ground states throughout this temperature range.¹⁶ The Curie Law observed for each complex in this temperature range (indicated by the linear plot of χ_m^{-1} versus T, **Figure 2.4b**) indicates that the ascribed spin states are the only states thermally populated. The powder EPR spectrum of **(dpma)Mn(py)₂** at 77 K reveals a complex multiline pattern consistent with multiple absorbances occurring for the high-spin Mn^{II} in a weak field ligand environment (**Figure 2.5a**). The powder EPR spectrum for the Co^{II} complex **(dpma)Co(py)₂** exhibits a isotropic signal in the region of $g \approx 3.48$, consistent with high-spin Co^{II} ($S = 3/2$) – though the signal persists even to 298 K (**Figure 2.6b**). The

(16) Bill, E. *julX: Simulation of Molecular Magnetic Data*, version 1.41; Max Plank Institute for Bioinorganic Chemistry: Mülheim an der Ruhr, Germany, 2008.

EPR data for **(dpma)Co(py)₂** was simulated using a large zero field splitting parameter $D = 7.86 \text{ cm}^{-1}$ and $E/D = 0$ as determined from fitting the SQUID data, with $g_{\perp} = 2.02$, $g_{\parallel} = 2.31$.¹⁷

The Mössbauer spectrum of **(dpma)Fe(py)₂** shows multiple components modeled as two subspectra (**Figure 2.7a**). The two component subspectra have nearly identical isomer shifts ($\delta = 0.80$, 0.86 mm/s) with different quadrupole splittings (component A: $|\Delta E_Q| = 3.46 \text{ mm/s}$ (84%); component B: $|\Delta E_Q| = 2.63 \text{ mm/s}$ (16%)), both consistent with Fe^{II} nuclei. The minor component grows in intensity the longer time between spectrum is acquisition and material preparation, even though ¹H NMR analysis does not reveal any change for the bulk material over a similar time frame. Analysis of **(dpma)Fe(py)₂** by ¹H NMR following Mössbauer measurements shows only peaks for **(dpma)Fe(py)₂** without any observable decomposition (e.g. pyridine loss or dpma ligand dissociation). Neither subspectra are representative of the FeCl₂(py)₂ starting material.¹⁸ One possibility for the presence of two components could be structural isomers due to variation in pyridine binding to the Fe center.¹⁸ The Mössbauer spectrum for **(dpma)Fe(bpy)** (**Figure 2.7b**), where the two pyridine ligands have been substituted for a single 2,2'-bipyridine ligand, reveals a single species featuring an isomer shift of 0.72 mm/s and a quadrupole splitting of 3.00 mm/s , consistent with the major component observed in the spectrum of **(dpma)Fe(py)₂**. The bipyridine ligand in **(dpma)Fe(bpy)** enforces a more acute $\angle(\text{N3-Fe-N4})$ bond angle (77.38°) as compared to the $\angle(\text{N3-Fe-N4})$ bond angle in **(dpma)Fe(py)₂** (97.32°). The large $|\Delta E_Q|$ for **(dpma)Fe(bpy)** is consistent with the greater deviation from an ideal tetrahedral geometry due to the bipyridine ligand. While the connectivity for **(dpma)Fe(py)₂** may not change, reorientation of the pyridine ligands in a more spherically symmetric fashion about Fe may produce the minor species detected in **Figure 2.7a**.

(17) A similar modeling scheme was employed to model the EPR spectra for a series of isoelectronic Cr^{III} complexes: Pedersen, E.; Toftlund, H. *Inorg. Chem.* **1974**, *13*, 1603-1612.

(18) Long, G. J.; Whitney, D. L.; Kennedy, J. E. *Inorg. Chem.* **1971**, *10*, 1406-1410.

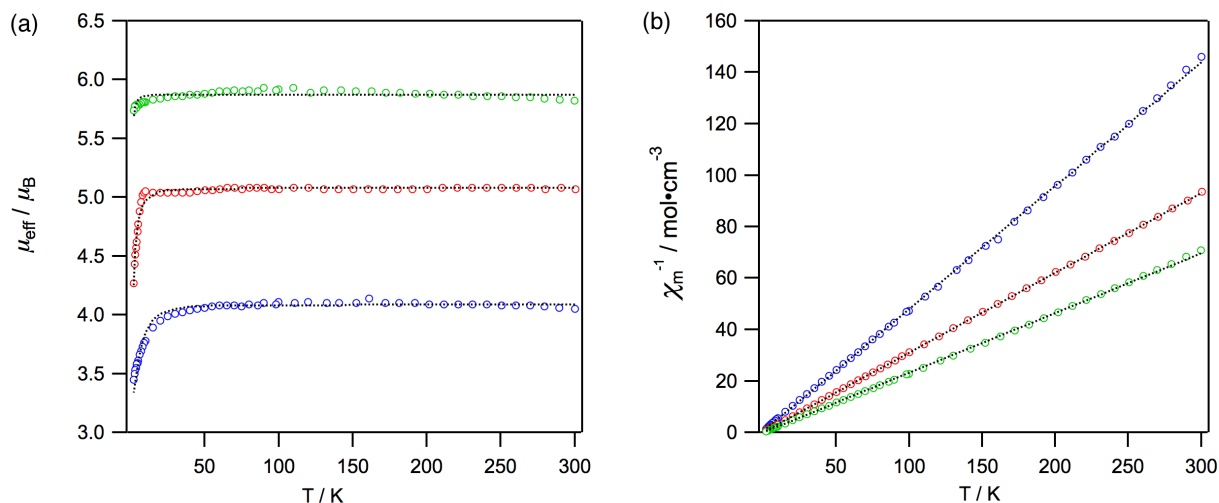


Figure 2.4. Magnetometry of paramagnetic dpma bis-pyridine complexes. (a) SQUID magnetization data for complexes $(\text{dpma})\text{Mn}(\text{py})_2$ (\circ), $(\text{dpma})\text{Fe}(\text{py})_2$ (\circ) and $(\text{dpma})\text{Co}(\text{py})_2$ (\circ) shown as a plot of μ_{eff} (BM) versus T (K) and (b) as a plot of χ_m^{-1} (mol/cm^3) versus T (K). Dotted lines are the simulations of each data set.¹⁶

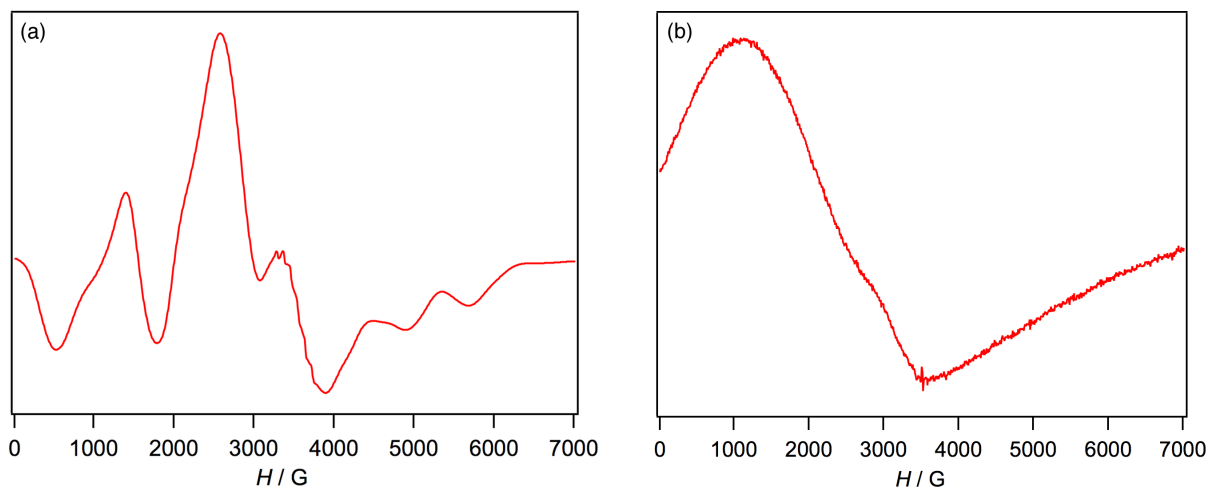


Figure 2.5. 77 K X-band EPR of Co and Mn dpma bis-pyridine complexes. Powder EPR spectrum of (a) $(\text{dpma})\text{Mn}(\text{py})_2$ and (b) $(\text{dpma})\text{Co}(\text{py})_2$ (dotted line is data simulation:¹⁷ $g_{\perp} 2.02$, $g_{\parallel} 2.31$; $A_{\perp} 0$, $A_{\parallel} 0.0112 \text{ cm}^{-1}$; $D 7.86 \text{ cm}^{-1}$, $E/D 0$) (77K, X-band, 9.397 GHz).

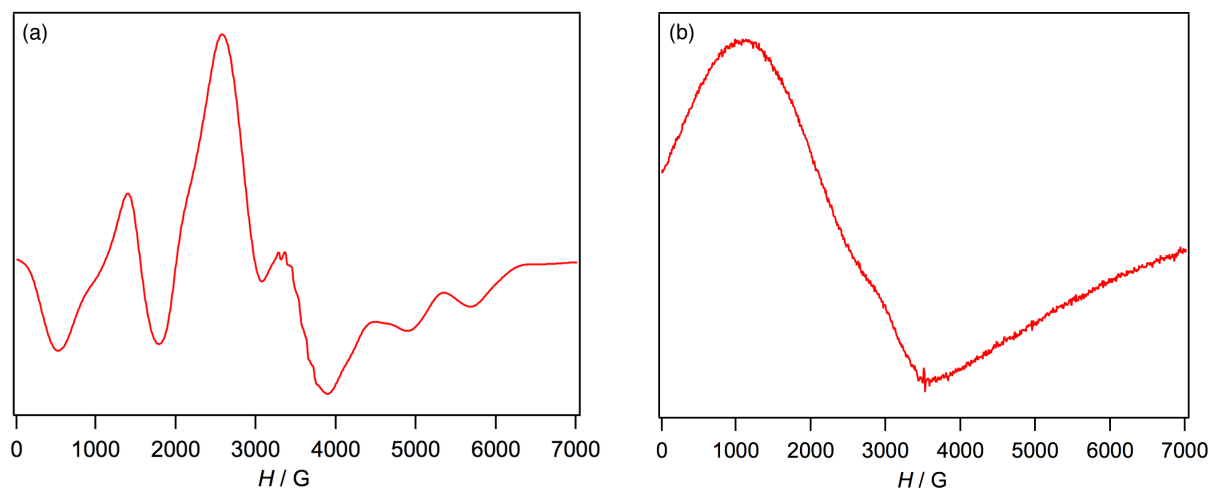


Figure 2.6. Room Temperature EPR of dpma Co and Mn bis-pyridine complexes. Powder EPR spectrum of (a) $(\text{dpma})\text{Mn}(\text{py})_2$ and (b) $(\text{dpma})\text{Co}(\text{py})_2$; (295 K, X-band, 9.852 GHz).

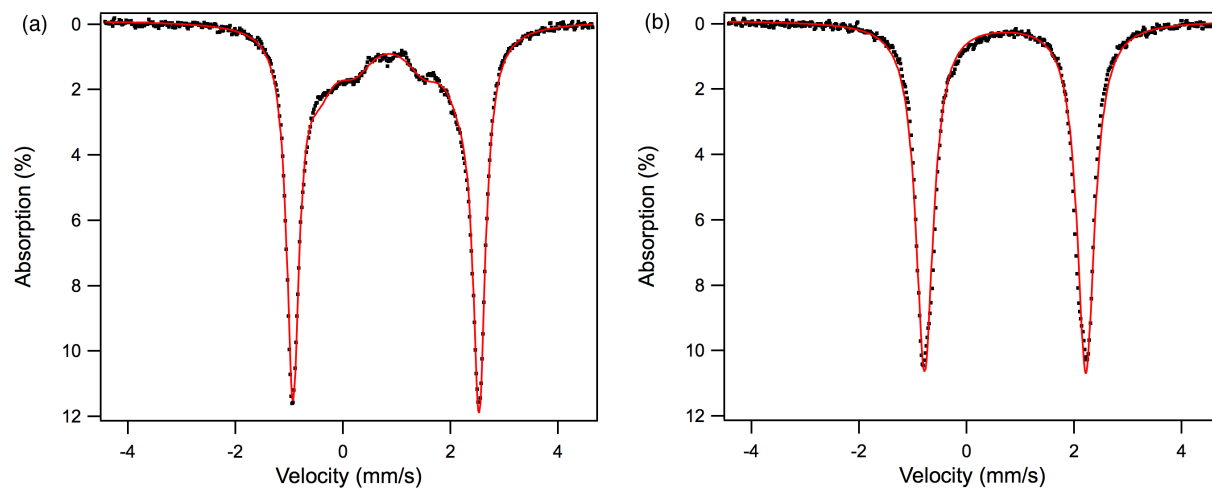


Figure 2.7. Mössbauer spectra of Fe dpma complexes. (a) $(\text{dpma})\text{Fe}(\text{py})_2$ and (b) $(\text{dpma})\text{Fe}(\text{bpy})$ at 4.2 K.

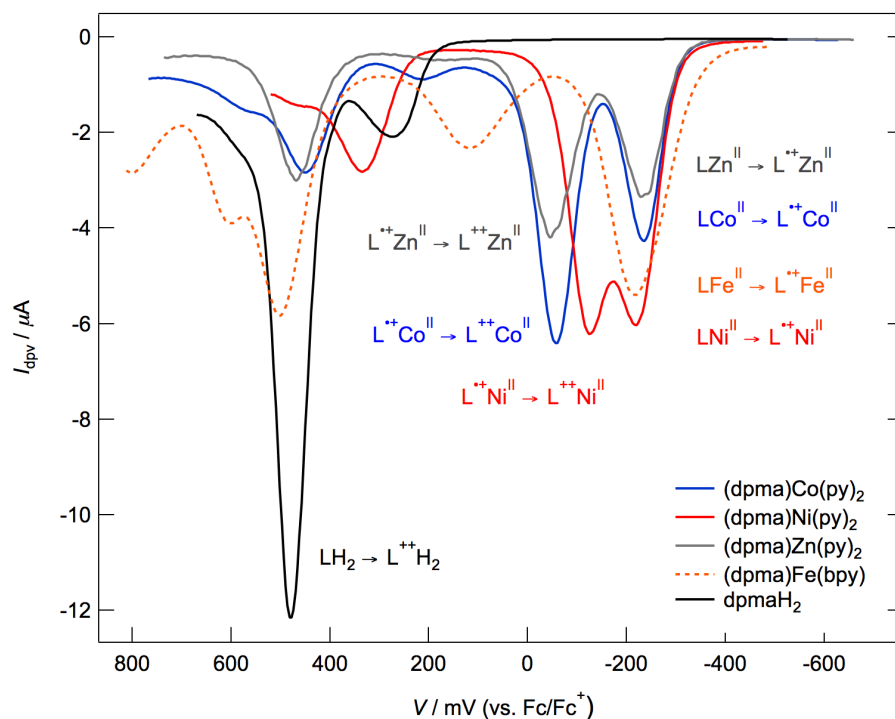


Figure 2.8. Differential Pulse Voltammograms of dpma complexes in ACN. Differential pulse voltammograms of 10^{-4} M acetonitrile solutions of $(\text{dpma})\text{Fe}(\text{py})_2$, $(\text{dpma})\text{Co}(\text{py})_2$, $(\text{dpma})\text{Ni}(\text{py})_2$, $(\text{dpma})\text{Zn}(\text{py})_2$, $(\text{dpma})\text{Fe}(\text{bpy})$, and dpmaH_2 ; $[\text{nBu}_4\text{N}][\text{PF}_6]$ (0.1 M); scan rate 20 mV/s; Pt electrode.

2-5. Electrochemical Behavior of Dipyrrromethane Complexes.

Cyclic voltammetry on the bis-pyridine complexes, $(\text{dpma})\text{Mn}(\text{py})_2$, $(\text{dpma})\text{Fe}(\text{py})_2$, $(\text{dpma})\text{Co}(\text{py})_2$, $(\text{dpma})\text{Ni}(\text{py})_2$, and $(\text{dpma})\text{Zn}(\text{py})_2$, showed no reversible oxidative or reductive events, and instead showed a rather complex series of irreversible oxidations. In order to probe their electrochemical behavior further, differential pulse voltammetry was used to assess the electrochemical potentials of these irreversible events. Using oxidative scans, all five species exhibited three major anodic peaks between -800 and $+600$ mV relative to Fc/Fc^+ in THF (1 mM analyte, 0.3 M $[\text{nBu}_4\text{N}][\text{PF}_6]$, **Figure 2.9a**). The potential of the initial peak corresponds well with the onset of current response in the cyclic voltammetry experiments, yet it was indeterminable if the oxidations represented one- or two-electron events. In acetonitrile solutions, the large oxidative waves for complexes $(\text{dpma})\text{Co}(\text{py})_2$,

(dpma)Ni(py)₂, **(dpma)Zn(py)₂** and **(dpma)Fe(bpy)** in THF separated into two well-defined one-electron events (**Figure 2.8**). For 1 mM solutions of **(dpma)Co(py)₂**, **(dpma)Ni(py)₂**, **(dpma)Zn(py)₂** and **(dpma)Fe(bpy)** in acetonitrile (0.1 M [ⁿBu₄N][PF₆], Pt working electrode) the initial peak was consistently observed at $E_p = -240$ mV. The Mn and Fe bis-pyridine complexes, **(dpma)Mn(py)₂** and **(dpma)Fe(py)₂**, proved too labile in acetonitrile solutions to give reliable data (**Figure 2.9b**). The Fe(bpy) analog **(dpma)Fe(bpy)**, however, was stable enough in acetonitrile solutions to provide reproducible data, included in **Figure 2.8**. The onset of oxidation for **(dpma)Fe(bpy)** is consistent with **(dpma)Co(py)₂**, **(dpma)Ni(py)₂**, and **(dpma)Zn(py)₂**, though it does not exhibit a second oxidation event within a similar range. Subsequent peaks were observed at different potentials but followed similar patterns for all four metals. The Co and Zn voltammograms overlay with little deviation of the observed potentials, while the Ni voltammogram features the second one-electron oxidation at a slightly lower potential. We interpret the redox inactive Zn^{II} data to imply the observed sequential one-electron oxidations are predominantly ligand-centered. Interestingly, although the oxidations appear to be ligand-centered and vary little with divalent cation substitution, the onset of oxidation for metallated dpma does shift nearly -700 mV from the free **dpmaH₂** ($E_p = +475$ mV).

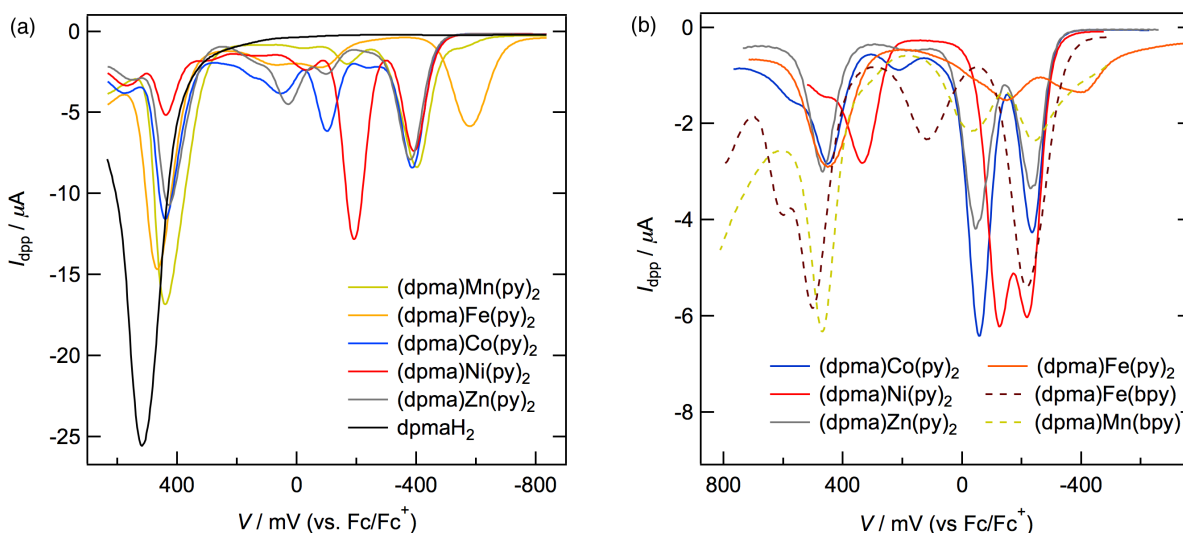


Figure 2.9. Differential Pulse Voltammograms of dpma complexes in ACN and THF. (a) 10^{-4} M THF solutions of **(dpma)Mn(py)₂**, **(dpma)Fe(py)₂**, **(dpma)Co(py)₂**, **(dpma)Ni(py)₂**, **(dpma)Zn(py)₂** and **dpmaH₂**; [ⁿBu₄N][PF₆] (0.3 M); scan rate 20 mV/s; glassy C electrode), and (b) 10^{-4} M solutions ACN of **(dpma)Co(py)₂**, **(dpma)Ni(py)₂**, **(dpma)Zn(py)₂** and **(dpma)Fe(bpy)**; $> 10^{-3}$ M acetonitrile solutions of **(dpma)Fe(py)₂** and **(dpm)Mn(bpy)**; [ⁿBu₄N][PF₆] (0.1 M); scan rate 20 mV/s; Pt electrode. [(**dpm**)Fe(py)₂ and (dpm)Mn(bpy) were not stable in ACN and the signal decayed after the initial scan, high concentration was needed to see any signal. Initial oxidation of (dpm)Mn(bpy) is consistent with the series. Initial oxidation of (**dpm**)Fe(py)₂ is at lower potential consistent with (**dpm**)Fe(py)₂ in THF.]

2-6. Computational Analysis.

To further probe the electronic structure of the **(dpma)M(py)₂** complexes, geometry optimized calculations on **(dpma)Mn(py)₂**, **(dpma)Fe(py)₂**, **(dpma)Co(py)₂**, **(dpma)Ni(py)₂**, and **(dpma)Zn(py)₂** were performed (B3LYP/TZVP/SV(P)).^{19,20} The orbital energies are presented in **Figure 2.10**. Dipyrrromethane orbitals are highlighted in red, metal 3d orbitals in grey, and pyridine orbitals are highlighted in black. In every instance the calculations indicate the highest lying occupied molecular orbitals (HOMO, HOMO-1) exclusively feature ligand π character on the pyrrole subunits, as illustrated for **(dpma)Co(py)₂** in **Figure 2.11**. The metal 3d orbitals do not significantly contribute to the frontier orbitals until HOMO-4, often 1–2 eV lower in energy than the dipyrrromethane-based

(19) Gaussian 03, version E.01; Gaussian, Inc.: Wallingford, CT, 2004.

(20) Weigend, F.; Ahlrichs, R. *Phys. Chem. Chem. Phys.* **2005**, *7*, 3297-3305.

HOMO. For the high-spin ion complexes $(\text{dpma})\text{Mn}(\text{py})_2$, $(\text{dpma})\text{Fe}(\text{py})_2$, and $(\text{dpma})\text{Co}(\text{py})_2$ the spin density plot ($\alpha - \beta$) reveals all of the spin localized on the metal ion (**Figure 2.11b**). These results indicate that electron pairing within the higher energy, delocalized dipyrromethane ligand π orbitals is energetically favored over electron pairing within lower energy, but localized metal ion $3d$ orbitals. This idea is consistent with encountering a significantly larger coulombic repulsion for pairing electrons in $3d$ orbitals in the intramolecular redox state $(\text{dpma}^{\text{n}+})\text{M}^{\text{n}-}$ (scenario 1), than pairing electrons in energetically higher-lying, though diffuse dipyrromethane-based π orbitals (scenario 3). The electronic structure suggested by the DFT results is consistent with the electrochemical behavior exhibited by the series of complexes. The pyrrolide π electrons are the most accessible energetically, thus we observe sequential pyrrole oxidation events with little perturbation by the chelated divalent ion.

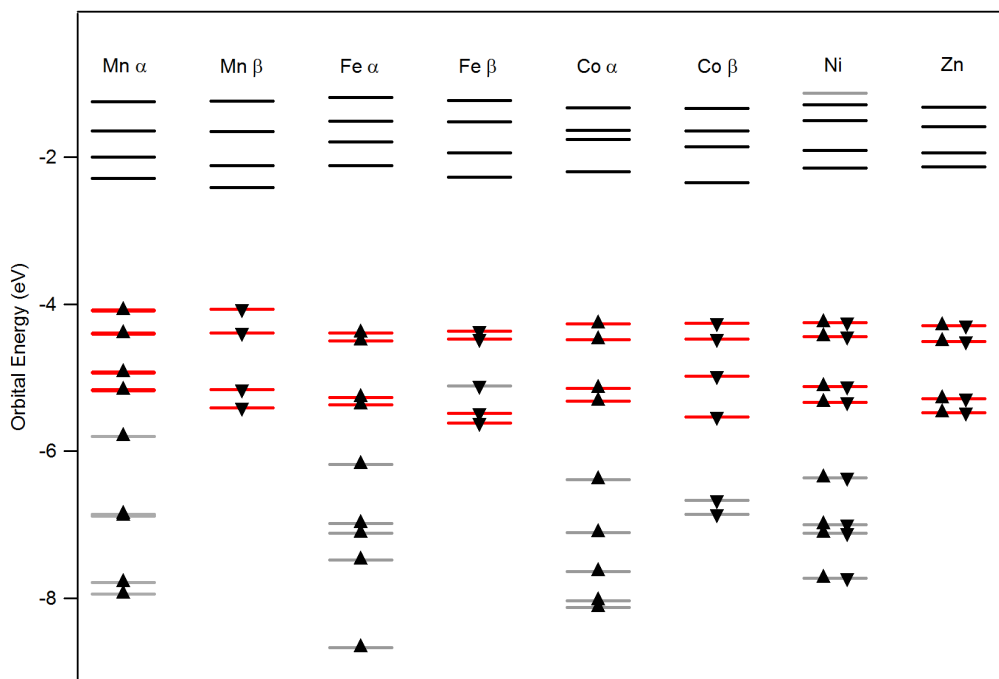


Figure 2.10. Computed molecular orbital energy levels for dpma bis-pyridine complexes. Calculated α (▲) and β (▼) orbital energies for $(\text{dpma})\text{Mn}(\text{py})_2$, $(\text{dpma})\text{Fe}(\text{py})_2$, $(\text{dpma})\text{Co}(\text{py})_2$. Calculated orbital energies for $(\text{dpma})\text{Ni}(\text{py})_2$ and $(\text{dpma})\text{Zn}(\text{py})_2$. Metal-based orbitals (grey); dipyrromethane ligand-based orbitals (red); and pyridine-based orbitals (black).

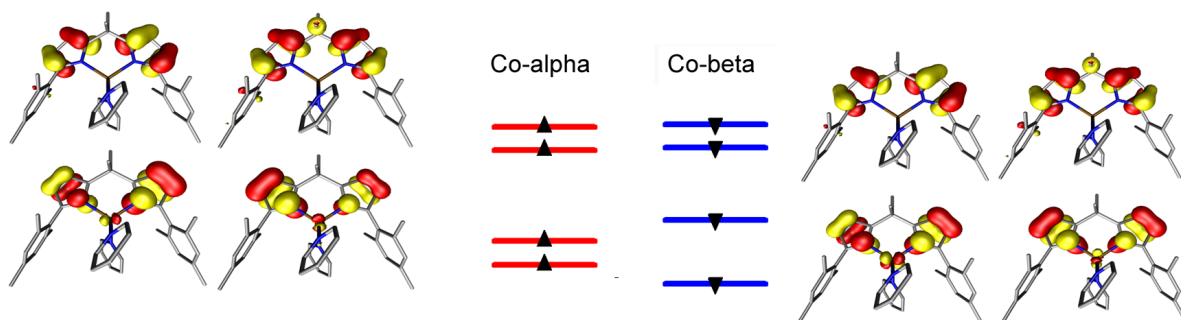


Figure 2.11. Calculated molecular orbitals of $(\text{dpma})\text{Co}(\text{py})_2$. HOMO to HOMO-4 from molecular orbital diagrams for $(\text{dpma})\text{Co}(\text{py})_2$ by DFT (B3LYP/TZVP/SV(P);²⁰ Gaussian 03¹⁹). (b)

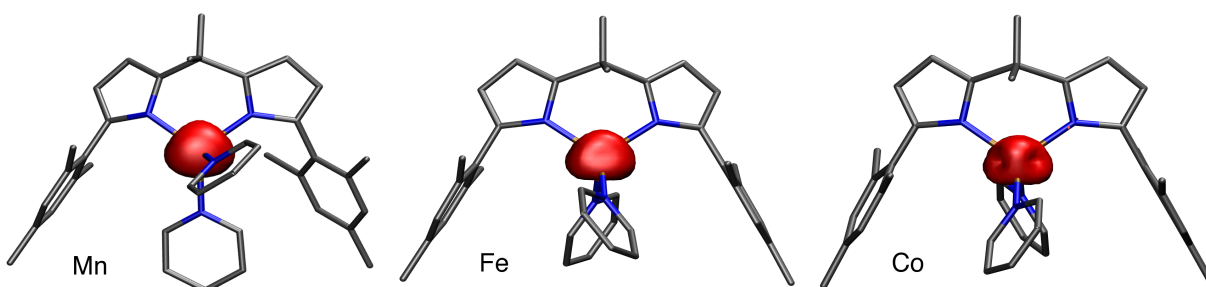
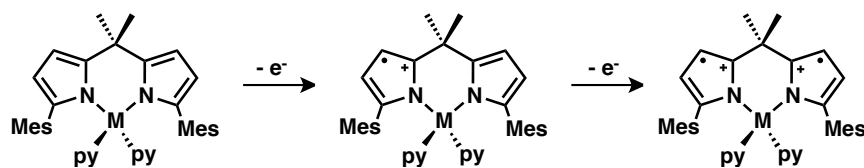


Figure 2.12. Calculated spin densities for paramagnetic dpma bis-pyridine complexes. Plots of calculated spin density ($\alpha-\beta$) for $(\text{dpma})\text{Mn}(\text{py})_2$ ($S = 5/2$), $(\text{dpma})\text{Fe}(\text{py})_2$ ($S = 2$), and $(\text{dpma})\text{Co}(\text{py})_2$ ($S = 3/2$).

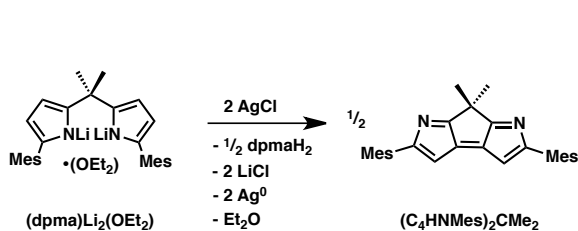


Scheme 2.2. Ligand centered oxidation in $(\text{dpma})\text{M}(\text{py})_2$ complexes.

2-7. Chemical Oxidation.

Metal porphyrinogen complexes are known to undergo similar pyrrole-based oxidations (chemical and electrochemical), as shown by Floriani¹³ and Nocera.¹⁴ Sequential one-electron oxidations led to cyclopropane formation about the porphyrinogen's *meso* position via radical coupling of adjacent pyrrole carbons in the 2 and 2' position. Sequential one-electron oxidation of the two pyrrole subunits

should lead to a transient diradical, illustrated in **Scheme 2.2**. Whether the dipyrromethane ligands can undergo a radical coupling similar to the porphyrinogen platform to form a cyclopropane unit has yet to be confirmed. Chemical oxidation of the dilithio species **(dpma)Li₂(OEt₂)** with two equivalents of AgCl in thawing THF solution produced one equivalent of free **dpmaH₂** and an equimolar amount of a new diamagnetic species. ¹H NMR, HRMS, and X-ray crystallography confirm the new species obtained is the *four*-electron oxidized product diazacyclopentapentalene **(C₄HNMe_s)₂CMe₂** (**Scheme 2.3**), which is inconsistent with two-electron oxidized, cyclopropane formation observed in porphyrinogen systems. Presumably this process occurs from radical coupling of the ligand C3 and C7 positions followed by further two-electron oxidation and deprotonation. Coupling the pyrrole C3 and C7 positions, in this case, occurs preferentially to cyclopropane formation from the C4 and C6 positions, likely arising from carbocation stabilization at the pyrrole C4 and C6 positions and radical localization at the pyrrole C3 and C7 positions. Cyclic voltammetry on **(C₄HNMe_s)₂CMe₂** in THF reveals only two reversible reduction events ($E_{1/2} = -1.14$ V, -2.28 V vs. Fc/Fc⁺), but no oxidation (**Figure 2.14**). Chemical oxidation of complexes **(dpma)Mn(py)₂**, **(dpma)Fe(py)₂**, **(dpma)Co(py)₂**, and **(dpma)Ni(py)₂** with two equivalents of Fc⁺PF₆⁻ did not produce detectable quantities of **(C₄HNMe_s)₂CMe₂**, only free ligand **dpmaH₂** and one equivalent of ferrocene were observed as the assignable products of oxidation. Likewise, attempts to directly synthesize a (dpma)M^{III} complex were unsuccessful. For example, metallation of M^{III} synthons (i.e. Mn^{III}(acac)₃, FeCl₃, Fe^{III}(acac)₃; acac = acetylacetonate) with **(dpma)Li₂(OEt₂)** only yielded complex mixtures of (dpma)M^{II}(L)_n species (L = pyridine, THF), free ligand, and unidentified metal salt mixtures, but no isolable (dpma)M^{III} materials.



Scheme 2.3. Chemical oxidation of $(dpma)^{2-}$.

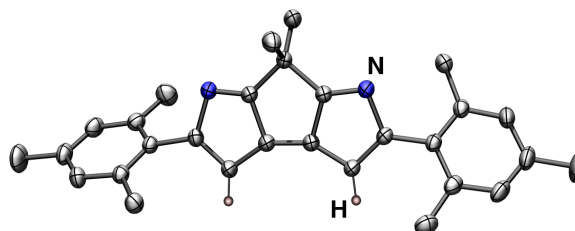


Figure 2.13. Structure of the diazapentalene. Thermal ellipsoids set at the 50% probability level (methyl and aryl hydrogen atoms omitted for clarity).

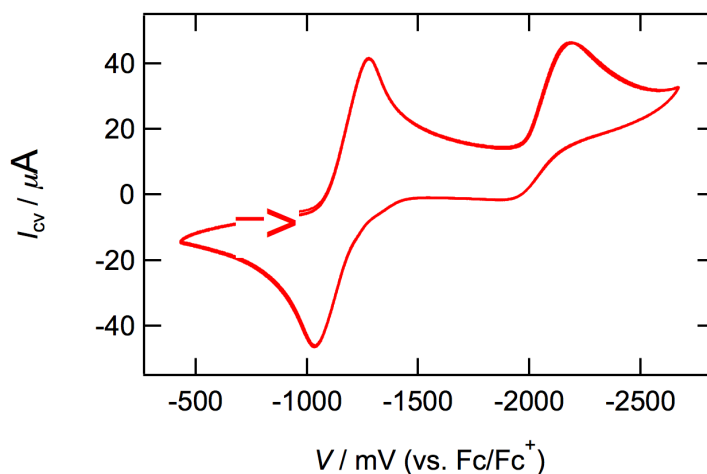


Figure 2.14. Cyclic voltammogram of the diazapentalene. Cyclic voltammogram of a 1 mM solutions of $(C_4HNMe)_2CMe_2$ in THF (0.3 M $[nBu_4N][PF_6]$) using a platinum electrode and Ag/Ag^+ reference electrode. Potential was internally referenced to Fc/Fc^+ . Scan rate = 500 mV/s.

2-8. Understanding the Electronic Structure of Dipyrromethane Complexes.

The most unusual feature of the complexes reported is the atypical electronic structure suggested by the electrochemical experiments. More precisely, the highest occupied molecular orbitals appear to be ligand-based (see **Section 2-5.** for details), even for the complexes featuring high-spin electron configurations ($(dpma)Mn(py)_2$, $(dpma)Fe(py)_2$, and $(dpma)Co(py)_2$). The dipyrromethane *pyrrole* π electrons are thus higher in energy than the frontier orbitals of the 3d transition metal ($Mn \rightarrow Zn$) investigated, making intramolecular redox between the ligand and metal possible. Having fully populated

ligand-based orbitals higher in energy than partially filled metal-based orbitals suggests that intramolecular redox is possible and might occur. We presented three possibilities for what types of intramolecular redox could be present, namely : (1) ligand-based electrons could reduce the bound metal ion filling the n partially filled $3d$ orbitals with $n e^-$, leaving n holes on the ligand platform; (2) the ligand and metal-based orbitals are closely matched in energy and spin state tautomerism is possible;¹⁵ (3) no intramolecular redox occurs, leaving each metal in the divalent state with the ligand fully reduced.

Should electronic structure scenario 1 be operative, the dipyrromethane ligand structure should manifest stepwise oxidation with concomitant bond elongation within the pyrrole subunits¹⁴ and the onset of oxidation in the electrochemical experiments should vary with metal ion substitution. Close inspection of all the bond lengths from the series (**Table 2.1**) does not reveal any perturbation of the dipyrromethane σ bonds or π bonds within the ligand architecture. The only significant variation discernible within the series are the M–N_{dpma} and M–N_{py} (bonds 1–2 and 3–4, respectively, **Table 2.1**) bond lengths which vary due to the variable ionic size for the metals in different spin states. The invariant electrochemical behavior of metals bound by the dipyrromethane ligand offer the most compelling evidence against scenario 1. Namely, the DPV experiments on the (dpma)M^{II}(py)₂ series reveal a common two-electron oxidation pathway that is entirely ligand-based, invariant to the divalent metal-bound (or its spin state) within the dpma framework. Moreover, the UV/Vis/NIR results do not reveal a significant LMCT band, suggesting there are not even any excited states featuring charge transfer from the dpma to the M^{II} ions.

The SQUID magnetometry results cannot rule out any of the electronic structure postulates, as all three can be consistent with the total spin for each complex being preserved over the temperature range investigated. The EPR for both complex (dpma)Mn(py)₂ and (dpma)Co(py)₂ are consistent for $S = 5/2$ Mn and $S = 3/2$ Co nuclei, respectively, with observed g values inconsistent for organic radicals, where

$g \approx 2$. The EPR signal for both **(dpma)Mn(py)₂** and **(dpma)Co(py)₂** persist over a broad temperature range (77–298K). While this observation is unusual for typical Co^{II} ions in tetrahedral environments where fast spin-lattice relaxation times of the high-spin Co^{II} nucleus usually limit observation of transitions to below $\sim 30\text{K}$,²¹ it also is inconsistent with spin state tautomerism as a function of temperature.¹⁵ The Mössbauer data for **(dpma)Fe(py)₂** and **(dpma)Fe(bpy)** suggest a single major nuclear environment for each of the Fe^{II} ions and do not show any variance between 4 and 77K. Based on the structural, electrochemical and magnetic data, we rule out electronic structure scenarios 1 and 2 in favor of scenario 3 wherein no intramolecular redox is observed. This assignment is corroborated by the DFT analysis.

2-9. Conclusions.

Transition metal complexes (Mn \rightarrow Zn) of the dipyrromethane ligand 1,9-dimesityl-5,5-dimethyldipyrromethane (dpma) have been prepared. Arylation of the dpma ligand *a* to the pyrrole nitrogen donors limits the accessibility of the pyrrole π electrons for transition metal coordination, instead forcing η^1, η^1 coordination to the divalent metal ion. Electrochemical studies on the (dpma)M^{II}(py)₂ series reveal a common two-electron oxidation pathway that is entirely ligand-based, invariant to the divalent metal-bound (or its spin state) within the dpma framework. The energetically high-lying π electrons from the dipyrromethane framework almost exclusively account for the observed redox behavior of the metal complexes studied. This latter observation indicates that fully populated ligand-based orbitals from the dpma construct lie above partially filled metal 3*d* orbitals without intramolecular redox chemistry or spin state tautomerism occurring. This unusual electronic structure is

(21) (a) Pilbrow, J. R. *Transition Ion Electron Paramagnetic Resonance*; Clarendon Press: Oxford, 1990. (b) Aasa, R.; Vanngard, T. *J. Magn. Reson.* **1975**, *19*, 308-315.

corroborated by DFT studies, revealing fully occupied ligand-based π orbitals at higher energies than half filled metal $3d$ orbitals for Mn–Zn. While chemical oxidation of the (dpma) M^{II} species did not yield a stable ligand-based diradical/dication, further experimental and computational studies are needed to elucidate the exact nature of the biradical generated as a result of both electrochemical and chemical oxidations.

2-10. Experimental Methods.

General Synthetic Considerations

All manipulations were carried out in the absence of water and dioxygen using standard Schlenk techniques, or in an inert atmosphere glovebox (M. Braun) under a dinitrogen atmosphere. All glassware was oven dried for a minimum of 1 h and cooled in an evacuated antechamber prior to use in the glovebox. Acetonitrile, benzene, diethyl ether, dichloromethane, *n*-hexane and tetrahydrofuran were dried and deoxygenated on a Glass Contour System (SG Water USA, Nashua, NH) and stored over 4 Å molecular sieves (Strem) prior to use. Chloroform-*d* was purchased from Cambridge Isotope Labs and used as received. Benzene-*d*₆ and dichloromethane-*d*₂ were purchased from Cambridge Isotope Labs and were degassed and stored over 4 Å molecular sieves prior to use. 2,2-dimethoxypropane and was purchased from Sigma-Aldrich, dried over CaCl₂, vacuum distilled, and degassed prior to use. Pyridinium *p*-toluenesulfonate, ferrocenium hexafluorophosphate, anthracene, bipyridine and anhydrous pyridine were purchased from Aldrich and used as received. Silver chloride, silver nitrate, anhydrous iron(II) chloride and anhydrous cobalt(II) chloride were purchased from Strem and used as received. Phenyllithium was prepared by lithiation of iodobenzene with *n*-butyllithium. 2-(2,4,6-

trimethylphenyl)-1*H*-pyrrole was synthesized according to literature procedures.²² Metal precursors $MCl_2(py)_2$ ($M = Mn, Fe, Co, Ni$) were synthesized based on literature procedure.^{18,23} Celite® 545 (J. T. Baker), silica gel 32–63 μ (Dynamic Adsorbents, Atlanta, GA), tetra-*n*-butylammonium hexafluorophosphate (Alfa Aesar) and zinc chloride (Aldrich) were dried in a Schlenk flask for 24 h under dynamic vacuum while heating to at least 150 °C. UV/Visible spectra were recorded on a Varian Cary 50 UV/Visible spectrometer, with a scan rate of 300 nm/min. ¹H and ¹³C NMR spectra were recorded on Varian Mercury 400 MHz or Varian Unity/Inova 500 MHz spectrometers. ¹H and ¹³C NMR chemical shifts are reported relative to SiMe₄ using the chemical shift of residual solvent peaks as reference. Mass spectrometry was performed at the Harvard University FAS Center for Systems Biology Mass Spectrometry and Proteomics Resource Laboratory on an Agilent 6210 TOF LC/MS with a dual nebulizer ESI source. Elemental Analyses were carried out at Desert Analytics, Inc. (Tucson, AZ) or Robertson Microlit Laboratories, Inc. (Madison, NJ).

Characterization and Physical Measurements.

Electrochemical experiments were carried out using a CH Instruments CHI660C Electrochemical Workstation. The electrolyte used was 0.1 M [ⁿBu₄N][PF₆] in acetonitrile or 0.3 M [ⁿBu₄N][PF₆] in THF. The concentration of all analytes was 1 mM. The working electrode was either platinum or glassy carbon. A platinum wire was used as the counter electrode. Non-aqueous Ag/Ag⁺ electrodes (10 mM AgNO₃) were used with the corresponding electrolyte solution. Cyclic voltammetry was performed with a scan rate of 100 mV/s or 500 mV/s. Differential pulse voltammetry was performed with a scan rate of 20 mV/s, a potential increment of 4 mV, a pulse amplitude of 50 mV, a sampling width of 16.7 ms, a pulse width of 50 ms, and a pulse period of 200 ms.

(22) Rieth, R. D.; Mankad, N. P.; Calimano, E.; Sadighi, J. P. *Org. Lett.* **2004**, *6*, 3981-3983.

(23) Allan, J. R.; Brown, D. H.; Nuttall, R. H.; Sharp, D. W. A. *J. Chem. Soc. A* **1966**, 1031-1034.

Magnetic measurements were recorded using a Quantum Designs SQUID magnetometer running MPMSR2 software (Magnetic Property Measurement System Revision 2). Data was recorded at 1000 Oe. Samples were suspended in the magnetometer in folded plastic bags contained in perforated Lily #4 gel capsules, inserted into plastic straws sealed under nitrogen. Loaded samples were centered within the magnetometer using the DC centering scan at 35 K and 1000 gauss. Data were acquired at 2–10 K (one data point/2 K), 10–60 K (one data point/5 K), 60–300 K (one data point/10 K).

Table 2.3. Equations for magnetic measurements.

$$\chi_m = \frac{\chi M}{mH} \quad (2.1)$$

$$\mu_{eff} = \sqrt{\frac{3k}{N\mu_B^2} \chi_m T} \quad (2.2)$$

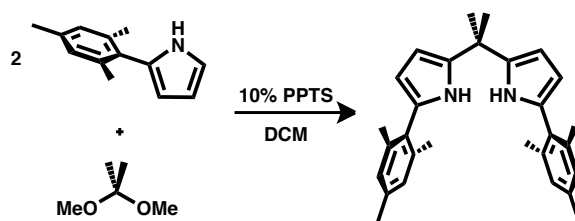
$$\chi_m = \frac{Ng^2\mu_B^2}{3kT} (S(S+1)) \quad (2.3)$$

The magnetic susceptibility was adjusted for diamagnetic contributions using the constitutive corrections of Pascal's constants. Processing and simulation was done with the julX 1.4.1 package,¹⁶ which was also used to correct for temperature independent paramagnetism. The molar magnetic susceptibility (χ_m) and effective magnetic moment (μ_{eff}) were calculated by converting the calculated magnetic susceptibility (χ) obtained from the magnetometer according to Eq. 2.1 and Eq. 2.2. Curie-Weiss behavior was verified by a plot of χ_m^{-1} versus T (**Figure 2.4b**). Solution magnetic susceptibilities were determined by Evans's method²⁴ using hexamethyldisiloxane as an internal reference and were adjusted for diamagnetic contributions using the contributions using the constitutive corrections of Pascal's constants.

(24) (a) Evans, D. F. *J. Chem. Soc.* **1959**, 2003-2005. (b) Sur, S. K. *J. Magn. Reson.* **1989**, 82, 169-173.

X-band EPR spectroscopic measurements were performed using a Bruker EMX spectrometer equipped with 13 inch magnets, an ER 4102ST cavity, and a Gunn diode microwave source. Powder samples were cooled using a liquid nitrogen cold finger dewar. Averaged g -factors can be extracted from the magnetic susceptibility data, assuming zero orbital contributions, using Eq. 2.3. These values were used in the simulation of the Co EPR powder spectrum. Simulation and fitting was done with the EasySpin 3.0.0²⁵ ToolBox for MATLAB.²⁶ In addition to g values, hyperfine (^{59}Co) and zero field splitting parameters the spectrum was also simulated by optimizing the FWHM value for the isotropic magnetic field domain broadening (FWHM = 1100 G), and the FWHM of the Gaussian distribution of g values (g_{\perp} 0.5, g_{\parallel} 1.0). ^{57}Fe Mössbauer spectra were measured with a constant acceleration spectrometer (SEE Co, Minneapolis, MN). Isomer shifts are quoted relative to Fe metal at room temperature. Data was analyzed and simulated with WMOSS software (Web Research Corp., Edina, MN).

Syntheses and Reactivity.

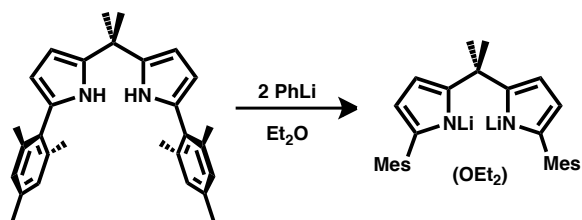


1,9-Dimesityl-5,5-dimethyldipyrromethane, dpmaH₂: This compound was prepared by a modification of a literature procedure.^{10b} A 250 mL round-bottomed flask was charged with 2-(2,4,6-trimethylphenyl)-1H-pyrrole (2.038 g, 11.00 mmol), 2,2-dimethoxypropane (11.0 g, 123 mmol, 11.2 equiv.), and 180 mL of CH₂Cl₂. After stirring for 5 min, pyridinium *p*-toluenesulfonate (0.280 g, 1.11 mmol, 0.101 equiv.) was added resulting in a color change from colorless to pale orange. The reaction

(25) Stoll, S.; Schweiger, A. *J. Magn. Reson.* **2006**, *178*, 42-55.

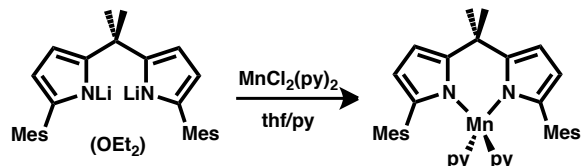
(26) *MATLAB*, version 7.6 (R2008a); The MathWorks, Inc.: Natick, MA, 2008.

was stirred at room temperature for 24 h. Solvent and volatiles were removed *in vacuo* resulting in an orange residue. The residue was extracted with 50 mL of Et₂O and filtered through a Celite plug to remove PPTS. The solvent was removed *in vacuo* and the residue redissolved in 50 mL CH₂Cl₂. The solution was filtered through a plug of silica gel (15 mL) to give a colorless filtrate. Solvent was removed *in vacuo* and the residue was triturated twice with 25 mL *n*-hexane followed by removal of the hexane *in vacuo*, affording **dpmaH₂** as a white powder (1.970 g, 87.24%). ¹H NMR (500 MHz, CDCl₃): δ/ppm 7.56 (br s, 2H, N-H), 6.88 (s, 4H, -C₆H₂Me₃), 6.09 (t, *J*_{HH} = 3.0 Hz, 2H, pyrrole C-H), 5.89 (t, *J*_{HH} = 2.8 Hz, 2H, pyrrole C-H), 2.29 (s, 6H, *para*-C₆H₂(CH₃)₃), 2.06 (s, 12H, *ortho*-C₆H₂(CH₃)₃), 1.69 (s, 6H, (CH₃)₂C=). ¹³C {¹H} NMR (125 MHz, CDCl₃): δ/ppm 138.7, 138.5, 137.6, 131.0, 128.9, 128.2, 107.6, 103.5, 35.5, 29.1, 21.2, 20.7. CHN% Calc. for C₂₉H₃₄N₂: C 84.83, H 8.34, N 6.82; Found: C 85.15, H 8.17, N 6.71.

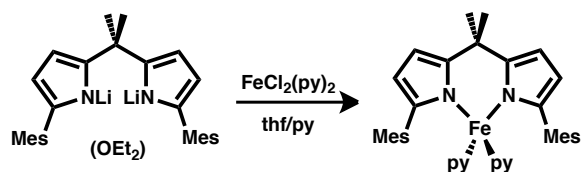


(dpma)Li₂(OEt₂): In a 20 mL scintillation vial **dpmaH₂** (1.000 g, 2.435 mmol) was dissolved in 10 mL of Et₂O. In another 20 mL vial phenyllithium (0.410 g, 4.88 mmol, 2.00 equiv.) was dissolved in 5 mL of Et₂O. The vials were placed in a liquid nitrogen cooled cold well until partially frozen. The solution phenyllithium was thawed and added dropwise via pipet to the thawing solution of **dpmaH₂**. The solution was stirred at room temperature for 2 h. Removal of the volatiles *in vacuo* gave an off white powder. The powder was washed with *n*-hexane on a glass frit and dried to afford **(dpma)Li₂(OEt₂)** as a white powder (0.893 g, 73.8%). ¹H NMR (500 MHz, C₆D₆ w/ THF): δ/ppm 6.86 (s, 4H, -C₆H₂Me₃), 6.66 (d, *J*_{HH} = 2.5 Hz, 2H, pyrrole C-H), 6.20 (d, *J*_{HH} = 2.5 Hz, 2H, pyrrole C-H), 3.26 (q, *J*_{HH} = 7 Hz,

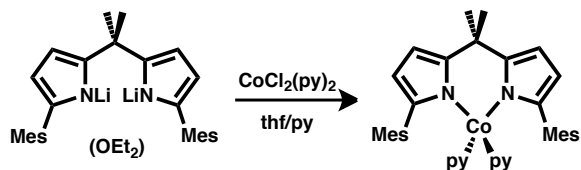
4H, ether), 2.25 (s, 12H, *ortho*-C₆H₂(CH₃)₃), 2.21 (s, 6H, *para*-C₆H₂(CH₃)₃), 2.10 (s, 6H, (CH₃)₂C=), 1.11 (t, *J*_{HH} = 7 Hz, 6H, ether). ¹³C {¹H} NMR (125 MHz, C₆D₆w/ THF): δ/ppm 151.5, 139.0, 138.7, 137.5, 134.8, 128.3, 105.5, 102.5, 65.8, 39.9, 31.7, 21.5, 21.1, 15.5. CHN% Calc. for C₃₃H₄₂N₂OLi₂: C 79.82, H 8.52, N 5.64; Found: C 79.53, H 8.41; N 5.56.



(dpma)Mn(py)₂: In a 20 mL scintillation vial **(dpma)Li₂(OEt₂)** (100 mg, 0.202 mmol) was dissolved in 8 mL of THF. In another 20 mL vial MnCl₂(py)₂ (57 mg, 0.20 mmol) was slurried in 8 mL of THF and 1 mL of pyridine. Both vials were placed in a liquid nitrogen cooled cold well until partially frozen. The solution of **(dpma)Li₂(OEt₂)** was thawed and added to the stirring slurry of MnCl₂(py)₂. The reaction mixture became a yellow solution as it warmed. The reaction was stirred at room temperature for 3 h. Removal of the solvent *in vacuo* gave a dark yellow residue. The residue was extracted into 5 mL of CH₂Cl₂ and filtered to remove lithium chloride. Removal of the solvent *in vacuo* gave a yellow residue. Trituration with 5 mL diethyl ether followed by removal of volatiles *in vacuo* gave **(dpma)Mn(py)₂** as a light yellow powder (100 mg, 80.4%). Crystals suitable for X-ray diffraction were grown from an Et₂O/THF solution of **(dpma)Mn(py)₂**. The crystal used for diffraction was found to be 80% **(dpma)Mn(py)₂**, and 20% (dpma)Mn(py)(thf), presumably formed during crystallization. μ_{eff} (CD₂Cl₂, 295 K) 6.1(1) μ_{B} . CHN% Calc. for C₃₉H₄₂N₄Mn: C 75.34, H 6.88, N 9.01; Found: C 74.83, H 6.88, N 8.62.

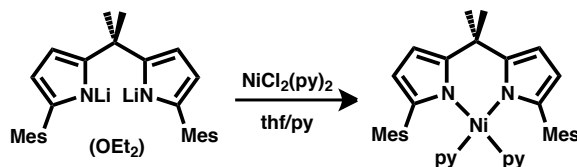


(dpma)Fe(py)₂: In a 20 mL scintillation vial **(dpma)Li₂(OEt₂)** (100 mg, 0.201 mmol) was dissolved in 8 mL of THF. In another 20 mL vial FeCl₂(py)₂ (57 mg, 0.20 mmol) was slurried in 8 mL of THF and 1 mL of pyridine. Both vials were placed in a liquid nitrogen cooled cold well until partially frozen. The solution of **(dpma)Li₂(OEt₂)** was thawed and added to the stirring slurry of FeCl₂(py)₂. The reaction mixture became an orange solution as it warmed. The reaction was stirred at room temperature for 3 h. Removal of the solvent *in vacuo* gave an orange residue. The residue was extracted into 5 mL of CH₂Cl₂ and filtered to remove lithium chloride. Removal of the solvent *in vacuo* gave a dark orange residue. Trituration with 5 mL diethyl ether followed by removal of volatiles *in vacuo* gave **(dpma)Fe(py)₂** as an orange-yellow powder (90 mg, 72%). Crystals suitable for X-ray diffraction were grown from an Et₂O solution of **(dpma)Fe(py)₂**. ¹H NMR (500 MHz, 295 K, CD₂Cl₂): δ/ppm 117.6 (br s), 36.6 (br s), 33.3 (s), 26.7 (s), 8.7 (s), 4.8 (br s), 4.3 (br s), 4.1 (s), -4.0 (br s). UV/Vis (CH₂Cl₂) λ_{max}/nm (ε/M⁻¹cm⁻¹) 420 (1520). μ_{eff} (CD₂Cl₂, 295 K) 5.2(1) μ_B. Results of combustion analysis for **(dpma)Fe(py)₂** were poor, four independent samples were tried and all were consistently low in carbon. Best result for C₃₉H₄₂N₄Fe, Calc.: C 75.23, H 6.80, N 9.00; Found: C 73.57 H 7.12 N 8.73.



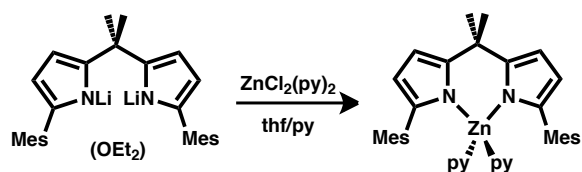
(dpma)Co(py)₂: In a 20 mL scintillation vial **(dpma)Li₂(OEt₂)** (100 mg, 0.201 mmol) was dissolved in 8 mL of THF. In another 20 mL vial CoCl₂(py)₂ (58 mg, 0.20 mmol) was slurried in 8 mL

of THF and 1 mL of pyridine. Both vials were placed in a liquid nitrogen cooled cold well until partially frozen. The solution of **(dpma)Li₂(OEt₂)** was thawed and added to the stirring slurry of CoCl₂(py)₂. The reaction mixture became a dark blue solution as it warmed. The reaction was stirred at room temperature for 3 h. Removal of the solvent *in vacuo* gave a blue residue. The residue was extracted into 5 mL of CH₂Cl₂ and filtered to remove lithium chloride. Removal of the solvent *in vacuo* gave a dark blue residue. Trituration with 5 mL diethyl ether followed by removal of volatiles *in vacuo* gave **(dpma)Co(py)₂** as a blue powder (82.5 mg, 66%). Crystals suitable for X-ray diffraction were grown from an Et₂O solution of **(dpma)Co(py)₂**. ¹H NMR (500 MHz, 295 K, CD₂Cl₂): δ/ppm 148.4 (br s), 66.1 (s), 50.8 (s), 43.0 (s), 10.0 (br s), 3.5 (s), 3.1 (s), 0.5 (s), -12.5 (s). UV/Vis (CH₂Cl₂) λ_{max}/nm (ε/M⁻¹cm⁻¹) 535 (410), 585 (620), 613 (870). μ_{eff} (CD₂Cl₂, 295 K) 4.5(1) μ_B. CHN% Calc. for C₃₉H₄₂N₄Co: C 74.86, H 6.77, N 8.95; Found: C 74.37, H 6.23, N 8.60.



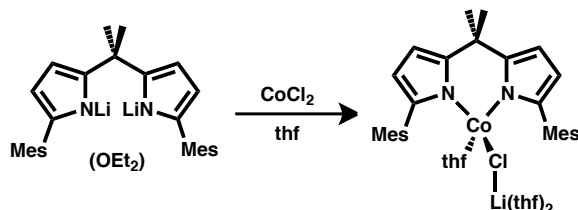
(dpma)Ni(py)₂: In a 20 mL scintillation vial **(dpma)Li₂(OEt₂)** (100 mg, 0.201 mmol) was dissolved in 8 mL of THF. In another 20 mL vial NiCl₂(py)₂ (58 mg, 0.20 mmol) was slurried in 8 mL of THF and 1 mL of pyridine. Both vials were placed in a liquid nitrogen cooled cold well until partially frozen. The solution of **(dpma)Li₂(OEt₂)** was thawed and added to the stirring slurry of NiCl₂(py)₂. The reaction mixture gradually turned dark red as it warmed. The reaction was stirred at room temperature for 18 h. Removal of the solvent *in vacuo* gave a dark red residue. The residue was extracted into 5 mL of CH₂Cl₂ and filtered to remove lithium chloride. Removal of the solvent *in vacuo* gave a dark red solid which was triturated with 5 mL diethyl ether. Removal of the solvent *in vacuo* gave

(dpma)Ni(py)₂ as a brick red powder (90 mg, 72%). Crystals suitable for X-ray diffraction were grown via vapor diffusion of Et₂O into a THF solution of **(dpma)Ni(py)₂**. ¹H NMR (500 MHz, 295 K, CD₂Cl₂): δ/ppm 8.41 (br s), 7.24 (t, *J*_{HH} = 7.50 Hz), 6.66 (br s), 5.93 (s), 5.52 (s), 2.24 (s). ¹³C {¹H} NMR (125 MHz, CD₂Cl₂): δ/ppm 150.6, 145.2, 138.6, 137.8, 137.0, 135.2, 127.9, 124.9, 110.9, 101.3, 38.5, 32.0, 23.0, 21.0. UV/Vis (CH₂Cl₂) λ_{max}/nm (ε/M⁻¹cm⁻¹) 503 (190). CHN% Calc. for C₃₉H₄₂N₄Ni: C 74.89, H 6.77, N 8.96; Found: C 74.62, H 6.69, N 8.71.

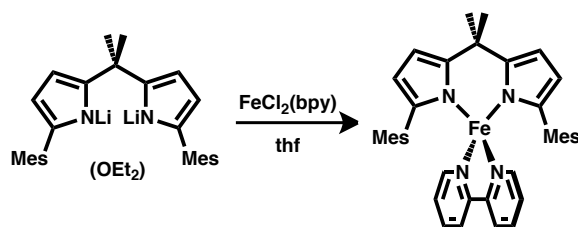


(dpma)Zn(py)₂: In a 20 mL scintillation vial **(dpma)Li₂(OEt₂)** (100 mg, 0.201 mmol) was dissolved in 8 mL of THF. In another 20 mL vial ZnCl₂ (27 mg, 0.20 mmol) was slurried in 8 mL of THF and 1 mL of pyridine. Both vials were placed in a liquid nitrogen cooled cold well until partially frozen. The solution of **(dpma)Li₂(OEt₂)** was thawed and added to the stirring slurry of ZnCl₂. The reaction mixture gradually turned yellow as it warmed. The reaction was stirred at room temperature for 3 h. Removal of the solvent *in vacuo* gave a yellow residue. The residue was extracted into 5 mL of CH₂Cl₂ and filtered to remove lithium chloride. Removal of the solvent *in vacuo* gave yellow solid. Trituration with 5 mL diethyl ether followed by removal of volatiles *in vacuo* gave **(dpma)Zn(py)₂** as a yellow powder. (82 mg, 65%). ¹H NMR (400 MHz, CD₂Cl₂): δ/ppm 7.86 (t, *J*_{HH} = 7.6 Hz, 2H, *p*-C₅H₅N), 7.60 (d, *J*_{HH} = 4.8 Hz, 4H, *o*-C₅H₅N), 7.25 (t, *J*_{HH} = 6.4 Hz, 4H, *m*-C₅H₅N), 6.45 (s, 4H, -C₆H₂Me₃), 6.16 (d, *J*_{HH} = 2.8 Hz, 2H pyrrole C-H), 5.79 (d, *J*_{HH} = 2.8 Hz, 2H pyrrole C-H), 2.08 (s, 6H, *para*-C₆H₂(CH₃)₃), 1.77 (s, 12H, *ortho*-C₆H₂(CH₃)₃), 1.76 (s, 6H, (CH₃)₂C=). ¹³C {¹H} NMR (100 MHz, CD₂Cl₂): δ/ppm 149.6, 149.4, 139.9, 138.2, 137.5, 136.0, 135.3, 127.9, 125.1, 106.9, 102.2,

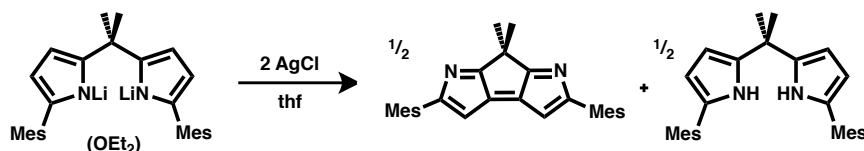
37.7, 33.0, 21.1, 20.9. CHN% Calc. for $C_{39}H_{42}N_4Zn$: C 74.10, H 6.70, N 8.86; Found: C 73.93, H 6.65, N 8.69.



$[(\text{dpma})\text{CoCl}(\text{thf})][\text{Li}(\text{thf})_2]$: In a 20 mL scintillation vial $(\text{dpma})\text{Li}_2(\text{OEt}_2)$ (200 mg, 0.403 mmol) was dissolved in 8 mL of THF. In another 20 mL vial CoCl_2 (56 mg, 0.40 mmol) was slurried in 8 mL of THF. Both vials were placed in a liquid nitrogen cooled cold well until partially frozen. The solution of $(\text{dpma})\text{Li}_2(\text{OEt}_2)$ was thawed and added to the stirring slurry of CoCl_2 . The reaction mixture became a dark teal solution as it warmed. The reaction was stirred at room temperature for 3 h. Removal of the solvent *in vacuo* gave a teal residue. The residue was extracted into 5 mL of CH_2Cl_2 and filtered to remove lithium chloride. Removal of the solvent *in vacuo* gave a dark teal residue. Trituration with 5 mL *n*-hexane followed by removal of volatiles *in vacuo* gave a teal powder. Drying *in vacuo* gave $[(\text{dpma})\text{CoCl}(\text{thf})][\text{Li}(\text{thf})_2]$ as a teal powder (158 mg, 54%). Crystals suitable for X-ray diffraction were grown from an Et_2O solution of $[(\text{dpma})\text{CoCl}(\text{thf})][\text{Li}(\text{thf})_2]$. ^1H NMR (500 MHz, 295 K, CD_2Cl_2): δ /ppm 71.61 (s), 61.22 (s), 58.05 (s), 48.34 (s), 27.90 (br s), 10.99 (br s), 3.16 (br s), 3.05 (br s), 1.04 (s), 0.97 (s), -10.99 (br s), -17.11 (s). μ_{eff} (CD_2Cl_2 , 295 K) 4.6(1) μ_{B} . Results of combustion analysis for $[(\text{dpma})\text{CoCl}(\text{thf})][\text{Li}(\text{thf})_2]$ were poor, three independent samples were tried and all were consistently low in carbon. Best result for $C_{41}H_{56}N_2O_3\text{CoClLi}$, Calc.: C 67.81, H 7.77, N 3.86; Found: C 66.60, H 7.55, N 3.97.



(dpma)Fe(bpy): A 20 mL scintillation vial was charged with FeCl_2 (51.7 mg, 0.408 mmol), bipyridine (63.8 mg, 0.408 mmol), and 8 mL of THF. After stirring for 12 h the mixture was a light red suspension. In another vial **(dpma)Li₂(OEt₂)** (200 mg, 0.402 mmol) was dissolved in 5 mL of THF. Both vials were placed in a liquid nitrogen cooled cold well until partially frozen. The solution of **(dpma)Li₂(OEt₂)** was thawed and added to the stirring slurry of $\text{FeCl}_2(\text{bpy})$. The reaction mixture became a dark red solution as it warmed. The reaction was stirred at room temperature for 3 h. Removal of the solvent *in vacuo* gave a dark red residue. The residue was extracted into 5 mL of CH_2Cl_2 and filtered to remove lithium chloride. Removal of the solvent *in vacuo* gave a dark red residue. Trituration with 5 mL diethyl ether followed by removal of volatiles *in vacuo* gave **(dpma)Fe(bpy)** as a brown powder (223 mg, 89.4%). Crystals suitable for X-ray diffraction could be grown from THF. ^1H NMR (500 MHz, 295 K, CD_2Cl_2): δ /ppm 70.1 (s), 60.4 (br s), 46.5 (s), 44.7 (s), 38.7 (s), 11.2 (br s), 9.2 (s), 7.5 (s), -3.3 (s), -33.8 (s). UV/Vis (CH_2Cl_2) $\lambda_{\text{max}}/\text{nm}$ ($\epsilon/\text{M}^{-1}\text{cm}^{-1}$) 299 (11200), 395 (1100, sh). μ_{eff} (CD_2Cl_2 , 295 K) 5.1(1) μ_{B} . CHN% Calc. for $\text{C}_{29}\text{H}_{32}\text{N}_2\text{Zn}(\text{C}_6\text{H}_5\text{N})_2$: C 75.47, H 6.50, N 9.03; Found: C 75.22, H 6.60, N 8.78.



2,5-Dimesityl-7,7-dimethyl-7H-1,6-diazacyclopenta[a]pentalene, $(\text{C}_4\text{HNMe}_s)_2\text{CMe}_2$: In a 20 mL scintillation vial **(dpma)Li₂(OEt₂)** (250 mg, 0.503 mmol) was dissolved in 10 mL of THF. In

another 20 mL vial AgCl (156 mg, 1.09 mmol, 2.15 equiv.) was slurried in 5 mL of THF. Both vials were placed in a liquid nitrogen cooled cold well until frozen. The solution of **(dpma)Li₂(OEt₂)** was thawed and added to the thawing slurry of AgCl. The reaction mixture darkened as it warmed, becoming red after several hours. Stirring was continued overnight. The mixture was filtered through Celite to remove Ag⁰ and THF was removed *in vacuo*. The residue was extracted into 5 mL CH₂Cl₂ and filtered through Celite to remove LiCl, followed by the removal of solvent *in vacuo*. The desired product was separated from the side product **dpmaH₂** by dissolving the residue in 5 mL benzene and filtering the solution through a plug of silica gel, the silica was washed with an additional 5 mL benzene. The fraction of material remaining on the silica was then isolated by washing with Et₂O. Concentration of the benzene fraction *in vacuo* gave **dpmaH₂** (89 mg, 43% based on lithium complex). Concentration of the ether fraction *in vacuo* gave **(C₄HNMe_s)₂CMe₂** as a dark red powder (60 mg, 29% based on lithium complex). Note that the maximum yield based on **(dpma)Li₂(OEt₂)** for each **dpmaH₂** and **(C₄HNMe_s)₂CMe₂** is 50%. Crystals suitable for X-ray diffraction were grown from an Et₂O solution of **(C₄HNMe_s)₂CMe₂**. ¹H NMR (400 MHz, CD₂Cl₂): δ/ppm 6.98 (s, 4H, -C₆H₂Me₃), 6.27 (s, 2H, (C₅NHMe_s)₂CMe₂), 2.34 (s, 18H, *ortho/para*-C₆H₂(CH₃)₃), 1.67 (s, 6H, (H₃C)₂C=). ¹³C {¹H} NMR (100 MHz, CD₂Cl₂): δ/ppm 191.0, 176.8, 147.3, 139.1, 137.3, 132.7, 128.9, 108.4, 39.3, 26.1, 21.3, 21.0. HRMS (ESI⁺): *m/z* 407.24696 [M+H]⁺, 424.27494 [M+NH₄]⁺.

General Procedure for Chemical Oxidations of M(py)₂ Complexes: In a 20 mL scintillation vial (dpma)M(py)₂ (20 mg, 0.032 mmol, M = Mn, Fe, Co, or Ni) was dissolved in 3 mL THF. In another 20 mL vial Fc⁺PF₆⁻ (10.6 mg, 0.0320 mmol, 1.00 equiv.) was slurried in 2 mL THF. Both vials were placed in a liquid nitrogen cooled cold well until partially frozen. The solution of metal complex was thawed and added to the thawing slurry of ferrocenium. The reaction mixture was stirred for 2 h. After 2 h a solution of anthracene (5.7 mg, 0.032 mmol, 1.0 equiv.) in 1 mL benzene was added to the reaction

mixture, solvents were then removed *in vacuo*. A portion of the residue was dissolved in CD₂Cl₂ and filtered through a glass frit to remove any insoluble materials. ¹H NMR in CD₂Cl₂ with a long delay time (10 s) was used to provide accurate integrations of ferrocene (δ 4.15 ppm, 10 H) versus the internal standard anthracene (δ/ppm 8.44 (s, 2H); 8.02 (m, 4H); 7.47 (m, 4H)) to judge the consumption of Fc⁺PF₆⁻. Within errors of the experiment and integration one equivalent of ferrocene was observed. Yield of Fc as observed by ¹H NMR: Mn 96%, Fe 109%, Co 100%, Ni 92%.

Computational Methods.

The electronic structures of (dpma)Mn(py)₂, (dpma)Fe(py)₂, (dpma)Co(py)₂, (dpma)Ni(py)₂, and (dpma)Zn(py)₂ were examined using Gaussian 03.¹⁹ Geometry optimizations were done using the atomic coordinates of the crystal structures as a starting point. No truncations of the ligand platform were made and no symmetry was imposed upon the molecules. All optimizations were carried out with B3LYP²⁷ hybrid functional. The all-electron polarized triple-ξ quality Karlsruhe²⁰ basis sets (TZVP) were used for the metals and coordinated N atoms. For the remaining C and H atoms the all-electron polarized split valence double-ξ quality (SV(P)) Karlsruhe basis sets were used. The Ni and Zn structures were optimized as singlets. The paramagnetic systems were optimized with multiplicities based on their magnetic moments from SQUID and solution NMR determination, Mn – sextet, Fe – quintet, Co – quartet. Spin density plots and molecular orbital pictures were generated from Gaussian cube files using Visual Molecular Dynamics 1.8.6.²⁸

(27) (a) Becke, A. D. *J. Chem. Phys.* **1993**, 98, 5648-5652. (b) Vosko, S. H.; Wilk, L.; Nusair, M. *Can. J. Phys.* **1980**, 58, 1200-1211. (c) Lee, C. T.; Yang, W. T.; Parr, R. G. *Phys. Rev. B: Solid State* **1988**, 37, 785-789.

(28) Humphrey, W.; Dalke, A.; Schulten, K. *J. Mol. Graphics Modell.* **1996**, 14, 33-38.

X-ray Diffraction Techniques.

All structures were collected on either a Siemens or Brüker three-circle platform goniometer equipped with either a Brüker Apex I or Apex II CCD and an Oxford cryostream cooling device. Radiation was from a graphite fine focus sealed tube Mo $K\alpha$ (0.71073 Å) source. Crystals were mounted on a cryoloop using Paratone N oil. Structures were collected at 193 K or 100 K. Data was collected as a series of φ and/or ω scans. Data was integrated using SAINT²⁹ and scaled with either a numerical or multi-scan absorption correction using SADABS²⁹. The structures were solved by direct methods or Patterson maps using SHELXS-97³⁰ and refined against F^2 on all data by full matrix least squares with SHELXL-97.³⁰ All non-hydrogen atoms were refined anisotropically. Hydrogen atoms were placed at idealized positions and refined using a riding model. The isotropic displacement parameters of all hydrogen atoms were fixed to 1.2 times the U value of the atoms they are linked to (1.5 times for methyl groups). Further details on several structures are noted below.

(dpma)Mn(py)₂: One of the bound pyridine molecules on one of the Mn centers exhibited substitutional disorder. The disorder was refined with pyridine as the major part (60%) and a THF molecule as the minor part (40%). The pyridine and THF were both refined with the help of similarity restraints on 1–2 and 1–3 distances. The pyridine was refined with the help of a flat restraint. Similarity and rigid bond restraints were also placed on the anisotropic displacement parameters of all disordered atoms. The 40% THF disorder on one of the two molecules in the asymmetric units means the composition of the crystal is 80% **(dpma)Mn(py)₂** (4), and 20% (dpma)Mn(py)(thf).

(dpma)Fe(py)₂: One of the bound pyridine molecules in the structure exhibited positional disorder. The disorder was refined with the help of similarity restraints on 1–2 and 1–3 distances. Each disordered

(29) APEX2 Software Suite; Brüker AXS: Madison, WI, 2009.

(30) (a) Sheldrick, G. M. *Acta Crystallogr., Sect. A: Found. Crystallogr.* **1990**, *46*, 467-473. (b) Sheldrick, G. M. *SHELX-97*; University of Göttingen: Göttingen, Germany, 1997.

ring was also restrained to be flat. In addition similarity and rigid bond restraints were placed on the anisotropic displacement parameters of all disordered atoms. The major part of the disorder refined to 84%.

(dpma)Co(py)₂: For the solvent THF molecule found in the unit cell similarity restraints on 1–2 and 1–3 distances were used to restrain the ring to be symmetric, though there was no apparent disorder. Similarity and rigid bond restraints on the anisotropic displacement parameters of the THF atoms were also employed.

(dpma)Ni(py)₂: The crystal was refined as a non-merohedral twin. The two primary domains were separated using CELL_NOW.²⁹ The data was integrated against both domains and scaled using TWINABS.²⁹ The structure was solved with the set of reflections from the primary domain, and refined against the set of reflections from the primary domain and overlapping reflections. Some residual density around heavy atoms was evident, and probably results from overlap with reflections from the omitted domains with smaller contributions.

[(dpma)CoCl(thf)][Li(thf)₂]: For the three THF molecules similarity and rigid bond restraints were placed on the anisotropic displacement parameters of all THF atoms. Possible positional disorders were present in the lithium bound THF molecules but were not modeled due to overall low structure quality and the minimal contribution (<10%) of such disorders when refined.

(dpma)Fe(bpy): One of the two solvent THF molecules exhibited positional disorder. The disorder was treated with the help of similarity restraints on 1–2 and 1–3 distances. Similarity and rigid bond restraints on the anisotropic displacement parameters of the disordered THF molecule were also employed.

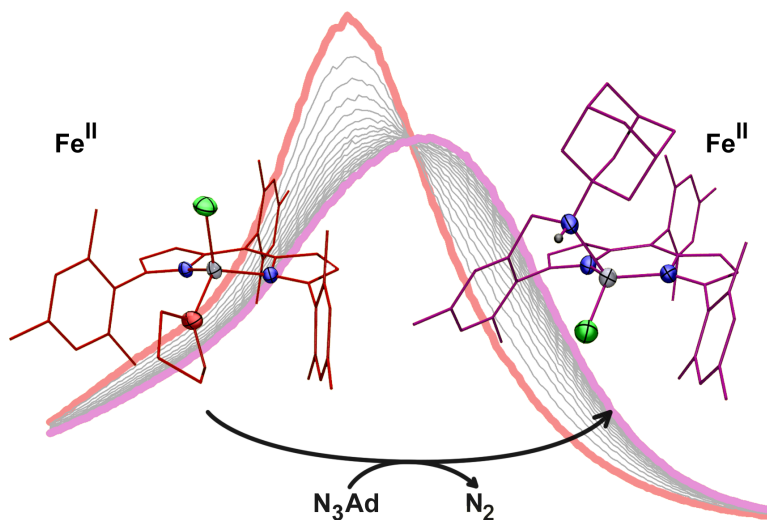
Table 2.4. X-ray diffraction experimental details.^{a,b}

	(dpma)M(py)₂					[(dpma)CoCl(thf)]	(dpma)Fe(bpy)	(C₄HNMe_s)₂CMe₂
	Mn	Fe	Ni	Co	Zn	[Li(thf)₂]		
Moiety formula	C ₃₉ H ₄₂ MnN ₄	C ₃₉ H ₄₂ FeN ₄	C ₃₉ H ₄₂ CoN ₄	C ₃₉ H ₄₂ NiN ₄ , C ₄ H ₈ O	C ₃₉ H ₄₂ N ₄ Zn	C ₄₁ H ₅₆ ClCo LiN ₂ O ₃	C ₃₉ H ₄₀ FeN ₄ , 2×(C ₄ H ₈ O)	C ₂₉ H ₃₀ N ₂
FW	621.71	622.62	625.7	697.58	632.14	726.2	764.81	406.55
Space group	<i>P</i> $\bar{1}$	<i>P</i> 2 ₁ / <i>n</i>	<i>P</i> 2 ₁ / <i>c</i>	<i>P</i> 2 ₁ / <i>n</i>	<i>P</i> $\bar{1}$	<i>P</i> 2 ₁ / <i>n</i>	<i>P</i> 2 ₁ / <i>c</i>	<i>P</i> 2 ₁ / <i>c</i>
a (Å)	12.0232(2)	14.1937(2)	16.0900(8)	9.2319(10)	11.9617(16)	13.7199(7)	10.7737 (3)	14.389(3)
b (Å)	15.6642(3)	10.4697(1)	12.8230(7)	27.390(3)	15.652(2)	12.6669(5)	23.0411 (5)	7.4555(10)
c (Å)	18.9630(3)	23.1322(3)	17.9711(9)	14.7364(15)	19.660(3)	22.8413(12)	16.5575 (4)	21.930(9)
α (°)	70.650(1)	90	90	90	67.369(2)	90	90	90
β (°)	87.145(1)	104.822(1)	114.562(1)	96.221(2)	87.695(3)	103.487(3)	90.090(1)	103.20(3)
γ (°)	83.730(1)	90	90	90	82.901(2)	90	90	90
V (Å³)	3349.13(10)	3323.15(7)	3372.3(3)	3704.4(7)	3371.3(8)	3860.1(3)	4110.2(2)	2290.4(11)
Z	4	4	4	4	4	4	4	4
μ (mm⁻¹)	0.427	0.487	0.541	0.562	0.761	0.553	0.410	0.068
Reflections	37811	77111	32345	47190	17583	15948	11617	44213
Comp. (%)	99.9	100.0	99.9	100.0	99.4	100.0	99.9	99.0
to 2(θ)	(25.04°)	(27.50°)	(27.50°)	(27.50°)	(27.48°)	(27.50°)	(29.68°)	(28.77°)
GOF on F²	1.013	1.019	1.037	1.027	1.058	0.983	1.029	1.018
R1, wR2^c	0.0511,	0.0392,	0.0382,	0.0463,	0.0488,	0.0524,	0.0418,	0.0524,
[I > 2σ(I)]	0.1093	0.0937	0.0975	0.1052	0.1164	0.1111	0.1013	0.1369
R_{indices} (all)	0.0977,	0.0627,	0.0482,	0.0662,	0.0830,	0.1125,	0.0618,	0.0683,
(R1, wR2)	0.1281	0.1061	0.1058	0.1162	0.1313	0.1455	0.1122	0.1527

^a λ (Å) = 0.71073

^b Collection temperature (T) = 193(2) K for all, except 100(2) K for (C₄HNMe_s)₂CMe₂.

^c R1 = Σ||F_o - |F_c|| / Σ|F_o|, wR2 = {Σ[w(F_o² - F_c²)²] / Σ[w(F_o²)²]}^{1/2}



Chapter 3: Intramolecular C–H Amination from an Iron Dipyrrromethene Complex¹

3-1. Introduction.

Introducing functionality into unactivated C–H bonds remains a significant challenge both in the realm of complex molecule synthesis as well as in the elaboration of simple hydrocarbon feed stocks into value-added commodity chemicals.² Current state of the art C–H bond functionalization techniques mainly utilize late transition metal catalysts that facilitate C–H activation and functionalization. Several limitations exist in these methods: C–H bond activation typically requires forcing conditions where oxidation processes can become unselective under the conditions required for bond activation to occur,³ or C–H bond activation only occurs proximal to substrate directing groups.⁴ The development of new inorganic/organometallic catalysts to effect atom or group transfer processes will mitigate the reliance

(1) This chapter was adapted with permission from King, E. R.; Betley, T. A. *Inorg. Chem.* **2009**, *48*, 2361-2363. Copyright 2009 American Chemical Society.

(2) Bergman, R. G. *Nature* **2007**, *446*, 391-393.

(3) Labinger, J. A.; Bercaw, J. E. *Nature* **2002**, *417*, 507-514.

(4) (a) Hinman, A.; Du Bois, J. J. *Am. Chem. Soc.* **2003**, *125*, 11510-11511. (b) Fiori, K. W.; Du Bois, J. J. *Am. Chem. Soc.* **2007**, *129*, 562-568. (c) Zalatan, D. N.; Du Bois, J. J. *Am. Chem. Soc.* **2008**, *130*, 9220-9221. (d) Dick, A. R.; Sanford, M. S. *Tetrahedron* **2006**, *62*, 2439-2463. (e) Das, S.; Incarvito, C. D.; Crabtree, R. H.; Brudvig, G. W. *Science* **2006**, *312*, 1941-1943.

on directing groups to activate C–H bonds,⁵ thereby minimizing waste generation during synthetic procedures.⁶ One potential strategy for sequential C–H bond activation and functionalization is to utilize the transient formation of metal-ligand multiple bonds to effect atom or group transfer processes.⁷ Herein we report an intramolecular C–H bond amination mediated by the reaction of a coordinatively and electronically unsaturated dipyrromethene Fe^{II} complex with organic azides.

A variety of ligand platforms have been employed that utilize strongly donating substituents (e.g. phosphines,⁸ amines,⁹ carbenes,¹⁰ β -diketiminates¹¹) resulting in strongly nucleophilic metal complexes capable of supporting metal-ligand multiple bond formation. To target metal-ligand multiple bonds potentially more reactive towards bond activation pathways, we sought an oxidatively resistant ligand system that sterically enforces minimal coordination at the metal center while maintaining an

(5) (a) Periana, R. A.; Taube, D. J.; Gamble, S.; Taube, H.; Satoh, T.; Fujii, H. *Science* **1998**, *280*, 560-564. (b) Iverson, C. N.; Smith, M. R. *J. Am. Chem. Soc.* **1999**, *121*, 7696-7697. (c) Chen, H. Y.; Schlecht, S.; Semple, T. C.; Hartwig, J. F. *Science* **2000**, *287*, 1995-1997.

(6) (a) Costas, M.; Chen, K.; Que, L., Jr. *Coord. Chem. Rev.* **2000**, *200*, 517-544. (b) Company, A.; Gomez, L.; Guell, M.; Ribas, X.; Luis, J. M.; Que, L., Jr.; Costas, M. *J. Am. Chem. Soc.* **2007**, *129*, 15766-15767. (c) Chen, M. S.; White, M. C. *Science* **2007**, *318*, 783-787.

(7) (a) Cummins, C. C.; Baxter, S. M.; Wolczanski, P. T. *J. Am. Chem. Soc.* **1988**, *110*, 8731-8733. (b) Cummins, C. C.; Schaller, C. P.; Vanduyne, G. D.; Wolczanski, P. T.; Chan, A. W. E.; Hoffmann, R. *J. Am. Chem. Soc.* **1991**, *113*, 2985-2994. (c) Walsh, P. J.; Hollander, F. J.; Bergman, R. G. *J. Am. Chem. Soc.* **1988**, *110*, 8729-8731. (d) Hoyt, H. M.; Michael, F. E.; Bergman, R. G. *J. Am. Chem. Soc.* **2004**, *126*, 1018-1019. (e) Badiei, Y. M.; Dinescu, A.; Dai, X.; Palomino, R. M.; Heinemann, F. W.; Cundari, T. R.; Warren, T. H. *Angew. Chem., Int. Ed.* **2008**, *47*, 9961-9964. (f) Davies, H. M. L.; Manning, J. R. *Nature* **2008**, *451*, 417-424.

(8) Phosphines: (a) Mindiola, D. J.; Hillhouse, G. L. *J. Am. Chem. Soc.* **2001**, *123*, 4623-4624. (b) Mindiola, D. J.; Hillhouse, G. L. *J. Am. Chem. Soc.* **2002**, *124*, 9976-9977.; (c) Jenkins, D. M.; Betley, T. A.; Peters, J. C. *J. Am. Chem. Soc.* **2002**, *124*, 11238-11239. (d) Brown, S. D.; Betley, T. A.; Peters, J. C. *J. Am. Chem. Soc.* **2003**, *125*, 322-323. (e) Betley, T. A.; Peters, J. C. *J. Am. Chem. Soc.* **2004**, *126*, 6252-6254.

(9) Amines: (a) Meyer, K.; Bill, E.; Mienert, B.; Weyhermüller, T.; Wieghardt, K. *J. Am. Chem. Soc.* **1999**, *121*, 4859-4876. (b) Rohde, J. U.; In, J. H.; Lim, M. H.; Brennessel, W. W.; Bukowski, M. R.; Stubna, A.; Münck, E.; Nam, W.; Que, L., Jr. *Science* **2003**, *299*, 1037-1039. (c) Berry, J. F.; Bill, E.; Bothe, E.; George, S. D.; Mienert, B.; Neese, F.; Wieghardt, K. *Science* **2006**, *312*, 1937-1941.

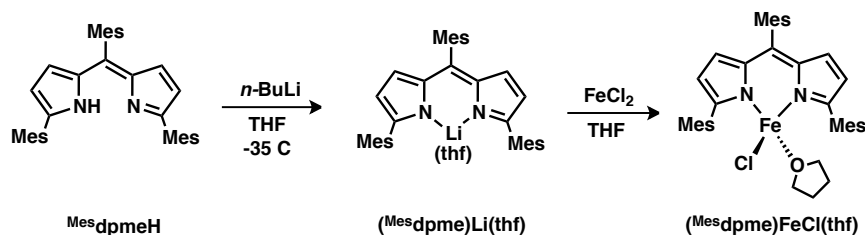
(10) Carbenes: (a) Hu, X. L.; Meyer, K. *J. Am. Chem. Soc.* **2004**, *126*, 16322-16323. (b) Vogel, C.; Heinemann, F. W.; Sutter, J.; Anthon, C.; Meyer, K. *Angew. Chem., Int. Ed.* **2008**, *47*, 2681-2684. (c) Cowley, R. E.; Bontchev, R. P.; Sorrell, J.; Sarracino, O.; Feng, Y. H.; Wang, H. B.; Smith, J. M. *J. Am. Chem. Soc.* **2007**, *129*, 2424-2425. (d) Nieto, I.; Ding, F.; Bontchev, R. P.; Wang, H. B.; Smith, J. M. *J. Am. Chem. Soc.* **2008**, *130*, 2716-2717. (e) Scepaniak, J. J.; Fulton, M. D.; Bontchev, R. P.; Duesler, E. N.; Kirk, M. L.; Smith, J. M. *J. Am. Chem. Soc.* **2008**, *130*, 10515-10516.

(11) β -Diketiminates: (a) Dai, X. L.; Kapoor, P.; Warren, T. H. *J. Am. Chem. Soc.* **2004**, *126*, 4798-4799. (b) Kogut, E.; Wiencko, H. L.; Zhang, L. B.; Cordeau, D. E.; Warren, T. H. *J. Am. Chem. Soc.* **2005**, *127*, 11248-11249. (c) Eckert, N. A.; Vaddadi, S.; Stoian, S.; Lachicotte, R. J.; Cundari, T. R.; Holland, P. L. *Angew. Chem., Int. Ed.* **2006**, *45*, 6868-6871. (d) Holland, P. L. *Acc. Chem. Res.* **2008**, *41*, 905-914.

electrophilic metal environment, which may confer unique reactivity to the resulting metal complexes. Arylated dipyrromethene ligands are good candidates to satisfy both desired design criteria.¹²

3-2. Synthesis and Characterization of Dipyrromethene Complexes.

Using pyridinium *p*-toluenesulfonate as a catalyst (5%), 2-mesityl pyrrole was condensed with mesitaldehyde dimethyl acetal to form the dipyrromethane. Subsequent oxidation with 2,3-dichloro-5,6-dicyano-1,4-benzoquinone (DDQ) in acetone affords the target 1,5,9-trimesityldipyrromethene ^{Mes}dpmeH, in 68% overall yield. Dipyrromethene ^{Mes}dpmeH precipitates from the acetone solution upon oxidation, obviating the need for chromatography as a purification step. Deprotonation of the ligand can be effected by treatment of ^{Mes}dpmeH with 1.2 equivalents of *n*-BuLi in thawing THF solutions to produce the solvated lithio complex (^{Mes}dpme)Li(thf), which was in turn suitable for installing the ^{Mes}dpme moiety onto transition metals.



Scheme 3.1. Synthesis of (^{Mes}dpme)FeCl(thf).

Reaction of the lithio complex (^{Mes}dpme)Li(thf) with a thawing slurry of FeCl₂ in THF furnished the four-coordinate, solvated species (^{Mes}dpme)FeCl(thf) as a red solid (**Scheme 3.1**). The solid state structure for (^{Mes}dpme)FeCl(thf) is provided in **Figure 3.1**, confirming the solvated state adopts a pseudo-tetrahedral environment at iron. The THF in (^{Mes}dpme)FeCl(thf) is labile and can be exchanged for stronger binding ligands like pyridine to yield (^{Mes}dpme)FeCl(py). Likewise, the Zn^{II}

(12) Wood, T. E.; Thompson, A. *Chem. Rev.* **2007**, *107*, 1831-1861.

congener was synthesized by reaction of $(^{\text{Mes}}\text{dpme})\text{Li}(\text{thf})$ with ZnCl_2 in thawing THF, followed by treatment with pyridine to furnish $(^{\text{Mes}}\text{dpme})\text{ZnCl}(\text{py})$ as an isolable orange solid. The Fe and Zn complexes could be isolated as analytically pure solids in 75–84% yield. The zinc complex $(^{\text{Mes}}\text{dpme})\text{ZnCl}(\text{py})$ adopts a similar geometry to $(^{\text{Mes}}\text{dpme})\text{FeCl}(\text{thf})$ in the solid state (**Figure 3.8**).

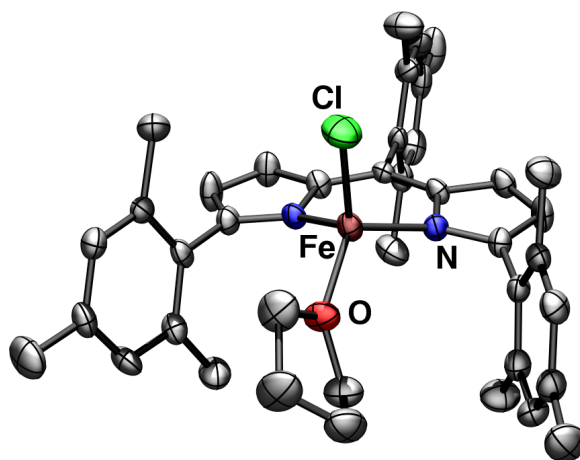


Figure 3.1. Structure of $(^{\text{Mes}}\text{dpme})\text{FeCl}(\text{thf})$. Thermal ellipsoids set at the 50% probability level (hydrogen atoms and solvent molecules omitted for clarity). Bond lengths (Å): Fe–N1, 2.017(3); Fe–N2, 2.034(4); Fe–Cl, 2.263(1); Fe–O, 2.029(3).

Much like their porphyrin congeners, dipyrromethenes and their metal complexes exhibit intense ligand $\pi \rightarrow \pi^*$ transitions afforded by the conjugation and aromaticity of the dipyrromethene ligand system.¹³ The dominant charge transfer occurs in the range of 460–500 nm for the parent ligand $^{\text{Mes}}\text{dpmeH}$ and its metal complexes (**Figure 3.2** and **Figure 3.6**), ($\lambda_{\text{max}}(\epsilon)$): $^{\text{Mes}}\text{dpmeH}$: 467 nm (49,000 $\text{M}^{-1}\text{cm}^{-1}$), $(^{\text{Mes}}\text{dpme})\text{Li}(\text{thf})$: 499 nm (97,000 $\text{M}^{-1}\text{cm}^{-1}$), $(^{\text{Mes}}\text{dpme})\text{FeCl}(\text{thf})$: 503 nm (74,000 $\text{M}^{-1}\text{cm}^{-1}$), $(^{\text{Mes}}\text{dpme})\text{FeCl}(\text{py})$: 506 nm (69,000 $\text{M}^{-1}\text{cm}^{-1}$), $(^{\text{Mes}}\text{dpme})\text{ZnCl}(\text{py})$: 501 nm (140,000 $\text{M}^{-1}\text{cm}^{-1}$). The observed $\pi \rightarrow \pi^*$ transitions for ligand $^{\text{Mes}}\text{dpmeH}$ is not unlike other dipyrromethene ligand derivatives which are often employed as fluorescence tags, or the parent porphyrin constructs.¹³ While the Zn complex $(^{\text{Mes}}\text{dpme})\text{ZnCl}(\text{py})$ is a diamagnetic species, the room temperature solution

(13) (a) Williams, R. J. P. *Chem. Rev.* **1956**, 56, 299-328. (b) Loudet, A.; Burgess, K. *Chem. Rev.* **2007**, 107, 4891-4932.

magnetic moment of complex $(^{\text{Mes}}\text{dpme})\text{FeCl}(\text{thf})$ and $(^{\text{Mes}}\text{dpme})\text{FeCl}(\text{py})$ are 5.2(1) and 5.3(1) μ_{B} , respectively, both consistent with high-spin ($S = 2$) iron centers (Evans's method).¹⁴ Cyclic voltammetry on $(^{\text{Mes}}\text{dpme})\text{FeCl}(\text{thf})$ and $(^{\text{Mes}}\text{dpme})\text{FeCl}(\text{py})$ reveal fully reversible $\text{Fe}^{\text{II/III}}$ redox waves centered at -400 V versus an internal ferrocene reference (**Figure 3.2** inset, scan rate = 100 mV/s). Cyclic voltammetry on complex $(^{\text{Mes}}\text{dpme})\text{ZnCl}(\text{py})$ revealed fully reversible, one-electron reduction (-2.00 V) and oxidation ($+550$ mV) events originating from the ligand platform (**Figure 3.3**). Reduction waves are observed for complexes $(^{\text{Mes}}\text{dpme})\text{FeCl}(\text{thf})$ and $(^{\text{Mes}}\text{dpme})\text{FeCl}(\text{py})$ at similar potentials, whereas the onset of oxidation is shifted by ca. -300 mV and the processes are no longer reversible.

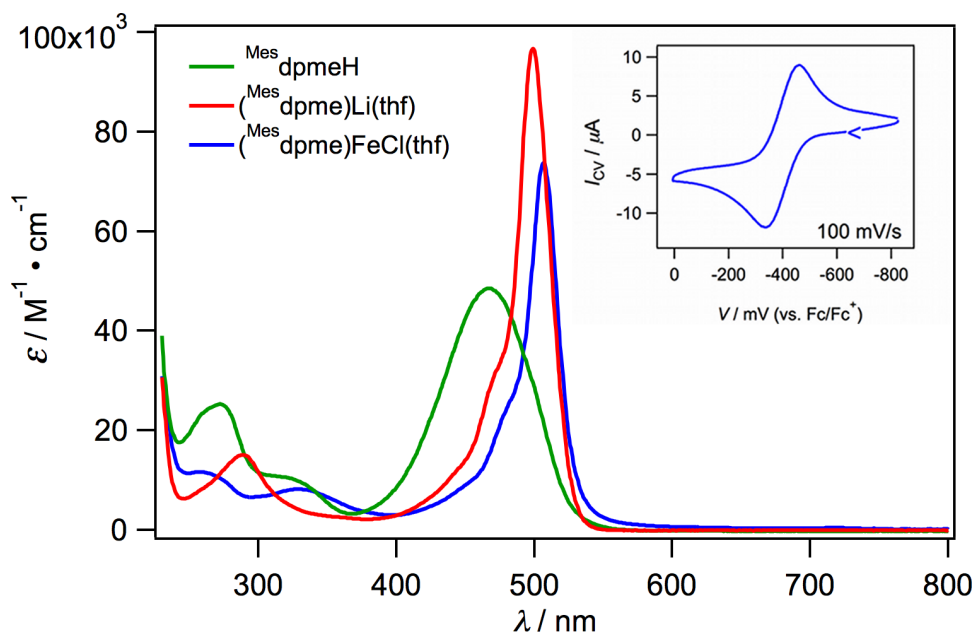


Figure 3.2. Absorption spectra and cyclic voltammogram of $(^{\text{Mes}}\text{dpme})\text{FeCl}(\text{thf})$. UV/Vis spectra of $^{\text{Mes}}\text{dpmeH}$, $(^{\text{Mes}}\text{dpme})\text{Li}(\text{thf})$, and $(^{\text{Mes}}\text{dpme})\text{FeCl}(\text{thf})$. Inset shows cyclic voltammogram of complex $(^{\text{Mes}}\text{dpme})\text{FeCl}(\text{thf})$ in THF (1 mM) with 0.3 M Bu_4NPF_6 ; scan rate 100 mV/s; glassy C electrode.

(14) (a) Evans, D. F. *J. Chem. Soc.* **1959**, 2003-2005. (b) Sur, S. K. *J. Magn. Reson.* **1989**, 82, 169-173.

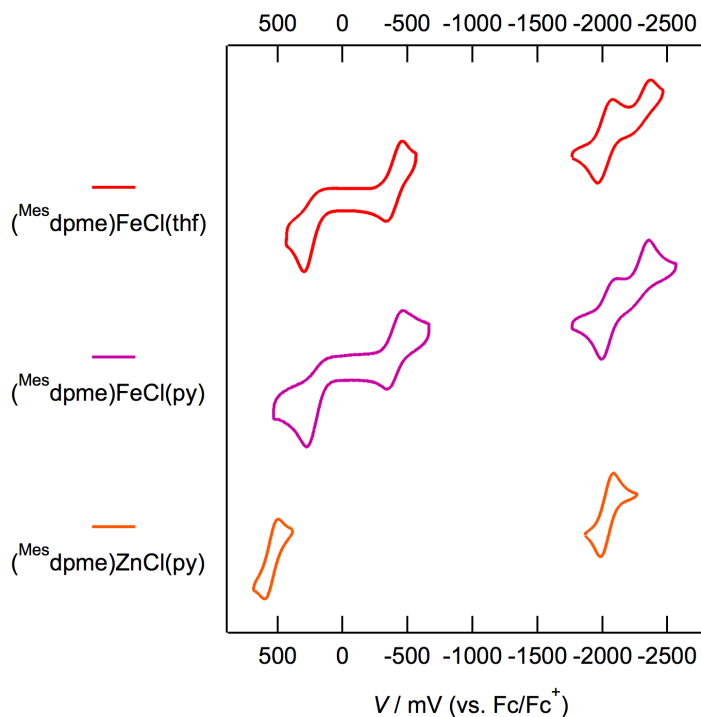


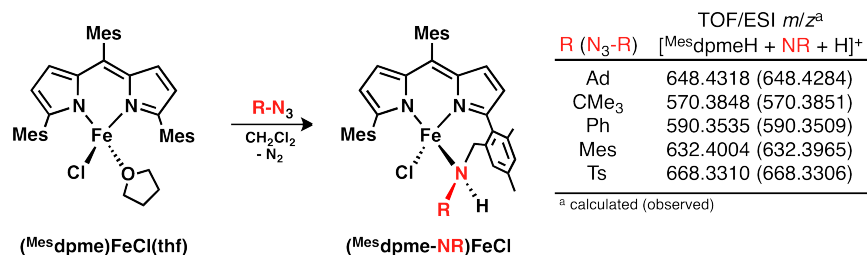
Figure 3.3. Comparison of Fe and Zn cyclic voltammograms. 1 mM solution of the analyte in THF (0.3 M [ⁿBu₄N][PF₆]) using a glassy carbon electrode and Ag/Ag⁺ reference electrode. Potential of each trace was internally referenced to Fc/Fc⁺. Scan rate = 500 mV/s. Current amplitudes were normalized for one-electron peaks.

3-3. Intramolecular C–H Amination.

To test whether the dipyrromethene ligand could confer the same reactivity at the Fe^{II} center as their porphyrin counterparts, we canvassed the reactivity of (**Mes dpme**)FeCl(**thf**) with a series of organic azides to examine whether nitrene transfer could be effected.¹⁵ Adding a thawing solution of (**Mes dpme**)FeCl(**thf**) in dichloromethane to a stoichiometric amount of 1-adamantyl azide quantitatively produces a new paramagnetic, iron containing complex, evidenced by the increase in the number of observable proton resonances apparent in the ¹H NMR, consistent with desymmetrization of the ligand environment (see **Section 3-5.** for ¹H NMR details). Solutions of (**Mes dpme**)FeCl(**thf**) in

(15) (a) Breslow, R.; Gellman, S. H. *J. Chem. Soc., Chem. Commun.* **1982**, 1400-1401. (b) Bolm, C.; Legros, J.; Le Pailh, J.; Zani, L. *Chem. Rev.* **2004**, *104*, 6217-6254.

thawing DCM react quickly with organic azides (N_3Ph , N_3Mes , N_3Ad) to expel dinitrogen, as evidenced by the disappearance of the azide stretch in the IR spectrum, and cleanly produce a new high-spin Fe^{II} product distinct from $(^{Mes}dpme)FeCl(thf)$ by 1H NMR, displaying a similar desymmetrization of the ligand proton resonances.



Scheme 3.2. Intramolecular C–H amination.

Characterization of crude reaction mixtures by ESI mass spectrometry revealed parent ions consistent with azide derived nitrene insertion into a ligand C–H bond (**Scheme 3.2**). The masses obtained from the independent reactions of $(^{Mes}dpme)FeCl(thf)$ with N_3R ($R = ^tBu, 1-Ad, Ph, Mes, Ts$) do not suggest that multiple nitrene insertions into the ligand does not occur, even when the azide reagent is used in excess (metal dissociation was consistently observed using this ionization method). Vapor diffusion of Et_2O into a THF solution of $(^{Mes}dpme)FeCl(thf)$ and N_3Ad produced crystals suitable for X-ray diffraction analysis. The molecular structure of the product reveals insertion of the [NAd] fragment into a benzylic C–H bond from one of the ligand pyrrole mesityl aryl groups (**Scheme 3.2**). The molecular structure of aminated product $(^{Mes}dpme-NAd)FeCl$ is shown in **Figure 3.4**. The local geometry about the Fe in the structure for $(^{Mes}dpme-NAd)FeCl$ adopts a distorted trigonal monopyramidal structure, where the azide derived amine (N_3) remains bound to the Fe.

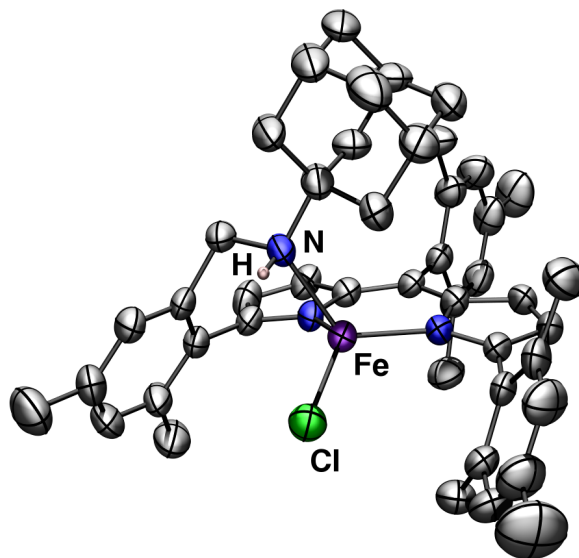


Figure 3.4. Structure of intramolecular C–H amination product (^{Mes}dpme–NAd)FeCl. Thermal ellipsoids set at the 50% probability level (H atoms, solvent molecules, and positional disorder omitted for clarity). Bond lengths (Å) for (^{Mes}dpme–NAd)FeCl: Fe–N1, 2.079(5); Fe–N2, 2.038(5); Fe–Cl, 2.245(2); Fe–N3, 2.190(5).

One mechanistic possibility for the observed insertion reaction involves azide addition to (^{Mes}dpme)FeCl(thf) (displacing the coordinated THF), followed by N₂ expulsion from the azide to yield a high-valent Fe^{IV} imide complex. Formation of the Fe^{IV} imide complex could then be quickly followed by H-atom abstraction and a radical rebound mechanism to form the N–C bond found in the product in a hydroxylase-like fashion.¹⁶ Variable temperature (VT) ¹H NMR experiments did not reveal any discernible intermediate along the proposed pathway, only the starting material (^{Mes}dpme)FeCl(thf) and the emergence of the C–H bond activated product (^{Mes}dpme–NAd)FeCl beginning at –30 °C (**Figure 3.9**). The emergence of the product peaks for (^{Mes}dpme–NAd)FeCl appear with a concomitant decrease in the observed peaks for (^{Mes}dpme)FeCl(thf) in a roughly 1:1 fashion. This latter observation was confirmed by following the reaction by the absorption spectrum changes. The spectral changes for the reaction of (^{Mes}dpme)FeCl(thf) with 10 equivalents of 1-adamantyl azide (**Figure 3.5**) only show the decay of (^{Mes}dpme)FeCl(thf) and the growth of the

(16) Groves, J. T. *J. Chem. Educ.* **1985**, 62, 928-931.

product ($^{\text{Mes}}\text{dpme-NAd})\text{FeCl}$ ($\lambda_{\text{max}}(\epsilon)$: 518 nm ($57,000 \text{ M}^{-1}\text{cm}^{-1}$)) with an isosbestic point at 516 nm, indicating that there is no build up of an observable intermediate in the reaction. While *in situ* IR analysis of the reaction mixture did not reveal a shift in the azide stretch on the IR timescale, ^1H NMR analysis of the reaction of ($^{\text{Mes}}\text{dpme})\text{FeCl}(\text{thf})$ with $^t\text{BuN}_3$ did reveal a dynamic exchange of the azide ligand (from the shift of the ^tBu resonance) bound to a ($^{\text{Mes}}\text{dpme})\text{FeCl}$ complex preceding the formation of nitrene-inserted product (**Figure 3.10**).

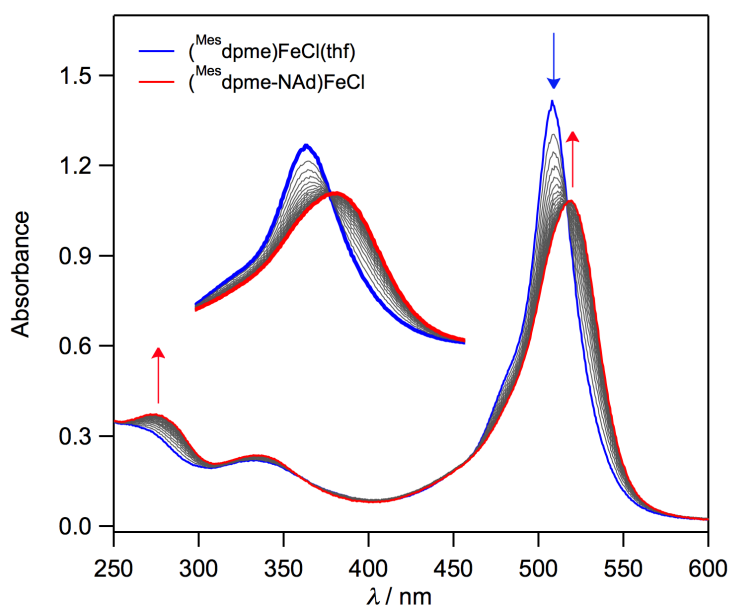


Figure 3.5. Changes in the electronic absorption spectrum during conversion of ($^{\text{Mes}}\text{dpme})\text{FeCl}(\text{thf})$ to ($^{\text{Mes}}\text{dpme-NAd})\text{FeCl}$. Initial concentration: 3 mM ($^{\text{Mes}}\text{dpme})\text{FeCl}(\text{thf})$ in DC; 23°C; scans 60 s apart. Arrows denote the evolution of absorption spectrum with time. Inset highlights the isosbestic point at 515 nm.

3-4. Conclusions.

Several high-valent Fe^{IV} imide complexes have now been synthesized and characterized.^{10c, 17} Furthermore, the reaction of phenyl-*N*-tosylimideiodinane and organic azides with Fe^{II} complexes have been reported to produce iron amide or anilide products and have been proposed to go through Fe^{IV}

(17) (a) Verma, A. K.; Nazif, T. N.; Achim, C.; Lee, S. C. *J. Am. Chem. Soc.* **2000**, *122*, 11013-11014. (b) Thomas, C. M.; Mankad, N. P.; Peters, J. C. *J. Am. Chem. Soc.* **2006**, *128*, 4956-4957.

imide intermediates.¹⁸ Radical reactivity has also been observed from related Fe^{III} and Co^{III} imide complexes and typically leads to H-atom abstraction products.^{11c,19} While a non-redox involved process cannot be ruled out in the conversion of (^{Mes}dpme)FeCl(thf) to (^{Mes}dpme–NAd)FeCl, reaction of the Zn complex (^{Mes}dpme)ZnCl(py) in place of the Fe complex (^{Mes}dpme)FeCl(thf) does not afford any aminated product even after prolonged heating of (^{Mes}dpme)ZnCl(py) with excess organic azide (7 days, 50°C). The Fe pyridine analog (^{Mes}dpme)FeCl(py) does produce the same aminated product (^{Mes}dpme–NAd)FeCl, although the reaction proceeds much slower (50% completion after 7 days, 50°C), presumably due to the presence of the less labile pyridine ligand.

In conclusion, we have reported a simple dipyrromethene ferrous complex that is capable of mediating intramolecular C–H bond amination from an organic azide precursor. This reaction pathway diverges from typical radical H-abstraction reactions in that the entire amine is transferred to the C–H bond substrate. The presence of the electrophilic Fe^{II} in (^{Mes}dpme–NAd)FeCl serves to trap the aminated product, likely inhibiting further reaction. Further development of this work will focus on validating or improving the mechanistic hypothesis and targeting intermolecular versions of this reaction and related C–C and C–O bond forming reactions via similar C–H activation pathways.

3-5. Experimental Methods.

General Synthetic Considerations.

All manipulations were carried out in the absence of water and dioxygen using standard Schlenk techniques, or in an inert atmosphere glovebox (M. Braun) under a dinitrogen atmosphere. All glassware was oven dried for a minimum of 1 h and cooled in an evacuated antechamber prior to use in

(18) (a) Jensen, M. P.; Mehn, M. P.; Que, L., Jr. *Angew. Chem., Int. Ed.* **2003**, *42*, 4357-4360. (b) Lucas, R. L.; Powell, D. R.; Borovik, A. S. *J. Am. Chem. Soc.* **2005**, *127*, 11596-11597.

(19) Shay, D. T.; Yap, G. P. A.; Zakharov, L. N.; Rheingold, A. L.; Theopold, K. H. *Angew. Chem., Int. Ed.* **2005**, *44*, 1508-1510.

the glovebox. Acetonitrile, benzene, diethyl ether, dichloromethane, *n*-hexane and tetrahydrofuran were dried and deoxygenated on a Glass Contour System (SG Water USA, Nashua, NH) and stored over 4 Å molecular sieves (Strem) prior to use. Chloroform-*d* was purchased from Cambridge Isotope Labs and used as received. Benzene-*d*₆ and dichloromethane-*d*₂ were purchased from Cambridge Isotope Labs and were degassed and stored over 4 Å molecular sieves prior to use. Acetone was refluxed with CaSO₄ for 1 h, distilled under argon, and stored over 3 Å molecular sieves (Aldrich) prior to use. Pyridinium *p*-toluenesulfonate, anhydrous pyridine, 2.5 M *n*-butyllithium in hexanes, DDQ, and 1-adamantyl azide were purchased from Aldrich and used as received. Anhydrous iron(II) chloride and silver(I) nitrate were purchased from Strem and used as received. 2-(2,4,6-trimethylphenyl)-1*H*-pyrrole,²⁰ mesitaldehyde dimethyl acetal,²¹ bis-pyridine iron(II) chloride,²² *tert*-butyl azide,²³ mesityl azide,²⁴ phenyl azide,²⁵ and tosyl azide²⁶ were synthesized according to literature procedures. Celite® 545 (J. T. Baker), silica gel 32–63 μ (Dynamic Adsorbents, Atlanta, GA), tetra-*n*-butylammonium hexafluorophosphate (Alfa Aesar) and zinc chloride (Aldrich) were dried in a Schlenk flask for 24 h under dynamic vacuum while heating to at least 150 °C.

Characterization and Physical Measurements.

UV/Visible spectra were recorded on a Varian Cary 50 UV/Visible spectra using quartz cuvettes and a scan rate of 300 or 600 nm/min. Scanning kinetics data was obtained using a KBr liquid IR cell (in place of a UV/Vis cuvette) with a path length of 0.1 mm, and scan rates of 600 nm/min. ¹H and ¹³C

(20) Rieth, R. D.; Mankad, N. P.; Calimano, E.; Sadighi, J. P. *Org. Lett.* **2004**, *6*, 3981-3983.

(21) Ji, N.; O'Dowd, H.; Rosen, B. M.; Myers, A. G. *J. Am. Chem. Soc.* **2006**, *128*, 14825-14827.

(22) Reinhardt, G.; Jonas, E.; Kewitz, D.; Karadag, A.; Prehler, H. (Clariant GmbH, Germany). Use of transition metal complexes as bleach catalysts Application U.S. Patent 6,875,734, April 5, 2005

(23) Bottero, J.; Penwell, P.; Schmitt, R. *Synth. Commun.* **1997**, *27*, 1465-1467.

(24) Murata, S.; Abe, S.; Tomioka, H. *J. Org. Chem.* **1997**, *62*, 3055-3061.

(25) Smith, P. A. S.; Boyer, J. H. *Org. Synth.* **1957**, *37*, 1.

(26) McElwee-White, L.; Dougherty, D. A. *J. Am. Chem. Soc.* **1984**, *106*, 3466-3474.

NMR spectra were recorded on Varian Mercury 400 MHz or Varian Unity/Inova 500 MHz spectrometers. ^1H and ^{13}C NMR chemical shifts are reported relative to SiMe_4 using the chemical shift of residual solvent peaks as reference. Solution magnetic susceptibilities were determined by Evans's method¹⁴ using hexamethyldisiloxane as an internal reference. Mass spectrometry was performed at the Harvard University FAS Center for Systems Biology Mass Spectrometry and Proteomics Resource Laboratory on an Agilent 6210 TOF LC/MS with a dual nebulizer ESI source. Elemental Analyses were carried out at Robertson Microlit Laboratories, Inc. (Madison, NJ).

Electrochemical experiments were carried out using a CH Instruments CHI660C Electrochemical Workstation. The electrolyte used was 0.3 M $[\text{nBu}_4\text{N}][\text{PF}_6]$ in THF. The concentration of all analytes was 1 mM. The working electrode was glassy carbon. A platinum wire was used as the counter electrode. Non-aqueous Ag/Ag^+ electrodes (10 mM AgNO_3) were used with the corresponding electrolyte solution. Cyclic voltammetry was performed with a scan rate of 100 mV/s or 500 mV/s.

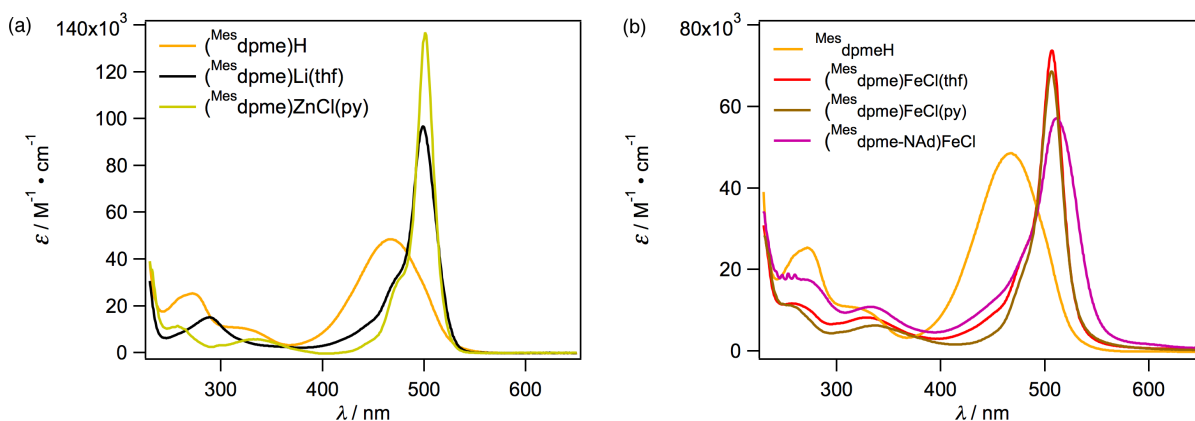
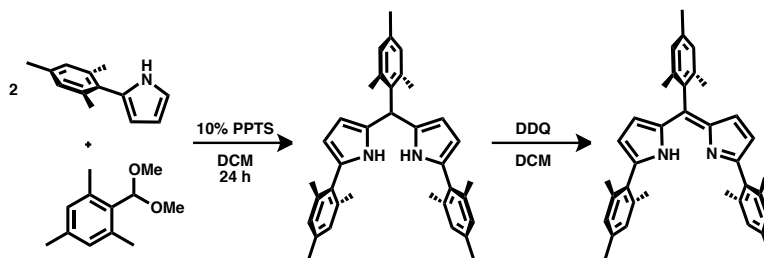


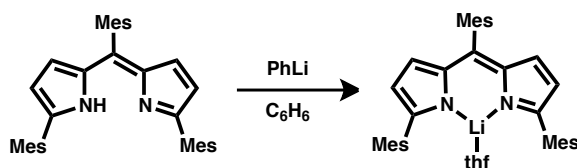
Figure 3.6. Absorption spectra of Mes dpmeH and its metal complexes. (a) Spectra of Mes dpmeH , $(\text{Mes dpme})\text{Li}(\text{thf})$ in THF, and $(\text{Mes dpme})\text{ZnCl}(\text{py})$ in DCM; (b) Spectra of Mes dpmeH and $(\text{Mes dpme})\text{ZnCl}(\text{py})$ in THF, and $(\text{Mes dpme})\text{FeCl}(\text{py})$ and $(\text{Mes dpme-NAd})\text{FeCl}$ in DCM. Molar absorptivities are based on measurements at 4 concentrations.

Syntheses.



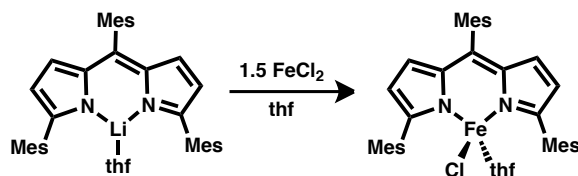
1,5,9-trimesityldipyrromethene, ^{Mes}dpmeH: A 500 mL round-bottomed flask was charged with 2-(2,4,6-trimethylphenyl)-1H-pyrrole (10.00 g, 53.98 mmol), mesitaldehyde dimethyl acetal (5.243 g, 26.99 mmol, 0.5000 equiv.), and 250 mL of CH₂Cl₂. After stirring until all materials were dissolved, pyridinium *p*-toluenesulfonate (1.360 g, 5.412 mmol, 0.1003 equiv.) was added resulting in a color change from colorless to pale orange. The reaction was stirred at room temperature for 24 h. The solution was filtered through a plug of silica gel (30 mL) to give a pale yellow filtrate. Solvent was removed *in vacuo* and the solid was triturated twice with 50 mL *n*-hexane followed by removal of the hexane *in vacuo*, affording 1,5,9-trimesityldipyrromethene as a pale orange powder (13.124 g, 97.11%). ¹H NMR (500 MHz, CD₂Cl₂): δ/ppm 7.80 (s, 2H, N-H), 6.90 (s, 4H, aryl C-H), 6.87 (s, 2H, aryl C-H), 6.11 (t, *J*_{HH} = 2.5 Hz, 2H, pyrrole C-H), 6.04 (s, 1H, MesCH(C₄H₂MesNH)₂), 5.99 (t, *J*_{HH} = 3 Hz, 2H, pyrrole C-H), 2.29 (s, 6H, *para*-C₆H₂(CH₃)₃), 2.26 (s, 3H, *para*-C₆H₂(CH₃)₃), 2.18 (s, 6H, *ortho*-C₆H₂(CH₃)₃), 2.14 (s, 12H, *ortho*-C₆H₂(CH₃)₃). ¹³C {¹H} NMR (125 MHz, CD₂Cl₂): δ/ppm 138.5, 137.78, 137.6, 136.8, 135.3, 131.2, 131.0, 130.6, 128.3, 108.9, 106.8, 38.8, 21.1, 20.9, 20.9, 20.9. The product (13.00 g, 25.96 mmol) was dissolved in 200 mL anhydrous acetone. The oxidant, 2,3-dichloro-5,6-dicyanoquinone (DDQ) (5.893 g, 25.96 mmol), was added to give a dark red solution. After stirring for 12 h a precipitate was visible. The precipitate was collected on a 30 mL medium porosity glass frit and washed with 20 mL acetone and 20 mL *n*-hexane to give ^{Mes}dpmeH as a bright yellow-orange powder (8.805 g, 68.01%). ¹H NMR (500 MHz, CD₂Cl₂): δ/ppm 12.48 (s, 1H, N-H),

6.98 (s, 2H, aryl C–H), 6.90 (s, 4H, aryl C–H), 6.39 (d, $J_{\text{HH}} = 4$ Hz, 2H, pyrrole C–H), 6.23 (d, $J_{\text{HH}} = 4$ Hz, 2H, pyrrole C–H), 2.38 (s, 3H, *para*-C₆H₂(CH₃)₃), 2.28 (s, 6H, *para*-C₆H₂(CH₃)₃), 2.19 (s, 12H, *ortho*-C₆H₂(CH₃)₃), 2.18 (s, 6H, *ortho*-C₆H₂(CH₃)₃). ¹³C {¹H} NMR (125 MHz, CDCl₃): δ /ppm 154.4, 140.7, 138.8, 137.9, 137.4, 137.3, 137.1, 134.1, 132.0, 128.6, 127.9, 127.0, 119.5, 21.4, 21.3, 20.9, 20.2. UV/Vis (THF) λ_{max} /nm (ϵ /M⁻¹cm⁻¹) 467 (49000, br), 322 (11000, sh), 271 (25000), 264 (24000, sh), 222 (71000, sh). CHN% Calc. for C₃₆H₃₈N₂: C 86.70, H 7.68, N 5.62; Found: C 86.41, H 7.62, N 5.53.

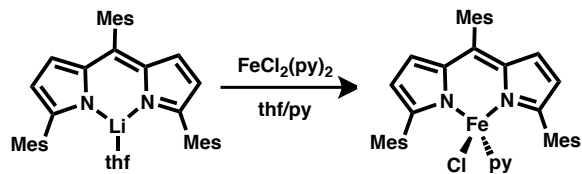


(^{Mes}dpme)Li(thf): In a 200 mL round bottom ^{Mes}dpmeH (2.000 g, 4.010 mmol) was dissolved in 100 mL of THF. A 20 mL vial was charged with 1.6 M *n*-butyllithium in hexanes (2.000 g, 2.93 mL, 4.7 mmol, 1.2 equiv.). The flask and vial were placed in a liquid nitrogen cooled cold well until partially frozen. The solution of butyllithium was thawed and added drop wise via pipet to the thawing solution of ^{Mes}dpmeH. The solution was stirred at room temperature for 5 h and became a dark orange solution. The mixture was filtered through a medium porosity glass frit with Celite to remove a small amount of insoluble material and afford an orange solution. The THF was removed *in vacuo* to give (^{Mes}dpme)Li(thf) as a bright orange powder (2.048 g, 88.55%). ¹H NMR (500 MHz, CD₂Cl₂): δ /ppm 6.94 (s, 2H, aryl C–H), 6.84 (s, 4H, aryl C–H), 6.38 (d, $J_{\text{HH}} = 4$ Hz, 2H, pyrrole C–H), 6.10 (d, $J_{\text{HH}} = 4$ Hz, 2H, pyrrole C–H), 3.26 (m, 4H, THF), 2.38 (s, 3H, *para*-C₆H₂(CH₃)₃), 2.25 (s, 6H, *para*-C₆H₂(CH₃)₃), 2.19 (s, 12H, *ortho*-C₆H₂(CH₃)₃), 2.13 (s, 6H, *ortho*-C₆H₂(CH₃)₃), 1.61 (m, 4H, THF). ¹³C {¹H} NMR (125 MHz, CD₂Cl₂): δ /ppm 159.4, 146.8, 141.4, 138.6, 137.2, 137.0, 136.7, 136.5, 136.4, 130.1, 128.1, 127.5, 117.6, 67.9, 25.6, 21.3, 21.1, 20.6, 20.1. UV/Vis (THF) λ_{max} /nm (ϵ /M⁻¹cm⁻¹)

501 (97000), 472 (32000, sh), 287 (15000), 223 (48000, sh). Results of combustion analysis for $(^{\text{Mes}}\text{dpme})\text{Li}(\text{thf})$ were poor, three independent samples were tried and all were low in carbon. Best result: CHN% Calc. for $\text{C}_{40}\text{H}_{45}\text{N}_2\text{LiO}$: C 83.30, H 7.86, N 4.86; Found: C 82.09, H 7.66; N 4.79.



$(^{\text{Mes}}\text{dpme})\text{FeCl}(\text{thf})$: In a 20 mL scintillation vial $(^{\text{Mes}}\text{dpme})\text{Li}(\text{thf})$ (1.000 g, 17.34 mmol) was dissolved in 10 mL of THF. In another 20 mL vial FeCl_2 (0.328 g, 25.9 mmol, 1.49 equiv.) was slurried in 10 mL of THF. Both vials were placed in a liquid nitrogen cooled cold well until frozen. The solution of $(^{\text{Mes}}\text{dpme})\text{Li}(\text{thf})$ was thawed and added to the thawing slurry of FeCl_2 . The reaction mixture became a dark orange solution. The reaction was stirred at room temperature for 4 h. The mixture was filtered through a medium porosity glass frit with Celite to remove excess FeCl_2 . Removal of the solvent *in vacuo* gave a dark brown solid. The solid was extracted into 20 mL benzene and filtered to remove lithium chloride. Sublimation of the benzene *in vacuo* gave $(^{\text{Mes}}\text{dpme})\text{FeCl}(\text{thf})$ as a brown powder (0.853 g, 74.4%). Crystals suitable for X-ray diffraction were grown from an Et_2O solution of $(^{\text{Mes}}\text{dpme})\text{FeCl}(\text{thf})$. $^1\text{H NMR}$ (500 MHz, CD_2Cl_2): δ /ppm 48.1 (s), 26.3 (br s), 16.2 (s), 9.7 (s) 9.2 (s), 7.3 (s), 5.5 (s), 3.9 (s), 3.1 (s), -8.1 (br s). UV/Vis (THF) $\lambda_{\text{max}}/\text{nm}$ ($\epsilon/\text{M}^{-1}\text{cm}^{-1}$) 505 (74000), 475 (21000, sh), 328 (8200, br), 259 (12000), 223 (40000, sh). μ_{eff} (296 K) 5.21(5) μ_{B} . CHN% Calc. for $\text{C}_{40}\text{H}_{45}\text{N}_2\text{ClFeO}$: C 72.67, H 6.86, N 4.23; Found: C 72.43, H 7.04, N 4.25.



(^{Mes}dpme)FeCl(py): In a 20 mL scintillation vial (^{Mes}dpme)Li(thf) (200 mg, 0.347 mmol) was dissolved in 10 mL of THF. In another 20 mL vial FeCl₂(py)₂ (98.8 mg, 0.347 mmol) was slurried in 9 mL of THF and 1 mL pyridine. Both vials were placed in a liquid nitrogen cooled cold well until frozen. The solution of (^{Mes}dpme)Li(thf) was thawed and added to the thawing slurry of FeCl₂. The reaction mixture became a dark orange solution. The reaction was stirred at room temperature for 4 h. Removal of the solvent *in vacuo* gave a dark brown solid. The residue was extracted into 10 mL benzene and filtered to remove lithium chloride. Sublimation of the benzene *in vacuo* gave (^{Mes}dpme)FeCl(py) as a brown powder (188.9 mg, 81.5%). ¹H NMR (500 MHz, CD₂Cl₂): δ/ppm 168.5 (br s), 51.6 (s), 42.5 (s), 24.4 (br s), 24.3 (s), 13.2 (s), 5.2 (s), 2.9 (s), 2.3 (s), -11.9 (br s), -18.3 (br s). UV/Vis (CH₂Cl₂) λ_{max}/nm (ε/M⁻¹cm⁻¹) 506 (69000), 338 (6500, br), 257 (11000, sh). μ_{eff} (296 K) 5.29(1) μ_B. CHN% Calc. for C₄₁H₄₂N₃ClFe: C 73.71, H 6.34, N 6.29; Found: C 73.36, H 6.36, N 6.12.

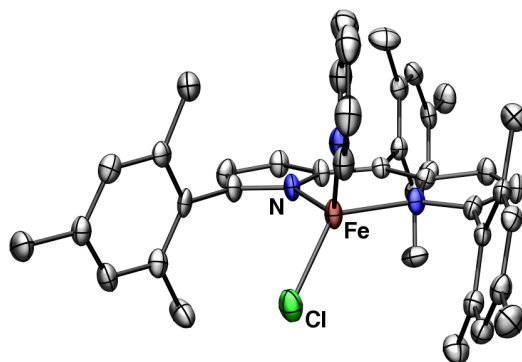
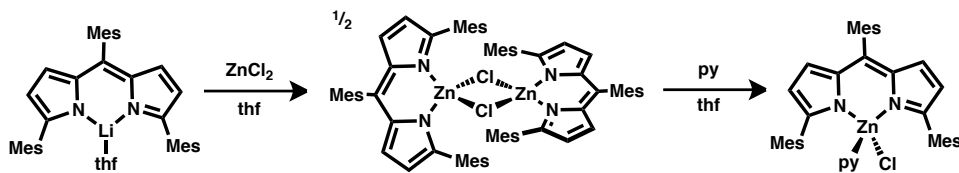


Figure 3.7. Structure of (^{Mes}dpme)FeCl(py). Thermal ellipsoids set at the 50% probability level (hydrogen atoms omitted for clarity).²⁷

(27) This structure was determined by Austin B. Scharf.



$(^{\text{Mes}}\text{dpme})\text{ZnCl}(\text{py})$ (**5**): In a 20 mL scintillation vial $(^{\text{Mes}}\text{dpme})\text{Li}(\text{thf})$ (200 mg, 0.347 mmol) was dissolved in 10 mL of THF. In another 20 mL vial ZnCl_2 (76.2 mg, 0.559 mmol, 1.61 equiv.) was dissolved in 10 mL of THF. Both vials were placed in a liquid nitrogen cooled cold well until frozen. The solution of $(^{\text{Mes}}\text{dpme})\text{Li}(\text{thf})$ was thawed and added to the thawing zinc chloride solution. The reaction was stirred for 3 h and remained an orange solution throughout. The mixture was filtered through a medium porosity glass frit with Celite to remove excess ZnCl_2 . Removal of the solvent *in vacuo* gave a light orange solid. The residue was extracted into 10 mL benzene and filtered to remove lithium chloride. Sublimation of the benzene *in vacuo* gave $[(^{\text{Mes}}\text{dpme})\text{ZnCl}]_2$ as an orange powder (205.9 mg, 99.1%). ^1H NMR (500 MHz, CD_2Cl_2): δ /ppm 6.98 (s, 2H, aryl C–H), 6.78 (s, 4H, aryl C–H), 6.57 (d, $J_{\text{HH}} = 4$ Hz, 2H, pyrrole C–H), 6.19 (d, $J_{\text{HH}} = 4$ Hz, 2H, pyrrole C–H), 2.39 (s, 3H, *para*- $\text{C}_6\text{H}_2(\text{CH}_3)_3$), 2.23 (s, 6H, *para*- $\text{C}_6\text{H}_2(\text{CH}_3)_3$), 2.19 (s, 6H, *ortho*- $\text{C}_6\text{H}_2(\text{CH}_3)_3$), 2.06 (s, 12H, *ortho*- $\text{C}_6\text{H}_2(\text{CH}_3)_3$). In a 20 mL scintillation vial the product (120 mg, 0.101 mmol) was dissolved in 15 mL of Et_2O . To this solution 0.5 mL pyridine was added resulting in immediate precipitation of an orange solid. The mixture was stirred for 30 min and the solid was collected on a medium porosity glass frit. The orange solid was dissolved in 10 mL benzene. Sublimation of the benzene *in vacuo* helped removed excess pyridine and gave $(^{\text{Mes}}\text{dpme})\text{ZnCl}(\text{py})$ as an orange powder (103.2 mg, 75.4%). Crystals suitable for X-ray diffraction were grown via hexanes diffusion into a THF solution of $(^{\text{Mes}}\text{dpme})\text{ZnCl}(\text{py})$. ^1H NMR (500 MHz, CD_2Cl_2): δ /ppm 7.94 (br m, 2H, py), 7.82 (br m, 1H, py), 7.26 (br m, 2H, py), 7.00 (s, 2H, aryl C–H), 6.83 (br s, 2H, aryl C–H), 6.59 (d, $J_{\text{HH}} = 4$ Hz, 2H, pyrrole C–H), 6.44 (br s, 2H, aryl C–H), 6.17 (d, $J_{\text{HH}} = 4$ Hz, 2H, pyrrole C–H), 2.40 (s, 3H, *para*- $\text{C}_6\text{H}_2(\text{CH}_3)_3$), 2.25 (s, 6H, *para*- $\text{C}_6\text{H}_2(\text{CH}_3)_3$),

2.20 (br s, 6H, *ortho*-C₆H₂(CH₃)₃) 2.19 (s, 6H, *ortho*-C₆H₂(CH₃)₃), 1.44 (br s, 6H, *ortho*-C₆H₂(CH₃)₃).
¹³C {¹H} NMR (125 MHz, CD₂Cl₂): δ/ppm 161.5, 148.7, 145.9, 140.0, 139.7, 138.7, 137.7, 137.6, 136.7, 136.2, 133.0, 131.9, 127.9, 127.2, 125.0, 126.0, 119.0, 21.2, 21.1, 20.9, 20.0, 19.7. UV/Vis (CH₂Cl₂) λ_{max}/nm (ε/M⁻¹cm⁻¹) 502 (136000), 475 (31000, sh), 337 (5700, br), 262 (11000). Results of combustion analysis for (^{Mes}dpme)ZnCl(py) were poor, three independent samples were tried and all were low in carbon. Best result: CHN% Calc. for C₄₁H₄₂N₃ClZn: C 72.67, H 6.24, N 6.20; Found: C 69.95, H 5.90, 6.15.

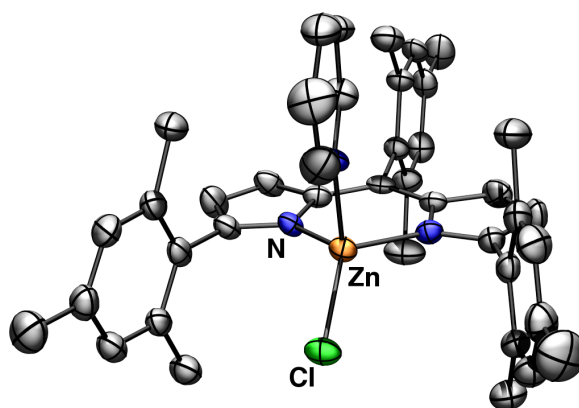
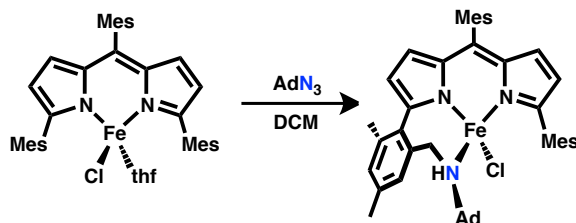


Figure 3.8. Structure of (^{Mes}dpme)ZnCl(py). Thermal ellipsoids set at the 50% probability level (hydrogen atoms omitted for clarity).



(^{Mes}dpme-NAd)FeCl: In a 20 mL scintillation vial (^{Mes}dpme)FeCl(thf) (100.1 mg, 0.1513 mmol) was dissolved in 10 mL of CH₂Cl₂. In another 20 mL vial 1-adamantyl azide (26.8 mg, 0.151 mmol) was dissolved in 10 mL of CH₂Cl₂. Both vials were placed in a liquid nitrogen cooled cold well until frozen. The azide solution was thawed and added to the thawing slurry of (^{Mes}dpme)FeCl(thf). The reaction

was stirred for 3 h. Removal of the solvent *in vacuo* gave a dark brown solid. The solid was extracted into 10 mL benzene, filtered through a glass frit with Celite, and sublimation of the benzene *in vacuo* gave (**Mes dpme-NAd**)FeCl as a dark red-brown powder (85.3 mg, 76.5%). Crystals suitable for X-ray diffraction were grown from an Et₂O solution of (**Mes dpme-NAd**)FeCl. ¹H NMR (500 MHz, CD₂Cl₂): δ/ppm 119.6 (s), 68.2 (s), 49.7 (s), 45.3 (br s), 20.8 (s), 19.2 (s), 18.7 (s), 15.02 (s), 13.9 (s), 13.7 (s), 11.7 (s), 11.4 (s), 7.3 (s), 7.0 (s), 5.4 (s), -3.2 (s), -11.2 (s), -18.0 (s), -21.3 (s), -21.9 (s), -22.4 (s), -61.9 (br s). UV/Vis (CH₂Cl₂) λ_{max}/nm (ε/M⁻¹cm⁻¹) 518 (57000), 335 (11000), 272 (18000). μ_{eff} (296 K) 5.15(2) μ_B. CHN% Calc. for C₄₆H₅₂N₃ClFe: C 74.84, H 7.10, N 5.69; Found: C 75.12, H 7.36, N 5.42.

General Procedure for Azide Addition to (Mes dpme**)FeCl(thf).** In a 20 mL scintillation vial (**Mes dpme**)FeCl(thf) (50 mg) was dissolved in 5 mL THF. In another 20 mL vial N₃R (1 equiv.) was slurried in 2 mL THF. Both vials were placed in a liquid nitrogen cooled cold well until partially frozen. The azide solution was thawed and added to the thawing solution of (**Mes dpme**)FeCl(thf). The reaction mixture was stirred for 2 h. Solvent was removed *in vacuo*, and NMR of the crude solid confirmed consumption of (**Mes dpme**)FeCl(thf) and evidence of a new paramagnetic complex. HRMS of the product showed peaks corresponding to nitrene [NR] insertion into the dipyrromethene ligand. HRMS (ESI⁺): *m/z* 648.4284 [**Mes dpme**H+NAd+H]⁺, 570.3851 [**Mes dpme**H+N^tBu+H]⁺, 632.3965 [**Mes dpme**H+NMes+H]⁺, 590.3509 [**Mes dpme**H+NPh+H]⁺, 668.3306 [**Mes dpme**H+NTs+H]⁺.

Procedure for Reactions Monitored by UV/Vis. In a 20 mL scintillation vial (**Mes dpme**)FeCl(thf) (15 mg) was dissolved in 7 g of CH₂Cl₂. In another 20 mL vial 1-adamantyl azide (10 equiv.) was dissolved in 3 g of CH₂Cl₂. Both vials were placed in a liquid nitrogen cooled cold well until frozen. The azide solution was thawed and added to the thawing slurry of (**Mes dpme**)FeCl(thf). The reaction was stirred until all solvent was completely thawed. A portion of the solution was then quickly transferred to

a KBr liquid IR cell and placed into the UV/Vis spectrometer. A scan from 800 nm to 200 nm was taken every minute for 30 min. Data shown in **Figure 3.5**.

Procedures for VT-NMR. A solution of (^{Mes}dpme)FeCl(thf) (20.0 mg, 0.0303 mmol) in 1 mL CD₂Cl₂ was added to a J. Young NMR tube and the solution was frozen in a liquid nitrogen cold well. Once frozen an additional 0.5 mL was added to the tube and frozen on top of the previous frozen sample. Finally a solution of 1-adamantyl azide (5.5 mg, 0.031 mmol, 1.0 equiv.) in 0.5 mL CD₂Cl₂ was added to the tube and again frozen as the third frozen layer. The tube was thawed at -78 °C in a dry ice/acetone bath, removing from the cold bath only briefly to mix. The tube could then be inserted into the spectrometer and monitored at the desired temperature(s). The probe was cooled to -60 °C, and spectra were recorded every 10 °C up to -30 °C, and then recorded in 5 °C increments up to +30 °C. The average time between measurements was 10 minutes during which the temperature was changed and equilibrated and the magnet shimmed. Data shown in **Figure 3.9**.

A solution of (^{Mes}dpme)FeCl(thf) (10.0 mg, 0.0151 mmol) in 1 mL CD₂Cl₂ was added to a J. Young NMR tube and the solution was frozen in a liquid nitrogen cold well. Once frozen an additional 0.5 mL was added to the tube and frozen on top of the previous frozen sample. Finally, a solution of *tert*-butyl azide (4.5 mg, 0.045 mmol, 3.0 equiv.) in 0.5 mL CD₂Cl₂ was added to the tube and again frozen as the third frozen layer. The tube was thawed at -78 °C in a dry ice/acetone bath. The tube was removed from the bath and inserted into the spectrometer. The sample and probe were kept at a temperature of 25 °C. Spectra were recorded every 5 min for 45 min, and a final spectrum was taken after 2 h total reaction time. Data shown in **Figure 3.10**. VT-NMR of pure compounds (^{Mes}dpme)FeCl(thf) and (^{Mes}dpme-NAd)FeCl in CD₂Cl₂ were taken in order to verify the assignment of starting material and product peaks in the reaction monitored by VT-NMR because of the strong temperature dependence on

chemical shift. Spectra were recorded from $-60\text{ }^{\circ}\text{C}$ to $+30\text{ }^{\circ}\text{C}$ in $10\text{ }^{\circ}\text{C}$ increments. Data shown in **Figure 3.11** and **Figure 3.12**.

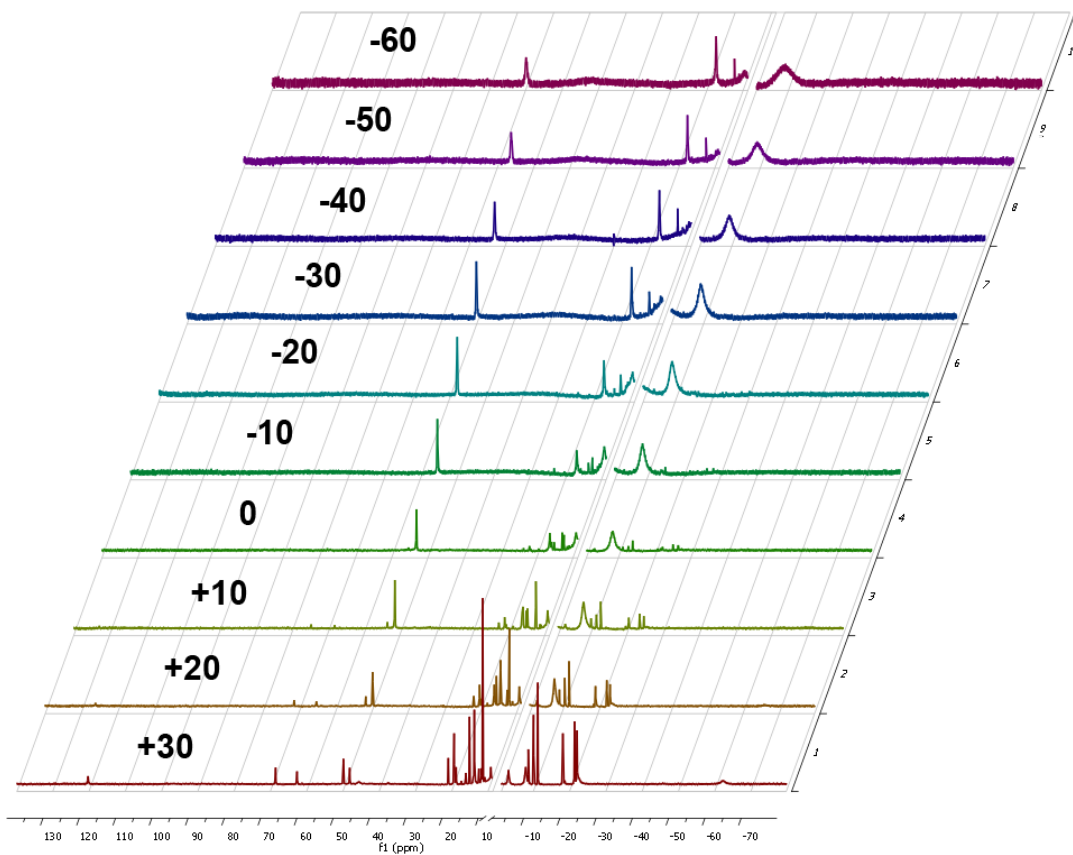


Figure 3.9. Variable temperature ^1H NMR of $(^{\text{Mes}}_2\text{dpme})\text{FeCl}(\text{thf}) + \text{N}_3\text{Ad}$ in DCM. Collected in 10 min increments from $-70\text{ }^{\circ}\text{C}$ to $+20\text{ }^{\circ}\text{C}$. Collected at $+30\text{ }^{\circ}\text{C}$ after heating at $+30\text{ }^{\circ}\text{C}$ for 30 min. Diamagnetic region omitted for better clarity of paramagnetic peaks.

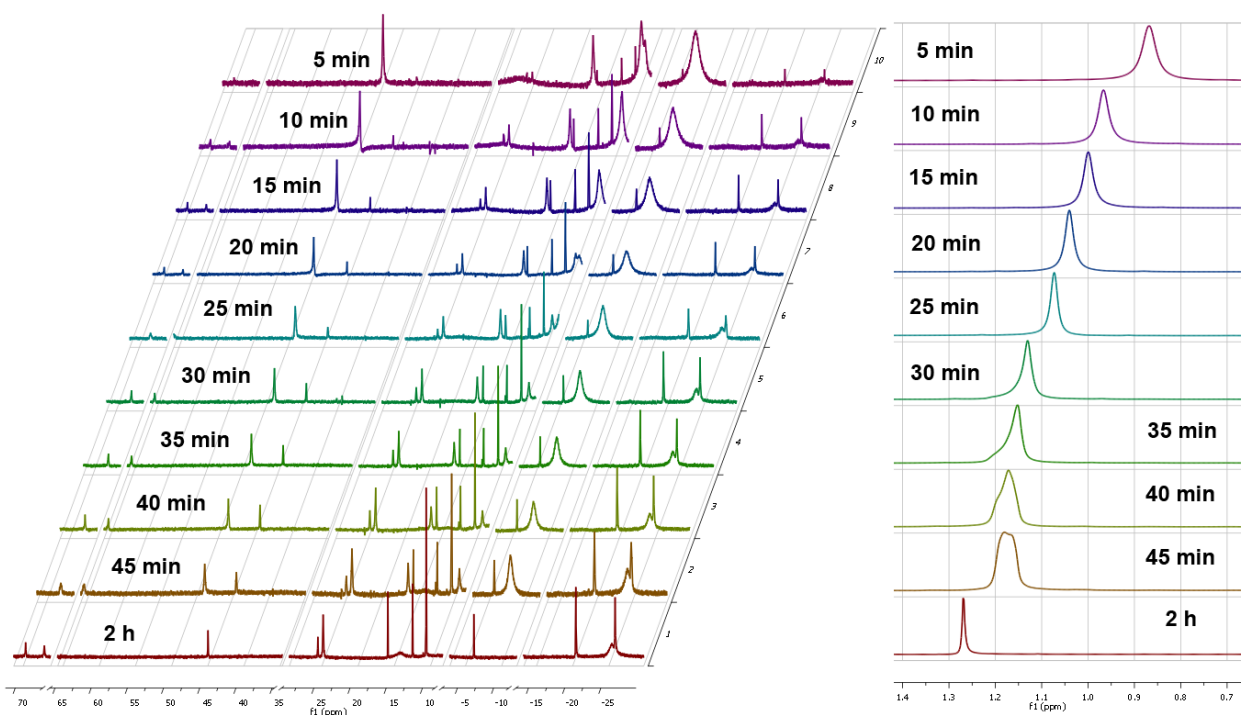


Figure 3.10. ^1H NMR of $(\text{Mes dpme})\text{FeCl}(\text{thf}) + \text{N}_3^t\text{Bu}$ in DCM. (left) Collected in 5 min increments for 45 min, temperature held at $+25^\circ\text{C}$. Final spectra taken at 2 h since start of reaction at $+25^\circ\text{C}$. Diamagnetic region and several regions with instrument noise are omitted for clarity. (right) Only the region from 0.7 to 1.4 ppm is shown, highlighting the shift of the $\text{N}_3\text{C}(\text{CH}_3)_3$ peak during reaction progress. Final peak at 1.26 ppm is consistent with free *tert*-butyl azide (present in slight excess).

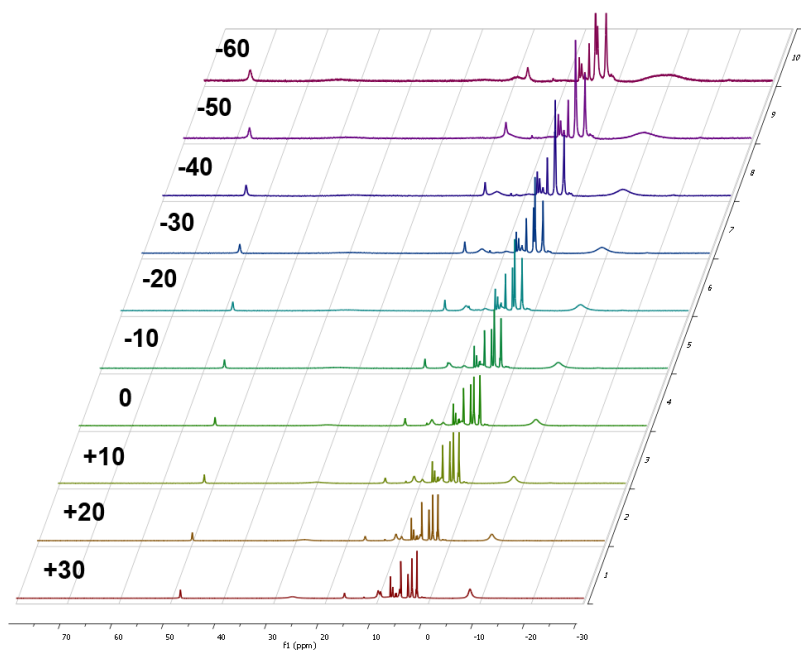


Figure 3.11. Variable temperature ^1H NMR of $(^{\text{Mes}}\text{dpme})\text{FeCl}(\text{thf})$ DCM. Collected in 10 degree increments from -70 $^{\circ}\text{C}$ to $+30$ $^{\circ}\text{C}$.

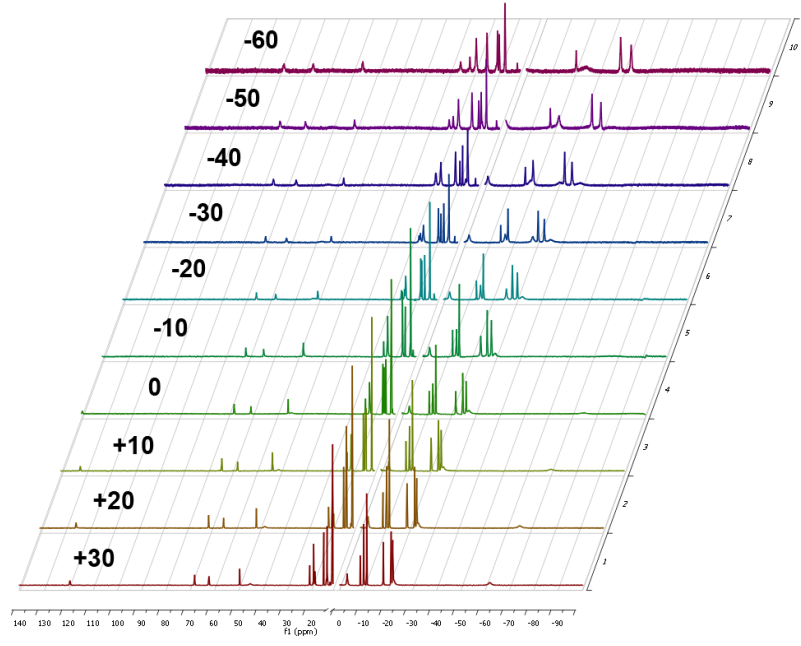


Figure 3.12. Variable temperature ^1H NMR of $(^{\text{Mes}}\text{dpme-NAd})\text{FeCl}$ in DCM. Collected in 10 degree increments from -70 $^{\circ}\text{C}$ to $+20$ $^{\circ}\text{C}$. Diamagnetic region omitted for better clarity of paramagnetic peaks.

X-ray Diffraction Techniques.

All structures were collected on either a Siemens or Brüker three-circle platform goniometer equipped with either a Brüker Apex I or Apex II CCD and an Oxford cryostream cooling device. Radiation was from a graphite fine focus sealed tube Mo K α (0.71073 Å) source. Crystals were mounted on a cryoloop using Paratone N oil. Structures were collected at 193 K. Data was collected as a series of φ and/or ω scans.

Data was integrated using SAINT²⁸ and scaled with either a numerical or multi-scan absorption correction using SADABS.²⁸ The structures were solved by direct methods or Patterson maps using SHELXS-97²⁹ and refined against F^2 on all data by full matrix least squares with SHELXL-97.²⁹ All non-hydrogen atoms were refined anisotropically. Hydrogen atoms were placed at idealized positions and refined using a riding model. The isotropic displacement parameters of all hydrogen atoms were fixed to 1.2 times the U of atoms they are linked to (1.5 times for methyl groups). Further details on particular structures are noted below.

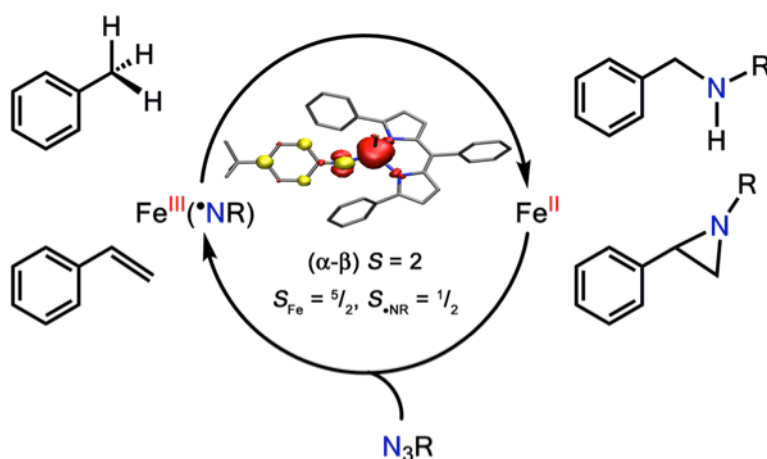
(^{Mes}dpme)FeCl(thf): The structure was solved in the $P2_1/c$ space group with 4 molecules per unit cell. No solvent molecules were found and no disorder was evident.

(^{Mes}dpme)ZnCl(py): The structure was solved in the $P2_1/c$ space group with 4 molecules per unit cell. The crystal was twinned and 2 primary domains were separated using CELL_NOW.²⁹ The data was integrated against both domains and scaled using TWINABS.²⁹ The structure was solved with and refined against the set of reflections from the primary domain. Some residual density around heavy atoms was evident, and probably results from overlap with reflections from the omitted domains with smaller contributions. No solvent molecules were found and no disorders were apparent.

(28) APEX2 Software Suite; Brüker AXS: Madison, WI, 2009.

(29) (a) Sheldrick, G. M. *Acta Crystallogr., Sect. A: Found. Crystallogr.* **1990**, *46*, 467-473. (b) Sheldrick, G. M. *SHELX-97*; University of Göttingen: Göttingen, Germany, 1997.

(^{Mes}dpme-NAd)FeCl (**6**). The structure was solved in the $P2_1/c$ space group with 4 molecules per unit cell. The amine hydrogen was picked from the difference Fourier map and refined semi-freely by restraining the N–H distance to 0.91 Å (the average effective distance for sp^3 N–H bonds at -80 °C), and the by setting the isotropic displacement parameter to 1.2 times the U value of the nitrogen. The adamantyl group exhibited rotational disorder and was modeled as two components with a similarity restraint on the 1–2 and 1–3 distances of the disordered atoms. The major part refined to 55%. A diethyl ether solvent molecule was present in the asymmetric unit, but was modeled as a partial occupancy (87%) disorder because of very weak peaks in the difference map. 1–2 and 1–3 distances were restrained to typical C–C and C–O values and the atoms were restrained to lie in a plane. The anisotropic displacement parameters of the ether atoms were restrained to behave isotropically. Similarity and rigid bond restraints on the anisotropic displacement parameters of all atoms were also used.



Chapter 4: Catalytic C–H Bond Amination from High-Spin Iron Imide Complexes^{1,2}

4-1. Introduction.

Introducing functionality into unactivated C–H bonds remains a significant challenge both in the realm of complex molecule synthesis as well as in the elaboration of simple hydrocarbon feed stocks into value-added commodity chemicals.^{3,4} Biological C–H bond functionalization is primarily performed by iron containing enzymes that utilize dioxygen as the terminal oxidant. A key structural element of the putative hydroxylation catalyst in both heme (where iron is embedded in a porphyrin) and non-heme systems is a transiently formed terminal iron oxo, typically thought to involve multiple bond character.^{5,6} Furthermore, the reactivity of this intermediate is believed to be dictated by its electronic structure.⁷ In

(1) This chapter was adapted with permission from King, E. R.; Hennessy, E. T.; Betley, T. A. *J. Am. Chem. Soc.* **2011**, *133*, 4917-4923. Copyright 2011 American Chemical Society.

(2) The experiments for the catalytic systems described are the work of Elizabeth T. Hennessy.

(3) Bergman, R. G. *Nature* **2007**, *446*, 391-393.

(4) Labinger, J. A.; Bercaw, J. E. *Nature* **2002**, *417*, 507-514.

(5) *Cytochrome P450 : Structure, Mechanism, and Biochemistry*; 4th ed.; Ortiz de Montellano, P. R., Ed.; Kluwer Academic/Plenum Publishers: New York, 2005.

(6) Krebs, C.; Fujimori, D. G.; Walsh, C. T.; Bollinger, J. M. *Acc. Chem. Res.* **2007**, *40*, 484-492.

(7) (a) Decker, A.; Rohde, J. U.; Klinker, E. J.; Wong, S. D.; Que, L., Jr.; Solomon, E. I. *J. Am. Chem. Soc.* **2007**, *129*, 15983-15996. (b) Bernasconi, L.; Louwerse, M. J.; Baerends, E. J. *Eur. J. Inorg. Chem.* **2007**, 3023-3033. (c) Ye, S. F.; Neese, F. *Curr. Opin. Chem. Biol.* **2009**, *13*, 89-98.

non-heme enzymes four such Fe^{IV}(oxo) complexes have been characterized, and their reactivity has been linked to a common electronic feature, namely a high-spin ground state ($S = 2$).⁶ However, an isolable, high-spin synthetic analog has not been reported that mimics the catalytic transfer of the metal-ligand multiply bonded functionality found in the biological systems.⁸

Parallel to the work targeted at iron mediated hydroxylation chemistry, C–H bond amination⁹ and olefin aziridination^{9a,9c,10} has been the focus of much recent synthetic work, although many mechanistic details and their interplay in effecting chemoselectivity and regioselectivity remain poorly understood. The synthesis and characterization of Fe(imide) complexes as isoelectronic surrogates to Fe(oxo) functionalities have been targeted in pursuit of effecting viable catalytic delivery of the nitrene functional unit to C–H bond or olefinic substrates. Iron imide complexes have now been characterized in four oxidation states spanning a range of spin states (Fe^{II}, $S = 0$;¹¹ Fe^{III}, $S = 1/2, 1, 3/2$;¹² Fe^{IV}, $S = 1$;¹³ Fe^V, $S =$

(8) (a) Pestovsky, O.; Stoian, S.; Bominaar, E. L.; Shan, X. P.; Münck, E.; Que, L., Jr.; Bakac, A. *Angew. Chem., Int. Ed.* **2005**, *44*, 6871-6874. (b) Kaizer, J.; Klinker, E. J.; Oh, N. Y.; Rohde, J. U.; Song, W. J.; Stubna, A.; Kim, J.; Münck, E.; Nam, W.; Que, L., Jr. *J. Am. Chem. Soc.* **2004**, *126*, 472-473. (c) Kumar, D.; Hirao, H.; Que, L., Jr.; Shaik, S. *J. Am. Chem. Soc.* **2005**, *127*, 8026-8027. (d) England, J.; Martinho, M.; Farquhar, E. R.; Frisch, J. R.; Bominaar, E. L.; Münck, E.; Que, L., Jr. *Angew. Chem., Int. Ed.* **2009**, *48*, 3622-3626. (e) England, J.; Guo, Y. S.; Farquhar, E. R.; Young, V. G.; Münck, E.; Que, L., Jr. *J. Am. Chem. Soc.* **2010**, *132*, 8635-8644. (f) Lacy, D. C.; Gupta, R.; Stone, K. L.; Greaves, J.; Ziller, J. W.; Hendrich, M. P.; Borovik, A. S. *J. Am. Chem. Soc.* **2010**, *132*, 12188-12190.

(9) (a) Müller, P.; Fruit, C. *Chem. Rev.* **2003**, *103*, 2905-2919. (b) Davies, H. M. L.; Long, M. S. *Angew. Chem., Int. Ed.* **2005**, *44*, 3518-3520. (c) Halfen, J. A. *Curr. Org. Chem.* **2005**, *9*, 657-669. (d) Cenini, S.; Gallo, E.; Caselli, A.; Ragaini, F.; Fantauzzi, S.; Piangiolino, C. *Coord. Chem. Rev.* **2006**, *250*, 1234-1253. (e) Davies, H. M. L.; Manning, J. R. *Nature* **2008**, *451*, 417-424. (f) Collet, F.; Dodd, R. H.; Dauban, P. *Chem. Commun.* **2009**, 5061-5074. (g) Zalatan, D. N.; Du Bois, J. *Top. Curr. Chem.* **2010**, *292*, 347-378.

(10) (a) Tanner, D. *Angew. Chem., Int. Ed. Engl.* **1994**, *33*, 599-619. (b) Osborn, H. M. I.; Sweeney, J. *Tetrahedron: Asymmetry* **1997**, *8*, 1693-1715. (c) Sweeney, J. B. *Chem. Soc. Rev.* **2002**, *31*, 247-258.

(11) Fe^{II}: Brown, S. D.; Peters, J. C. *J. Am. Chem. Soc.* **2005**, *127*, 1913-1923.

(12) Fe^{III}: (a) Brown, S. D.; Betley, T. A.; Peters, J. C. *J. Am. Chem. Soc.* **2003**, *125*, 322-323. (b) Betley, T. A.; Peters, J. C. *J. Am. Chem. Soc.* **2003**, *125*, 10782-10783. (c) Bart, S. C.; Lobkovsky, E.; Bill, E.; Chirik, P. J. *J. Am. Chem. Soc.* **2006**, *128*, 5302-5303. (d) Lu, C. C.; Saouma, C. T.; Day, M. W.; Peters, J. C. *J. Am. Chem. Soc.* **2007**, *129*, 4-5. (e) Scepianiak, J. J.; Young, J. A.; Bontchev, R. P.; Smith, J. M. *Angew. Chem., Int. Ed.* **2009**, *48*, 3158-3160. (f) Cowley, R. E.; DeYonker, N. J.; Eckert, N. A.; Cundari, T. R.; DeBeer, S.; Bill, E.; Ottenwaelder, X.; Flaschenriem, C.; Holland, P. L. *Inorg. Chem.* **2010**, *49*, 6172-6187.

(13) Fe^{IV}: (a) Verma, A. K.; Nazif, T. N.; Achim, C.; Lee, S. C. *J. Am. Chem. Soc.* **2000**, *122*, 11013-11014. (b) Thomas, C. M.; Mankad, N. P.; Peters, J. C. *J. Am. Chem. Soc.* **2006**, *128*, 4956-4957. (c) Nieto, I.; Ding, F.; Bontchev, R. P.; Wang, H. B.; Smith, J. M. *J. Am. Chem. Soc.* **2008**, *130*, 2716-2717.

$1/2^{14}$), and have been shown to engage in group transfer to carbon monoxide to produce isocyanates,^{12a,15} isocyanides to product carbodiimides,¹⁵ undergo hydrogenation,^{12c} and perform H-atom abstraction from C–H bonds.^{16, 17} Herein we report room temperature, catalytic C–H bond and olefin functionalization from a transiently formed, high-spin ($S = 2$) iron imide complex.

4-2. Development of New Dipyrrromethene Platforms.

During our investigations of dipyrrromethene iron complexes as heme surrogates, we observed that reaction of an Fe^{II} complex with organic azides led to facile intramolecular delivery of the nitrene functional group into a ligand C–H bond.¹⁷ The reaction was postulated to proceed via a high-valent Fe^{IV}(NR) species, akin to the hydroxylation pathway of cytochrome P450 and its functional analogs.^{18,19} Extending this reactivity to an intermolecular reaction required removal of reactive C–H bonds from the ligand platform. Thus, dipyrrromethene platforms were targeted featuring sterically encumbered aryl or alkyl substituents that lack weak C–H bonds to circumvent intramolecular C–H bond activation pathways. Pyrroles substituted in the 2-position were afforded using modified Negishi coupling for 2-aryl pyrroles, and directed Friedel-Crafts alkylations for 2-alkyl pyrroles. For example, 2,4,6-Ph₃-C₆H₂Br was cleanly coupled to sodium pyrrolide to afford 2-Ar(pyrrole) using conditions outlined by Sadighi and coworkers (3 eq. sodium pyrrolide, 3 eq. ZnCl₂, Pd₂(dba)₃ (0.67%)/SPhos (1.33%); THF, 90 °C, 24 h, 84%; Ar = 2,4,6-Ph₃C₆H₂; see **Scheme 4.1a**).²⁰ Alkyl-substituted pyrroles were synthesized in good yields by reaction of the corresponding alkyl chloride (RCl), AlCl₃, and ethyl pyrrole-2-carboxylate

(14) Fe^V: Ni, C. B.; Fettinger, J. C.; Long, G. J.; Brynda, M.; Power, P. P. *Chem. Commun.* **2008**, 6045-6047.

(15) Cowley, R. E.; Eckert, N. A.; Elhaik, J.; Holland, P. L. *Chem. Commun.* **2009**, 1760-1762.

(16) Cowley, R. E.; Holland, P. L. *Inorg. Chim. Acta* **2011**, 369, 40-44.

(17) See Chapter 3: Intramolecular C–H Amination from an Iron Dipyrrromethene Complex or King, E. R.; Betley, T. A. *Inorg. Chem.* **2009**, 48, 2361-2363.

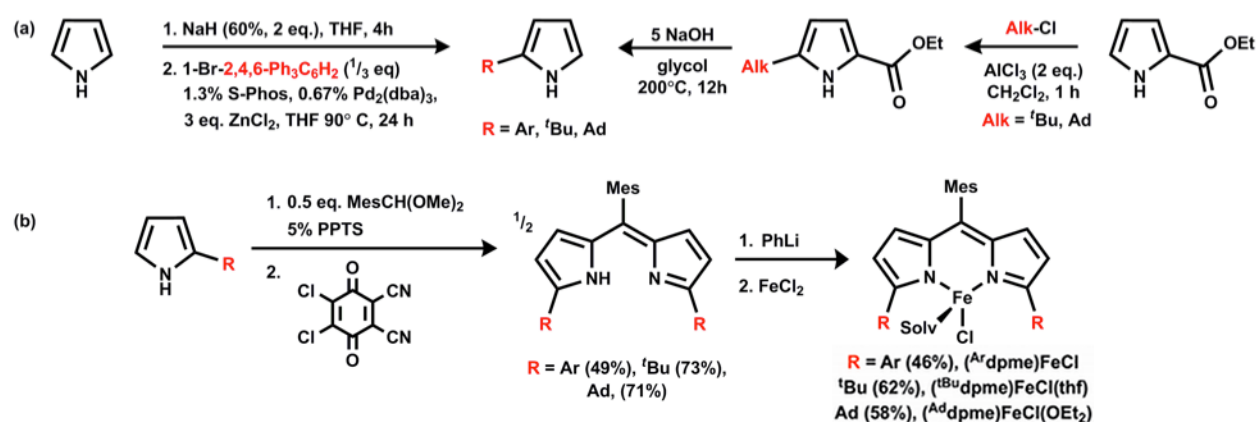
(18) Groves, J. T. *J. Chem. Educ.* **1985**, 62, 928-931.

(19) Sono, M.; Roach, M. P.; Coulter, E. D.; Dawson, J. H. *Chem. Rev.* **1996**, 96, 2841-2887.

(20) Rieth, R. D.; Mankad, N. P.; Calimano, E.; Sadighi, J. P. *Org. Lett.* **2004**, 6, 3981-3983.

following decarboxylation (KOH, glycol, 200 °C, 12 h, R = 1-adamantyl 88%, ^tBu 65%).^{21, 22}

Disubstituted dipyrromethene ligands (^Xdpme, X = 1,9 substituent) were prepared using literature procedures to produce the ligands in good overall yields (^{Ar}dpmeH, 49%; ^tBu dpmeH, 73%; ^{Ad}dpmeH, 71%; **Scheme 4.1b**).¹⁷ Dipyrromethene deprotonation with phenyl lithium in thawing benzene afforded the lithium salts (^{Ar}dpme)Li, (^tBu dpme)Li, and (^{Ad}dpme)Li as brightly colored powders in nearly quantitative yields (88–92%) for subsequent transmetalation to iron (**Scheme 4.1b**).



Scheme 4.1. Synthesis of the dpme ligands and their metal complexes.

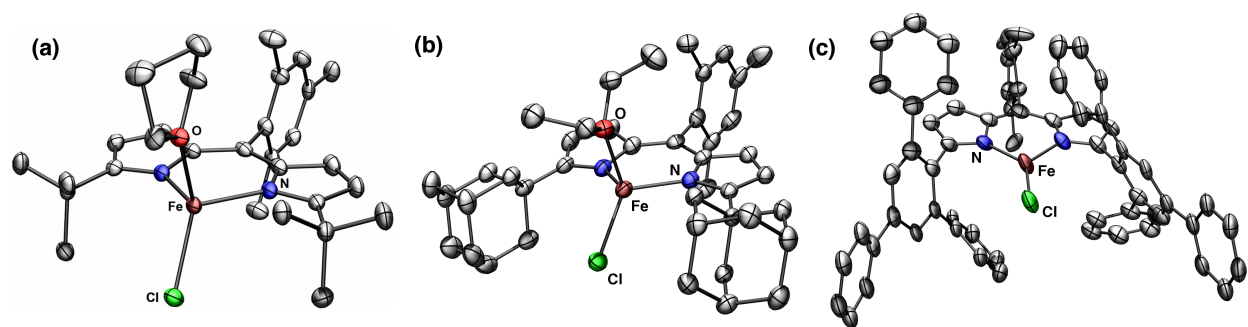


Figure 4.1. Solid-state molecular structures of Fe^{II} dpme complexes. (a) (^tBu dpme)FeCl(thf), (b) (^{Ad}dpme)FeCl(OEt₂), and (c) (^{Ar}dpme)FeCl with thermal ellipsoids at 50% probability level (Fe orange, Cl green, C black, N blue; hydrogens, solvent molecules, and aryl ring disorder in (^{Ar}dpme)FeCl are omitted for clarity). Bond lengths (Å) for (^tBu dpme)FeCl(thf): Fe–N1, 2.026(2); Fe–N2, 2.028(2); Fe–Cl, 2.255(1); Fe–O, 2.077(2); (^{Ad}dpme)FeCl(OEt₂): Fe–N1, 2.028(3); Fe–N2, 2.042(3); Fe–Cl, 2.250(2); Fe–O, 2.090(2); (^{Ar}dpme)FeCl: Fe–N1, 1.966(5); Fe–N2, 1.966(5); Fe–Cl, 2.154(2).

(21) Bailey, D. M.; Johnson, R. E.; Albertson, N. F. *Org. Synth.* **1988**, 50-9, 618-619.

(22) Harman, W. H.; Harris, T. D.; Freedman, D. E.; Fong, H.; Chang, A.; Rinehart, J. D.; Ozarowski, A.; Sougrati, M. T.; Grandjean, F.; Long, G. J.; Long, J. R.; Chang, C. J. *J. Am. Chem. Soc.* **2010**, 132, 18115-18126.

4-3. Synthesis and Characterization of Potential Catalysts.

Formation of the iron dipyrromethene complexes proceeds cleanly from reaction of the lithio dipyrromethene species with a thawing slurry of FeCl₂ in an ethereal solvent. For example, reaction of (Ad₂dpme)Li with FeCl₂ in thawing diethyl ether cleanly affords the solvated complex (Ad₂dpme)FeCl(OEt₂) as a luminescent green-brown solid following precipitation (yield: 58%; **Scheme 4.1c**). Utilizing the aryl-substituted ligand (Ar₂dpme)Li under similar reaction conditions afforded the three-coordinate species (Ar₂dpme)FeCl as a bright purple solid following crystallization (46%). The compositions and purity of (Ad₂dpme)FeCl(OEt₂) and (Ar₂dpme)FeCl were established by ¹H NMR, UV/Visible spectroscopy, ⁵⁷Fe Mössbauer spectroscopy, and combustion analysis, some of which are compiled in **Table 4.1**. The respective geometries of four-coordinate (Ad₂dpme)FeCl(OEt₂) and three-coordinate (Ar₂dpme)FeCl were verified by X-ray diffraction studies on a single crystal of each (**Figure 4.1**). The solid-state molecular structure of (Ad₂dpme)FeCl(OEt₂) shows a trigonal monopyramidal geometry with a diethyl ether molecule capping the pyramid. Complex (Ar₂dpme)FeCl has a trigonal planar geometry about iron, wherein the large 2,4,6-Ph₃C₆H₂ ligand substituents flank iron above and below the [N₂FeCl] plane. The average bond lengths of the four-coordinate complex (Fe–N_L 2.035(4) Å, Fe–Cl 2.249(1) Å) are expanded relative to three-coordinate species (Fe–N_L 1.966(7) Å, Fe–Cl 2.154(2) Å). The shorter bond lengths in the three-coordinate species are likely a result of both decreased steric repulsion and the increased electrophilicity of iron in the absence of a fourth donor. The room temperature solution magnetic moments determined using the method of Evans²³ are 5.2(2) μ_B for (Ad₂dpme)FeCl(OEt₂) and 5.1(2) μ_B for (Ar₂dpme)FeCl, both consistent with high-spin (S = 2) iron(II). Zero field, ⁵⁷Fe Mossbauer analysis of (Ad₂dpme)FeCl(OEt₂) (δ, |ΔE_Q| (mm/s) 0.98, 3.70) and (Ar₂dpme)FeCl (δ, |ΔE_Q| (mm/s) 0.67, 0.68) corroborate this assignment (see **Table 4.1**). The three-

(23) (a) Evans, D. F. *J. Chem. Soc.* **1959**, 2003-2005. (b) Sur, S. K. *J. Magn. Reson.* **1989**, 82, 169-173.

coordinate chloride (**^{Ar}dpme**)FeCl features a lower isomer shift than all of the other four-coordinate dipyrromethene Fe^{II} complexes and a particularly small quadrupole splitting, but has similarly unique parameters to those reported structurally similar trigonal planar, three-coordinate β -diketimate complexes.²⁴

Table 4.1. Spectral and magnetic properties of (dpme)Fe complexes.

complex	μ_{eff} / μ_B	S	$\lambda / \text{nm} (\epsilon / \text{M}^{-1} \cdot \text{cm}^{-1})$	$\delta / \text{mm/s}^b$	$ \Delta E_Q / \text{mm/s}^b$
(^{tBu} dpme)FeCl(thf)	5.2(2)	2	497 (40000) ^a	–	–
(^{Ad} dpme)FeCl(OEt ₂)	5.1(1)	2	494 (59000) ^a	0.98	3.70
(^{Ar} dpme)FeCl	5.1(2)	2	554 (26000)	0.68	0.68
[(^{Ar} dpme)FeCl] ₂ (μ -N(Ph)(C ₆ H ₅)N)	7.8(2)	⁵ / ₂ , ⁵ / ₂	551 (27000)	0.33	2.15
(^{Ar} dpme)FeCl(NC ₆ H ₄ - <i>p</i> -Bu)	5.3(1)	2	553 (26000)	0.29	2.29

^a UV/Vis reported for pyridine adduct.

^b Recorded at 105 K.

4-4. Catalytic C–H Amination.²⁵

As the reaction of organic azides with (^{Mes}dpme)FeCl(thf) gives rise to intramolecular amination of a ligand C–H bond,¹⁷ we canvassed the reactivity of complex (^{Ad}dpme)FeCl(OEt₂) with organic azides. When alkyl azides (e.g., *tert*-butyl azide, 1-adamantyl azide) are added to (^{Ad}dpme)FeCl(OEt₂) in toluene, rapid azide consumption is evident and the product of intermolecular, nitrene insertion into a benzylic C–H bond of toluene (PhCH₂NHR) is observed. Catalytic turnover is observed at room temperature when multiple equivalents of azide are used. Reactions of 1-adamantyl azide (N₃Ad) with (^{Ad}dpme)FeCl(OEt₂) in toluene at room temperature yielded a mixture of benzyladamantylamine (95%), benzyladamantylimine (2.8%), and adamantylamine (1.8%) for a total of 6.7 turnovers (TON) (see **Table 4.2**). Turnover is maximized by running the reaction at 60 °C (TON = 10–12), but decreases substantially at elevated temperatures (TON: 8.7 at 90 °C; 6.0 at 120 °C). The ratios of the

(24) Andres, H.; Bominaar, E. L.; Smith, J. M.; Eckert, N. A.; Holland, P. L.; Münck, E. *J. Am. Chem. Soc.* **2002**, *124*, 3012-3025.

(25) This section describes work done by Elizabeth T. Hennessy that was reported in King, E. R.; Hennessy, E. T.; Betley, T. *A. J. Am. Chem. Soc.* **2011**, *133*, 4917-4923.

amination products changes at elevated temperatures as well (at 120 °C: benzyladamantylamine (75%), benzyladamantylimine (4%), and adamantylamine (21%)). At elevated temperatures (120 °C) the presence of 1,2-diphenylethane (product of coupling two PhCH₂[•]) is also detectable by ¹H NMR. While elevated temperatures may facilitate amine dissociation from the iron catalyst, it does so at the expense of the thermal stability of the iron catalyst. Complex (^{Ad}dpme)FeCl(OEt₂) is also effective for nitrene delivery to olefinic substrates. Near quantitative nitrene transfer was observed when (^{Ad}dpme)FeCl(OEt₂) is reacted with N₃Ad in styrene at room temperature, giving 85% of the corresponding aziridine (17 TON based on 20 equivalents of azide).

Catalysis screens for the amination of toluene showed complex (^{Ad}dpme)FeCl(OEt₂) to be the most active, whereas the *tert*-butyl analog (^{tBu}dpme)FeCl(thf) only showed evidence for 5.6 turnovers at 60 °C, and complex (^{Ar}dpme)FeCl showed only trace amounts of aminated product by mass spectrometry. While THF found in the precatalyst (e.g. (^{Ad}dpme)FeCl(thf)) is tolerated during catalysis, added THF to the reaction suppresses amination. Addition of five equivalents of THF to an amination reaction (20 equivalents N₃Ad/[Fe]) yields only 50% benzyladamantylamine with respect to the iron catalyst (^{Ad}dpme)FeCl(OEt₂). Addition of 50 equivalents of THF completely suppresses the reaction as THF presumably outcompetes the azide from binding to the catalyst. Addition of a Lewis acid promoter (i.e., one equivalent of B(C₆F₅)₃) to scavenge THF from the precatalyst did not increase the turnover observed for any of the precatalysts screened. Furthermore, the reaction is impeded by product inhibition. Addition of 10 equivalents of adamantylamine or 15 equivalents of benzyladamantylamine to (^{Ad}dpme)FeCl(OEt₂) under typical catalytic conditions (5% (^{Ad}dpme)FeCl(OEt₂), toluene 60°C) suppresses the catalytic amination to an undetectable amount.

Table 4.2. LC/MS (¹H NMR) yields at various temperatures of products generated in catalytic amination reaction with (^{Ad}dpme)FeCl(OEt₂).

Temp / °C	yield / 10 ⁻² mmol				TON
	BnAdNH	PhC(H)NAd	AdNH ₂	PhCH ₂ CH ₂ Ph	
25	6.5 (4.8)	0.19 (0.20)	0.12	–	6.7 (5.0)
60	9.8 (11)	0.19 (0.10)	0.46	(0.17)	10 (11)
90	8.1 (8.1)	0.58 (0.72)	2.1	(0.81)	8.7 (8.8)
120	5.7 (5.6)	0.29 (0.13)	1.6	(1.7)	6.0 (5.7)

The detection of 1,2-diphenylethane during the formation of benzyladamantylamine strongly suggests an H-atom abstraction pathway is operative. As a probe for direct H-atom transfer, a competition experiment employing a 1:1 ratio of toluene to its perdeutero analog provides a kinetic isotope effect, k_H/k_D , of 12.8(5) for precatalyst (^{Ad}dpme)FeCl(OEt₂). The k_H/k_D ratio is consistent with a C–H bond breaking event contributing to the rate determining step and the reaction proceeding by a hydrogen atom abstraction/rebound mechanism as illustrated in **Scheme 4.2**. The observed KIE exceeds the values Che and coworkers reported for stoichiometric C–H amination from isolated Ru^{VI} bis-imide complexes (KIE: 4.8–11)²⁶ and those reported by Warren and coworkers for nitrene delivery from a putative [Cu]₂(imide) complex (KIE: 5–6),²⁷ though the isotope effect reported for ethylbenzene amination by a Cu(amide) is substantially higher (KIE: 70).²⁸ The large KIE value exceeds the classical value for hydrogen atom transfer (6.5),²⁹ and is thus suggestive of H atom tunneling akin to that observed in TauD monooxygenases (KIE: 37)⁶ and several Fe^{IV} oxo model complexes reported by Que and Nam (KIE: 18–50).^{8d,30}

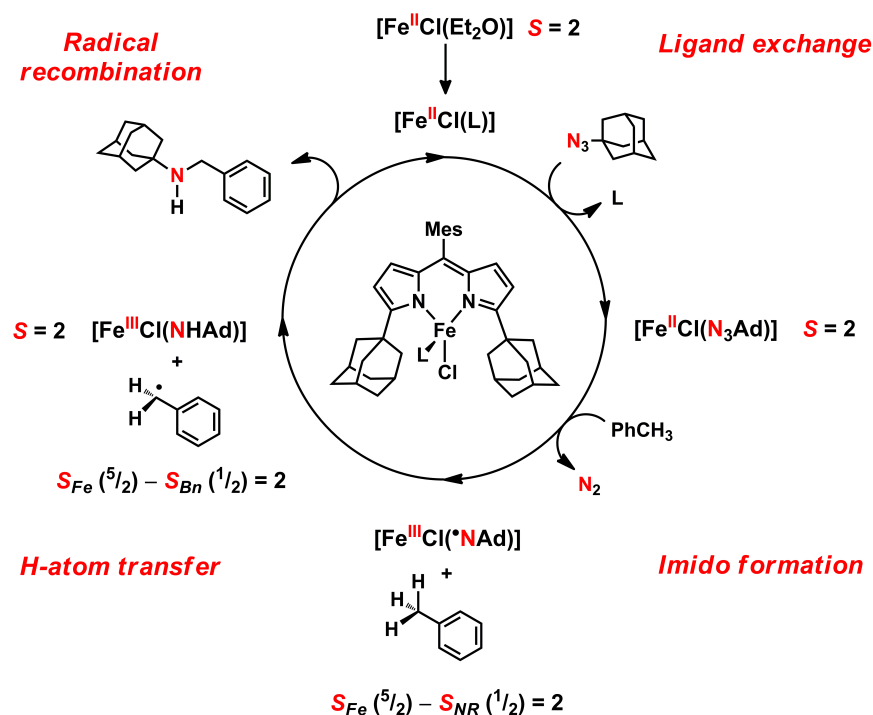
(26) (a) Au, S. M.; Huang, J. S.; Yu, W. Y.; Fung, W. H.; Che, C. M. *J. Am. Chem. Soc.* **1999**, *121*, 9120-9132. (b) Leung, S. K. Y.; Tsui, W. M.; Huang, J. S.; Che, C. M.; Liang, J. L.; Zhu, N. Y. *J. Am. Chem. Soc.* **2005**, *127*, 16629-16640.

(27) Badiei, Y. M.; Dinescu, A.; Dai, X.; Palomino, R. M.; Heinemann, F. W.; Cundari, T. R.; Warren, T. H. *Angew. Chem., Int. Ed.* **2008**, *47*, 9961-9964.

(28) Wiese, S.; Badiei, Y. M.; Gephart, R. T.; Mossin, S.; Varonka, M. S.; Melzer, M. M.; Meyer, K.; Cundari, T. R.; Warren, T. H. *Angew. Chem., Int. Ed.* **2010**, *49*, 8850-8855.

(29) Anslyn, E. V.; Dougherty, D. A. *Modern physical organic chemistry*; University Science: Sausalito, CA, 2006.

(30) (a) Que, L., Jr. *Acc. Chem. Res.* **2007**, *40*, 493-500. (b) Nam, W. *Acc. Chem. Res.* **2007**, *40*, 522-531. (c) Klinker, E. J.; Shaik, S.; Hirao, H.; Que, L., Jr. *Angew. Chem., Int. Ed.* **2009**, *48*, 1291-1295.



Scheme 4.2. Proposed catalytic cycle for the amination of C–H bonds by reaction of $(^{Ad}dpme)FeCl(OEt_2)$ with organic azides.

4-5. Isolation and Characterization of an Intermediate.

While our proposed mechanism suggests the intermediacy of an Fe^{IV} imide complex prior to the rate-determining step of H atom abstraction, we sought to validate this hypothesis via isolation or characterization of the putative intermediate. Reacting a thawing solution of $(^{Ar}dpme)FeCl$ in benzene with a stoichiometric amount of phenyl azide quantitatively produces an 1H NMR silent complex following consumption of the azide as ascertained by the disappearance of the azide stretch (ν_{N_3}) by infrared spectroscopy. An X-ray diffraction study on crystals grown from the reaction revealed the product to be the bimolecularly coupled species $[(^{Ar}dpme)FeCl]_2(\mu-N(Ph)(C_6H_5)N)$, $[Fe^{III}]_2$, depicted in **Scheme 4.3** and structure shown in **Figure 4.3a** (for untruncated structure see **Figure 4.11**). The bimetallic species $[Fe^{III}]_2$ presumably arises from radical coupling of two monomeric

(^{Ar}dpme)FeCl(NPh) moieties to intermolecularly form a new N–C bond. The coupled product [**Fe^{III}**]₂ features chemically distinct N(Ph)R ligation to one iron center (Fe1) and ketimide ligation to the second (Fe2). The (NPh) ketimide formulation is supported by the dearomatization of the C1–C6 ring, featuring localized double bonds (C2–C3 1.328(3) Å, C5–C6 1.331(3) Å, C1–N6 1.276(3) Å). The room temperature magnetic moment for [**Fe^{III}**]₂ is 7.8(2) μ_B, slightly lower than the calculated value of 8.3 μ_B for two non-interacting high-spin Fe^{III} centers ($S = 5/2$). The Fe^{III} formulation is corroborated by zero field ⁵⁷Fe Mössbauer analysis at 100 K which reveals that both iron centers in [**Fe^{III}**]₂ have isomer shifts and quadrupole splitting parameters consistent with high-spin Fe^{III} (δ , $|\Delta E_Q|$ (mm/s) 0.33, 2.15). The parameters are significantly distinct from both the Fe^{II} precursor (^{Ar}dpme)FeCl (δ , $|\Delta E_Q|$ (mm/s) 0.68, 0.68) and the four-coordinate Fe^{II} species (^{Ad}dpme)FeCl(OEt₂) (δ , $|\Delta E_Q|$ (mm/s) 0.98, 3.70) (Table 4.1).

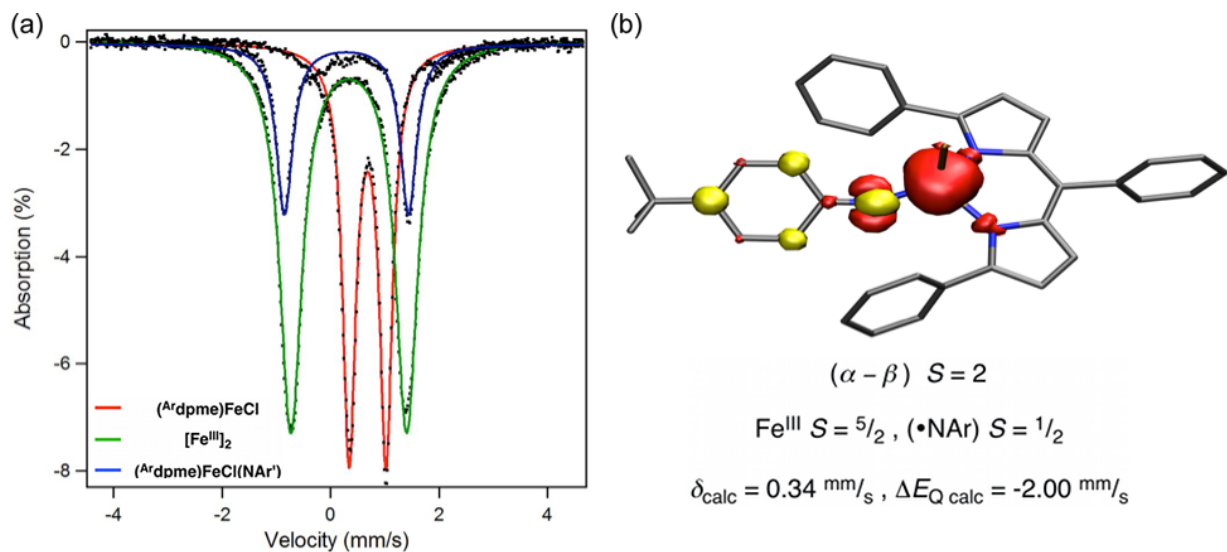


Figure 4.2. Mössbauer of ^{Ar}dpme complexes and calculated model for the imide radical. (a) The terminal imide radical complex (^{Ar}dpme)FeCl(NC₆H₄-*p*-^tBu) exhibits nearly identical Mössbauer metrical parameters to the bimolecularly coupled diferric [**Fe^{III}**]₂, illustrated by the the zero field, 100 K ⁵⁷Fe Mössbauer spectra data, (black dots with spectral fits as solid lines) (δ , $|\Delta E_Q|$ (mm/s)): (^{Ar}dpme)FeCl (red) 0.68, 0.68; [**Fe^{III}**]₂ (green) 0.33, 2.15; and (^{Ar}dpme)FeCl(NAr^{tBu}) (blue) 0.29, 2.29. (b) The antiferromagnetic coupling between the high-spin Fe^{III} ion and the terminal imide radical in (^{Ar}dpme)FeCl(NAr^{tBu}) shown by the calculated spin density population ($\alpha - \beta$) for ($S = 2$) by DFT (B3LYP/TZVP, SV(P); ORCA 2.7).³⁷

In an effort to obtain a monomeric imide complex, (^{Ar}dpme)FeCl was reacted with *p*-tBuC₆H₄N₃ where the aryl *para*-substitution was selected to sterically prevent the radical coupling pathway observed in the formation of [Fe^{III}]₂.³¹ In contrast to the dimerization observed in the reaction of (^{Ar}dpme)FeCl with phenyl azide, a new product from reaction of (^{Ar}dpme)FeCl with *p*-tBuC₆H₄N₃ is easily discernible by ¹H NMR as a C₂ symmetric species distinct from the starting material. The room temperature magnetic moment for this species is 5.3(1) μ_B, consistent with an S = 2 complex. Zero field ⁵⁷Fe Mössbauer analysis of the crude reaction product at 100 K reveals a single iron containing species (δ, |ΔE_Q| (mm/s) 0.29, 2.29) that is nearly superimposable with the spectrum obtained for [Fe^{III}]₂, suggesting the new product also contains Fe^{III} (Figure 4.2a).

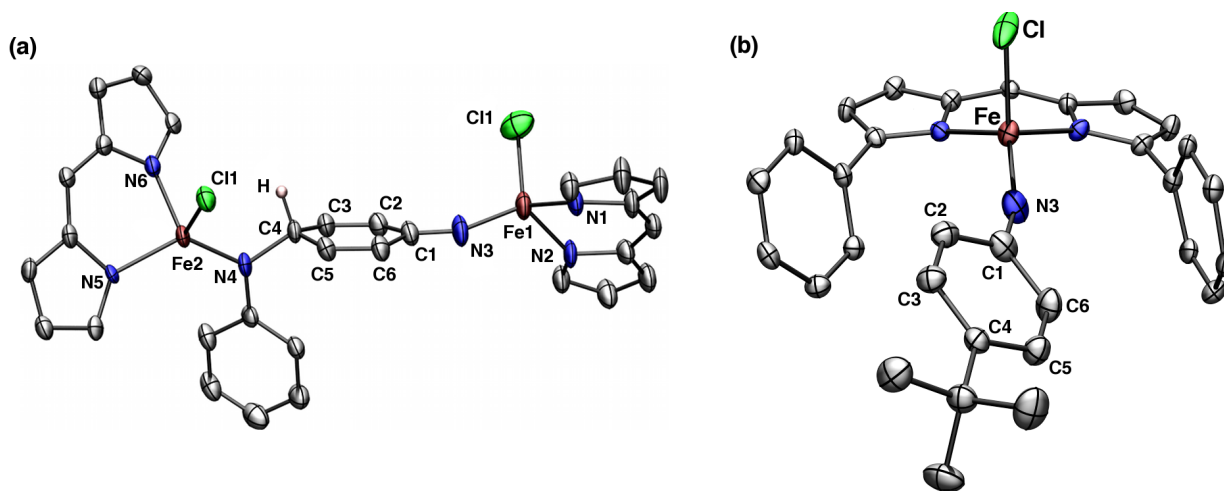


Figure 4.3. Truncated solid-state molecular structures of isolated ^{Ar}dpme Fe^{III} complexes. (a) [Fe^{III}]₂ and (b) (^{Ar}dpme)FeCl(NAr^{tBu}) (ligand aryl substituents, hydrogen atoms and solvent molecules are omitted for clarity). Bond lengths (Å) for [Fe^{III}]₂: Fe1–N3, 1.810(2); Fe1–Cl1, 2.202(1); Cl1–N3, 1.276(3); Cl1–C2, 1.462(4); C2–C3, 1.328(3); C3–C4, 1.490(4); C4–C5, 1.489(4); C5–C6, 1.331(3); C6–C1, 1.462(4); N4–C4, 1.484(3); Fe2–Cl2, 2.228(1); Fe2–N4, 1.886(2); for (^{Ar}dpme)FeCl(NAr^{tBu}): Fe–Cl, 2.210(1); Fe–N3, 1.768(2); N3–Cl, 1.331(2); C1–C2, 1.423(3); C2–C3, 1.372(3); C3–C4, 1.406(3); C4–C5, 1.405(3); C5–C6, 1.378(3); C6–C1, 1.414(3).

(31) Peters and co-workers reported a Cu di-*p*-tolyl aminyl radical, in which the tolyl methyl groups prevented the radical coupling to give aryl-aryl linked dimers which was otherwise seen in the diphenyl analog. See: Mankad, N. P.; Antholine, W. E.; Szilagy, R. K.; Peters, J. C. *J. Am. Chem. Soc.* **2009**, *131*, 3878-3879.

Table 4.3. Metal–ligand bond lengths of dpme complexes.

complex	Bond lengths / Å					
	Fe–N _L (1)	Fe–N _L (2)	Fe–Cl	Fe–O	Fe–N(3)	
(^{Ad} dpme)FeCl(OEt ₂)	2.028(3)	2.042(3)	2.250(1)	2.090(2)	–	
(^{tBu} dpme)FeCl(thf) ^a	2.0264(19)	2.0276(19)	2.2549(7)	2.0766(15)	–	
(^{Ar} dpme)FeCl	1.966(5)	1.966(5)	2.154(2)	–	–	
[Fe ^{III}] ₂	Fe(1) ^b	2.008(2)	1.981(2)	2.02(1)	–	1.810(2)
	Fe(2) ^b	1.9704(19)	1.997(2)	2.2282(8)	–	1.886(2)
(^{Ar} dpme)FeCl(NAr ^{tBu})	2.0128(14)	1.9965(14)	2.2100(6)	–	1.7677(17)	

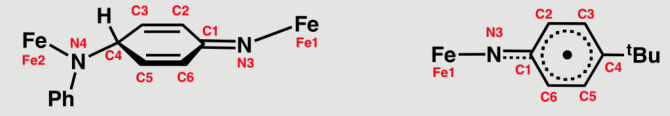
^a Average for 2 molecules in the asymmetric unit.^b Fe(1) is bound to the ketimide, Fe(2) is bound to the amide (see **Table 4.4**)

An X-ray diffraction study on single crystals grown from the reaction of (^{Ar}dpme)FeCl with *p*-^tBuC₆H₄N₃ revealed the product to be a monomeric species bearing a terminally bound imide ligand (^{Ar}dpme)FeCl(NAr^{tBu}), Ar^{tBu} = *p*-*tert*-butylphenyl (**Figure 4.3b**). The Fe–Cl (2.210(1) Å) and Fe–N_L (2.005(2) Å) bond lengths are consistent with those found in the bimolecularly coupled Fe^{III} dimer [Fe^{III}]₂. The Fe–NAr bond length in (^{Ar}dpme)FeCl(NAr^{tBu}) (1.768(2) Å) is elongated relative to previously reported terminal imide complexes (e.g. [PhBP₃]Fe(N-*p*-tol) 1.659(2) Å, *S* = 1/2;^{12a} (^{Me}nacnac)Fe(NAd) 1.662(2) Å, *S* = 3/2;^{12f} (PDI)Fe(NAr') 1.705(2)–1.717(2) Å, *S* = 1;^{12c} [(N4Py)Fe(NTs)]²⁺ 1.73(1) Å, *S* = 1³²),³³ suggesting any iron imide multiple bond character is severely attenuated. To account for the anomalously long Fe–NAr bond length in (^{Ar}dpme)FeCl(NAr^{tBu}), the similar Mössbauer parameters for [Fe^{III}]₂ and (^{Ar}dpme)FeCl(NAr^{tBu}), and the observed magnetic moment of monomeric (^{Ar}dpme)FeCl(NAr^{tBu}), we propose (^{Ar}dpme)FeCl(NAr^{tBu}) is comprised of a high-spin Fe^{III} (*d*⁵, *S* = 5/2) center antiferromagnetically coupled to an imide-based radical (*S* = 1/2). The presence of an aryl delocalized radical can be gleaned from the C–C bond distances within the nitrene

(32) Klinker, E. J.; Jackson, T. A.; Jensen, M. P.; Stubna, A.; Juhasz, G.; Bominaar, E. L.; Münck, E.; Que, L., Jr. *Angew. Chem., Int. Ed.* **2006**, *45*, 7394–7397.(33) PhBP₃ = tris(diphenylphosphino)phenylborate; ^{Me}nacnac = *N,N'*-bis(2,6-diisopropylphenyl)pentane-2,4-diimine; PDI = 2,6-bis[1-(2,6-diisopropylphenylimino)ethyl]pyridine, Ar' = 2,6-diisopropylphenyl or mesityl; N4Py = 1,1-di(pyridin-2-yl)-*N,N*-bis(pyridin-2-ylmethyl)methanamine.

aryl ring ($d(\text{Å})$; N3–C1, 1.331(2); C1–C2, 1.423(3); C2–C3, 1.372(3); C3–C4, 1.406(3); C4–C5, 1.405(3); C5–C6, 1.378(3); C6–C1, 1.414(3), see **Table 4.4**).³⁴ In comparison to a *para* substituted Fe^{III} imide that does not feature radical character, the average bond distances within the imide aryl moiety are C–N, 1.382(3) Å, $C_{\text{ipso}}-C_{\text{ortho}}$, 1.401(2) Å, $C_{\text{ortho}}-C_{\text{meta}}$, 1.378(2) Å, and $C_{\text{meta}}-C_{\text{para}}$, 1.387(3) Å.^{12a} Probing the electronic structure by DFT corroborates the proposed electronic structure. Broken symmetry calculations estimate the antiferromagnetic magnetic exchange coupling (J)³⁵ to be -673 cm^{-1} and the calculated Mössbauer parameters match well with those observed for (^{Ar}dpme)FeCl(NAr^{tBu}) (calculated δ , $|\Delta E_Q|$ (mm/s) 0.34, -2.00).^{36, 37} The calculated spin density plot ($\alpha - \beta$) for (^{Ar}dpme)FeCl(NAr^{tBu}), shown in **Figure 4.2b**, illustrates this exchange interaction.

Table 4.4. Bond Lengths and Angles of [Fe^{III}]₂ and (^{Ar}dpme)FeCl(NAr^{tBu}).

Bond Length / Å or Angle / °		
	[Fe ^{III}] ₂	(^{Ar} dpme)FeCl(NAr ^{tBu})
N(1)–C(1)	1.276(3)	1.331(2)
C(1)–C(2)	1.462(4)	1.423(3)
C(2)–C(3)	1.328(3)	1.372(3)
C(3)–C(4)	1.490(4)	1.406(3)
C(4)–C(5)	1.489(4)	1.405(3)
C(5)–C(6)	1.331(3)	1.378(3)
C(6)–C(1)	1.462(4)	1.414(3)
C(4)–N(4)	1.484(3)	–
Fe(1)–N(3)–C(1)	154.6(2)	156.43(17)
Fe(2)–N(4)–C(4)	114.86(16)	–

(34) Chaudhuri, P.; Verani, C. N.; Bill, E.; Bothe, E.; Weyhermüller, T.; Wieghardt, K. *J. Am. Chem. Soc.* **2001**, *123*, 2213-2223.

(35) See **Table 4.6** for equations for spin Hamiltonian and coupling constant.

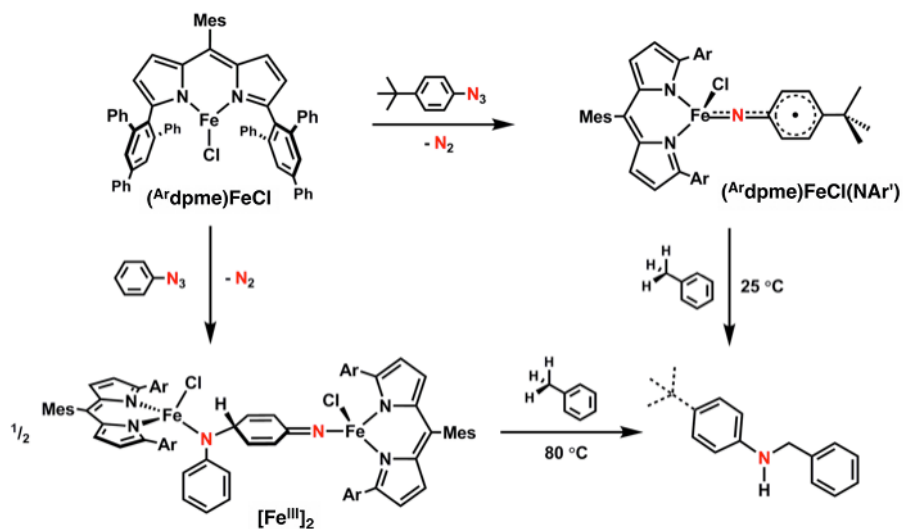
(36) Ye, S. F.; Tuttle, T.; Bill, E.; Simkhovich, L.; Gross, Z.; Thiel, W.; Neese, F. *Chem.-Eur. J.* **2008**, *14*, 10839-10851.

(37) Neese, F. *ORCA - An ab initio, Density Functional and Semi-empirical Electronic Structure Package*, version 2.7; Universität Bonn: Bonn, Germany, 2009.

4-6. Reactivity of the Imide Radical.

Gratifyingly, monomeric ($^{\text{Ar}}\text{dpme})\text{FeCl}(\text{NAr}^{\text{tBu}})$ is a reactive source of aryl nitrene. Complex ($^{\text{Ar}}\text{dpme})\text{FeCl}(\text{NAr}^{\text{tBu}})$ reacts rapidly with 1,4-cyclohexadiene to produce $\text{H}_2\text{N}(\text{C}_6\text{H}_4\text{-}p\text{-}^{\text{tBu}})$ and benzene, in addition to reacting with PMe_2Ph to produce the phosphinimide $\text{Me}_2\text{PhP}=\text{N}(\text{C}_6\text{H}_4\text{-}p\text{-}^{\text{tBu}})$ and ($^{\text{Ar}}\text{dpme})\text{FeCl}$. Stirring ($^{\text{Ar}}\text{dpme})\text{FeCl}(\text{NAr}^{\text{tBu}})$ in toluene at room temperature produces the benzylic C–H amination product, $\text{PhCH}_2\text{NH}(\text{C}_6\text{H}_4\text{-}p\text{-}^{\text{tBu}})$ (42% yield by ^1H NMR), where the remainder of aryl azide is converted into the free aniline. The kinetic isotope effect for C–H activation by the putative imide ($^{\text{Ar}}\text{dpme})\text{FeCl}(\text{NAr}^{\text{tBu}})$ was determined via a competition experiment employing a 1:1 ratio of toluene to its perdeutero analog, providing a kinetic isotope effect, $k_{\text{H}}/k_{\text{D}}$, of 24(3). While this value exceeds the kinetic isotope effect determined for precatalyst ($^{\text{Ad}}\text{dpme})\text{FeCl}(\text{OEt}_2)$, it is of the same order of magnitude and suggests complex ($^{\text{Ar}}\text{dpme})\text{FeCl}(\text{NAr}^{\text{tBu}})$ is representative of the transient group transfer reagent formed in the catalytic runs employing ($^{\text{Ad}}\text{dpme})\text{FeCl}(\text{OEt}_2)$ as a precatalyst. Reacting ($^{\text{Ar}}\text{dpme})\text{FeCl}(\text{NAr}^{\text{tBu}})$ with styrene (200 equivalents) at room temperature produces the aziridine $\text{Ph}(\text{CHCH}_2)\text{N}(\text{C}_6\text{H}_4\text{-}p\text{-}^{\text{tBu}})$ in good yield (76% by ^1H NMR). One competitive reaction pathway observed in the aziridination reaction is the radical polymerization of styrene initiated by ($^{\text{Ar}}\text{dpme})\text{FeCl}(\text{NAr}^{\text{tBu}})$, though this could be minimized by dilution of the styrene substrate. In both the amination and aziridination reactions free amine, $\text{H}_2\text{NC}_6\text{H}_4\text{-}p\text{-}^{\text{tBu}}$, was observed by HRMS, and ($^{\text{Ar}}\text{dpme})\text{FeCl}(\text{NAr}^{\text{tBu}})$ was formed as the predominant iron containing product as ascertained by ^1H NMR. Heating ($^{\text{Ar}}\text{dpme})\text{FeCl}(\text{NAr}^{\text{tBu}})$ in the presence of substrate leads to decreased yields of the corresponding amine and aziridine products. Traces of diazene ($\text{RN}=\text{NR}$) are also observable in the HRMS of pure ($^{\text{Ar}}\text{dpme})\text{FeCl}(\text{NAr}^{\text{tBu}})$, though how it forms remains unclear. Furthermore, dimeric $[\text{Fe}^{\text{III}}]_2$ is also a reactive source of phenyl nitrene, affording PhCH_2NHPh upon heating $[\text{Fe}^{\text{III}}]_2$ in

toluene to 80 °C (observed by HRMS). Thus, dimeric $[\text{Fe}^{\text{III}}]_2$ must be in equilibrium with its monomeric precursor, $(^{\text{Ar}}\text{dpme})\text{FeCl}(\text{NPh})$, which reacts analogously to $(^{\text{Ar}}\text{dpme})\text{FeCl}(\text{NAr}^{\text{tBu}})$ to effect intermolecular C–H bond amination (**Scheme 4.3**).



Scheme 4.3. Synthesis of the bimolecularly coupled Fe^{III} imide precursor $[\text{Fe}^{\text{III}}]_2$ and the terminal imide complex $(^{\text{Ar}}\text{dpme})\text{FeCl}(\text{NAr}^{\text{tBu}})$ with a delocalized imide-based radical, $\text{Fe}^{\text{III}}(^{\bullet}\text{NAr}^{\text{tBu}})$, and their subsequent reactivity with C–H bonds.

Given the reactivity observed for $(^{\text{Ar}}\text{dpme})\text{FeCl}(\text{NAr}^{\text{tBu}})$, we propose that an imide radical strongly coupled to a high-spin Fe^{III} ion, $(^{\text{x}}\text{dpme})\text{Fe}^{\text{III}}\text{Cl}(^{\bullet}\text{NR})$, is the putative group transfer reagent in both the amination and aziridination catalytic processes. The reactive species reported herein is a departure from the typical Fe^{IV} assignment invoked in Fe mediated group transfer catalysis.^{5,18,19} The isolation of the stable terminal imide radical $(^{\text{Ar}}\text{dpme})\text{FeCl}(\text{NAr}^{\text{tBu}})$ and the imide precursor $[\text{Fe}^{\text{III}}]_2$ lend support to this assignment. Reaction with alkyl azides in the catalytic reaction should localize the radical character on the imide N, giving rise to the observed enhanced reactivity towards C–H bond or olefinic substrates. We attribute the observed group transfer catalysis to the electronic structure, more specifically the localized radical character on the imide N, as the reactivity reported here is distinct from other

Fe(imide) complexes.^{11,12,13,14,32,38} Metal imide complexes which bear radical character on the imide fragment have been invoked in other transition metal complexes to explain observed reactivity.^{27,39,40} Warren and coworkers invoke a terminal Cu^{III}(imide)²⁷ and have demonstrated that a terminal Cu^{II}(amide),²⁸ both of which are proposed to have radical character at N, are key intermediates in their C–H bond amination chemistry. A cobalt(III) imide, published by Theopold, which aminates an intramolecular C–H bond is also believed to have nitrogen radical character at room temperature despite a diamagnetic ground state.⁴¹ Thus, while the terminal imide radical bound to a ferric center (**(Ar₂dpme)FeCl(NAr^{tBu})**) is the first example of an isolated complex featuring this type of high-spin electronic configuration, the electronic structure may arise in other synthetic and biochemical catalytic cycles.^{6,7c,42,43}

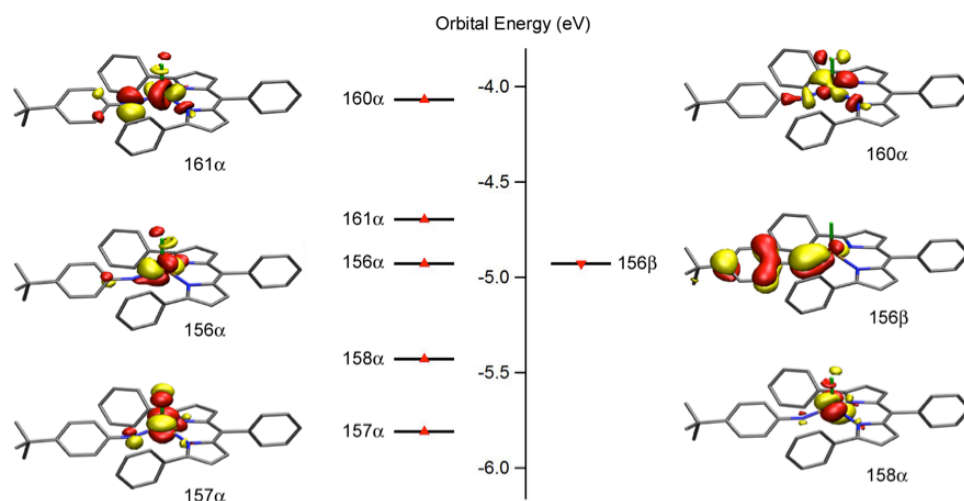


Figure 4.4. Molecular orbitals and energy levels for (**Ar₂dpme**)Fe(**NAr^{tBu}**) derived from the BS(5,1) solution. Unrestricted corresponding orbitals for the spin-coupled pair (156 α ,156 β) and quasi-restricted orbitals (157 α –160 α)

(38) Mankad, N. P.; Müller, P.; Peters, J. C. *J. Am. Chem. Soc.* **2010**, *132*, 4083-4084.

(39) Lu, C. C.; George, S. D.; Weyhermüller, T.; Bill, E.; Bothe, E.; Wieghardt, K. *Angew. Chem., Int. Ed.* **2008**, *47*, 6384-6387.

(40) Kogut, E.; Wiencko, H. L.; Zhang, L. B.; Cordeau, D. E.; Warren, T. H. *J. Am. Chem. Soc.* **2005**, *127*, 11248-11249.

(41) Shay, D. T.; Yap, G. P. A.; Zakharov, L. N.; Rheingold, A. L.; Theopold, K. H. *Angew. Chem., Int. Ed.* **2005**, *44*, 1508-1510.

(42) (a) Groves, J. T.; Van Der Puy, M. *J. Am. Chem. Soc.* **1974**, *96*, 5274-5275. (b) Groves, J. T.; McClusky, G. A. *J. Am. Chem. Soc.* **1976**, *98*, 859-861.

(43) (a) Chen, M. S.; White, M. C. *Science* **2007**, *318*, 783-787. (b) Chen, M. S.; White, M. C. *Science* **2010**, *327*, 566-571.

4-7. Conclusions.

Catalytic C–H bond amination and olefin aziridination have been observed from the reaction of organic azides with a simple iron(II) coordination complex supported by dipyrromethene ligands. Kinetic isotope analysis of the amination reaction suggests the C–H bond breaking event contributes to rate limiting step of the reaction, followed by a radical rebound. Isolation of a reactive intermediate reveals the putative nitrene delivery precursor to be a high-spin ($S = 2$) iron complex featuring a terminal imide ligand. Crystallographic, spectroscopic, and theoretical analyses suggest a formulation for this reactive species to be a high-spin iron(III) center antiferromagnetically coupled to an imide-based radical. The terminal imide complex was effective for delivering the nitrene moiety to both C–H bond and olefinic substrates. The similarities observed in the kinetic isotope effects observed during catalytic runs and those using the isolated imide suggest the high-spin, $\text{Fe}^{\text{III}}(\text{imide radical})$ is representative of the group transfer reagent in the catalytic sequence. Given the breadth of iron imide complexes spanning several oxidation states ($\text{Fe}^{\text{II}}\text{--}\text{Fe}^{\text{V}}$) and several spin states ($S = 0 \rightarrow 3/2$), we propose the unusual electronic structure of the described high-spin iron imide complexes contributes to the observed catalytic reactivity. The high-spin nature and radical nitrene character serve to destabilize the Fe imide bond which presumably leads to the observed reactivity.

4-8. Experimental Methods.

General Considerations.

All manipulations of metal complexes were carried out in the absence of water and dioxygen using standard Schlenk techniques, or in an inert atmosphere glovebox (M. Braun) under a dinitrogen atmosphere. Ligand and ligand precursor syntheses were carried out in air, except where noted. All glassware was oven dried for a minimum of 1 h and cooled in an evacuated antechamber prior to use in

the glovebox. Benzene, diethyl ether, dichloromethane, *n*-hexane, tetrahydrofuran, and toluene were dried and deoxygenated on a Glass Contour System (SG Water USA, Nashua, NH) and stored over 4 Å molecular sieves (Strem) prior to use. Anhydrous *n*-pentane, hexamethyldisiloxane, styrene, and trifluoromethylbenzene were purchased from Aldrich, degassed if necessary, and stored over 4 Å molecular sieves prior to use. Chloroform-*d* was purchased from Cambridge Isotope Labs and used as received. Benzene-*d*₆, dichloromethane-*d*₂ and toluene-*d*₈ were purchased from Cambridge Isotope Labs and were degassed and stored over 4 Å molecular sieves prior to use. Pyridinium *p*-toluenesulfonate, DDQ, 1,4-cyclohexadiene, 1-adamantyl azide, 1-chloroadamantane, *tert*-butyl chloride, aluminum trichloride, 1-aminoadamantane and *tert*-butylisocyanide were purchased from Aldrich and used as received. Anhydrous iron(II) chloride, 2-dicyclohexylphosphino-2',6'-dimethoxy-1,1'-biphenyl (SPhos), dipalladium tris(dibenzylideneacetone), dimethylphenylphosphine, tris(pentafluorophenyl)borane and zinc chloride were purchased from Strem and used as received. Ethyl 1*H*-pyrrole-2-carboxylate,²¹ 2-*tert*-butyl-1*H*-pyrrole,²² mesitaldehyde dimethyl acetal,⁴⁴ phenyl azide,⁴⁵ and 4-*tert*-butylphenyl azide,⁴⁵ 2-bromo-1,3,5-triphenylbenzene,⁴⁶ and sodium pyrrolide²⁰ were synthesized according to literature procedures. Celite® 545 (J. T. Baker) and silica gel 32–63 μ (Dynamic Adsorbents, Atlanta, GA), were dried in a Schlenk flask for 24 h under dynamic vacuum while heating to at least 150 °C prior to use in a glovebox.

Characterization and Physical Measurements.

UV/Visible spectra were recorded on a Varian Cary 50 UV/Visible spectra using quartz cuvettes and a scan rate of 300 or 600 nm/min. Extinction coefficients were determined from a minimum of three

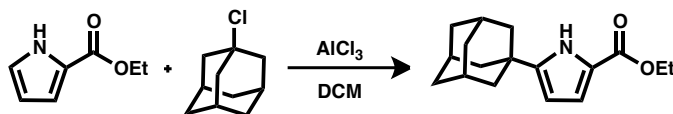
(44) Ji, N.; O'Dowd, H.; Rosen, B. M.; Myers, A. G. *J. Am. Chem. Soc.* **2006**, *128*, 14825-14827.

(45) Smith, P. A. S.; Hall, J. H. *J. Am. Chem. Soc.* **1962**, *84*, 480-485.

(46) Lawson Daku, L. M.; Pecaut, J.; Lenormand-Foucaut, A.; Vieux-Melchior, B.; Iveson, P.; Jordanov, J. *Inorg. Chem.* **2003**, *42*, 6824-6850.

concentrations per sample, and were calculated by a linear regression fit of the absorbance vs. concentration data. ^1H , ^{13}C , ^{19}F , and ^{31}P NMR spectra were recorded on Varian Mercury 400 MHz or Varian Unity/Inova 500 MHz spectrometers. ^1H and ^{13}C NMR chemical shifts are reported relative to SiMe_4 using the chemical shift of residual solvent peaks as reference. Solution magnetic susceptibilities were determined by Evans's method²³ using hexamethyldisiloxane or trifluoromethylbenzene as an internal reference. Mass spectrometry was performed at the Harvard University FAS Center for Systems Biology Mass Spectrometry and Proteomics Resource Laboratory on an Agilent 6210 TOF LC/MS with a dual nebulizer ESI source for HRMS and on a Waters Q-TOF Micro LC/MS/MS with a ESI source for yield determination. Elemental analyses were carried out by Complete Analysis Laboratories, Inc. (Parsippany, NJ). ^{57}Fe Mössbauer spectra were measured on liquid nitrogen cooled samples at zero magnetic field with a constant acceleration spectrometer (SEE Co., Edina, MN). Solid or crystalline samples were prepared as Paratone N mulls in a glovebox and frozen in liquid nitrogen prior to handling in air. Isomer shifts are quoted relative to Fe foil at room temperature. Data was processed, simulated, and analyzed using an in-house package written by E.R.K. for IGOR Pro 6 (Wavemetrics, Lake Oswego, OR).

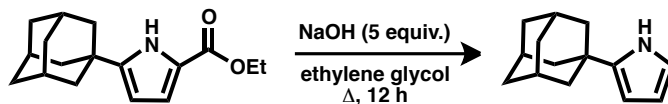
Ligand Syntheses.



Ethyl 5-(1-adamantyl)-1H-pyrrole-2-carboxylate:⁴⁷ A dry, 3 L round-bottomed flask was charged with ethyl 1H-pyrrole-2-carboxylate (20.40 g, 146.7 mmol) and 1.5 L of dry dichloromethane. The flask was purged with nitrogen and AlCl_3 (41.15 g, 308.7 mmol, 2.104 equiv.) was added in one portion,

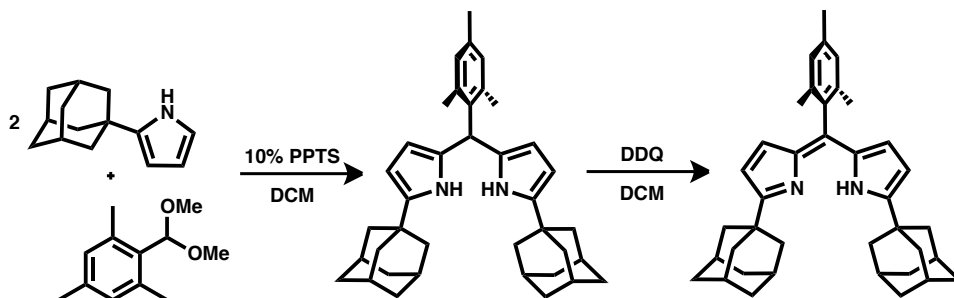
(47) Modified from the synthesis of 2-*tert*-butylpyrrole. See reference 22.

followed by the *immediate* addition of 1-adamantyl chloride (25.00 g, 146.7 mmol, 1.000 equiv.), The resulting mixture was stirred under nitrogen for 1 h. The reaction mixture was then quenched by careful addition to a saturated solution of aqueous NaHCO₃ (750 mL). Diethyl ether was added and the organic layer separated. The aqueous layer was further extracted with ether (2 x 200 mL) and the combined organics dried over anhydrous MgSO₄ and concentrated by rotary evaporation to yield off-white solid ethyl 5-(1-adamantyl)-1*H*-pyrrole-2-carboxylate (26.9 g, 67.1%), which was used without further purification. ¹H NMR (500 MHz, CDCl₃): δ/ppm 8.80 (br s, 1H, N–H), 6.83 (m, 1H, pyrrole C–H), 5.99 (m, 1H, pyrrole C–H), 4.31 (m, 2H, OCH₂CH₃), 2.08 (br s, 3H, adamantyl 3° C–H), 1.90 (s, 6H), 1.80–1.73 (m, 6H), 1.34 (m, 3H, OCH₂CH₃). ¹³C {¹H} NMR (100 MHz, C₆D₆): δ/ppm 161.4, 148.0, 120.8, 115.5, 104.9, 60.0, 42.3, 36.5, 33.5, 28.3, 14.5. HRMS (ESI⁺) *m/z* Calc. 274.18070 [C₃₈H₄₆N₂+H]⁺, Found 274.18016 [M+H]⁺.



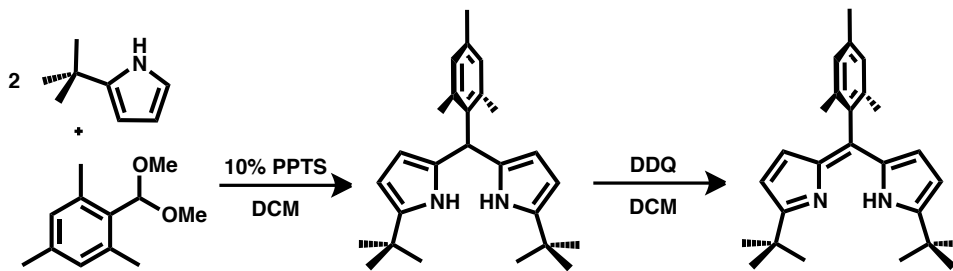
2-(1-adamantyl)-1*H*-pyrrole:⁴⁷ A slurry of ethyl 5-(1-adamantyl)-1*H*-pyrrole-2-carboxylate (26.90 g, 98.46 mmol) and powdered NaOH (19.70 g, 492.5 mmol, 5.002 equiv.) in ethylene glycol (200 mL) was brought to reflux with the aid of a heating mantle. After 12 h, the reaction mixture was allowed to cool to room temperature, diluted with water (300 mL) and extracted with CH₂Cl₂ (5 x 100 mL). The organic portions were dried over anhydrous Na₂SO₄ and concentrated by rotary evaporation to yield a light brown solid which was recrystallized from hexanes, affording 2-(1-adamantyl)-1*H*-pyrrole (17.4 g, 87.8%) as a tan powdery solid. ¹H NMR (500 MHz, CDCl₃): δ/ppm 8.0 (br s, 1H, N–H), 6.67 (m, 1H), 6.14 (m, 1H), 5.92 (m, 1H), 2.06 (br s, 3H), 1.90 (s, 6H), 1.8–1.73 (m, 6H), 1.35 (t, 3H). ¹³C {¹H}

NMR (100 MHz, C₆D₆): δ /ppm 141.7, 115.9, 108.2, 102.5, 43.1, 37.1, 33.3, 29.0. HRMS (ESI⁺) m/z
 Calc. 202.15957 [C₃₈H₄₆N₂+H]⁺, Found 202.15903 [M+H]⁺.



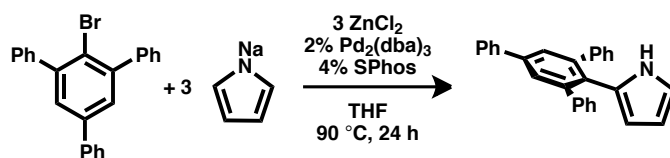
1,9-di(1-adamantyl)-5-mesityldipyrromethene, (Ad^{Ad}dpme)H: Under an inert atmosphere a 500 mL round-bottomed flask was charged with 2-(1-adamantyl)-1H-pyrrole (10.00 g, 49.71 mmol), mesitaldehyde dimethyl acetal (4.830 g, 24.86 mmol, 0.5001 equiv.), and 250 mL of dry CH₂Cl₂. After stirring until all materials were dissolved, pyridinium *p*-toluenesulfonate (1.249 g, 4.971 mmol, 0.1000 equiv.) was added resulting in a color change from colorless to emerald green. The reaction was stirred at room temperature for 3 h. The solution was concentrated *in vacuo* and filtered through a plug of silica gel in a medium porosity frit (30 mL) with CH₂Cl₂ to give a pale yellow filtrate. Solvent was removed *in vacuo* and the solid was triturated twice with 50 mL hexanes, followed by removal of the hexanes *in vacuo*, affording 1,9-di(1-adamantyl)-5-mesityldipyrromethane (13.0 g, 98.2%) as a pale pink powder. ¹H NMR (500 MHz, C₆D₆): δ /ppm 7.68 (br s, 2H, pyrrole N-H), 6.78 (s, 2H, aryl C-H), 6.05 (m, 2H, pyrrole C-H), 6.02 (t, *J* = 3 Hz, 2H, pyrrole C-H), 5.89 (s, 1H, MesCH(C₄H₂AdNH)₂), 2.16 (s, 6H, *ortho*-C₆H₂(CH₃)₃), 2.11 (s, 3H, *para*-C₆H₂(CH₃)₃), 1.81 (s, 6H, adamantyl 3° C-H), 1.73 (s, 12H, adamantyl 2° C-H), 1.58–1.50 (m, 12H, adamantyl 2° C-H); ¹³C{¹H} NMR (100 MHz, CD₂Cl₂): δ /ppm 141.8, 137.6, 136.3, 135.4, 130.3, 130.0, 105.8, 101.7, 43.2, 38.9, 37.0, 33.3, 29.0, 20.7, 20.4. The product (8.00 g, 15.0 mmol) was dissolved in 300 mL CH₂Cl₂. The oxidant, 2,3-dichloro-5,6-dicyanoquinone (DDQ) (3.392 g, 15.01 mmol, 1 equiv.), was added to immediately give a dark brown

solution. After stirring for 12 h, the solution was concentrated *in vacuo* and filtered through a plug of silica gel in a medium porosity frit (30 mL) with benzene to give a dark brownish yellow filtrate. Solvent was removed *in vacuo* and the dark brown solid was washed with diethyl ether (2 x 50 mL) to give (^{Ad}dpme)H (5.57 g, 70.0%) as a mustard yellow powder. ¹H NMR (500 MHz, C₆D₆): δ/ppm 6.76 (s, 2H, aryl C–H), 6.54 (d, *J* = 4 Hz, 2H, pyrrole C–H), 6.23 (d, *J* = 4 Hz, 2H, pyrrole C–H), 2.15 (s, 3H, *para*-C₆H₂(CH₃)₃), 2.14 (s, 6H, *ortho*-C₆H₂(CH₃)₃), 2.06 (d, *J* = 3 Hz, 12H, adamantyl 2° C–H), 1.95 (br s, 6H, adamantyl 3° C–H), 1.67 (br s, 12H, adamantyl 2° C–H). ¹³C {¹H} NMR (100 MHz, CD₂Cl₂): δ/ppm 166.6, 138.7, 137.6, 137.1, 134.0, 128.7, 128.3, 128.0, 113.6, 42.3, 37.2, 35.8, 29.0, 21.2, 20.1. HRMS (ESI⁺) *m/z* Calc. 531.3739 [C₃₈H₄₆N₂+H]⁺, Found 531.3763 [M+H]⁺.



1,9-di-*tert*-butyl-5-mesityldipyrromethene, (^{tBu}dpme)H: Under an inert atmosphere a 200 mL round-bottomed flask was charged with 2-*tert*-butylpyrrole (2.130 g, 17.30 mmol), mesitaldehyde dimethyl acetal (1.680 g, 8.652 mmol, 0.5001 equiv.), and 85 mL of dry CH₂Cl₂. After stirring until all materials were dissolved, pyridinium *p*-toluenesulfonate (0.435 g, 1.730 mmol, 0.1000 equiv.) was added resulting in a color change from colorless to bright yellow. The reaction was stirred at room temperature for 3 h. The solution was concentrated *in vacuo* and filtered through a plug of silica gel (30 mL) in CH₂Cl₂ to give a pale yellow filtrate. Solvent was removed *in vacuo* and the solid was triturated twice with 50 mL hexanes, followed by removal of the hexanes *in vacuo*, affording 1,9-di-*tert*-butyl-5-mesityldipyrromethane (3.25 g, 99.7%) as a pale yellow oil. ¹H NMR (500 MHz, CD₂Cl₂): δ/ppm 7.78

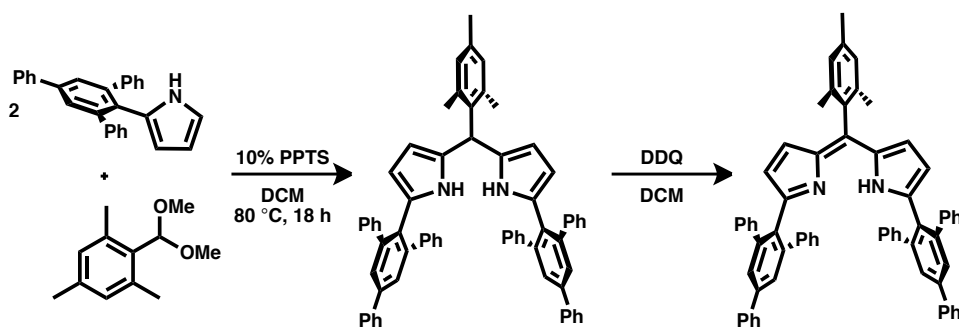
(br s, 2H, pyrrole N-H), 6.86 (s, 2H, aryl C-H), 5.81 (s, 1H, MesCH(C₄H₂^tBuNH)₂), 5.79 (m, 2H, pyrrole C-H), 5.62 (s, 2H, pyrrole C-H), 2.27 (s, 3H, *para*-C₆H₂(CH₃)₃), 2.08 (s, 6H, *ortho*-C₆H₂(CH₃)₃), 1.24 (s, 18H, C(CH₃)₃). ¹³C{¹H} NMR (125 MHz, CD₂Cl₂): δ/ppm 141.2, 137.7, 136.5, 135.5, 130.5, 106.0, 102.6, 39.0, 34.5, 31.5, 30.7, 22.8, 20.6. The product (3.252 g, 8.642 mmol) was dissolved in 175 mL hexanes. The oxidant, 2,3-dichloro-5,6-dicyanoquinone (DDQ) (1.962 g, 8.642 mmol, 1.000 equiv.), was added to give a mustard yellow solution. After stirring for 6 h, the solution was concentrated *in vacuo* and filtered through Celite in hexanes, followed by a plug of silica gel (30 mL) in hexanes to give an orange-yellow filtrate. Solvent was removed *in vacuo* to give (t^{bu}dpme)H (2.36 g, 72.9%) as an orange-yellow crystalline solid. ¹H NMR (400 MHz, CDCl₃): δ/ppm 13.57 (1H, s), 6.79 (s, 2H, aryl C-H), 6.55 (d, *J* = 4.4 Hz, 2H, pyrrole C-H), 6.23 (d, *J* = 4.4 Hz, 2H, pyrrole C-H), 2.19 (s, 9H, *para/ortho*-C₆H₂(CH₃)₃), 1.35 (s, 18H, C₄H₉). ¹³C {¹H} NMR (100 MHz, CD₂Cl₂): δ/ppm 166.3, 139.4, 137.7, 137.5, 137.1, 133.9, 128.0, 126.9, 114.3, 33.7, 30.0, 21.2, 20.1. HRMS (ESI⁺) *m/z* Calc. 375.2800 [C₂₆H₃₅N₂+H]⁺, Found 375.2794 [M+H]⁺.



2-(2,4,6-triphenylphenyl)-1H-pyrrole:⁴⁸ In the glovebox a 1 L air-free storage flask with a Teflon valve was charged with a stir bar, sodium pyrrolide (31.2 g, 351 mmol, 3.00 equiv.), and 400 mL anhydrous THF. While stirring zinc chloride (47.8 g, 351 mmol, 3.00 equiv.) was slowly added over the course of 20 min, evolving heat and causing the solvent to reflux. In a 20 mL scintillation vial, SPhos (1.92 g, 4.68 mmol, 0.0400 equiv.) and dipalladium tris(dibenzylideneacetone) (2.14 g, 2.34 mmol, 0.0200 equiv.) were stirred in 15 mL THF. The catalyst mixture was then added to the reaction mixture,

(48) Modified from the syntheses of 2-arylpyrroles. See reference 20.

followed by the addition of 2-bromo-1,3,5-triphenylbenzene (45.0 g, 117 mmol). The flask was placed under partial vacuum and the valve sealed. The reaction was heated in an oil bath at 90 °C for 24 h. After cooling to room temperature the reaction mixture was extracted with water and Et₂O. The organic fractions were combined, dried over MgSO₄, and the solvent was removed by rotary evaporation. The dark brown solids were then dissolved in dichloromethane, flashed through a 15 in × 1 in silica column, dried over MgSO₄, and the solvent was removed by rotary evaporation. The light tan solid was washed on a frit with 250 mL pentane. The solid was dried *in vacuo* to yield 31.8 g (73.2%) of 2-(2,4,6-triphenylphenyl)-1*H*-pyrrole. ¹H NMR (500 MHz, CDCl₃): δ/ppm 5.56 (m, 1H, pyrrole C–H), 5.94 (m, 1H, pyrrole C–H), 6.46 (m, 1H, pyrrole C–H), 7.25 (m, 4H, aryl C–H), 7.28–7.32 (m, 6H, aryl C–H), 7.38 (t, *J* = 7.3 Hz, 1H, aryl C–H), 7.46 (t, *J* = 7.3 Hz, 2H, aryl C–H), 7.66 (s, 2H), 7.69 (d, *J* = 7.3 Hz, 2H aryl C–H), 7.80 (br s, 1H, N–H) ¹³C {¹H} NMR (125 MHz, CDCl₃): δ/ppm 108.3, 111.8, 117.2, 126.7, 127.1, 127.5, 127.9, 128.4, 128.8, 129.1, 129.6, 129.7, 140.1, 140.3, 142.0, 142.6. HRMS (ESI⁺) *m/z* Calc. 372.1747 [C₂₈H₂₁N+H]⁺, Found 372.1762 [M+H]⁺.



5-mesityl-1,9-di(2,4,6-triphenylphenyl)dipyrromethene, (^{Ar}dpme)H: In the glovebox a 1 L air-free storage flask with a Teflon valve was charged with a stir bar, 2-(2,4,6-triphenylphenyl)-1*H*-pyrrole (31.18 g, 83.94 mmol), mesitaldehyde dimethyl acetal (8.15 g, 42.0 mmol, 0.500 equiv.), and 300 mL anhydrous dichloromethane. Pyridinium *p*-toluenesulfonate (1.055 g, 4.198 mmol, 0.05001 equiv.) was

added resulting in immediate color change from light orange to dark brown. The bomb was placed under partial vacuum, sealed with a Teflon screw-cap, and heated to 80 °C for 18 h in an oil bath. After cooling to room temperature the dichloromethane solution was filtered through a silica plug, dried over MgSO₄, and the solvent was removed via rotary evaporation yielding 5-mesityl-1,9-(2,4,6-triphenylphenyl)dipyrromethane as a light orange powder (31.75 g, 86.64%). ¹H NMR (500 MHz, CD₂Cl₂): δ/ppm 1.75 (br s, 6H, *ortho*-C₆H₂(CH₃)₃), 2.21 (s, 3H, *para*-C₆H₂(CH₃)₃), 5.20 (t, *J* = 3.2 Hz, 2H, pyrrole C–H), 5.35 (s, 1H, methine C–H), 5.39 (t, *J* = 3.2 Hz, 2H, pyrrole C–H), 6.70 (s, 2H, N–H), 6.95 (s, 2H, C₆H₂(CH₃)₃), 7.14 (m, 8H, aryl C–H), 7.17–7.21 (m, 12H, aryl C–H), 7.35 (t, *J* = 8.3 Hz, 2H, aryl C–H), 7.44 (t, *J* = 7.8 Hz, 4H, aryl C–H), 7.61 (s, 4H), 7.68 (d, *J* = 8.3 Hz, 4H, aryl C–H). ¹³C {¹H} NMR (125 MHz, CD₂Cl₂): δ/ppm 20.7, 20.8, 38.2, 106.7, 112.5, 126.4, 127.1, 127.4, 127.9, 128.2, 128.5, 129.2, 129.5, 129.7, 130.1, 130.4, 130.8, 134.5, 136.4, 140.3, 140.6, 142.5, 143.2. In a 500 mL round-bottomed flask equipped with a stir bar the product (31.75 g, 36.36 mmol) was dissolved in 300 mL anhydrous dichloromethane. 2,3-Dichloro-5,6-dicyano-1,4-benzoquinone (8.50 g, 37.4 mmol, 1.03 equiv.) was added resulting in an immediate color change from light orange to dark purple. The reaction was stirred for 3 h and then solvent was removed via rotary evaporation. The resulting solids were dissolved in benzene and filtered through a silica plug to give a red solution, which was dried over MgSO₄, and dried by rotary evaporation to give a red solid. The product was refluxed in 200 mL hexanes for 2 h, then stirred for an additional 12 h, before filtering to collect 5-mesityl-1,9-(2,4,6-triphenylphenyl)dipyrromethane as a red powder (18.14 g, 57.27%). Crystals suitable for X-ray diffraction were grown from a 2:1 benzene/*n*-hexane solution at –35 °C. ¹H NMR (500 MHz, CD₂Cl₂): δ/ppm 2.03 (s, 6H, *ortho*-C₆H₂(CH₃)₃), 2.34 (s, 3H, *para*-C₆H₂(CH₃)₃), 5.56 (d, *J* = 4.1 Hz, 2H, pyrrole C–H), 5.89 (d, *J* = 4.1 Hz, 2H, pyrrole C–H), 6.90 (s, 2H, C₆H₂(CH₃)₃), 7.13 (t, *J* = 7.3 Hz, 8H, aryl C–H), 7.21–7.28 (m, 12H, aryl C–H), 7.45 (t, *J* = 8.2 Hz, 2H, aryl C–H), 7.55 (t, *J* = 7.8 Hz, 4H, aryl

C–H), 7.84 (s, 4H, C₆H₂Ph₃), 7.87 (d, *J* = 7.8 Hz, 4H, aryl C–H), 11.50 (br s, 1H, N–H). ¹³C {¹H} NMR (125 MHz, CD₂Cl₂): δ/ppm 19.5, 21.3, 120.9, 125.1, 127.1, 127.6, 127.9, 128.0, 128.1, 128.3, 129.3, 129.8, 131.9, 133.9, 136.8, 137.5, 138.0, 140.6, 140.8, 141.3, 142.1, 143.1, 152.4. HRMS (ESI⁺) *m/z* Calc. 871.4052 [C₂₈H₂₁N+H]⁺, Found 871.4048 [M+H]⁺. UV/Vis (THF) λ_{max}/nm (ε/M⁻¹cm⁻¹) 245 (65000), 321 (27000), 510 (31000).

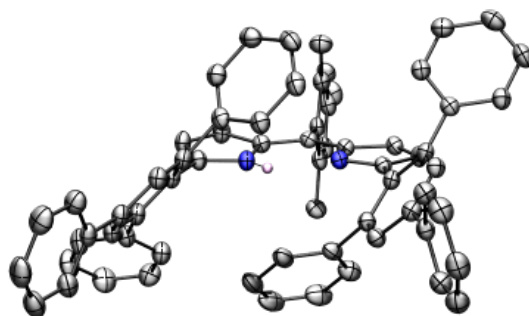
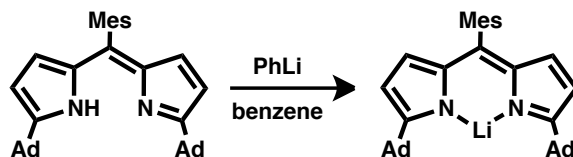


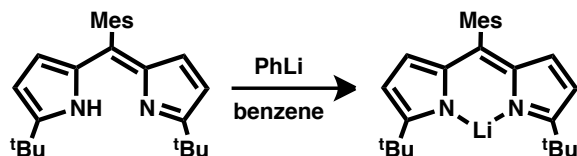
Figure 4.5. Structure of ^{Ar}dpmeH. Thermal ellipsoids at 50% probability level. Hydrogens attached to carbons and benzene solvent molecules omitted for clarity.

Metal Complex Syntheses.

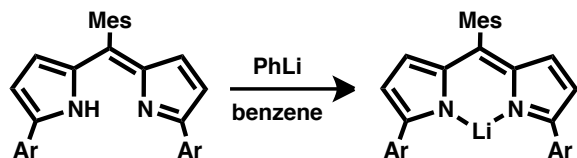


(^{Ad}dpme)Li: In a 200 mL round-bottomed flask (^{Ad}dpme)H (2.000 g, 3.771 mmol) was dissolved in 100 mL benzene and placed in a liquid nitrogen cooled cold well until partially frozen. Phenyl lithium (380.6 mg, 4.525 mmol, 1.200 equiv.) was added as a solid. The solution was allowed to stir overnight and became dark yellow-orange. The mixture was filtered through a medium porosity glass frit with Celite to remove a small amount of insoluble material and afford an orange solution. The benzene was removed *in vacuo* to give (^{Ad}dpme)Li as a bright orange powder (1.86 g, 91.9%). ¹H NMR (500 MHz, C₆D₆): δ/ppm 6.87 (s, 2H, aryl C–H), 6.86 (d, *J* = 4 Hz, 2H, pyrrole C–H), 6.43 (d, *J* = 4 Hz, 2H,

pyrrole C–H), 2.39 (s, 6H, *ortho*-C₆H₂(CH₃)₃), 2.23 (s, 3H, *para*-C₆H₂(CH₃)₃), 1.90 (br s, 6H, adamantyl 3° C–H), 1.87 (s, 12H, adamantyl 2° C–H), 1.62 (m, 12H, adamantyl 2° C–H); ¹³C {¹H} NMR (CD₂Cl₂): δ/ppm 171.2, 138.6, 138.0, 136.8, 136.5, 130.4, 128.7, 127.6, 112.7, 42.9, 37.2, 36.7, 29.2, 21.2, 20.1.

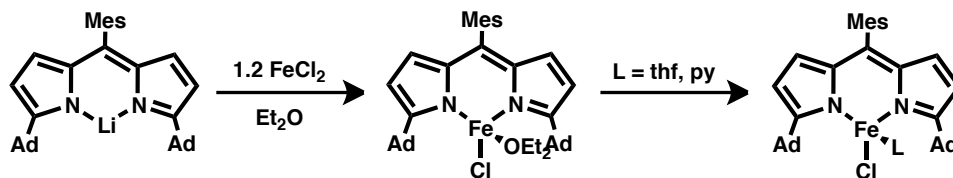


(^{tBu}dpme)Li: In a 250 mL round-bottomed flask (^{tBu}dpme)H (2.357 g, 6.297 mmol) was dissolved in 150 mL diethyl ether and placed in a liquid nitrogen cooled cold well until partially frozen. Phenyl lithium (529.6 mg, 6.297 mmol, 1.000 equiv.) was added as a solid. The solution was allowed to stir overnight and became red-orange. The mixture was filtered through a medium porosity glass frit with Celite to remove a small amount of insoluble material and afford an orange solution. The benzene was removed *in vacuo* to give (^{tBu}dpme)Li as a bright orange powder (2.38 g, 99.3%). ¹H NMR (500 MHz, CD₂Cl₂): δ/ppm 6.91 (s, 2H, aryl C–H), 6.28 (d, *J* = 4 Hz, 2H, pyrrole C–H), 6.23 (d, *J* = 4 Hz, 2H, pyrrole C–H), 2.36 (s, 3H, *para*-C₆H₂(CH₃)₃), 2.08 (s, 6H, *ortho*-C₆H₂(CH₃)₃), 1.40 (s, 18H, C(CH₃)₃); ¹³C {¹H} NMR (125 MHz, CD₂Cl₂): δ/ppm 170.9, 145.7, 138.4, 137.8, 136.8, 136.6, 130.8, 128.7, 127.6, 113.3, 34.6, 30.4, 21.2, 20.1.



(^{Ar}dpme)Li: A 100 mL round-bottomed flask was charged with a stir bar, (^{Ar}dpme)H (3.00 g, 3.44 mmol), and 50 mL anhydrous benzene. The reaction mixture was frozen prior to addition of phenyl lithium (0.318 g, 3.79 mmol, 1.10 equiv.) as a solid. The reaction was allowed to thaw and was stirred for

16 h. Conversion was monitored by ^1H NMR on reaction aliquants, additional phenyllithium was added as necessary to consume remaining protonated ligand. Removal of the solvent *in vacuo* gave $(^{\text{Ar}}\text{dpme})\text{Li}$ (3.02 g, 99.9%) as a dark purple powder. ^1H NMR (400 MHz, C_6D_6): δ/ppm 2.25 (s, 3H, *para*- $\text{C}_6\text{H}_2(\text{CH}_3)_3$), 2.26 (s, 6H, *ortho*- $\text{C}_6\text{H}_2(\text{CH}_3)_3$), 5.84 (d, $J = 4.9$ Hz, 2H, pyrrole C–H), 6.32 (d, $J = 4.9$ Hz, 2H, pyrrole C–H), 6.84 (s, 2H, $\text{C}_6\text{H}_2(\text{CH}_3)_3$), 7.03 (t, $J = 7.7$ Hz, 8H), 7.09 (t, $J = 7.0$ Hz, 4H, aryl C–H), 7.22 (t, $J = 7.7$ Hz, 2H, aryl C–H) 7.25 (d, $J = 7.7$ Hz, 8H, aryl C–H), 7.30 (t, $J = 7.7$ Hz, 4H, aryl C–H), 7.62 (d, $J = 7.7$ Hz, 4H, aryl C–H), 7.76 (s, 4H, $\text{C}_6\text{H}_2\text{Ph}_3$). ^{13}C $\{^1\text{H}\}$ NMR (100 MHz, C_6D_6): δ/ppm 19.8, 21.2, 120.5, 127.4, 127.5, 127.8, 127.9, 128.4, 128.7, 129.2, 129.2, 129.4, 135.5, 136.2, 136.6, 138.1, 140.6, 140.8, 141.3, 142.1, 142.6, 146.4, 155.7. UV/Vis (CH_2Cl_2) $\lambda_{\text{max}}/\text{nm}$ ($\epsilon/\text{M}^{-1}\text{cm}^{-1}$) 253 (75000), 331 (29000), 565 (57000). CHN% Calc. for $\text{C}_{66}\text{H}_{49}\text{LiN}_2$: C 90.38, H 5.63, N 3.19; Found: C 90.36, H 5.65, N 3.16.



$(^{\text{Ad}}\text{dpme})\text{FeCl}(\text{L})$: A 100 mL oven-dried, round-bottomed flask was charged with $(^{\text{Ad}}\text{dpme})\text{Li}$ (2.000 g, 3.730 mmol) and 40 mL of diethyl ether. The flask was placed in a liquid nitrogen cooled cold well until frozen. FeCl_2 (0.5635 g, 4.476 mmol, 1.200 equiv.) was added to the thawing slurry of $(^{\text{Ad}}\text{dpme})\text{Li}$. After stirring for 3 hours, the dark brown reaction mixture was concentrated and filtered through a medium porosity glass frit with Celite to remove excess FeCl_2 and LiCl in benzene. Removal of the solvent *in vacuo* gave a dark brown solid. $(^{\text{Ad}}\text{dpme})\text{FeCl}(\text{OEt}_2)$: The solid was washed with Et_2O and collected on a medium porosity glass frit to give $(^{\text{Ad}}\text{dpme})\text{FeCl}(\text{OEt}_2)$ as a luminescent green brown solid (1.50 g, 57.8%). Crystals suitable for X-ray diffraction were grown from an Et_2O solution of

(^{Ad}dpme)FeCl(OEt₂). ¹H NMR (500 MHz, C₆D₆): δ/ppm 62.47 (s), 16.21 (s), 9.56 (s), 2.50 (s), 1.36 (s), -0.20 (br s), -4.29 (br s). μ_{eff} (296 K) 5.2(2) μ_B. (^{Ad}dpme)FeCl(thf): The solid was redissolved in THF and reconcentrated to give (^{Ad}dpme)FeCl(thf) as a brown powder (1.89 g, 73.1%). ¹H NMR (500 MHz, C₆D₆): δ/ppm 52.8 (s), 19.0 (br, s), 17.5 (s), 10.7 (s), 7.35 (s), 5.91 (s), 3.63 (s), 2.77 (s), 1.14 (s), -3.28 (br, s). CHN% Calc. for C₄₂H₅₂N₂ClFeO: C 72.88, H 7.57, N 4.05; Found: C 72.93, H 7.46, N 3.98. (^{Ad}dpme)FeCl(py): Several drops of pyridine were added to a stirring solution of (^{Ad}dpme)FeCl(OEt₂) (20.0 mg, 0.0288 mmol) in 2 mL benzene in a 5 mL scintillation vial. The dark red solution was stirred for 2 hours. Solvent was removed *in vacuo* to yield (^{Ad}dpme)FeCl(py) as a brown powder (20.0 mg, 99.2%). ¹H NMR (500 MHz, C₆D₆): δ/ppm 50.7 (s), 41.7 (br s), 19.3 (s), 8.5 (s), 3.3 (s), 2.1 (s), 1.3 (s), -3.16 (br s). Due to instability of THF and Et₂O adducts at high dilutions, the pyridine complex was synthesized to obtain UV/Vis data: (THF) λ_{max}/nm (ε/M⁻¹cm⁻¹) 497 (40000).

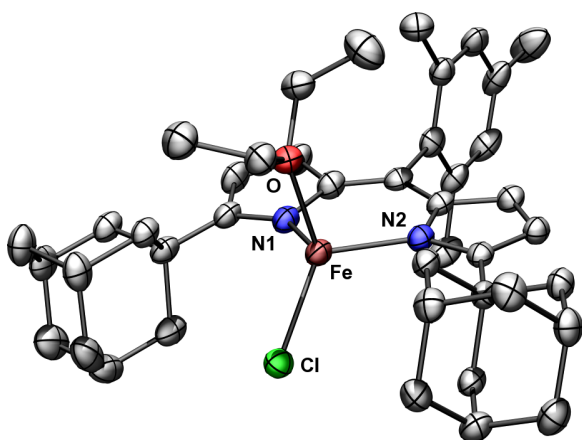


Figure 4.6. Structure of (^{Ad}dpme)FeCl(OEt₂). Thermal ellipsoids at 50% probability level. Hydrogens and an ether solvent molecule omitted for clarity.

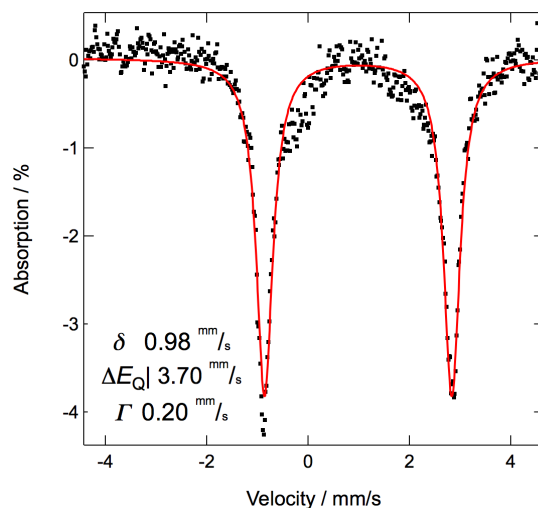
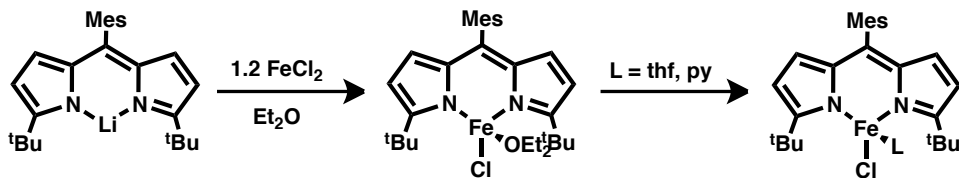


Figure 4.7. Mössbauer of (^{Ad}dpme)FeCl(OEt₂). 100 K data (black) and fit (red) using listed parameters.



(^tBu₂dpme)FeCl(L): A 100 mL oven-dried, round-bottomed flask was charged with (^tBu₂dpme)Li (2.00 g, 5.26 mmol) and 40 mL of diethyl ether. The flask was placed in a liquid nitrogen cooled cold well until frozen. FeCl₂ (0.9270 g, 7.363 mmol, 1.400 equiv.) was added to the thawing slurry of (^tBu₂dpme)Li. After stirring for 3 hours, the dark brown reaction mixture was concentrated and filtered through a medium porosity glass frit with Celite to remove excess FeCl₂ and LiCl in benzene. Removal of the solvent *in vacuo* gave a dark brown solid. The solid was washed with TMS₂O and collected on a medium porosity glass frit. (^tBu₂dpme)FeCl(OEt₂): The solid was redissolved in Et₂O and reconcentrated to give (^tBu₂dpme)FeCl(OEt₂) (1.750 g, 61.7%) as a reddish-brown solid. ¹H NMR (500 MHz, C₆D₆): δ/ppm 65.0 (s), 7.83 (s), 5.75 (s), 2.15 (s), 1.75 (s), 1.32 (s), 1.26 (s), -9.39 (br s). μ_{eff} (296 K) 5.3(1) μ_B. (^tBu₂dpme)FeCl(thf): The solid was redissolved in THF and reconcentrated to give (^tBu₂dpme)FeCl(thf) (1.265 g, 44.8%) as a dark brown solid. Crystals suitable for X-ray diffraction were grown from a hexanes/THF solution of (^tBu₂dpme)FeCl(THF). ¹H NMR (500 MHz, C₆D₆): δ/ppm 53.3 (s), 19.5 (s), 9.93 (br s), 7.77 (s), 5.16 (s), 4.58 (s), 2.95 (s), 1.92 (br s). μ_{eff} (296 K) 5.1(1) μ_B. CHN% Calc. for C₃₀H₄₀N₂ClFeO: C 67.23, H 7.52, N 5.23; Found: C 67.18, H 7.39, N 5.18. (^tBu₂dpme)FeCl(py): Several drops of pyridine were added to a stirring solution of (^tBu₂dpme)FeCl(OEt₂) (19.8 mg, 0.0374 mmol) in 2 mL benzene in a 5 mL scintillation vial. The dark red solution was stirred for 2 hours. Solvent was removed *in vacuo* to yield (^tBu₂dpme)FeCl(py) as a brown powder (19.3 mg, 94.9%). ¹H NMR (500 MHz, C₆D₆): δ/ppm 50.7 (s), 42.0 (br s), 19.4 (s), 8.50 (s), 3.32 (s), 2.14 (s), 1.30 (s), -3.18 (br s). Due to instability of THF and Et₂O adducts at high

dilutions, the pyridine complex was synthesized to obtain UV/Vis data: (THF) $\lambda_{\text{max}}/\text{nm}$ ($\epsilon/M^{-1}\text{cm}^{-1}$) 494 (59000).

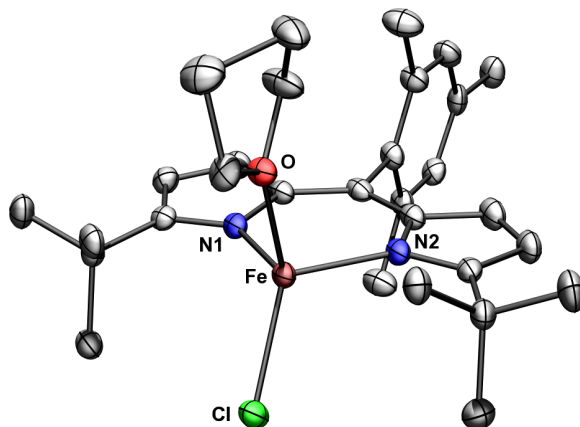
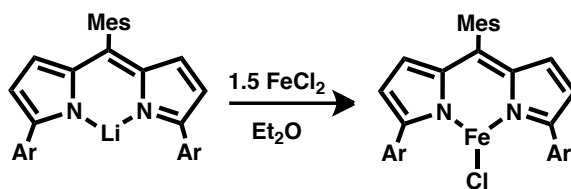


Figure 4.8. Structure of (^tBu dpme)FeCl(THF). Thermal ellipsoids at 50% probability level. One of 2 molecules present in the asymmetric unit shown. Hydrogens and THF disorder omitted for clarity.



(^{Ar}dpme)FeCl: In a 20 mL vial (^{Ar}dpme)Li (500 mg, 0.570 mmol) was dissolved in 15 mL of diethyl ether. In another 20 mL vial FeCl₂ (108 mg, 0.852 mmol, 1.49 equiv.) was slurried in 5 mL of THF. Both vials were placed in a liquid nitrogen cooled cold well until frozen. The solution of (^{Ar}dpme)Li was thawed and added to the thawing slurry of FeCl₂. The reaction was stirred at room temperature for 16 h, changing from an orange and pink slurry to a dark violet solution. The mixture was filtered through a medium porosity glass frit with Celite and washed with 15 mL diethyl ether and 30 mL benzene until the Celite was nearly colorless. Solvent was removed *in vacuo* to give a dark purple powder which was redissolved in 6 mL benzene, followed by addition of 12 mL *n*-hexane. The solution was left in the freezer (−35 °C) to recrystallize overnight. Short dark purple needles were collected, by decanting the benzene/hexane mixture and washing the crystals with hexane. Drying *in vacuo* gave (^{Ar}dpme)FeCl

(252 mg, 46.0%) as a bright purple crystalline solid. $^1\text{H NMR}$ (400 MHz, C_6D_6): δ/ppm -34.00, -20.93, -15.98, 10.42, 10.61, 10.78, 11.79, 13.99, 20.29, 25.16, 61.44, 65.56. UV/Vis (CH_2Cl_2) $\lambda_{\text{max}}/\text{nm}$ ($\epsilon/\text{M}^{-1}\text{cm}^{-1}$) 244 (58,000), 321 (14,000), 554 (26,000). μ_{eff} (295 K) 5.1(2) μ_{B} . CHN% Calc. for $\text{C}_{66}\text{H}_{49}\text{ClFeN}_2$: C 82.45, H 5.14, N 2.91; Found: C 82.38, H 5.29, N 2.75.

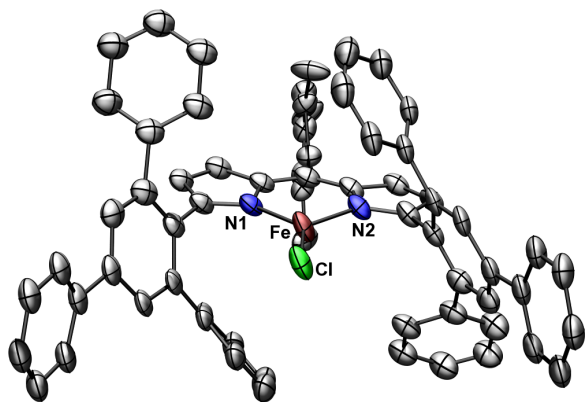


Figure 4.9. Structure of $(\text{Ar dpme})\text{FeCl}$. Thermal ellipsoids at 50% probability level. Half of the molecule is a symmetry equivalent. Aryl ring disorder and benzene solvent molecules omitted for clarity.

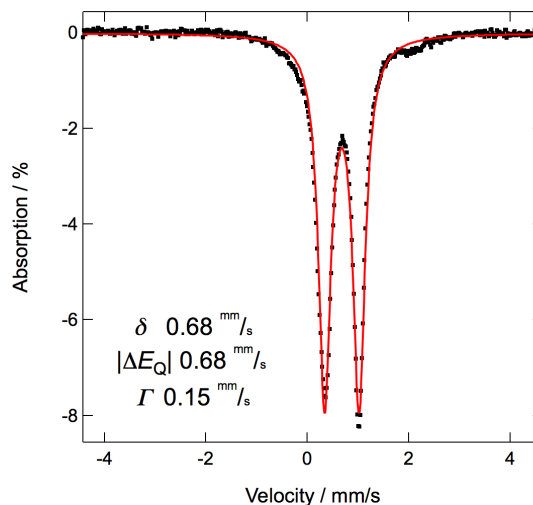
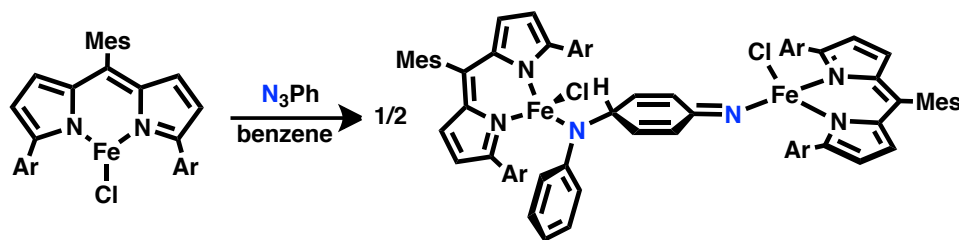


Figure 4.10. Mössbauer of $(\text{Ar dpme})\text{FeCl}$. 100 K data (black) and fit (red) using listed parameters.



$[(\text{Ar dpme})\text{FeCl}]_2(\mu\text{-NPh}(\text{C}_6\text{H}_5)\text{N})$, $[\text{Fe}^{\text{III}}]_2$: In a 20 mL vial $(\text{Ar dpme})\text{FeCl}$ (110 mg, 0.114 mmol,) was dissolved in 4 mL of benzene. In a 5 mL vial phenyl azide (13.6 mg, 0.114 mmol, 1.00 equiv.) was dissolved in 2 mL of benzene and was then added to the iron complex. The reaction was stirred for 1 h, turning from dark violet to dark purple. Addition of 12 mL *n*-hexane followed by crystallization overnight at -35°C afforded $[\text{Fe}^{\text{III}}]_2$ as black crystals (106 mg, 88.3%). UV/Vis (CH_2Cl_2) $\lambda_{\text{max}}/\text{nm}$

($\epsilon/\text{M}^{-1}\text{cm}^{-1}$) 247 (88000), 314 (21000), 528 (27000, sh), 551 (30000). μ_{eff} (295 K) 7.8(2) μ_{B} . CHN%

Calc. for $\text{C}_{144}\text{H}_{108}\text{Cl}_2\text{Fe}_2\text{N}_6$: C 82.16, H 5.17, N 3.99; Found: C 82.22, H 5.26, N 3.86.

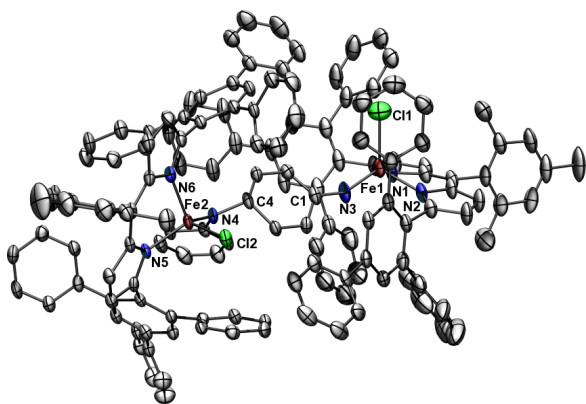


Figure 4.11. Structure of $[\text{Fe}^{\text{III}}]_2$. Thermal ellipsoids at 50% probability level. Hydrogens and benzene solvent molecules omitted for clarity.

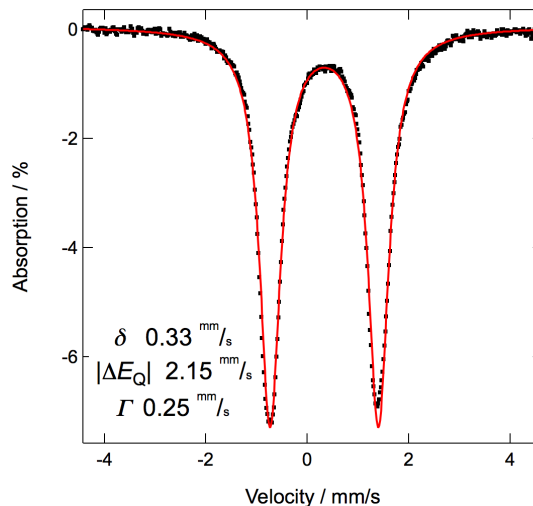
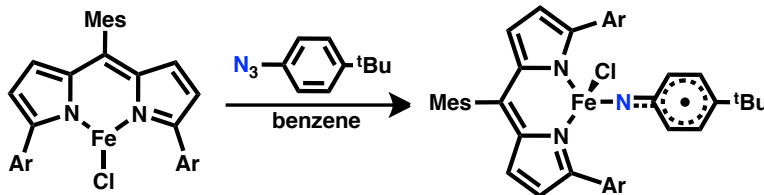


Figure 4.12. Mössbauer spectrum of $[\text{Fe}^{\text{III}}]_2$. 100 K data (black) and fit (red) using listed parameters.



$(^{\text{Ar}}\text{dpme})\text{FeCl}(\text{NAr}^{\text{tBu}})$: In a 20 mL vial $(^{\text{Ar}}\text{dpme})\text{FeCl}$ (100 mg, 0.104 mmol) was dissolved in 4 mL of benzene. In a 5 mL vial 4-*tert*-butylphenyl azide (18.3 mg, 0.104 mmol, 1.00 equiv.) was dissolved in 2 mL of benzene and was then added to the iron complex. The reaction was stirred for 1 h, turning from dark violet to dark red. The solution was frozen and benzene was removed by sublimation *in vacuo* affording $(^{\text{Ar}}\text{dpme})\text{FeCl}(\text{NAr}^{\text{tBu}})$ (105.6 mg, 95.3%) as a dark purple powder. Crystals suitable for X-ray diffraction were grown from a concentrated *n*-pentane solution at $-35\text{ }^\circ\text{C}$. ^1H NMR (400 MHz, C_6D_6): δ/ppm $-17.14, 0.46, 1.97, 5.73, 5.86, 6.20, 7.10, 7.42, 7.67, 10.27, 10.83, 27.48, 38.19, 60.17$. UV/Vis

(CH₂Cl₂) $\lambda_{\text{max}}/\text{nm}$ ($\epsilon/\text{M}^{-1}\text{cm}^{-1}$) 247 (73000), 323 (17000), 377 (15000), 553 (26000). μ_{eff} (295 K) 5.3(1) μ_{B} . CHN% Calc. for C₇₆H₆₂Cl₂FeN₃: C 82.34, H 5.64, N 3.79; Found: C 82.32, H 5.58, N 3.73.

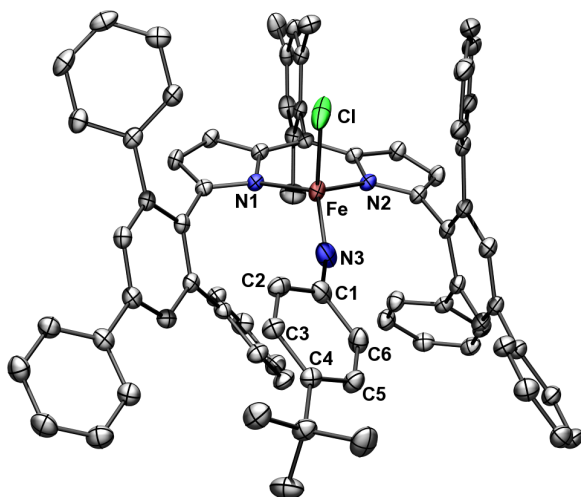


Figure 4.13. Structure of (^{Ar}dpme)FeCl(NAr^{tBu}). Thermal ellipsoids at 50% probability level. Hydrogens and a pentane solvent molecule omitted for clarity.

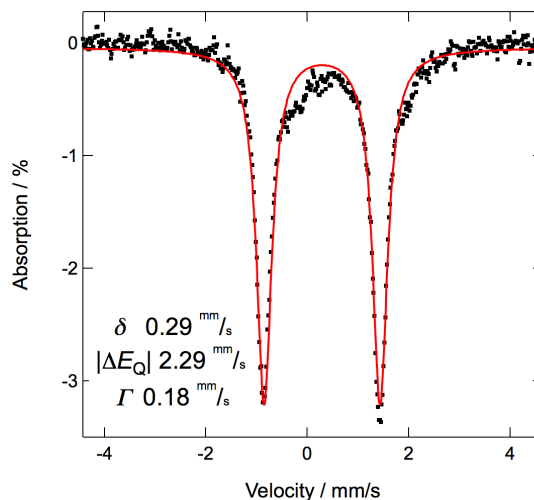


Figure 4.14. Mössbauer spectrum of (^{Ar}dpme)FeCl(NAr^{tBu}). 100 K data (black) and fit (red) using listed parameters.

Reactivity and Catalysis Experiments.

Determination of Intermolecular Primary Kinetic Isotope Effect for C–H Insertion Reactions

via Competition Experiments. Under an inert N₂ atmosphere, 1-azidoadamantane (51.0 mg, 0.288 mmol, 10.0 equiv.) was added to a stirring solution of (^{Ad}dpme)FeCl(OEt₂) (20.0 mg, 0.0288 mmol) in an equimolar mixture of toluene (540 mg, 5.43 mmol) and toluene-*d*₈ (500 mg, 5.43 mmol) in a pressure vessel. After heating for 12 hours at 60 °C, an aliquot of the solution (0.05 mL) was diluted with 20 mL MeOH and analyzed by LC/MS. Comparison of the area of the selected ion recording (SIR) of the formed proteo/deutero amine products ($A_{\text{H}}/A_{\text{D}}$) were equated to $k_{\text{H}}/k_{\text{D}}$ to give a value of 12.8(5). Three runs were performed to obtain the reported value and the calculated standard deviation.

Yield Determination of Catalytic Amination Reactions with 1-Adamantyl Azide using LC/MS.

Under an inert N₂ atmosphere, 1-adamantyl azide (35.4 mg, 0.200 mmol, 20.0 equiv.) was added to a

stirring solution of (^{Ad}dpme)FeCl(OEt₂) (6.9 mg, 0.010 mmol) in 1 mL of toluene in a sealed pressure vessel. The resultant inky, dark red solution reacted for 12 hours at the specified temperature. The pressure vessel was then cooled and an LC/MS sample of this solution was prepared for yield determination. The solution was diluted to 10 mL with MeOH. An aliquot (0.1 mL) of this solution was diluted to 10 mL with MeOH and analyzed by LC/MS. A series of standard samples composed of a 1:1:1 molar ratio of PhCH₂NHAd:PhCHNAd:AdNH₂ with concentrations ranging from 3x10⁻⁸ to 1x10⁻⁴ M were run prior to each set of experiments to establish a calibration curve. Peak areas of the formed products were compared to the calibration curve and gave the turnover numbers and product distributions reported in the table below.

Yield Determination of Catalytic Amination Reactions with 1-Adamantyl Azide using ¹H NMR.

Under an inert N₂ atmosphere, 1-adamantyl azide (35.4 mg, 0.200 mmol, 20 equiv.) was added to a stirring solution of (^{Ad}dpme)FeCl(OEt₂) (6.9 mg, 0.010 mmol) and ferrocene (1.9 mg, 0.010 mmol, 1.0 equiv.) in 1 mL of toluene in a sealed pressure vessel. The resultant inky, dark red solution reacted for 12 hours at the specified temperature. The pressure vessel was then cooled and the solvent was removed *in vacuo*. The resulting dark brown oil was dissolved in a 20:1 mixture of CH₂Cl₂ and MeOH and flash chromatographed through a short pipette of deactivated silica gel to give a clear bright orange solution. ¹H NMR yields were determined via integration against ferrocene and are reported in the table below.

Yield Determination of Catalytic Aziridination Reactions with 1-Adamantyl Azide using ¹H NMR. Under an inert N₂ atmosphere, 1-adamantyl azide (51.0 mg, 0.288 mmol, 20.0 equiv.) was added to a stirring solution of (^{Ad}dpme)FeCl(OEt₂) (10.0 mg, 0.0144 mmol) and the internal standard ferrocene (2.7 mg, 0.014 mmol, 1 equiv.) in 1 mL of styrene in a 20 mL scintillation vial. The resultant inky, dark red solution was stirred for 12 hours at 25 °C. The solvent was removed *in vacuo*. The resulting dark brown oil was dissolved in a 20:1 mixture of CH₂Cl₂ and MeOH and flash

chromatographed through a short pipette of silica gel to give a clear bright orange solution. The crude ^1H NMR yields were determined via integration against ferrocene to be 85% (based on azide, averaged over two runs).

Yield Determination of Catalytic Amination Reactions with 1-Adamantyl Azide and ($^{\text{tBu}}\text{dpme}$)FeCl(thf) using ^1H NMR. Under an inert N_2 atmosphere, 1-adamantyl azide (35.4 mg, 0.200 mmol, 20.0 equiv.) was added to a stirring solution of ($^{\text{tBu}}\text{dpme}$)FeCl(thf) (5.4 mg, 0.010 mmol) and ferrocene (1.9 mg, 0.010 mmol, 1.0 equiv.) in 1 mL of toluene in a sealed pressure vessel. The resultant inky, dark red solution reacted for 12 hours at 60 °C. The pressure vessel was then cooled and the solvent was removed *in vacuo*. The resulting dark brown oil was dissolved in a 20:1 mixture of CH_2Cl_2 and MeOH and flash chromatographed through a short pipette of deactivated silica gel to give a clear bright orange solution. ^1H NMR yields were determined via integration against ferrocene and a TON of 5.6 was established.

Catalytic Amination Reactions with 1-Adamantyl Azide in the Presence of THF Scavenger. Under an inert N_2 atmosphere, 1-adamantyl azide (35.4 mg, 0.200 mmol, 20.0 equiv.) was added to a stirring solution of ($^{\text{tBu}}\text{dpme}$)FeCl(thf) (10 mg, 0.019 mmol), ferrocene (3.5 mg, 0.019 mmol, 1.0 equiv.) and the Lewis acid $\text{B}(\text{C}_6\text{F}_5)_3$ (9.7 mg, 0.019 mmol, 1.0 equiv.) in 1 mL of toluene in a sealed pressure vessel. The resultant inky, dark red solution reacted for 12 hours at the specified temperature. The pressure vessel was then cooled and the solvent was removed *in vacuo*. The resulting dark brown oil was dissolved in a 20:1 mixture of CH_2Cl_2 and MeOH and flash chromatographed through a short pipette of deactivated silica gel to give a clear bright orange solution. ^1H NMR yields were determined via integration against ferrocene and a TON of 4.6 was established.

Product Inhibition in Catalytic Amination Reactions. Under an inert N_2 atmosphere, 1-adamantyl azide (35.4 mg, 0.200 mmol, 20.0 equiv.) was added to a stirring solution of

(^{Ad}dpme)FeCl(OEt₂) (6.9 mg, 0.010 mmol), ferrocene (1.9 mg, 0.010 mmol, 1.0 equiv.), and benzyl adamantylamine (36.3 mg, 0.150 mmol, 15.0 equiv.) in 1 mL of toluene in a sealed pressure vessel. The resultant inky, dark red solution reacted for 12 hours at the specified temperature. The pressure vessel was then cooled and the solvent was removed *in vacuo*. The resulting dark brown oil was dissolved in a 20:1 mixture of CH₂Cl₂ and MeOH and flash chromatographed through a short pipette of deactivated silica gel to give a clear bright orange solution. No additional benzyl adamantylamine was formed as determined by ¹H NMR.

Adamantyl Amine Inhibition in Catalytic Amination Reactions. Under an inert N₂ atmosphere, 1-adamantyl azide (35.4 mg, 0.200 mmol, 20.0 equiv.) was added to a stirring solution of (^{Ad}dpme)FeCl(OEt₂) (6.9 mg, 0.010 mmol), ferrocene (1.9 mg, 0.010 mmol, 1.0 equiv.), and adamantylamine (15.1 mg, 0.100 mmol, 10 equiv.) in 1 mL of toluene in a sealed pressure vessel. The resultant inky, dark red solution reacted for 12 hours at the specified temperature. The pressure vessel was then cooled and the solvent was removed *in vacuo*. The resulting dark brown oil was dissolved in a 20:1 mixture of CH₂Cl₂ and MeOH and flash chromatographed through a short pipette of deactivated silica gel to give a clear bright orange solution. No benzyl adamantylamine was formed as determined by ¹H NMR.

Addition of 1,4-Cyclohexadiene. A J. Young tube was charged with either (^{Ar}dpme)FeCl(NAr^{tBu}) or [Fe^{III}]₂ (10.0 mg) and 1 mL dichloromethane-*d*₂. 1,4-Cyclohexadiene (5 equiv.) was dissolved in 0.5 mL dichloromethane-*d*₂ and then transferred to the J. Young tube, which was closed and mixed. ¹H NMR (400 MHz, CD₂Cl₂) after 5 min showed resonances for both benzene (δ/ppm 7.36) and 1,4-cyclohexadiene (δ/ppm 2.66, 5.69).

Addition of Dimethylphenylphosphine. A J. Young tube was charged with (^{Ar}dpme)FeCl(NAr^{tBu}) (10.0 mg) and 1 mL benzene-*d*₆. Two equivalents Me₂PhP were added as a 1% *w/w* stock solution in

benzene-*d*₆. The tube was sealed and mixed. Formation of the phosphinimide, Me₂PhP=N(C₆H₄-*p*-^tBu) was confirmed by ³¹P NMR (160 MHz, C₆D₆) which showed a single peak at 2.79 ppm and disappearance of phosphine at -45.46 ppm. The chemical shift of the phosphinimide product was confirmed by independent synthesis directly from the reaction of Me₂PhP and N₃(C₆H₄-*p*-^tBu) in benzene-*d*₆.

General Procedure for C–H Insertion from (Ar^{dpme})FeCl. A 5 mL vial was charged with a stir bar, (Ar^{dpme})FeCl (10.0 mg), and 1 mL toluene-*d*₈. 1-Azido-4-*tert*-butylbenzene or 1-azidobenzene (1 equiv.) was added as a 1% *w/w* solution in toluene-*d*₈. The mixture stirred for 1 h and was then transferred to a J. Young tube. Conversion of (Ar^{dpme})FeCl to (Ar^{dpme})FeCl(NAr^{tBu}) or [Fe^{III}]₂ was confirmed by ¹H NMR. The tube was heated to 85 °C in an oil bath for 2 h. Consumption of (Ar^{dpme})FeCl(NAr^{tBu}) or [Fe^{III}]₂ was confirmed by ¹H NMR, and formation of the C–H insertion products was confirmed by HRMS: (ESI⁺) *m/z* (C₆D₅)CD₂NH(C₆H₄-*p*-^tBu) Calc. [C₁₇H₁₄D₇N+H]⁺ 247.2184, Found 247.2180 [M+H]⁺; (C₆D₅)CD₂NH(C₆H₅) Calc. [C₁₃H₆D₇N+H]⁺ 191.1558, Found 191.1560 [M+H]⁺.

Computational Methods.

Computations were carried out utilizing the ORCA 2.7³⁷ program package. The B3LYP⁴⁹ functional was used with the def2-TZVP (Fe, N, Cl) and def2-SV(P) (C, H) basis sets.⁵⁰ For single point calculations and property calculations the def2-TZVP/J (Fe, N, Cl) and def2-SVP/J (C, H) auxiliary basis sets⁵¹ were employed to utilize the RIJCOSX⁵² approximation for accelerating the calculation. For

(49) (a) Becke, A. D. *J. Chem. Phys.* **1993**, *98*, 5648-5652. (b) Lee, C. T.; Yang, W. T.; Parr, R. G. *Phys. Rev. B: Solid State* **1988**, *37*, 785-789.

(50) (a) Schäfer, A.; Horn, H.; Ahlrichs, R. *J. Chem. Phys.* **1992**, *97*, 2571-2577. (b) Schäfer, A.; Huber, C.; Ahlrichs, R. *J. Chem. Phys.* **1994**, *100*, 5829-5835. (c) Weigend, F.; Ahlrichs, R. *Phys. Chem. Chem. Phys.* **2005**, *7*, 3297-3305.

(51) Weigend, F. *Phys. Chem. Chem. Phys.* **2006**, *8*, 1057-1065.

(52) Neese, F.; Wennmohs, F.; Hansen, A.; Becker, U. *Chem. Phys.* **2009**, *356*, 98-109.

the calculation of Mössbauer parameters the basis set at Fe was expanded to the CP(PPP) basis.⁵³ The ^{Ar}dpme ligand was approximated as 1,5,9-triphenyldipyrromethene, ^{Ph}dpme'. Geometries were taken from X-ray structures and truncated by replacing –Ph or –Me with –H where appropriate.

Table 4.5. Equations for computationally determined Mössbauer parameters.

$$\Delta E_Q = \frac{1}{2} eQV_{zz} \sqrt{1 + \frac{1}{3}\eta^2} \quad (4.1)$$

$$\delta = a(\rho_0 - C) + b \quad (4.2)$$

Mössbauer. Mössbauer parameters were obtained from additional single point calculations, following methods described by F. Neese.^{36,54} Quadrupole splittings (ΔE_Q) were calculated from the electric field gradient, Eq. 4.1. The nuclear quadrupole moment $Q(^{57}\text{Fe})$ was taken to be 0.16 barn.⁵⁴ The principal tensor components of the EFG are V_{xx} , V_{yy} , and V_{zz} , from which the asymmetry parameter $\eta = (V_{xx} - V_{yy})/V_{zz}$ can be defined. Isomer shifts (δ) were calculated from the electron density at the nucleus ρ_0 , using a linear equation, Eq. 4.2,⁵⁴ with constants determined by fitting the calculated densities to experimental isomer shifts for a series of dipyrromethane, dipyrromethene, and tripyrroethane complexes synthesized in our lab.⁵⁵ The basis sets and functional described above were used for all structures. X-ray coordinates were used, and spin states were assigned based on magnetic measurements and experimental Mössbauer data. For this series of compounds the parameters were determined to be $C = 11797.145 \text{ au}^{-3}$, $a = -0.402 \text{ au}^3 \text{ mm s}^{-1}$, and $b = 8.605 \text{ mm}$. The maximum disagreement between calculated and experimental isomer shift was 0.05 mm s^{-1} .

(53) Neese, F. *Inorg. Chim. Acta* **2002**, 337, 181-192.

(54) Sinnecker, S.; Slep, L. D.; Bill, E.; Neese, F. *Inorg. Chem.* **2005**, 44, 2245-2254.

(55) Compounds used for the calibration of δ to ρ_0 : (^{Me}dpme)FeCl(thf) (King, E. R.; Betley, T. A. *Inorg. Chem.* **2009**, 48, 2361-2363.); (dpma)Fe(py)₂, (dpma)Fe(bpy) (King, E. R.; Betley, T. A. *J. Am. Chem. Soc.* **2009**, 131, 14374-14380.); (tpe)Fe(py)¹⁻ (Sazama, G. T.; Betley, T. A. *Inorg. Chem.* **2010**, 49, 2512-2524.); (^{tBu}dpme)FeCl(thf), (^{Ad}dpme)FeCl(OEt₂), (^{Ar}dpme)FeCl (King, E. R.; Hennessy, E. T.; Betley, T. A. *J. Am. Chem. Soc.* **2011**, 133, 4917-4923. (tpe = tris(2-mesitylpyrrolyl)ethane).

Broken Symmetry Model of 4. A broken symmetry solution was used to model the antiferromagnetically coupled Fe^{III} imide radical. The broken symmetry notation BS(*m,n*)⁵⁶ refers to a system with (*m+n*) unpaired electrons, and a net spin of (*m-n*)/2 (if antiferromagnetically coupled). One fragment will bear *m* α spin electrons, and the other fragment *n* β spin electrons. For the Fe^{III} imide radical, (Ph₃dpme')FeCl(NAr^{tBu}) (the truncated analog of (Ar₃dpme)FeCl(NAr^{tBu})), BS(5,1) was the appropriate description for a high-spin Fe^{III} (*S* = 5/2) coupled to a imide radical (*S* = 1/2). The corresponding orbital transformation,⁵⁶ and the resultant corresponding orbital overlap were used as an indicator of a spin-coupled system. One pair of corresponding orbitals (**Figure 4.4**) had overlap of 0.59, which is significantly less than 1, and suggests a broken symmetry solution. The broken symmetry solution (BS(5,1), $E_{BS} = -3315.28806 E_h$) was found to have the same energy as the unrestricted quintet (*S* = 2, $E = -3315.28800 E_h$). The exchange coupling constant *J* was determined from the energy difference between the high-spin (*S* = 3, $E_{HS} = -3315.27162 E_h$) and broken symmetry states, using the spin Hamiltonian in Eq. 4.3, and the formula in Eq. 4.4.⁵⁷ Based on the energy difference of $E_{HS} - E_{BS} = 3610 \text{ cm}^{-1}$, the antiferromagnetic coupling constant is estimated to be $J = -673 \text{ cm}^{-1}$.

Table 4.6. Equations for calculation of Broken Symmetry Energies and Couplings.

$$\mathbf{H} = -2J\vec{\mathbf{S}}_{Fe} \cdot \vec{\mathbf{S}}_{NR} \quad (4.3)$$

$$J = -\frac{E_{HS} - E_{BS}}{\langle S^2 \rangle_{HS} - \langle S^2 \rangle_{BS}} \quad (4.4)$$

(56) Kirchner, B.; Wennmohs, F.; Ye, S. F.; Neese, F. *Curr. Opin. Chem. Biol.* **2007**, *11*, 134-141.

(57) (a) Yamaguchi, K.; Takahara, Y.; Feuono, T. In *Applied Quantum Chemistry: Proceedings of the Nobel Laureate Symposium on Applied Quantum Chemistry in Honor of G. Herzberg*, R.S. Mulliken, K. Fukui, W. Lipscomb, and R. Hoffman, Honolulu, HI, 16-21 December 1984; Herzberg, G., Smith, V. H., Schaefer, H. F., Morokuma, K., Eds.; D. Reidel: Dordrecht, the Netherlands, 1986, p 155. (b) Soda, T.; Kitagawa, Y.; Onishi, T.; Takano, Y.; Shigeta, Y.; Nagao, H.; Yoshioka, Y.; Yamaguchi, K. *Chem. Phys. Lett.* **2000**, *319*, 223-230.

X-ray Diffraction Techniques.

All structures were collected on a Brüker three-circle platform goniometer equipped with an Apex II CCD and an Oxford cryostream cooling device. Radiation was from a graphite fine focus sealed tube Mo K α (0.71073 Å) source. Crystals were mounted on a cryoloop or glass fiber pin using Paratone N oil. Structures were collected at 100 K. Data was collected as a series of φ and/or ω scans. Data was integrated using SAINT⁵⁸ and scaled with either a numerical or multi-scan absorption correction using SADABS.⁵⁸ The structures were solved by direct methods or Patterson maps using SHELXS-97⁵⁹ and refined against F^2 on all data by full matrix least squares with SHELXL-97.⁵⁹ All non-hydrogen atoms were refined anisotropically. Hydrogen atoms were placed at idealized positions and refined using a riding model. The isotropic displacement parameters of all hydrogen atoms were fixed to 1.2 times U of the atoms they are linked to (1.5 times for methyl groups). Further details on particular structures are noted below.

(^{tbu}dpme)FeCl(THF): The structure was solved in the triclinic space group $P\bar{1}$ with 4 molecules per unit cell. There were 2 equivalent molecules in the asymmetric unit. One of the bound THF molecules exhibited minor disorder.

(^{Ad}dpme)FeCl(OEt₂): The structure was solved in the monoclinic space group $P2_1/n$ with 4 molecules per unit cell. There was an additional molecule of uncoordinated diethyl ether present in the asymmetric unit.

^{Ar}dpmeH: The structure was solved in the triclinic space group $P\bar{1}$ with 2 molecules per unit cell. There was a single molecule of benzene present in the asymmetric unit. The acidic N–H hydrogen was picked from the Fourier map and refined semi-freely by restraining the N–H distance to 0.88 Å (the

(58) APEX2 Software Suite; Brüker AXS: Madison, WI, 2009.

(59) (a) Sheldrick, G. M. *Acta Crystallogr., Sect. A: Found. Crystallogr.* **2008**, *64*, 112-122. (b) Sheldrick, G. M. *SHELX-97*; University of Göttingen: Göttingen, Germany, 1997.

average effective distance for sp^2 N–H bonds at $-173\text{ }^\circ\text{C}$), and by setting the isotropic displacement parameter to 1.2 times that of the nitrogen atom.

(^{Ar}dpme)FeCl: The structure was solved in the monoclinic space group $C2/c$ with 4 molecules per unit cell, and half of the molecule in the asymmetric unit. The Fe and Cl atoms lie on a crystallographic mirror plane. Two of the phenyl rings exhibited disorder which was modeled by addition of a second position for each ring. The mesityl ring lies about a mirror plane and was modeled with all atoms at half-occupancy, with the second position being generated by symmetry. There were 2 benzene sites in the structure, one on a mirror plane, and the second exhibiting significant disorder, which could not be modeled as multiple positions but was improved by allowing partial occupancy (0.775). The difficulty of accurately modeling the disordered solvent molecules is the reason for the higher than usual R values but does not seriously affect the chemically significant features of the structure.

[(^{Ar}dpme)FeCl]₂(μ -NPh(C₆H₅)N), [Fe^{III}]₂: The structure was solved in the triclinic space group $P\bar{1}$ with 2 molecules per unit cell. There were four molecules of benzene present in the asymmetric unit. There were also residual density peaks corresponding to 2 molecules of *n*-hexane. Due to apparent low occupancy and high disorder of the hexane, an acceptable model could not be refined. Instead the hexanes were treated as diffuse contributors to the scattering using the SQUEEZE option in the PLATON⁶⁰ package. Similarity and rigid bond restraints of the anisotropic displacement parameters were placed on all atoms.

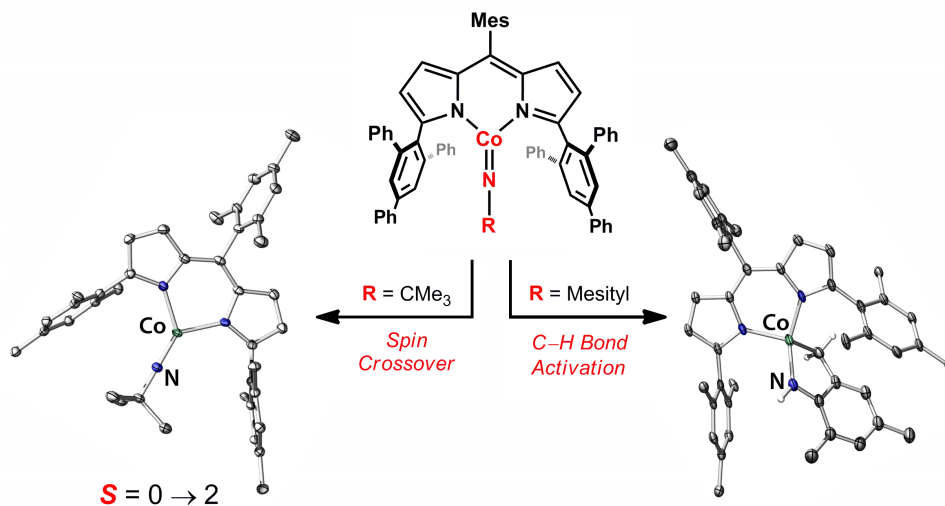
(^{Ar}dpme)FeCl(NAr^{tBu}): The structure was solved in the monoclinic space group $P2_1/c$ with 4 molecules per unit cell. There was a single molecule of *n*-pentane present in the asymmetric unit.

(60) Spek, A. L. *Acta Crystallogr., Sect. D: Bio. Crystallogr.* **2009**, *65*, 148-155.

Table 4.7. X-ray diffraction experimental details.^{a,b}

	^(tBu) dpme)FeCl(THF)	^(Ad) dpme)FeCl(OEt ₂)	^(Ar) dpme)H	^(Ar) dpme)FeCl	[Fe ^{III}] ₂	^(Ar) dpme)FeCl(NAr ^{tBu})
CCDC Deposit Number	791228	791229	792018	792019	792020	792021
Moiety Formula	C ₃₀ H ₄₁ ClFeN ₂ O	C ₄₂ H ₅₅ ClFeN ₂ O; C ₄ H ₁₀ O	C ₆₆ H ₅₀ N ₂ ; 3×(C ₆ H ₆)	C ₆₆ H ₄₉ ClFeN ₂ ; 2.55×(C ₆ H ₆)	C ₁₄₄ H ₁₀₈ Cl ₂ Fe ₂ N ₆ ; 4×(C ₆ H ₆)	C ₇₆ H ₆₂ ClFeN ₃ ; C ₅ H ₁₂
FW	536.95	769.3	1105.4	1160.64	2417.4	1180.73
Crystal System	triclinic	monoclinic	triclinic	monoclinic	triclinic	monoclinic
Space Group (Z)	<i>P</i> $\bar{1}$ (4)	<i>P</i> 2 ₁ /n (4)	<i>P</i> $\bar{1}$ (2)	<i>C</i> 2/c (4)	<i>P</i> $\bar{1}$ (2)	<i>P</i> 2 ₁ /c (4)
a (Å)	14.2661(5)	14.497(3)	12.5350(5)	15.840(5)	14.4691(12)	21.0117(10)
b (Å)	15.0088(5)	16.196(3)	13.6512(6)	21.273(7)	21.4975(18)	12.2392(6)
c (Å)	15.1843(5)	18.331(3)	20.4250(8)	19.136(9)	23.560(2)	25.0442(12)
α (°)	91.591(2)	90	75.509(2)	90	94.3420(10)	90
β (°)	99.021(2)	106.605(3)	85.664(2)	108.066(5)	93.7780(10)	91.1800(10)
γ (°)	115.438(2)	90	65.022(2)	90	102.9270(10)	90
Volume (Å³)	2883.16(17)	4124.4(13)	3065.6(2)	6130(4)	7096.1(10)	6439.2(5)
Calc. ρ (mg/m³)	1.237	1.239	1.198	1.258	1.131	1.218
μ (mm⁻¹)	0.640	0.470	0.068	0.338	0.295	0.323
Crystal Size (mm)	0.24×0.18×0.12	0.42×0.31×0.22	0.82×0.43×0.39	0.7×0.17×0.07	0.32×0.32×0.06	0.4×0.3×0.16
Reflections	20840	62277	41971	30219	120338	135338
Comp. (%) to 2θ	99.7% (27.52°)	99.6% (25.79°)	99.9% (26.37°)	100.0% (27.10°)	99.9% (26.79°)	100.0% (27.48°)
GOF on F²	1.018	1.008	1.022	1.000	0.878	1.041
R1, wR2^c [I > 2σ(I)]	0.0425, 0.1029	0.0525, 0.1202	0.0426, 0.1042	0.0859, 0.2152	0.0563, 0.1267	0.0423, 0.0954
Rindices [all] (R1, wR2)	0.0692, 0.1154	0.1005, 0.1471	0.0564, 0.1138	0.2403, 0.3056	0.1253, 0.1449	0.0645, 0.1074

^a λ = 0.71073 Å^b T = 100(2) K^c R1 = Σ||F_o| - |F_c||/Σ|F_o|, wR2 = {Σ[w(F_o² - F_c²)²]/Σ[w(F_o²)²]}^{1/2}



Chapter 5: Cobalt Imides Exhibiting Spin Crossover and C–H bond Activation¹

5-1. Introduction.

The principle interest in constructing complexes featuring metal-ligand multiple bonds is the premise that the terminal functionality may be transferred to unreactive substrates (e.g., olefins, C–H bonds).² A key determining factor for the reactivity of the multiply bonded functionality is the electronic structure of the transition metal ion to which it is bonded. Low-spin electronic configurations engender stability, whereas open shell configurations may populate the metal-ligand multiple bond antibonding orbitals, thereby producing a reactive species for atom or group transfer processes. While the ligand field strength of the metal-ligand multiple bond is inherent, utilizing weak field ancillary ligands may permit high-spin configurations. This electronic structure-to-reactivity relationship has been most heavily scrutinized in

(1) This chapter was adapted with permission from King, E. R.; Betley, T. A. *J. Am. Chem. Soc.* **2012**, *submitted*. Unpublished work Copyright 2012 American Chemical Society.

(2) Mayer Nugent, W. A.; Mayer, J. M. *Metal-Ligand Multiple Bonds: The Chemistry of Transition Metal Complexes Containing Oxo, Nitrido, Imido, Alkylidene, or Alkylidyne Ligands*; Wiley: New York, 1988.

high-valent Fe oxo chemistry.³ Within this family of complexes, the degree to which the Fe oxo is destabilized is governed by population of the Fe–O antibonding orbitals of σ and π character. Unlike the Fe oxo precedent, nearly all Co coordination compounds featuring a metal-ligand multiple bond feature low-spin ground states,^{4,5} producing inert complexes. The lone exception is Theopold's (Tp*)Co^{III}NAd which undergoes radical decomposition at higher temperatures where a thermally accessible high-spin configuration is invoked.⁶ Transient cobalt imides have been implicated in hydrogen atom abstraction reactions based on characterization of the resulting amides,⁷ but their spin states are unknown. We report herein the synthesis of Co^{III} imide complexes featuring the weak field dipyrinato platform that undergo thermal spin crossover and can effect C–H bond activation.

We have demonstrated the ability of the weakly donating dipyrin platform to stabilize low coordinate iron complexes in high-spin configurations.^{8,9,10} The sterically encumbered derivative **Ar^{tr}dpmeH**, 5-mesityl-1,9-(2,4,6-triphenylphenyl)dipyrromethene, in particular stabilized a three-coordinate Fe^{II} chloride species, and allowed for isolation of a reactive Fe^{III} imide radical species following treatment of the Fe^{II} chloride with an aryl azide.⁹ The imide radical is capable of stoichiometric C–H bond amination and styrene aziridination, while less bulky versions of the dipyrin ligand rendered

(3) (a) *Cytochrome P450 : Structure, Mechanism, and Biochemistry*; 4th ed.; Ortiz de Montellano, P. R., Ed.; Kluwer Academic/Plenum Publishers: New York, 2005. (b) Krebs, C.; Fujimori, D. G.; Walsh, C. T.; Bollinger, J. M. *Acc. Chem. Res.* **2007**, *40*, 484-492. (c) Ye, S. F.; Neese, F. *Curr. Opin. Chem. Biol.* **2009**, *13*, 89-98. (d) Que, L., Jr. *Acc. Chem. Res.* **2007**, *40*, 493-500. (e) Nam, W. *Acc. Chem. Res.* **2007**, *40*, 522-531.

(4) (a) Jenkins, D. M.; Betley, T. A.; Peters, J. C. *J. Am. Chem. Soc.* **2002**, *124*, 11238-11239. (b) Betley, T. A.; Peters, J. C. *J. Am. Chem. Soc.* **2004**, *126*, 6252-6254. (c) Hu, X. L.; Meyer, K. *J. Am. Chem. Soc.* **2004**, *126*, 16322-16323. (d) Mehn, M. P.; Brown, S. D.; Jenkins, D. M.; Peters, J. C.; Que, L., Jr. *Inorg. Chem.* **2006**, *45*, 7417-7427. (e) Cowley, R. E.; Bontchev, R. P.; Sorrell, J.; Sarracino, O.; Feng, Y. H.; Wang, H. B.; Smith, J. M. *J. Am. Chem. Soc.* **2007**, *129*, 2424-2425.

(5) (a) Dai, X. L.; Kapoor, P.; Warren, T. H. *J. Am. Chem. Soc.* **2004**, *126*, 4798-4799. (b) Jones, C.; Schulten, C.; Rose, R. P.; Stasch, A.; Aldridge, S.; Woodul, W. D.; Murray, K. S.; Moubaraki, B.; Brynda, M.; La Macchia, G.; Gagliardi, L. *Angew. Chem., Int. Ed.* **2009**, *48*, 7406-7410.

(6) Shay, D. T.; Yap, G. P. A.; Zakharov, L. N.; Rheingold, A. L.; Theopold, K. H. *Angew. Chem., Int. Ed.* **2005**, *44*, 1508-1510.

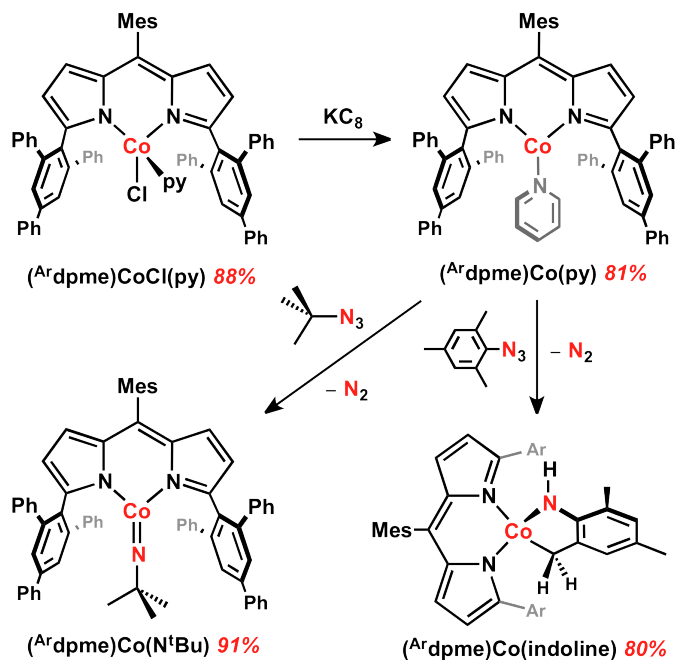
(7) (a) Thyagarajan, S.; Shay, D. T.; Incarvito, C. D.; Rheingold, A. L.; Theopold, K. H. *J. Am. Chem. Soc.* **2003**, *125*, 4440-4441. (b) Chomitz, W. A.; Arnold, J. *Chem. Commun.* **2008**, 3648-3650.

(8) King, E. R.; Betley, T. A. *Inorg. Chem.* **2009**, *48*, 2361-2363.

(9) King, E. R.; Hennessy, E. T.; Betley, T. A. *J. Am. Chem. Soc.* **2011**, *133*, 4917-4923.

(10) Scharf, A. B.; Betley, T. A. *Inorg. Chem.* **2011**, *50*, 6837-6845.

the nitrene transfer reaction catalytic.⁹ We hypothesized that use of the sterically encumbered dipyrin ligands with Co might similarly lead to open shell configurations with metal-ligand multiple bonded functionalities, rendering these typically inert complexes reactive for imide group transfer.



Scheme 5.1. Synthesis of (Ar dpme)Co(py), (Ar dpme)Co(N^tBu), and (Ar dpme)Co(indoline).

5-2. Synthesis and Characterization of Dipyrromethene Cobalt Complexes.

Metallation of the dipyrin platform **Ar dpmeH** with cobalt followed directly from the protocols previously reported to prepare the iron congeners.⁹ Following lithiation with phenyl lithium in benzene, (Ar dpme)Li was transmetallated using the cobalt dichloride bis-pyridine adduct¹¹ to afford the dark maroon pyridine complex (Ar dpme)CoCl(py). The product (Ar dpme)CoCl(py) exhibits a paramagnetically shifted ¹H NMR and a solution magnetic moment of 4.2(1) μ_B (C_6D_6 , 295 K), consistent with a quartet ground state. While the ferrous analog (Ar dpme)FeCl remains three-

(11) Allan, J. R.; Brown, D. H.; Nuttall, R. H.; Sharp, D. W. A. *J. Chem. Soc. A* **1966**, 1031-1034.

coordinate in the solid state,⁹ the presence of pyridine bound to the Co ion was confirmed by structural elucidation (see **Figure 5.4**) which shows a trigonal monopyramidal geometry at Co. Chemical reduction of (**Ar**dpme)CoCl(py) with KC₈ in benzene at room temperature cleanly produced the isolable Co^I pyridine adduct (**Ar**dpme)Co(py) as a purple solid. Conversion of (**Ar**dpme)CoCl(py) to (**Ar**dpme)Co(py) was ascertained by ¹H NMR. Like (**Ar**dpme)CoCl(py), complex (**Ar**dpme)Co(py) gives a paramagnetically shifted ¹H NMR spectrum with a solution magnetic moment of 2.9(1) μ_B (C₆D₆, 295 K), consistent with a triplet ground state. SQUID magnetometry on (**Ar**dpme)Co(py) (see **Figure 5.14a**) gives a room temperature χ_MT of 1.07 cm³ K/mol (μ_{eff} 2.94(2) μ_B), corroborating this assignment. The molecular structure of (**Ar**dpme)Co(py) as determined by single crystal X-ray diffraction is shown in **Figure 5.1a**, confirming chloride loss and revealing a trigonal planar geometry for the three-coordinate Co. With a suitable Co^I synthon in hand, we sought to examine its reactivity with two-electron group transfer reagents.

Addition of ^tBuN₃ to (**Ar**dpme)Co(py) shows rapid consumption of the azide and produced two new paramagnetic species as ascertained by ¹H NMR. The minor product contained in the spectrum could be made exclusively by addition of two equivalents of azide, leading us to assign it as the tetrazene complex (**Ar**dpme)Co(κ²-^tBuNNNN^tBu). Crystals of this complex were grown from diethyl ether and confirmed the structure as a coordinated tetrazene (see **Figure 5.7**). The structure more closely resembles the tetrazene complexes recently structurally characterized in S = 3/2 iron systems bearing weak field ligands,¹² than it does the strong field organometallic metallatetrazaoles first reported on either iron, Fe(CO)₃(κ²-MeNNNNMe),¹³ or cobalt, CpCo(κ²-C₆F₅NNNNC₆F₅).¹⁴

(12) (a) Mock, M. T.; Popescu, C. V.; Yap, G. P. A.; Dougherty, W. G.; Riordan, C. G. *Inorg. Chem.* **2008**, *47*, 1889-1891. (b) Cowley, R. E.; Bill, E.; Neese, F.; Brennessel, W. W.; Holland, P. L. *Inorg. Chem.* **2009**, *48*, 4828-4836.

(13) Doedens, R. J. *Chem. Commun.* **1968**, 1271-1272.

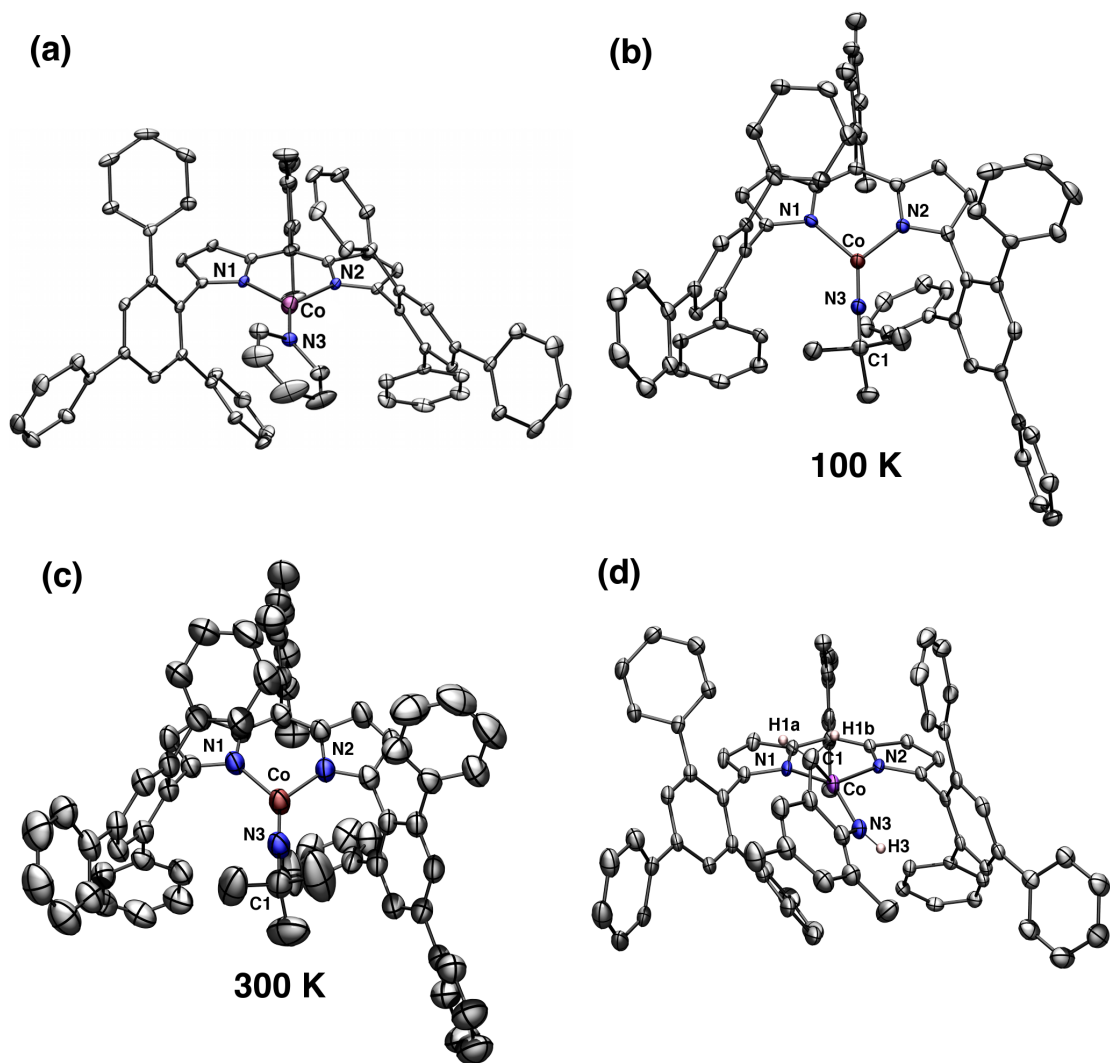


Figure 5.1. Solid-state structures for cobalt dipyrromethene complexes. (a) $(^{\text{Ar}}\text{dpme})\text{Co}(\text{py})$, (b) $(^{\text{Ar}}\text{dpme})\text{Co}(\text{N}^t\text{Bu})$ at 150 K, (c) $(^{\text{Ar}}\text{dpme})\text{Co}(\text{N}^t\text{Bu})$ at 300 K, and (d) $(^{\text{Ar}}\text{dpme})\text{Co}(\text{indoline})$ with the thermal ellipsoids set at the 40% probability level (hydrogen atoms, solvent molecules, and ligand phenyl substituents in $(^{\text{Ar}}\text{dpme})\text{Co}(\text{indoline})$ omitted for clarity; Co green, C grey, H white, N blue). Selected bond lengths (\AA) and angles ($^\circ$) for $(^{\text{Ar}}\text{dpme})\text{Co}(\text{py})$: Co–N1, 1.961(3); Co–N2, 1.961(3); Co–N3, 1.942(4); for $(^{\text{Ar}}\text{dpme})\text{Co}(\text{N}^t\text{Bu})$ (150 K): Co–N1, 1.926(3); Co–N2, 1.916(3); Co–N3, 1.609(3); N3–Co–C1 177.5(3); for $(^{\text{Ar}}\text{dpme})\text{Co}(\text{N}^t\text{Bu})$ (300 K): Co–N1, 1.930(3); Co–N2, 1.934(3); Co–N3, 1.632(3); N3–Co–C1 178.2(3); for $(^{\text{Ar}}\text{dpme})\text{Co}(\text{indoline})$: Co–N1, 1.927(3); Co–N2, 1.992(3); Co–N3, 1.848(4); Co–C1, 2.018(5).

(14) (a) Gross, M. E.; Trogler, W. C.; Ibers, J. A. *J. Am. Chem. Soc.* **1981**, *103*, 192-193. (b) Gross, M. E.; Trogler, W. C.; Ibers, J. A. *Organometallics* **1982**, *1*, 732-739.

5-3. Isolation of an Alkyl Cobalt Imide.

The major product kinetically formed in reaction of one equivalent $t\text{BuN}_3$ with $(^{\text{Ar}}\text{dpme})\text{Co}(\text{py})$ could be converted to the tetrazene product by addition of excess $t\text{BuN}_3$, suggesting the major product was a paramagnetic imide. To isolate the imide product free of tetrazene contamination, a dilute solution of $t\text{BuN}_3$ (1% w/w) in diethyl ether was added dropwise to a diethyl ether solution of $(^{\text{Ar}}\text{dpme})\text{Co}(\text{py})$. Slow addition of azide has been previously observed to bias product formation away from tetrazene in the synthesis of alkyl iron imides.¹⁵ Crystals of the kinetic imide product could be obtained from a benzene/hexane solution at $-35\text{ }^\circ\text{C}$. The structure of the putative imide $(^{\text{Ar}}\text{dpme})\text{Co}(\text{N}^t\text{Bu})$ was solved via X-ray diffraction, revealing a trigonal planar three-coordinate cobalt imide (**Figure 5.1b**). The Co–N distance of $1.609(3)\text{ \AA}$ is shorter than those previously reported for either three-⁵ or four-coordinate^{4,6} cobalt imides. The Co–N3–C67 angle was nearly linear ($178.8(1)^\circ$), and the imide does not deviate significantly from the plane formed by the dipyrin nitrogens (N1, N2) and the cobalt atom.

Imide $(^{\text{Ar}}\text{dpme})\text{Co}(\text{N}^t\text{Bu})$ displays a paramagnetically shifted ^1H NMR at room temperature (δ : 23.2 to -8.4 ppm) with a solution magnetic moment of $2.96(2)\ \mu_{\text{B}}$ (C_6D_6 , 295 K). However, cooling a sample of $(^{\text{Ar}}\text{dpme})\text{Co}(\text{N}^t\text{Bu})$ in toluene- d_8 in the NMR probe resulted in a dramatic contraction of the chemical shift range to 8.85 ppm to 0.29 ppm at $-80\text{ }^\circ\text{C}$ (see **Figure 5.11**). The ^1H resonances for the imide $t\text{Bu}$ substituent occur at δ 8.85 ppm (assigned via preparation of the deuterated analog, $(^{\text{Ar}}\text{dpme})\text{Co}(\text{N}^t\text{Bu}-d_9)$), still downfield from a diamagnetic *tert*-butyl group indicating the spin transition is incomplete at $-80\text{ }^\circ\text{C}$. The observed spectral features suggests a spin crossover transition from an open shell configuration (i.e., $S = 1$ or 2) to a singlet spin state, suggesting the ground state of $(^{\text{Ar}}\text{dpme})\text{Co}(\text{N}^t\text{Bu})$ is diamagnetic.

(15) Bowman, A. C.; Milsmann, C.; Bill, E.; Turner, Z. R.; Lobkovsky, E.; DeBeer, S.; Wieghardt, K.; Chirik, P. J. *J. Am. Chem. Soc.* **2011**, *133*, 17353-17369.

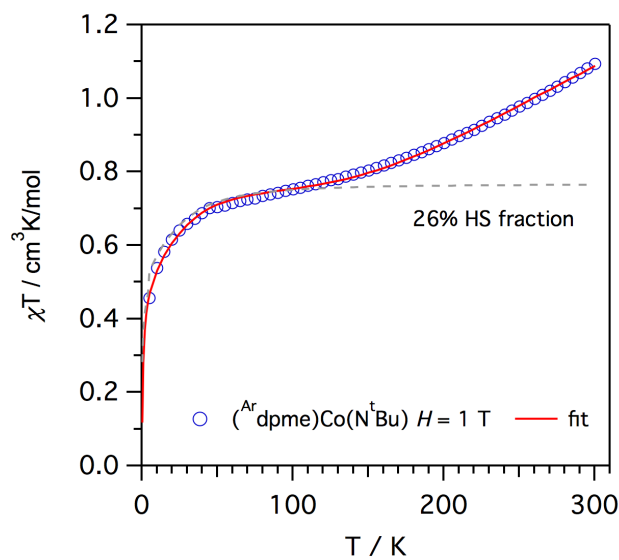


Figure 5.2. Variable temperature magnetic susceptibility data for $(^{\text{Ar}}\text{dpme})\text{Co}(\text{N}^{\text{t}}\text{Bu})$. (\circ) Data from 5 K to 300 K in an applied dc field of 1 T. (—) Zero field splitting/Boltzmann spin crossover fit described in the text. (---) Susceptibility model for HS fraction with no spin crossover.

To probe the magnetic behavior of $(^{\text{Ar}}\text{dpme})\text{Co}(\text{N}^{\text{t}}\text{Bu})$ further, variable temperature dc susceptibility data was collected in the temperature range of 5–300 K. For $(^{\text{Ar}}\text{dpme})\text{Co}(\text{N}^{\text{t}}\text{Bu})$, $\chi_{\text{M}}T$ at 300 K is $1.12 \text{ cm}^3 \text{ K/mol}$, consistent with the solution magnetic moment obtained at room temperature, but the plot of $\chi_{\text{M}}T$ is clearly rising at the temperature limit of the experiment (**Figure 5.2**). As the temperature is lowered, $\chi_{\text{M}}T$ undergoes a gradual decline to a value of $0.77 \text{ cm}^3 \text{ K/mol}$ near 50 K, followed by a subsequent decrease to $0.47 \text{ cm}^3 \text{ K/mol}$ at 5 K. As the susceptibility data never achieves a value consistent with a singlet ground state, we hypothesize that a fraction of the high-spin state remains at the low temperature extreme. To further probe the spin ground state, variable temperature magnetization data were collected in the temperature range of 1.8–10 K at fields of 1–7 T. The resulting plot of reduced magnetization (see **Figure 5.15**), features a series of non-superimposable isofield curves with the 7 T curve reaching a maximum value of $M = 0.62 \mu_{\text{B}}$ at 1.8 K, further indicating incomplete transition to the diamagnetic ground state. The $\chi_{\text{m}}T$ versus T curve for $(^{\text{Ar}}\text{dpme})\text{Co}(\text{N}^{\text{t}}\text{Bu})$ was fit as a spin transition (for x_{HS} , ΔH , and T_{c}) between a singlet and both a triplet and quintet state using equation

1;¹⁶ where x_{HS} is the fraction of molecules trapped in the high-spin state at low T (see **Table 5.2** for the expressions used for χ_{HS}).¹⁷ The reduced magnetization data were fit using ANISOFIT¹⁸ and the spin Hamiltonian in Eq. 5.2.

Table 5.1. Equations used to model the susceptibility and magnetization data.

$$\chi T = x_{HS}(\chi_{HS}T) + (1 - x_{HS}) \left(\frac{1}{1 + e^{(\Delta H/R)/(\frac{1}{T} - \frac{1}{T_c})}} \right) (\chi_{HS}T) \quad (5.1)$$

$$\mathbf{H} = \mu_B H g \cdot \mathbf{S} + D S_z^2 + E(S_x^2 - S_y^2) \quad (5.2)$$

Modeling the susceptibility and reduced magnetization data using a high-spin configuration of $S = 1$ did not produce a satisfactory fit for the reduced magnetization, nor account for the increasing susceptibility data at 300 K. A satisfactory model for the data, however, could be obtained invoking a spin transition from a singlet to quintet configuration with a small fraction of the high-spin component present at low temperatures. The plateau in susceptibility below 100 K is accounted for by a high-spin component of $x_{HS} = 25.6\%$ of the total Co concentration. Thus, the total fraction of high-spin component is given by this baseline value in addition to the portion suggested by the Boltzmann distribution for the remaining fraction governed by the thermodynamic parameters (ΔH 472 cm^{-1} ; T_c 1397 K) obtained by fitting our data with equation 1 and the χ_{HS} expression for $S = 2$ ($D = -20.2 \text{ cm}^{-1}$, $g = 2.0$). The very small change in the fraction of the high-spin component between low temperature and room temperature ($\sim 10\%$ from the Boltzmann parameters) is manifest in very small structural perturbations obtained at 100 K and 300 K. The 300 K structure reveals a modest elongation of the Co–N bond length from 1.609(3) Å to 1.632(3) Å (**Figure 5.1c**), consistent with electronic population of

(16) Kahn, O. *Molecular Magnetism*; VCH: New York, NY, 1993.

(17) Boča, R. *Coord. Chem. Rev.* **2004**, 248, 757-815.

(18) Shores, M. P.; Sokol, J. J.; Long, J. R. *J. Am. Chem. Soc.* **2002**, 124, 2279-2292.

orbitals consisting of both σ^* and π^* interactions (*vide infra*). Population of (Co–N) antibonding orbitals would suggest weakening of the Co imide bond, rendering it reactive for H-atom abstraction or viable for imide group transfer. While reaction with a two-electron reductant, PMe_2Ph , does facilitate imide group transfer to produce phosphinimide $\text{PhMe}_2\text{P}(\text{N}^t\text{Bu})$ (80 °C), we observed no evidence for C–H bond activation using $(^{\text{Ar}}\text{dpme})\text{Co}(\text{N}^t\text{Bu})$.

5-4. Reactivity of $(^{\text{Ar}}\text{dpme})\text{Co}(\text{py})$ with Aryl Azides.

Reacting the pyridine adduct $(^{\text{Ar}}\text{dpme})\text{Co}(\text{py})$ with aryl-substituted azides led to tetrazene formation unless the azide aryl substituent featured *ortho* substituents. For example, addition of 4-(*N,N*-dimethylamino)phenyl azide, $\text{N}_3\text{Ar}^{\text{NMe}_2}$, with $(^{\text{Ar}}\text{dpme})\text{Co}(\text{py})$ gave exclusively the tetrazene complex $(^{\text{Ar}}\text{dpme})\text{Co}(\kappa^2\text{-}^{\text{NMe}_2}\text{ArNNNNAr}^{\text{NMe}_2})$, which was structurally characterized (see **Figure 5.6**) and closely resembles $(^{\text{Ar}}\text{dpme})\text{Co}(\kappa^2\text{-}^t\text{BuNNNN}^t\text{Bu})$. Even with one or fewer equivalents and slow addition conditions akin to those used to isolate $(^{\text{Ar}}\text{dpme})\text{Co}(\text{N}^t\text{Bu})$, only the starting material and tetrazene complex were observed by NMR.

Reaction of $(^{\text{Ar}}\text{dpme})\text{Co}(\text{py})$ with one equivalent of mesityl azide in benzene consumed the azide (ascertained by disappearance of the ν_{N_3} stretch by IR), and cleanly afforded a new paramagnetic species following sublimation of the benzene. A single crystal diffraction experiment on crystals obtained from storing a concentrated solution of this reaction product in diethyl ether at –35 °C revealed not an imide product, but a metallacycloindoline product $(^{\text{Ar}}\text{dpme})\text{Co}(\text{indoline})$, indoline = $\kappa^2\text{-NHC}_6\text{H}_2\text{-2,4-Me}_2\text{-6-CH}_2$, the molecular structure of which is shown in **Figure 5.1d**. The mesityl nitrene unit has been modified via net H-atom transfer from a mesityl benzylic group to the imide N, binding Co as a dianionic chelate via one Co–anilide and one Co–alkyl bond to one of the benzylic carbons *ortho* to the

nitrogen. The positions of both the methylene hydrogens on the carbon and the amide hydrogen on the nitrogen were located in the difference Fourier map and refined semi-freely. Within the metallacycloindoline, the Co–N3 bond distance of 1.848(4) Å and the Co–C1 distance of 2.018(5) Å are consistent with single bonds to the Co ion.

Given the stability of imide ($^{\text{Ar}}\text{dpme})\text{Co}(\text{N}^t\text{Bu})$ we propose that ($^{\text{Ar}}\text{dpme})\text{Co}(\text{indoline})$ arises via formation of the terminal imide product ($^{\text{Ar}}\text{dpme})\text{Co}(\text{NMes})$ from reaction of mesityl azide with ($^{\text{Ar}}\text{dpme})\text{Co}(\text{py})$, followed by H–atom abstraction from one of the proximal *ortho*-methylene groups, followed by radical rebound between Co and pendant carbon radical. The intermediacy of the mesityl imide was supported by the appearance of a spectroscopically observable species by ^1H NMR immediately following addition of mesityl azide to ($^{\text{Ar}}\text{dpme})\text{Co}(\text{py})$. Reacting an *n*-hexane slurry of ($^{\text{Ar}}\text{dpme})\text{Co}(\text{py})$ with $\text{N}_3\text{Mes-}d_{11}$ (deuterated azide used to suppress H–atom abstraction) over 48 h at room temperature followed by isolation on a fritted glass funnel permitted isolation of a paramagnetic product that precedes the formation of metallacycloindoline. As isolated, the new purple species was stable in the solid-state for days, but converted to ($^{\text{Ar}}\text{dpme})\text{Co}(\text{indoline})\text{-}d_{11}$ slowly in solution and upon any attempt to crystallize. We propose the kinetic product to be ($^{\text{Ar}}\text{dpme})\text{Co}(\text{NMes})\text{-}d_{11}$, which exhibits a paramagnetically shifted ^1H NMR (μ_{eff} 3.6(2) μ_{B}) at room temperature. However, unlike ($^{\text{Ar}}\text{dpme})\text{Co}(\text{N}^t\text{Bu})$ imide ($^{\text{Ar}}\text{dpme})\text{Co}(\text{NMes})\text{-}d_{11}$ does not undergo a spin state transition as gleaned from variable temperature ^1H NMR (see **Figure 5.13**), suggesting the triplet configuration for aryl imide complex ($^{\text{Ar}}\text{dpme})\text{Co}(\text{NMes})$ is the likely electronic ground state.

5-5. Understanding the Electronic Structure of Open Shell Cobalt Imides.

Several unusual features of the Co imide complexes presented herein are unique to the (dipyrrin)Co platform: (1) all previously reported $\text{Co}^{\text{III}}(\text{imide})$ complexes have reported singlet ground states; (2)

alkyl imide ($^{\text{Ar}}\text{dpme})\text{Co}(\text{N}^{\text{t}}\text{Bu})$ undergoes a spin crossover from a singlet to quintet configuration; and (3) aryl imide ($^{\text{Ar}}\text{dpme})\text{Co}(\text{NMes})$ features a well-isolated triplet ground state with no apparent spin crossover behavior, yet undergoes H-atom abstraction along the Co–N_{Ar} bond. These observations can be rationalized from consideration of the frontier molecular orbital picture perturbations with the various ligand substitutions. The molecular orbital interactions arise from a N→Co σ interaction (N $2sp_z$ + Co $3d_z^2$) and two Co–N π interactions arising from overlap of the N $2p_x$ and $2p_y$ with the Co $3d_{xz}$ and $3d_{yz}$ orbitals, respectively (**Figure 5.3a**). A symmetry allowed mixing of the Co $4s$ and $3d_z^2$ orbital stabilizes the $3d_z^2$ to mitigate destabilizing effect of population of the Co–N σ^* interaction. For four-coordinate imide complexes, the Co $3d_{xz}$ and $3d_{yz}$ are degenerate and comprise bonding of the three ancillary ligand σ donors and the Co imide π manifold, leading a large energy gap between the occupied d_z^2 and empty d_{xz}/d_{yz} orbital set, favoring low-spin configurations.^{2,619} For three-coordinate species, the Co imide π manifold is comprised of two non-degenerate bonding interactions, as the Co $3d_{xz}$ orbital also bears σ^* character with respect to the ancillary bidentate ligand whereas the $3d_{yz}$ does not. For the previously reported three-coordinate Co^{III} imide complexes, the ancillary ligands employed (β -diketiminato,^{5a} guadinate^{5b}) feature π -donating N-based ancillary ligands, resulting in destabilization of the $3d_{yz}$ from π^* interactions with respect to the ancillary ligand as well as the imide interaction, leading to large HOMO–LUMO gaps like the four-coordinate systems to favor singlet ground states.⁵

The dipyrin σ donor strength is attenuated from non-*N*-heterocyclic donors,²⁰ manifesting in a reduction of d_{xz} destabilization ($\Delta_T(d_{xz}-d_{xy})$ is diminished, using the non-bonding orbital as a reference **Figure 5.3b**). The N-based π electrons in the dipyrin ligand are incorporated into the ligand aromatic π framework and therefore do not destabilize the d_{yz} orbital in the manner of the π -donating β -

(19) Mayer, J. M.; Thorn, D. L.; Tulip, T. H. *J. Am. Chem. Soc.* **1985**, *107*, 7454-7462.

(20) DiFranco, S. A.; Maciulis, N. A.; Staples, R. J.; Batrice, R. J.; Odom, A. L. *Inorg. Chem.* **2012**, *51*, 1187-1200.

diketiminato or guanidinato ligands. As d_{yz} drops in energy, the HOMO–LUMO gap ($\Delta_{H-L}(d_{yz}-d_z^2)$) is reduced to the extent that Δ_{H-L} is less than the mean spin pairing energy, permitting an open shell configuration to be obtained. The combination of these two effects for $(^{\text{Ar}}\text{dpme})\text{Co}(\text{N}^{\text{t}}\text{Bu})$ (Figure 5.3b) allows for population of d_{yz} and diminished Δ_{T} allows for the thermal induced spin crossover between the singlet and quintet states. Spin crossover between singlet and quintet states is most commonly observed for six-coordinate Fe^{II} complexes,²¹ but Co^{III} spin crossover complexes are not without precedent.²² Alkyl imide $(^{\text{Ar}}\text{dpme})\text{Co}(\text{N}^{\text{t}}\text{Bu})$, much like the recently reported alkyl iron imide complex by Chirik and coworkers,¹⁵ showcases spin crossover behavior on a complex bearing a metal–ligand multiple bond.

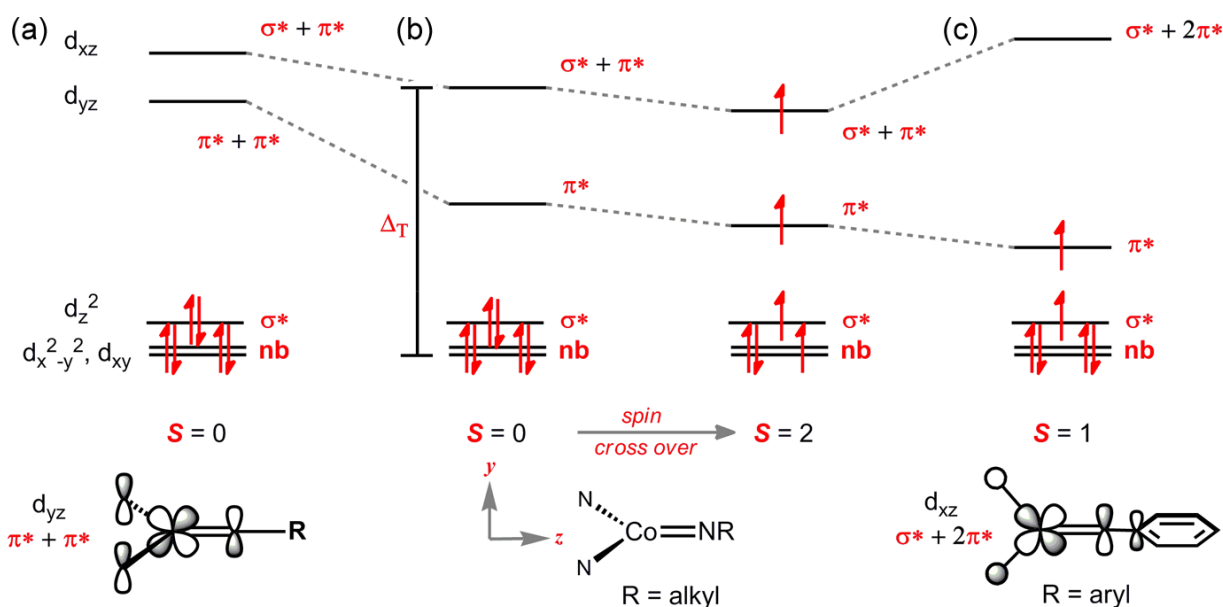


Figure 5.3. Frontier molecular orbital description for trigonal $\text{Co}^{\text{III}}(\text{NR})$. Featuring an ancillary ligand with π -donating substituents (a), no ancillary π -donation (b), and conjugation to imide N–aryl π system (c). Compression of the ligand field is illustrated in (b) to represent singlet to quintet spin crossover.

(21) Gütllich, P.; Hauser, A.; Spiering, H. *Angew. Chem., Int. Ed. Engl.* **1994**, 33, 2024–2054. and references contained therein.
 (22) (a) Kläui, W. *J. Chem. Soc., Chem. Commun.* **1979**, 700. (b) Gütllich, P.; McGarvey, B. R.; Kläui, W. *Inorg. Chem.* **1980**, 19, 3704–3706. (c) Navon, G.; Kläui, W. *Inorg. Chem.* **1984**, 23, 2722–2725. (d) Kläui, W.; Eberspach, W.; Gütllich, P. *Inorg. Chem.* **1987**, 26, 3977–3982.

Substitution of N^tBu with NMe₃ decreases the imide N 2p_x and 2p_y energies relative to the alkyl imide via orbital conjugation with the mesityl π system. Furthermore, orienting the mesityl unit perpendicular to the dipyrin plane to minimize steric interactions raises the imide N 2p_x through introduction of a π* interaction with the mesityl aromatic π electrons. Consequently, the (Co d_{xz}-N p_x) orbital interaction is destabilized further, increasing Δ_T relative to (Ar^{dpme})Co(N^tBu), favoring the triplet configuration ((d_{x²-y²)²(d_{xy})²(d_z)¹(d_{yz})¹) depicted in **Figure 5.3c**. The perpendicular orientation of the arylimide ligand positions the mesityl *ortho*-methyl groups directly above the frontier orbital possessing radical character (d_{yz}), ultimately leading to H-atom abstraction. Radical recombination to afford the metallacycloindoline (Ar^{dpme})Co(indoline) is entropically favored as opposed to direct C-N bond formation to make the four-membered ring of a bicyclic azetine.}

5-6. Conclusions.

The synthesis and characterization of the dipyrin cobalt(III) imides demonstrate that through limiting the ancillary ligand field strength electronic structures of higher spin can be made accessible. The configuration of molecular orbital interactions necessary to achieve a sufficiently compressed ligand field to favor unpaired arrangements of electrons rely on the ability of the ligand to enforce a low-coordinate geometry. In these complexes the trigonal geometry of the Co and the ligand geometry were also well matched to combine both σ and π effects in a favorable fashion. Gratifyingly the accessibility of open shell configurations was manifest in the observation of reactivity atypical of singlet cobalt(III) imides: an alkyl cobalt imide that partially populates a quintet state at room temperature carried out nitrene transfer to phosphine, and a triplet aryl cobalt imide underwent intermolecular hydrogen atom abstraction. These results in combination with the magnetic and structural characterization show that

direct targeting of metal-ligand multiple bonds with open shell configurations may unveil truly reactive species for atom and group transfer processes.

5-7. Experimental Methods.

General Considerations.

All manipulations of metal complexes were carried out in the absence of water and dioxygen using standard Schlenk techniques, or in an M. Braun inert atmosphere glovebox under a dinitrogen atmosphere. Ligand and ligand precursor syntheses were carried out in air, except where noted. All glassware was oven dried for a minimum of 1 h and cooled in an evacuated antechamber prior to use in the glovebox. Benzene, *n*-hexane, and diethyl ether were dried and deoxygenated on a Glass Contour System (SG Water USA, Nashua, NH) and stored over 4 Å molecular sieves (Strem) prior to use. Benzene-*d*₆ and toluene-*d*₈ were purchased from Cambridge Isotope Labs and were degassed and stored over 4 Å molecular sieves prior to use. Cobalt(II) chloride bis-pyridine,¹¹ 4-(dimethylamino)phenyl azide,²³ 4-(*tert*-butyl)phenyl azide,²³ *tert*-butyl azide,²⁴ and mesityl azide²⁵ were synthesized according to literature procedures. Mesitylene-*d*₁₂ was purchased from Cambridge Isotope Labs and following literature procedures converted to nitromesitylene-*d*₁₁,²⁶ mesitylaniline-*d*₁₁,²⁶ and finally mesityl azide-*d*₁₁.²⁵ Similarly, *tert*-butanol-*d*₁₀ (Cambridge Isotope Labs) was converted to *tert*-butyl azide-*d*₉ following the procedure²⁴ for the unlabeled analog. The ligand ^{Ar}dpmeH and lithium salt (^{Ar}dpme)Li were synthesized as previously reported.⁹ Potassium graphite was prepared by heating potassium with 8 equivalents of graphite powder at 150 °C in an evacuated flask for 1 h. Celite® 545 (J. T. Baker) was dried in a Schlenk flask for 24 h under dynamic vacuum while heating to at least 150 °C prior to glovebox use.

(23) Smith, P. A. S.; Hall, J. H. *J. Am. Chem. Soc.* **1962**, *84*, 480-485.

(24) Bottero, J.; Penwell, P.; Schmitt, R. *Synth. Commun.* **1997**, *27*, 1465-1467.

(25) Murata, S.; Abe, S.; Tomioka, H. *J. Org. Chem.* **1997**, *62*, 3055-3061.

(26) Leitao, E. M.; Dubberley, S. R.; Piers, W. E.; Wu, Q.; McDonald, R. *Chem.-Eur. J.* **2008**, *14*, 11565-11572.

Characterization and Physical Measurements.

UV/Visible spectra were recorded on a Varian Cary 50 UV/Visible spectra using quartz cuvettes and a scan rate of 300 or 600 nm/min. Extinction coefficients were determined from a minimum of three concentrations per sample, and were calculated by a linear regression fit of the absorbance vs. concentration data. ^1H NMR spectra were recorded on Varian Mercury 400 MHz or Varian Unity/Inova 500 MHz spectrometers. ^1H and ^{13}C NMR chemical shifts are reported relative to SiMe_4 using the chemical shift of residual solvent peaks as reference. Solution magnetic susceptibilities were determined by Evans's method²⁷ using hexamethyldisiloxane as an internal reference. Elemental analyses (%CHN) were carried out by Complete Analysis Laboratories, Inc. (Parsippany, NJ).

Table 5.2. Equations for susceptibility of triplet and quintet states with zero field splitting.

$$\mathbf{H} = \mu_B H \cdot \mathbf{g} \cdot \mathbf{S} + D \left[\mathbf{S}_z^2 - \frac{1}{3}S(S+1) \right] + E(\mathbf{S}_x^2 - \mathbf{S}_y^2) \quad (5.3)$$

$$\chi_{S=1} = \frac{1}{3} \left(\frac{2Ng_z^2\mu_B^2}{k(T-2zJ)} \cdot \frac{e^{-\frac{D}{kT}}}{1+2e^{-\frac{D}{kT}}} \right) + \frac{2}{3} \left(\frac{2Ng_x^2\mu_B^2}{D} \cdot \frac{1-e^{-\frac{D}{kT}}}{1+2e^{-\frac{D}{kT}}} \right) \quad (5.4)$$

$$\chi_{S=2} = \frac{1}{3} \left(\frac{2Ng_z^2\mu_B^2}{k(T-6zJ)} \cdot \frac{e^{-\frac{D}{kT}} + 4e^{-\frac{4D}{kT}}}{1+2e^{-\frac{D}{kT}} + 2e^{-\frac{4D}{kT}}} \right) + \frac{2}{3} \left(\frac{2Ng_x^2\mu_B^2}{D} \cdot \frac{3 - \frac{7}{3}e^{-\frac{D}{kT}} - \frac{2}{3}e^{-\frac{4D}{kT}}}{1+2e^{-\frac{D}{kT}} + 2e^{-\frac{4D}{kT}}} \right) \quad (5.5)$$

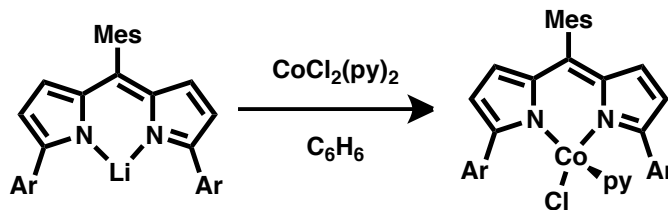
Magnetic data were collected using a Quantum Design MPMS-5S SQUID magnetometer. Measurements were obtained for finely ground microcrystalline powders restrained in a frozen eicosane matrix within polycarbonate capsules. Samples were prepared under a dry nitrogen atmosphere by packing the powder in a gel cap and adding warm liquid eicosane, which formed a solid wax upon cooling. Dc susceptibility measurements were collected in the temperature range 5–300 K under a dc

(27) (a) Evans, D. F. *J. Chem. Soc.* **1959**, 2003-2005. (b) Sur, S. K. *J. Magn. Reson.* **1989**, 82, 169-173.

field of 5000 or 10000 Oe. Dc magnetization measurements were obtained in the temperature range 1.8–10 K under dc fields of 1, 2, 3, 4, 5, 6, and 7 T. The susceptibility data was corrected for contributions from the sample holder and eicosane, as well as the core diamagnetism of the sample using Pascal's constants.

The $\chi_m T$ vs. T curve for $(^{\text{Ar}}\text{dpme})\text{Co}(\text{py})$ was fit (for D and g) using the equation for a spin triplet for $\chi_{S=1}$ presented in Eq. 5.4¹⁶ (derived from the Hamiltonian in Eq. 5.3), with fit variables D , g , and J . The parameter $2zJ$ was included to account for intermolecular interactions ($z = 12$ for $(^{\text{Ar}}\text{dpme})\text{Co}(\text{py})$, and $J = -0.11 \text{ cm}^{-1}$ is a coupling constant describing the strength of the interactions.). The $\chi_m T$ vs. T curve for $(^{\text{Ar}}\text{dpme})\text{Co}(\text{N}^{\text{t}}\text{Bu})$ was fit as an incomplete spin transition between a singlet and quintet state. Susceptibility, $\chi_{S=2}$, of the quintet was taken from Eq. 5.5¹⁷ (also derived from Eq. 5.3), with fit variables D , g , and J . The parameter $6zJ$ was included to account for intermolecular interactions ($z = 8$, $J = -0.012 \text{ cm}^{-1}$ for $(^{\text{Ar}}\text{dpme})\text{Co}(\text{N}^{\text{t}}\text{Bu})$). Eq. 5.1 was used to model χT for the incomplete spin crossover using the expression for $\chi_{S=2}$ from Eq. 5.5, α_{HS} is the mole fraction molecules that persist in the quintet state even at low temperature, and ΔH and T_c are the enthalpy and crossover temperature for the Boltzmann term. The reduced magnetization data were fit using ANISOFIT¹⁸ and the spin Hamiltonian in Eq. 5.2.

Syntheses.



$(^{\text{Ar}}\text{dpme})\text{CoCl}(\text{py})$: In a 20 mL vial $(^{\text{Ar}}\text{dpme})\text{Li}$ (1.000 g, 1.140 mmol) and $\text{CoCl}_2(\text{py})_2$ (0.394 g, 1.37 mmol, 1.20 equiv.) were dissolved in 20 mL benzene and stirred for 14 h. The dark maroon mixture was filtered through a coarse glass frit with Celite to remove lithium chloride and the excess cobalt. The

Celite was washed with an additional 20 mL benzene. The benzene was frozen and removed by sublimation *in vacuo*, the material was triturated with 20 mL *n*-hexane, and dried *in vacuo*. The resulting maroon powder was washed with *n*-hexane atop a medium porosity glass frit to remove (^{Ar}dpme)H and dried to give (^{Ar}dpme)CoCl(py) (1.050 g, 88.26%). Crystals suitable for X-ray diffraction were grown from a 2:1 *n*-hexane/benzene mixture at $-38\text{ }^{\circ}\text{C}$. ¹H NMR (400 MHz, 295 K, C₆D₆): δ /ppm 56.73, 47.91, 42.00, 18.40, 12.70, 9.84, 8.81, 7.68, 7.40, 7.08, 6.41, 5.00, 4.72, 3.27, 2.79, 2.32, 1.88, 1.22, 0.02 -5.72 . μ_{eff} (295 K, Evans') 4.2(1) μ_{B} . %CHN Calculated for C₇₁H₅₄ClCoN₃: C 81.71, H 5.22, N 4.03; Found: C 81.59, H 5.29, N 3.95.

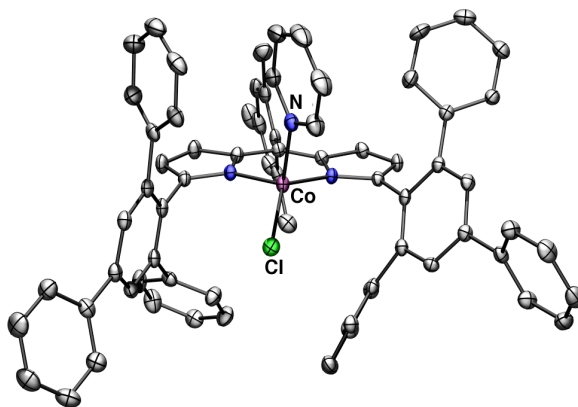
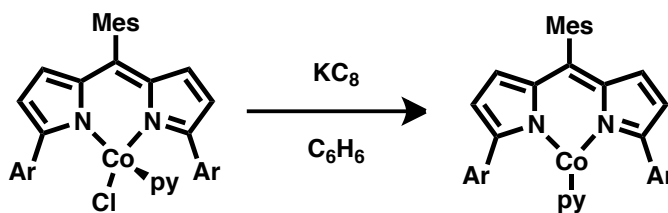


Figure 5.4. Structure of (^{Ar}dpme)CoCl(py). Thermal ellipsoids at the 50% probability level. Only one of two molecules present in the asymmetric unit shown. Hydrogen atoms omitted for clarity.



(^{Ar}dpme)Co(py): In a 20 mL vial (^{Ar}dpme)CoCl(py) (0.500 g, 0.479 mmol) was dissolved in 15 mL of benzene and potassium graphite (KC₈, 0.071 g, 0.53 mmol, 1.1 equiv.) was added. The reaction was stirred for 12 h, turning from dark maroon to dark purple. After letting settle for 10 min the mixture was filtered through a coarse glass frit with Celite. The Celite was washed with 40 mL benzene and the

solvent frozen and removed by sublimation *in vacuo* to afford (^{Ar}dpme)Co(py) as a dark purple powder (0.391 g, 81.0%). Crystals suitable for X-ray diffraction were grown from a 2:1 *n*-hexane/benzene mixture at -38 °C. ¹H NMR (400 MHz, 295 K, C₆D₆): δ/ppm 45.61, 14.29 (br s), 13.82, 12.52 (br s), 8.16 (d, *J* = 7.0 Hz), 7.58 (t, *J* = 6.7 Hz), 5.50, 5.11, 1.34, -1.60, -16.95 (br s). μ_{eff} (295 K, Evans') 2.9(1) μ_{B} . μ_{eff} (295 K, SQUID) 2.94(2) μ_{B} . %CHN calculated for C₇₁H₅₄CoN₃: C 84.59, H 5.40, N 4.17; Found: C 84.68, H 5.28, N 4.09.

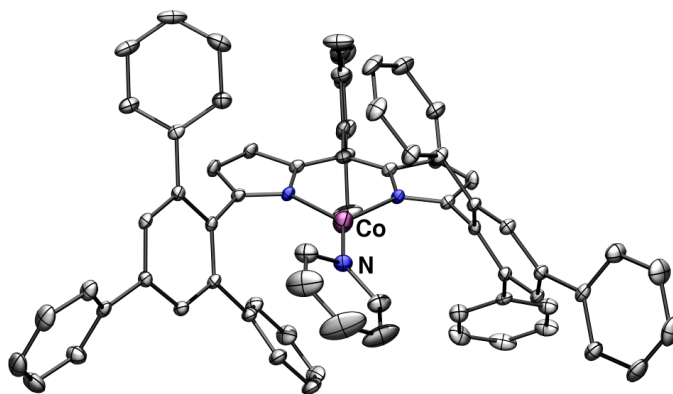
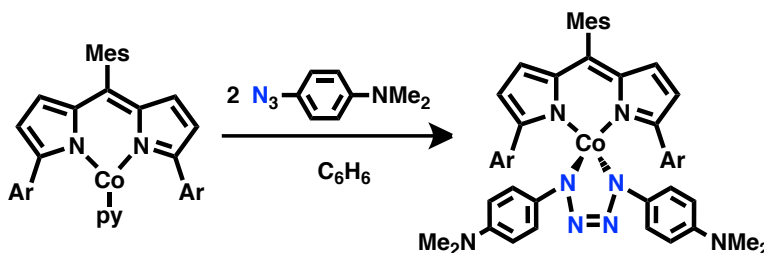


Figure 5.5. Structure of (^{Ar}dpme)Co(py). Thermal ellipsoids at the 50% probability level. Half of the molecule is generated by symmetry. Hydrogen atoms omitted for clarity.



(^{Ar}dpme)Co(N₄Ar^{NMe₂}): In a 20 mL vial (^{Ar}dpme)Co(py) (160 mg, 0.159 mmol) was dissolved in 5 mL of diethyl ether. A diethyl ether solution (1 mL) of dimethylamino)phenyl azide (51.5 mg, 0.317 mmol, 1.99 equiv.) was added resulting in an immediate color change from dark purple to dark red. After stirring for 10 min the ether was removed *in vacuo*, and the residue triturated with *n*-hexane to give the diaryl tetrazene complex, (^{Ar}dpme)Co(N₄Ar^{NMe₂}), as a dark red powder (166.8 mg, 85.9%). Crystals

suitable for X-ray diffraction were grown from a pentane/benzene solution at $-38\text{ }^{\circ}\text{C}$. ^1H NMR (400 MHz, 295 K, C_6D_6): δ/ppm 25.74, 23.64, 18.37 (br s), 16.14, 14.53, 8.50, 7.07 (d, $J = 6\text{ Hz}$), 6.87, 6.33, 3.00, 5.59, 3.12, 0.83 (br s), -9.49 , -39.58 . μ_{eff} (295 K, Evans') $3.2(1)\ \mu_{\text{B}}$. %CHN Calc. for $\text{C}_{82}\text{H}_{69}\text{CoN}_8$: C 80.37, H 5.68, N 9.14; Found: C 80.46, H 5.62, N 9.20.

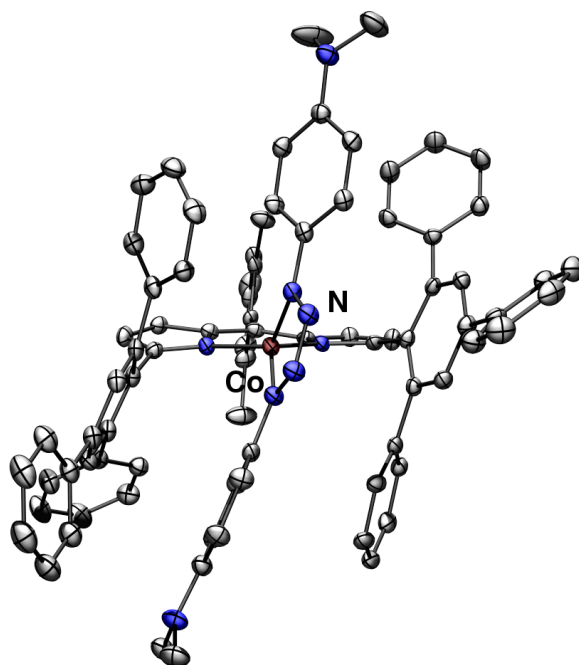
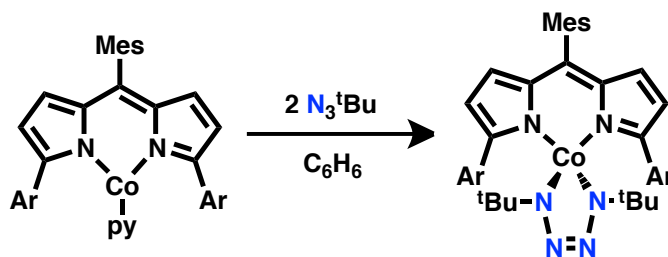


Figure 5.6. Structure of $(^{\text{Ar}}\text{dpme})\text{Co}(\text{N}_4\text{Ar}^{\text{NMe}_2})$. Thermal ellipsoids at the 50% probability level. Hydrogen atoms and one pentane molecule omitted for clarity.



$(^{\text{Ar}}\text{dpme})\text{Co}(\text{N}_4^{\text{tBu}}_2)$: In a 20 mL vial $(^{\text{Ar}}\text{dpme})\text{Co}(\text{py})$ (100 mg, 0.0992 mmol) was dissolved in 5 mL of diethyl ether. A solution of *tert*-butyl azide in diethyl ether (197 mg, 10.0% *w/w*, 0.199 mmol, 2.01 equiv.) was added resulting in an immediate color change from dark purple to dark red. After stirring for 10 min the ether was removed *in vacuo*, and the residue triturated with *n*-hexane to give the di-*tert*-butyl

tetrazene complex, $(^{\text{Ar}}\text{dpme})\text{Co}(\text{N}_4^{\text{tBu}}_2)$, as a red powder (97.4 mg, 88.6%). Crystals suitable for X-ray diffraction were grown from a concentrated diethyl ether solution at $-38\text{ }^\circ\text{C}$. ^1H NMR (400 MHz, 295 K, C_6D_6): δ/ppm 31.27, 21.06, 16.33, 13.00, 12.04, 9.43 (br s), 8.80, 6.11 (t, $J = 6.8\text{ Hz}$), 5.82, 5.58, 5.46, 5.16, 4.02, -0.57 , -3.70 (br s, $^{\text{tBu}}$), -6.49 , -43.69 (br s, $^{\text{tBu}}$). μ_{eff} (295 K, Evans') $3.0(1)\ \mu_{\text{B}}$. %CHN Calc. for $\text{C}_{74}\text{H}_{67}\text{CoN}_6$: C 80.85, H 6.14, N 7.64; Found: C 80.82, H 6.08, N 7.49. $(^{\text{Ar}}\text{dpme})\text{Co}(\text{N}_4(^{\text{tBu-d}_9})_2)$: Synthesized by following the same procedure as above with $(^{\text{Ar}}\text{dpme})\text{Co}(\text{py})$ (20.2 mg, 0.0200 mmol) and a solution of $\text{N}_3^{\text{tBu-d}_9}$ in diethyl ether (433 mg, 1.0% w/w , 0.040 mmol, 2.0 equiv.); yielding 21.4 mg (96%) of the deuterium labeled tetrazene complex. ^1H NMR (400 MHz, 295 K, C_6D_6): δ/ppm 31.17, 21.04, 16.30, 12.97, 12.02, 9.45 (br s), 8.79, 6.12 (t, $J = 7.0\text{ Hz}$), 5.82, 5.57, 5.46, 5.15, 4.03, -0.57 , -6.51 .

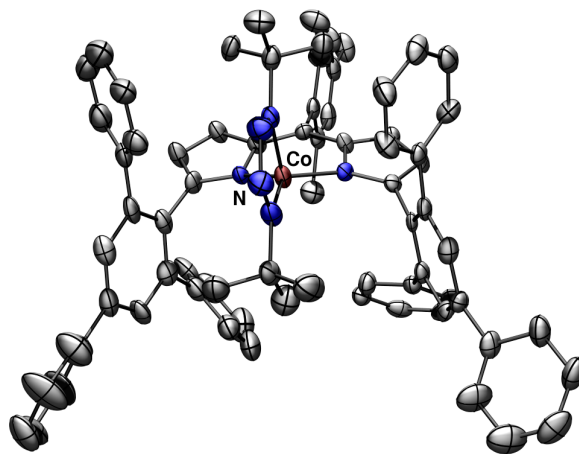
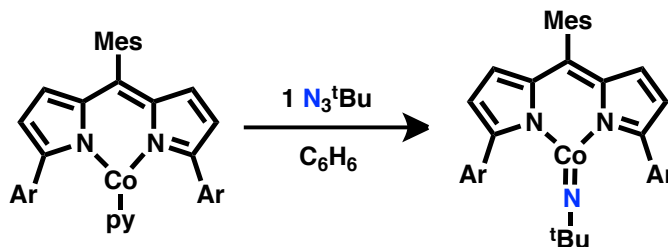


Figure 5.7. Structure of $(^{\text{Ar}}\text{dpme})\text{Co}(\text{N}_4^{\text{tBu}}_2)$. Thermal ellipsoids at the 50% probability level. Hydrogen atoms and one diethyl ether molecule omitted for clarity.



(^{Ar}dpme)Co(N^tBu): In a 20 mL vial (^{Ar}dpme)Co(py) (100 mg, 0.0992 mmol) was dissolved in 10 mL of diethyl ether. A 9 inch glass Pasteur pipette fitted with a glass microfiber filter was charged with a solution of *tert*-butyl azide in diethyl ether (983 mg, 1.0% *w/w*, 0.099 mmol, 1.0 equiv.). The azide solution was then allowed to slowly add gravimetrically the pipette filter to the stirring solution of (^{Ar}dpme)Co(py). Due to the volatility of ether and to ensure efficient mixing, the vial was manually rotated to allow the incoming solution to wash any precipitate that formed on the sides of the vial back into the solution. Over the course of the 20 min addition the solution gradually turned from dark purple to dark red. A small portion of azide solution remaining in the pipette tip was forced through the pipette with an additional 1 mL of diethyl ether. After an additional 5 min of stirring the ether was removed *in vacuo*, and the residue triturated with *n*-hexane to afford (^{Ar}dpme)Co(N^tBu) as a dark purple powder (90.6 mg, 91%). Crystals suitable for X-ray diffraction were grown from a 2:1 *n*-hexane/benzene mixture at $-38\text{ }^{\circ}\text{C}$. ¹H NMR (400 MHz, 295 K, C₆D₆): δ /ppm 23.45 (s, N^tBu), 11.09 (s), 10.97 (s), 10.15 (s), 8.01 (d, *J* = 7.1 Hz), 7.83 (t, *J* = 7.4 Hz) 7.68 (t, *J* = 7.4 Hz), 5.26 (s), 4.81 (s), 4.00 (d, *J* = 2.6 Hz), 3.42 (t, *J* = 7.3 Hz), 1.32 (t, *J* = 6.2 Hz), -8.59 (s). μ_{eff} (295 K, SQUID) 2.96(2) μ_{B} . %CHN Calc. for C₈₂H₆₉CoN₃: C 84.06, H 5.85, N 4.20; Found: C 84.06, H 5.81, N 4.12. (**(^{Ar}dpme)Co(N^tBu-*d*₉)**): Synthesized by following the same procedure as above with (^{Ar}dpme)Co(py) (20.0 mg, 0.0198 mmol) and a solution of N₃^tBu-*d*₉ in diethyl ether (215 mg, 1.0% *w/w*, 0.020 mmol, 1.0 equiv.); yielding 18.5 mg (92.6%) of the deuterium labeled imide. ¹H NMR (400 MHz, 295 K, C₆D₆): δ /ppm 10.69, 10.52, 9.38, 8.06 (d), 7.78 (t). 7.64 (t), 5.49, 4.67, 4.24, 3.75, 1.85, -7.15 .

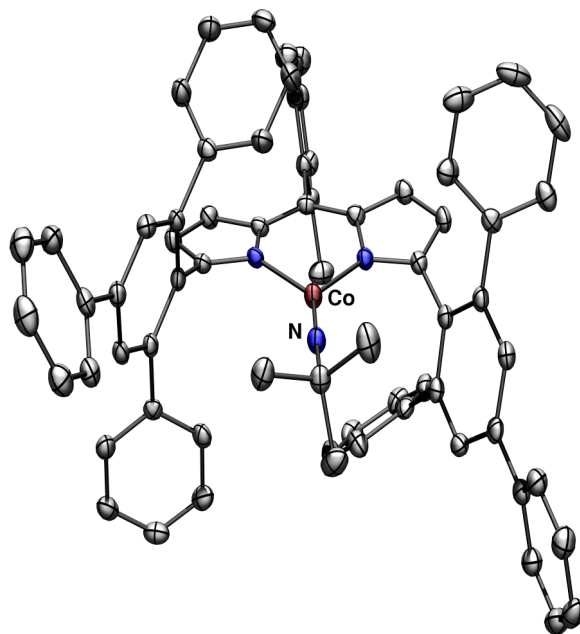
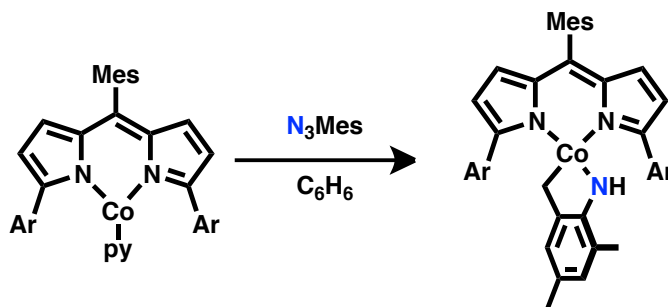


Figure 5.8. Structure of $(^{\text{Ar}}\text{dpme})\text{Co}(\text{N}^t\text{Bu})$. Thermal ellipsoids at 50% probability level. Hydrogen atoms, two molecules of benzene, and one additional solvent molecule (disordered as a mixture of *n*-hexane and benzene) omitted for clarity.



$(^{\text{Ar}}\text{dpme})\text{Co}(\text{indoline})$: In a 20 mL vial $(^{\text{Ar}}\text{dpme})\text{Co}(\text{py})$ (56.0 mg, 0.0555 mmol) was dissolved in 5 mL of benzene. A solution of mesityl azide in benzene (90 mg, 10.0% *w/w*, 0.056 mmol, 1.0 equiv.) was added. After stirring for 2 h the benzene was frozen and removed by sublimation *in vacuo*, and the resulting solid triturated with *n*-hexane to give the cobaltacycloindoline, $(^{\text{Ar}}\text{dpme})\text{Co}(\text{indoline})$, as a dark purple powder (47.2 mg, 80.1%). Crystals suitable for X-ray diffraction were grown from a concentrated diethyl ether solution at $-38\text{ }^{\circ}\text{C}$. $^1\text{H NMR}$ (400 MHz, 295 K, C_6D_6): δ /ppm 78.55, 74.38, 67.63, 52.85, 28.64, 9.68, 9.11, 8.68, 8.14, 7.81, 7.68, 4.06, 3.40, -0.36 , -45.07 , -82.52 . μ_{eff} (295 K,

Evans') 3.1(1) μ_B . %CHN Calc. for $C_{75}H_{60}CoN_3$: C 84.80, H 5.69, N 3.96; Found: C 84.68, H 5.73, N 3.89.

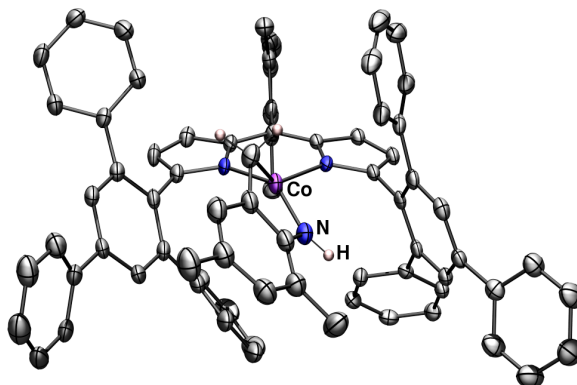
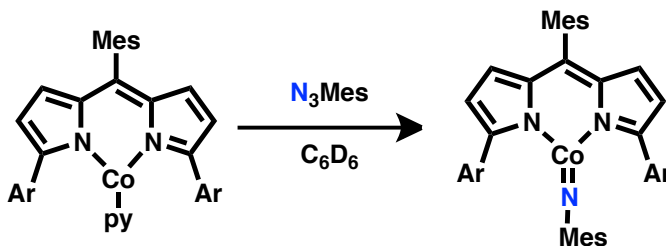


Figure 5.9. Structure for $(^{Ar}dpme)Co(indoline)$. Thermal ellipsoids at the 50% probability level. Peripheral hydrogen atoms and one diethyl ether molecule omitted for clarity.



$(^{Ar}dpme)Co(NMes-d_{11})$: In a 5 mL vial $(^{Ar}dpme)Co(py)$ (50.0 mg, 0.0496 mmol) was slurried in 1 mL *n*-hexane. A solution of N_3Mes-d_{11} in *n*-hexane (860 mg, 1.0% *w/w*, 0.050 mmol, 1.0 equiv.) was added. After stirring for 48 h the mixture was filtered through a medium porosity frit to obtain $(^{Ar}dpme)Co(NMes-d_{11})$ as a purple solid (38.2 mg, 71.8%) 1H NMR (400 MHz, 295 K, C_6D_6): δ/ppm 49.72, 32.21, 17.58, 15.13, 12.69 (d, $J = 7$ Hz), 11.58 (t, $J = 7$ Hz), 1.35, -0.54, -17.01, -22.08, -57.35. μ_{eff} (295 K, Evans') 3.6(2) μ_B . This species was stable in the solid state for days, but decayed slowly to the indoline in solution. All crystals obtained from solutions of the imide were determined by X-ray diffraction to be the insertion product. $(^{Ar}dpme)Co(NMes)$: In a J. Young tube $(^{Ar}dpme)Co(py)$ (10.0 mg, 0.0100 mmol) was dissolved in 1 mL benzene- d_6 . A solution of mesityl azide in benzene- d_6 (161 mg,

1.0% *w/w*, 0.010 mmol, 1.0 equiv.) was added. ^1H NMR (400 MHz, 295 K, $\text{C}_6\text{D}_5\text{CD}_3$): δ/ppm 112.41 (br s, $\text{NC}_6\text{H}_2\text{Me}_3$ or $\text{NC}_6\text{H}_2(\text{CH}_3)_3$), 50.08, 32.39, 17.69, 15.12, 12.70 (d, $J = 7$ Hz), 11.60 (t, $J = 7$ Hz), 1.36, -0.55, -17.19, -22.24, -43.1 (br s, $\text{NC}_6\text{H}_2\text{Me}_3$ or $\text{NC}_6\text{H}_2(\text{CH}_3)_3$), -57.72, -108.45 (br s, $\text{NC}_6\text{H}_2\text{Me}_3$ or $\text{NC}_6\text{H}_2(\text{CH}_3)_3$).

Reaction of ($^{\text{Ar}}\text{dpme})\text{Co}(\text{N}^t\text{Bu})$ with Dimethylphenylphosphine. A J. Young tube was charged with ($^{\text{Ar}}\text{dpme})\text{Co}(\text{py})$ (9.6 mg, 9.5 μmol) and 1 mL benzene- d_6 . A solution of *tert*-butyl azide in benzene- d_6 (94 mg, 1.0% *w/w*, 9.5 μmol , 1.0 equiv.) was added to the J. Young tube. Conversion of starting material to pure imide, ($^{\text{Ar}}\text{dpme})\text{Co}(\text{N}^t\text{Bu})$, and consumption of N_3^tBu was confirmed by ^1H NMR. A solution of phosphine, Me_2PhP , in benzene- d_6 (132 mg, 1.0% *w/w*, 9.6 μmol , 1.0 equiv.) was added to the tube. After 2 h, formation of the phosphinimide, $\text{Me}_2\text{PhP}=\text{N}^t\text{Bu}$ was confirmed by ^{31}P NMR (160 MHz, C_6D_6) which showed a single peak at -13.96 ppm and disappearance of phosphine at -45.45 ppm. The chemical shift of the phosphinimide product was confirmed by independent synthesis directly from the reaction of Me_2PhP and N_3^tBu in benzene- d_6 .

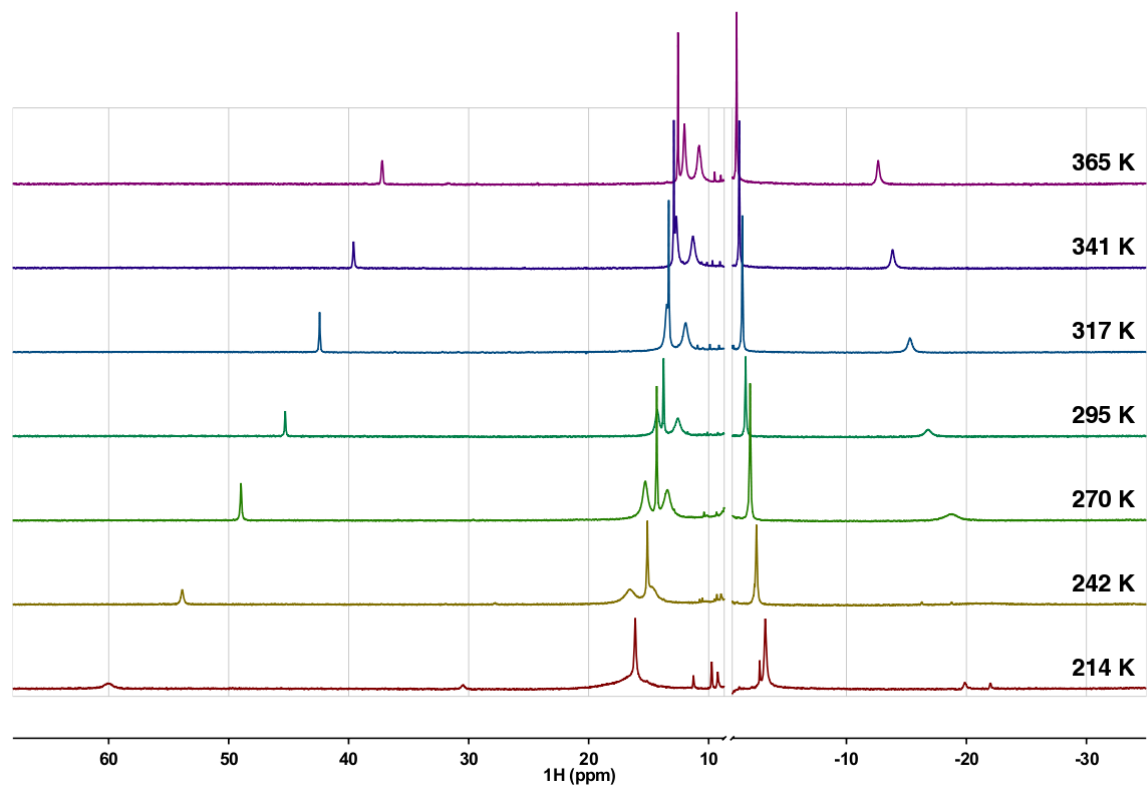


Figure 5.10. Variable temperature ^1H NMR of $(^{\text{Ar}}\text{dpme})\text{Co}(\text{py})$ in toluene- d_8 at 400 MHz. Diamagnetic region omitted for better clarity of paramagnetic peaks. Temperatures calibrated using the difference in chemical shifts of methylene and hydroxy protons in a sample either 4% methanol in methanol- d_4 (< 273 K) or ethylene glycol (> 273 K).

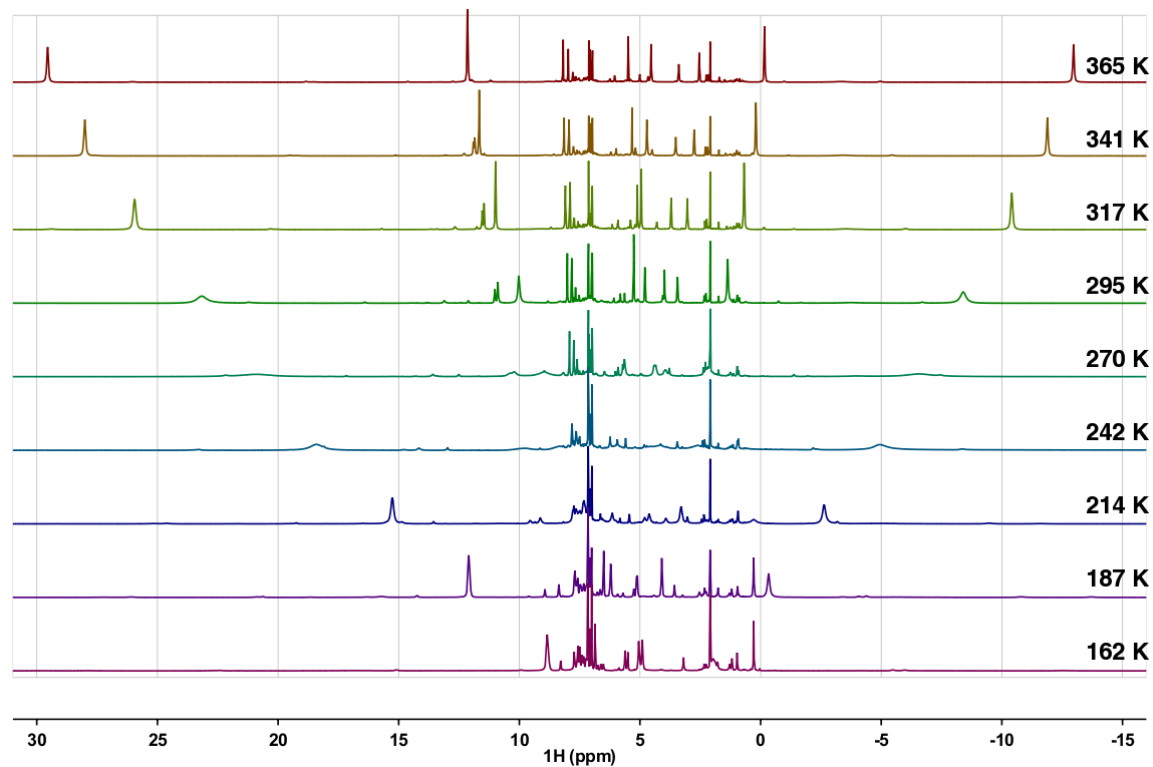


Figure 5.11. Variable temperature ^1H NMR of $(^{\text{Ar}}\text{dpme})\text{Co}(\text{N}^{\text{t}}\text{Bu})$ in $\text{toluene-}d_8$ at 400 MHz. Temperatures calibrated using the difference in chemical shifts of methylene and hydroxy protons in a sample either 4% methanol in $\text{methanol-}d_4$ (< 273 K) or ethylene glycol (> 273 K).

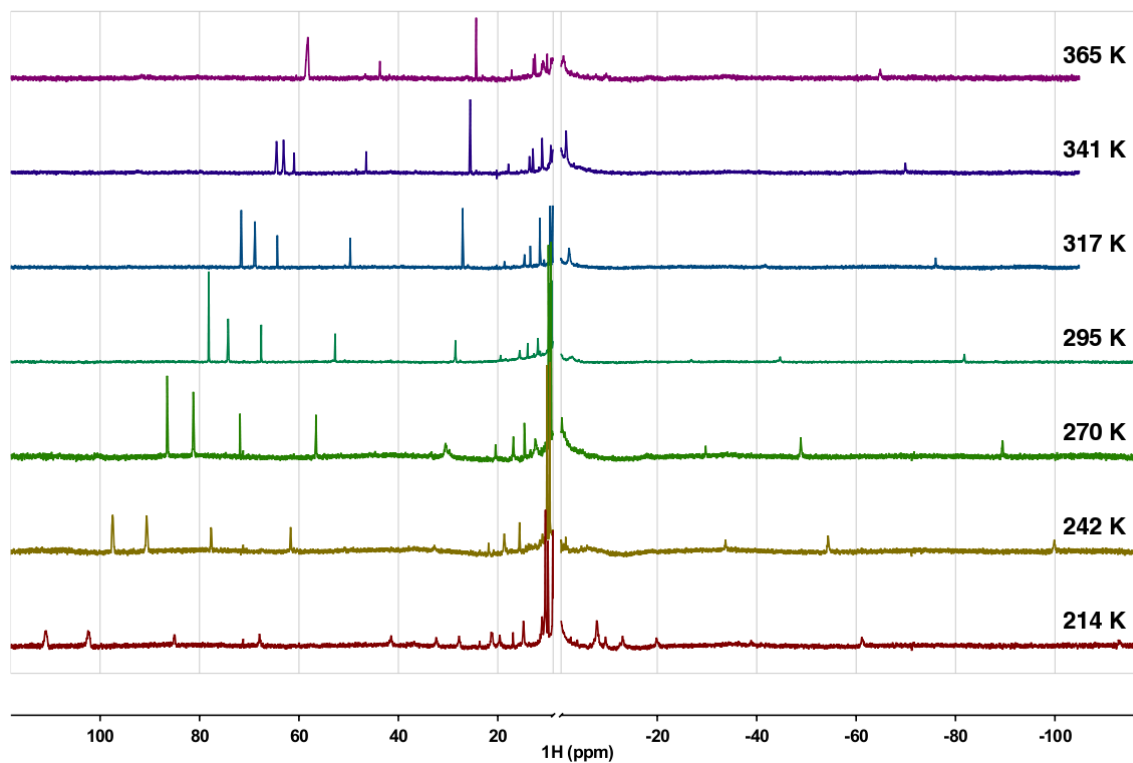


Figure 5.12. Variable temperature ^1H NMR of $(^{\text{Ar}}\text{dpme})\text{Co}(\text{indoline})$ in $\text{toluene-}d_8$ at 400 MHz. Diamagnetic region omitted for better clarity of paramagnetic peaks. Temperatures calibrated using the difference in chemical shifts of methylene and hydroxy protons in a sample either 4% methanol in $\text{methanol-}d_4$ (< 273 K) or ethylene glycol (> 273 K).

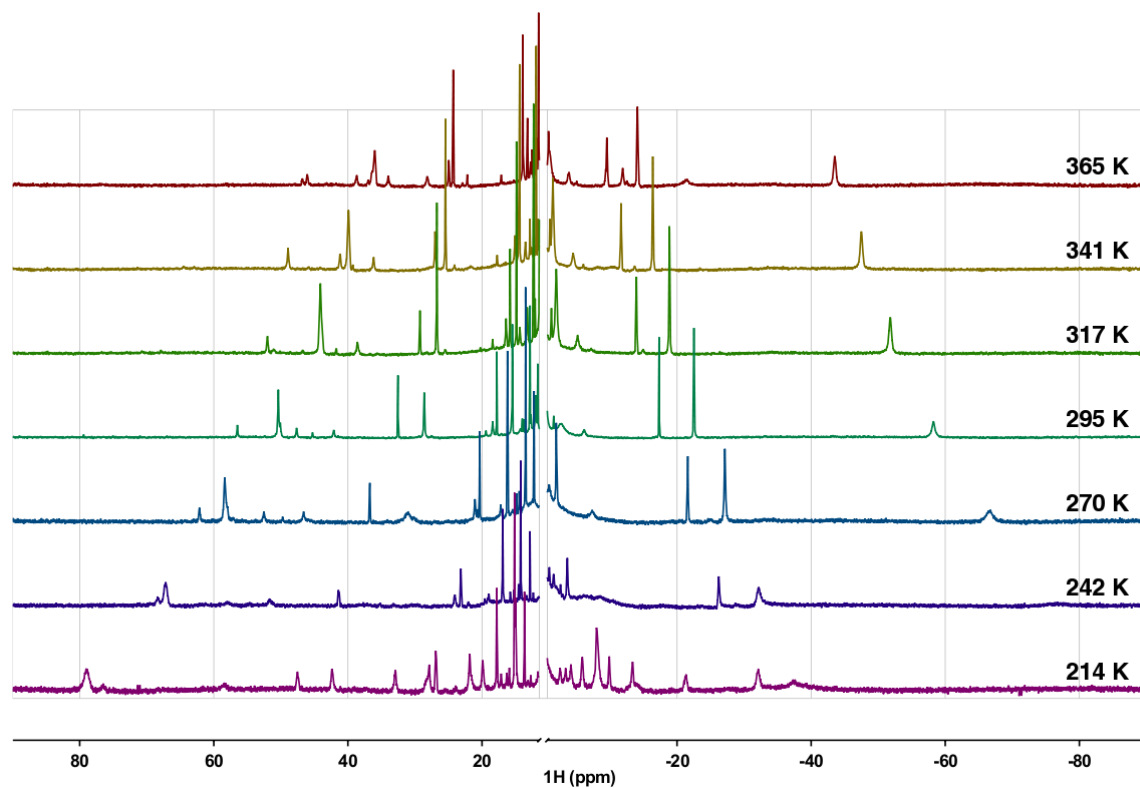


Figure 5.13. Variable temperature ^1H NMR of $(^{\text{Ar}}\text{dpme})\text{Co}(\text{NMes})\text{-}d_{11}$ in toluene- d_8 at 400 MHz. Diamagnetic region omitted for better clarity of paramagnetic peaks. Temperatures calibrated using the difference in chemical shifts of methylene and hydroxy protons in a sample either 4% methanol in methanol- d_4 (< 273 K) or ethylene glycol (> 273 K).

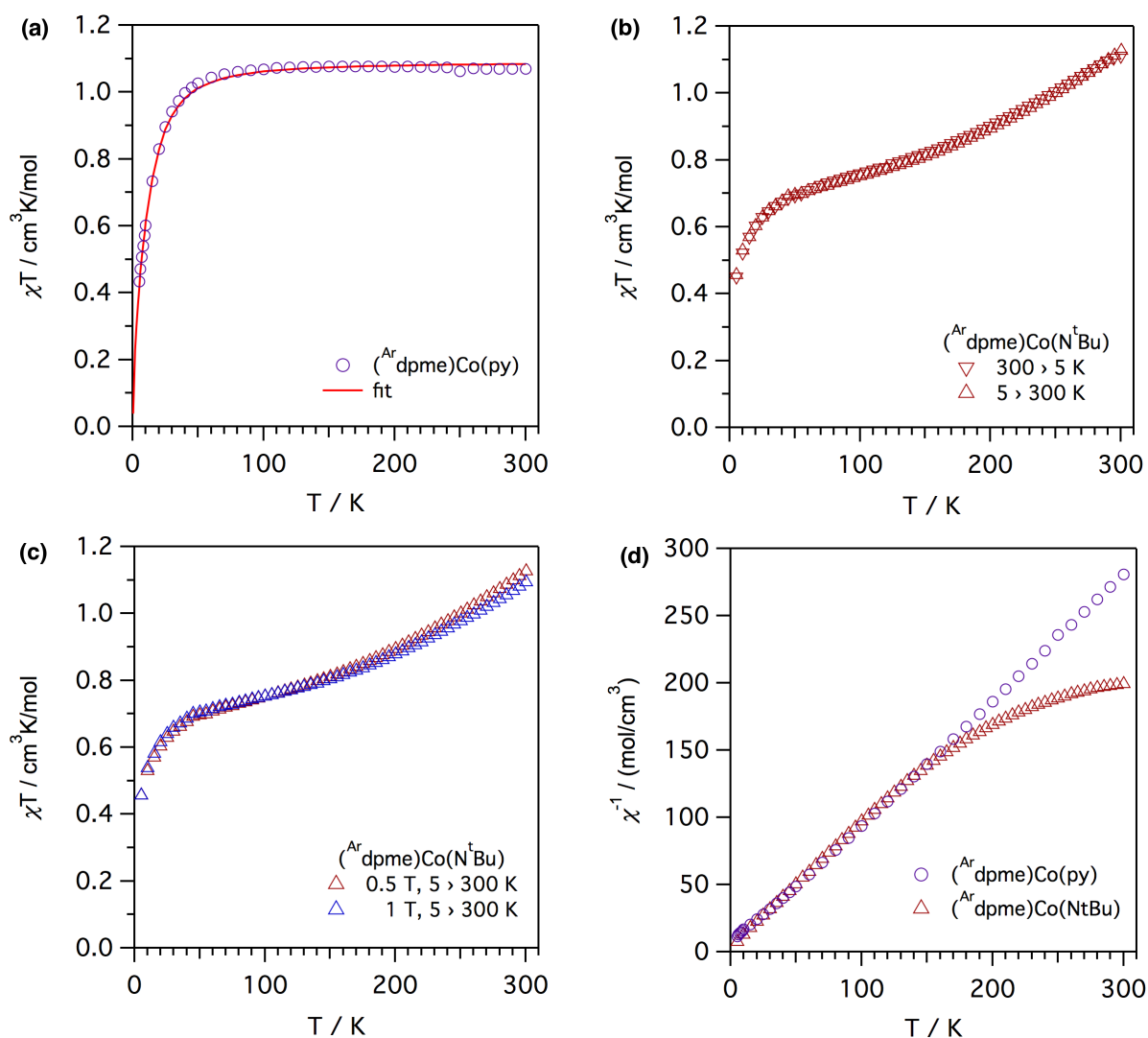


Figure 5.14. Magnetic susceptibility data for $(^{\text{Ar}}\text{dpme})\text{Co}(\text{py})$ and $(^{\text{Ar}}\text{dpme})\text{Co}(\text{N}^t\text{Bu})$. (a) $\chi_M T$ vs. T for $(^{\text{Ar}}\text{dpme})\text{Co}(\text{py})$ at 0.5 T from 5 K to 300 K and the corresponding fit (parameters: $g = 2.09$, $D = -35.8 \text{ cm}^{-1}$, $J = -0.11 \text{ cm}^{-1}$);²⁸ (b) $\chi_M T$ vs. T for $(^{\text{Ar}}\text{dpme})\text{Co}(\text{N}^t\text{Bu})$ at 0.5 T going from 300 to 5 K, and from 5 K to 300 K; (c) $\chi_M T$ vs. T for $(^{\text{Ar}}\text{dpme})\text{Co}(\text{N}^t\text{Bu})$ at 0.5 T and 1 T going from 5 K to 300 K; and (d) χ_M^{-1} vs. T for $(^{\text{Ar}}\text{dpme})\text{Co}(\text{py})$ and $(^{\text{Ar}}\text{dpme})\text{Co}(\text{N}^t\text{Bu})$.²⁹

(28) Using Eq. 5.4, see 5-7. Experimental Methods.

(29) Using Eq. 5.1 and Eq. 5.5, see 5-3. Isolation of an Alkyl Cobalt Imide, and 5-7. Experimental Methods.

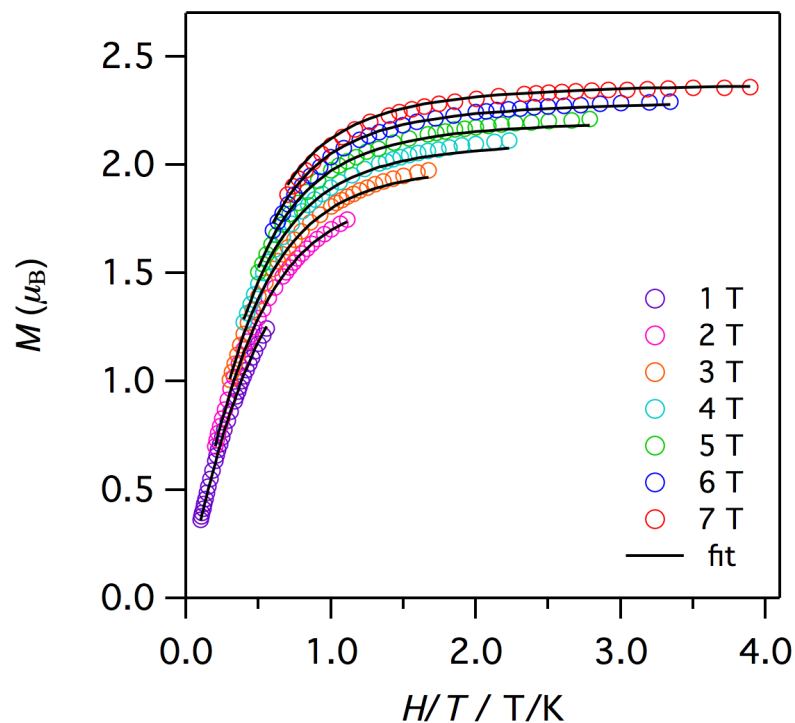


Figure 5.15. Reduced magnetization data (M vs. H/T) for $(^{\text{Ar}}\text{dpme})\text{Co}(\text{N}'\text{Bu})$. Collected at 7 fields (1–7 T) over the temperature range (1.8 K – 10 K). Reduced magnetization fit parameters: g 1.78, $D = -6.93 \text{ cm}^{-1}$, and $E = -1.94 \text{ cm}^{-1}$ from ANISOFIT.¹⁸ Data is scaled (by $1/0.256$) to account for the high-spin ($S = 2$) fraction making up 25.6% of the fraction as determined from a Boltzmann fit of the $\chi_{\text{M}}T$ vs. T plot (see **Figure 5.2**).

X-ray Diffraction Techniques.

Structures of $(^{\text{Ar}}\text{dpme})\text{CoCl}(\text{py})$, $(^{\text{Ar}}\text{dpme})\text{Co}(\text{py})$, $(^{\text{Ar}}\text{dpme})\text{Co}(\text{N}_4\text{Ar}^{\text{NMe}_2})$ and $(^{\text{Ar}}\text{dpme})\text{Co}(\text{N}'\text{Bu})$ were collected on a Brüker three-circle platform goniometer equipped with an Apex II CCD and an Oxford cryostream cooling device. Radiation was from a graphite fine focus sealed tube Mo $K\alpha$ (0.71073 Å) source. Crystals were mounted on a cryoloop or glass fiber pin using Paratone N oil. Structures were collected at 100 K. Data was collected as a series of φ and/or ω scans. The structures of $(^{\text{Ar}}\text{dpme})\text{Co}(\text{N}_4'\text{Bu}_2)$ and $(^{\text{Ar}}\text{dpme})\text{Co}(\text{indoline})$ were obtained on the ChemMatCARS beamline at the Advanced Photon Source at Argonne National Labs (Argonne, IL). Absorption parameters, f' and f'' , for all heavy atoms (Co, O, N, C) were adjusted to the appropriate values for the

synchrotron wavelength of 0.41328 Å during refinement. Data was integrated using SAINT³⁰ and scaled with either a numerical or multi-scan absorption correction using SADABS.³⁰ The structures were solved by direct methods or Patterson maps using SHELXS-97³¹ and refined against F^2 on all data by full matrix least squares with SHELXL-97.³¹ All non-hydrogen atoms were refined anisotropically. Hydrogen atoms were placed at idealized positions and refined using a riding model. The isotropic displacement parameters of all hydrogen atoms were constrained to be 1.2 times the parameter of the atoms they were linked to (1.5 times for methyl groups). Further details on particular structures are noted below.

(^{Ar}dpme)CoCl(py): The structure was solved in the triclinic space group $P\bar{1}$ with 4 molecules per unit cell, and 2 molecules in the asymmetric unit.

(^{Ar}dpme)Co(py): The structure was solved in the monoclinic space group $C2/c$ with 2 molecules per unit cell and half of a molecule in the asymmetric unit. The cobalt, pyridine nitrogen, and 4 carbon atoms of the pyridine or mesityl group lie on the crystallographic mirror plane. The hydrogens of the *para*-methyl group were refined as half-occupied to account for their disorder about the mirror plane.

(^{Ar}dpme)Co(N₄Ar^{NMe₂})₂: The structure was solved in the triclinic space group $P\bar{1}$ with 2 molecules per unit cell. The asymmetric unit also contained one molecule of pentane, with one atom on an inversion center. It was refined with the help of similarity and rigid bond restraints on the anisotropic displacement parameters.

(^{Ar}dpme)Co(N⁴Bu₂): The structure was solved in the triclinic space group $P\bar{1}$ with 2 molecules per unit cell, and half of the molecule in the asymmetric unit. The asymmetric unit also contained one molecule of ether, which was located near an inversion center. It was refined with the help of similarity and rigid bond restraints on the anisotropic displacement parameters.

(30) APEX2 Software Suite; Bruker AXS: Madison, WI, 2009.

(31) Sheldrick, G. M. Acta Crystallogr., Sect. A: Found. Crystallogr. **2008**, 64, 112-122.

(^{Ar}dpme)Co(N^tBu): The structure was solved in the triclinic space group $P\bar{1}$ with 2 molecules per unit cell. The asymmetric unit also contained half of three solvent molecules. Two of the solvent sites were benzene, while the third was best refined as a substitutional disorder of 83% *n*-hexane and 17% benzene.

(^{Ar}dpme)Co(indoline): The structure was solved in the triclinic space group $P\bar{1}$ with 2 molecules per unit cell. The asymmetric unit also one whole molecule of diethyl ether and one half ether which was disordered about an inversion center. The disordered molecule was refined by locating two positions for the ethyl arm, each with 50% occupancy. Both ethers were refined with the help of similarity and rigid bond restraints on the anisotropic displacement parameters. The hydrogen atoms of the amide and alkyl carbon were found in the difference map. Their positions were refined semi-freely with distance restraints ($d(\text{N-H})$ 0.88 Å, and $d(\text{C-H})$ 0.99 Å) The isotropic displacement parameters for the hydrogens were constrained to be 1.2 times that of the heavy atom.

Table 5.3. Metal-Ligand Bond Lengths of Dipyrrromethene Complexes.

complex	Bond lengths (Å)					
	^{Ar} dpme		Co-Cl	py/imide	tetrazene/indoline	
	Co-N(1)	Co-N(2)		Co-N(3)	Co-N(3)	Co-N(6)
(^{Ar} dpme)CoCl(py)	1.992(1)	1.996(1)	2.2468(4)	2.040(1)	–	–
(^{Ar} dpme)Co(py)	1.960(3)	1.960(3)	–	1.942(4)	–	–
(^{Ar} dpme)Co(N ₄ Ar ^{NMe₂})	1.959(3)	1.975(3)	–	–	1.921(3)	1.913(3)
(^{Ar} dpme)Co(N ₄ ^t Bu ₂)	1.979(6)	1.966(6)	–	–	1.943(7)	1.898(7)
(^{Ar} dpme)Co(N ^t Bu)	1.919(2)	1.923(2)	–	1.609(3)	–	Co-C(1)
(^{Ar} dpme)Co(indoline)	1.926(3)	1.993(3)	–	–	1.845(3)	2.022(4)

Table 5.4. X-ray diffraction experimental details.

	(^{Ar} dpme)CoCl(py)	(^{Ar} dpme)Co(py)	(^{Ar} dpme)Co(N ₄ Ar ^{NMe₂})	(^{Ar} dpme)Co(N ₄ ^t Bu ₂)	(^{Ar} dpme)Co(N ^t Bu)	(^{Ar} dpme)Co(indoline)
Moiety Formula	C ₇₁ H ₅₄ ClCoN ₃	C ₇₁ H ₅₄ CoN ₃	C ₈₂ H ₆₉ CoN ₈ ; C ₅ H ₁₂	C ₇₄ H ₆₇ CoN ₆ ; C ₄ H ₁₀ O	C ₇₀ H ₄₈ CoN ₃ ; 1.08×(C ₆ H ₆); 0.42×(C ₆ H ₁₄)	C ₇₅ H ₆₀ CoN ₃ ; 1.5×(C ₄ H ₁₀ O)
FW	1043.55	1008.10	1291.52	1173.39	1120.64	1173.37
λ (nm)	0.71073	0.71073	0.71073	0.41328	0.71073	0.41328
T (K)	100(2)	100(2)	100(2)	100(2)	100(2)	100(2)
Crystal System	triclinic	monoclinic	triclinic	triclinic	triclinic	triclinic
Space Group (Z)	<i>P</i> $\bar{1}$ (4)	<i>C</i> 2/c (4)	<i>P</i> $\bar{1}$ (2)	<i>P</i> $\bar{1}$ (2)	<i>P</i> $\bar{1}$ (2)	<i>P</i> $\bar{1}$ (2)
a (Å)	11.6333(3)	20.485(2)	12.5057(10)	11.464(3)	11.8393(19)	11.7041(13)
b (Å)	15.5748(4)	17.5727(17)	12.8018(10)	14.775(5)	16.045(3)	16.763(2)
c (Å)	32.6991(8)	14.6905(15)	21.6877(18)	18.824(4)	16.392(3)	17.822(2)
α (°)	101.060(1)	90	75.774(1)	93.842(6)	89.362(3)	70.312(2)
β (°)	99.252(1)	94.802(2)	81.273(1)	102.272(4)	87.774(3)	70.894(2)
γ (°)	110.141(1)	90	81.329(1)	101.405(4)	72.658(3)	78.788(2)
Volume (Å³)	5443.0(2)	5269.7(9)	3319.8(5)	3034.2(15)	7096.1(10)	3097.0(6)
Calc. ρ (mg/m³)	1.273	1.271	1.292	1.284	1.253	1.258
μ (mm⁻¹)	0.411	0.373	0.314	0.184	0.338	0.180
Crystal Size (mm)	0.74×0.21×0.15	0.16×0.16×0.16	0.24×0.15×0.12	0.02×0.02×0.02	0.43×0.17×0.09	0.02×0.02×0.02
Reflections	114945	44229	60394	9629	51555	58807
Comp. (%)	100.0	100.0	100.0	96.3	99.9	95.8
to 2(θ)	(27.48°)	(27.48°)	(25.68°)	(13.90°)	(27.10°)	(14.60°)
GOF on F²	1.010	1.047	1.030	1.060	1.010	1.042
R1, wR2^a						
[I > 2σ(I)]	0.0421, 0.0836	0.0743, 0.2230	0.0584, 0.1520	0.1122, 0.2797	0.0499, 0.1056	0.0658, 0.1645
(R1, wR2)						
[all data]	0.0727, 0.0946	0.1043, 0.2461	0.0960, 0.1742	0.1934, 0.3127	0.0930, 0.1222	0.1095, 0.1928

^aR1 = $\sum||F_o| - |F_c|| / \sum|F_o|$, wR2 = $\{\sum[w(F_o^2 - F_c^2)^2] / \sum[w(F_o^2)^2]\}^{1/2}$

Appendix A: Crystallographically Characterized Compounds

The following is a listing of all compounds that have been synthesized and crystallography characterized during the course of this thesis. Cases with poor quality data are noted. Compounds labeled *gae* and *bpk* were synthesized by Guy Edouard and Barrett Kenny, respectively, during their undergraduate research projects in the Betley Lab. The compounds labeled *abs* was structurally characterized by Austin Scharf and appears in Chapter 3. Elisabeth Hennessy is solely responsible for the compounds labeled *eth*, but they are included here for completeness as they appear in Chapter 4.

Table A.1. List of crystallographically characterized compounds.

compound/notes	dataset	structure
(dpma)Mn(py) ₂	erk004	
(dpma)Fe(py) ₂	erk002	
(dpma)Fe(bpy)	erk037	
[(dpma)CoCl(thf)][Li(thf) ₂]	erk001	See Chapter 2
(dpma)Co(py) ₂	erk006	
(dpma)Ni(py) ₂	erk004	
(dpma)Zn(py) ₂	erk034	
(C ₄ HN) ₂ CMe ₂	erk009	
(^{Mes} dpme)FeCl(thf)	erk012	
(^{Mes} dpme)FeCl(py)	abs1031	
(^{Mes} dpme–NAd)FeCl	erk029	
(^{Mes} dpme)ZnCl(py)	erk031	
^{Ar} dpmeH	erk042	See Chapter 4
(^{tBu} dpme)FeCl(thf)	eth1	
(^{Ad} dpme)FeCl(OEt ₂)	eth2	
(^{Ar} dpme)FeCl	erk044	
(^{Ar} dpme)	erk045	
(^{Ar} dpme)FeCl(NAr ^{tBu})	erk059	
(^{Ar} dpme)Co(py)	erk063	See Chapter 5
(^{Ar} dpme)CoCl(py)	erk060	
(^{Ar} dpme)Co(N ₄ Ar ^{NMe₂})	erk068	
(^{Ar} dpme)Co(N ₄ ^{tBu}) – collected at APS	ek2	
(^{Ar} dpme)Co(N ^{tBu})	erk070	
(^{Ar} dpme)Co(indoline) – collected at APS	ek1	

Table A.1. (continued)

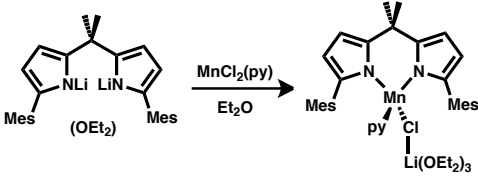
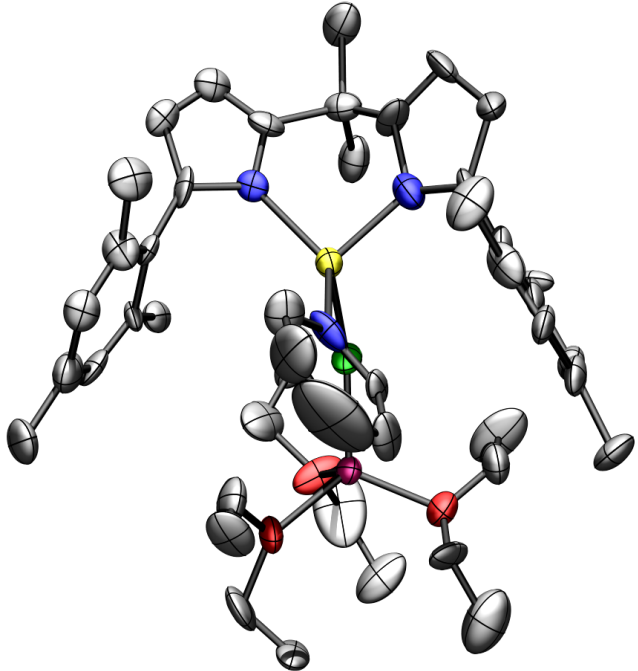
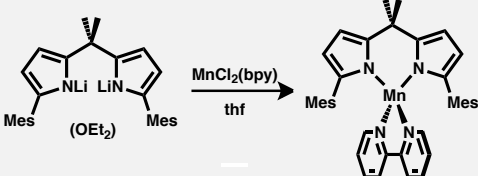
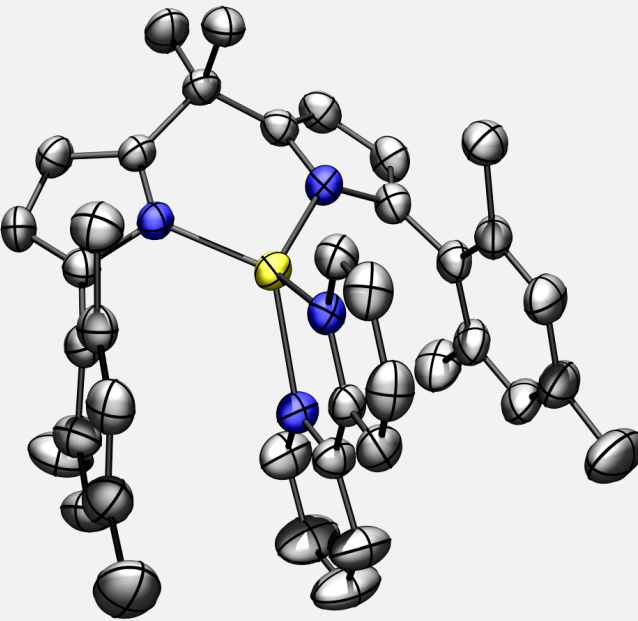
compound/notes	dataset	structure
<p>[(dpma)MnCl(py)][Li(OEt₂)₃]</p> 	erk003	
<p>(dpma)Mn(bpy)</p> 	erk033	

Table A.1. (continued)

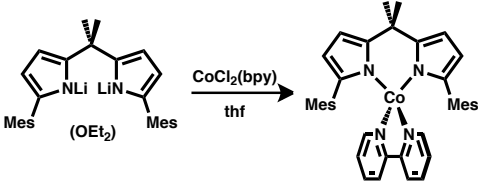
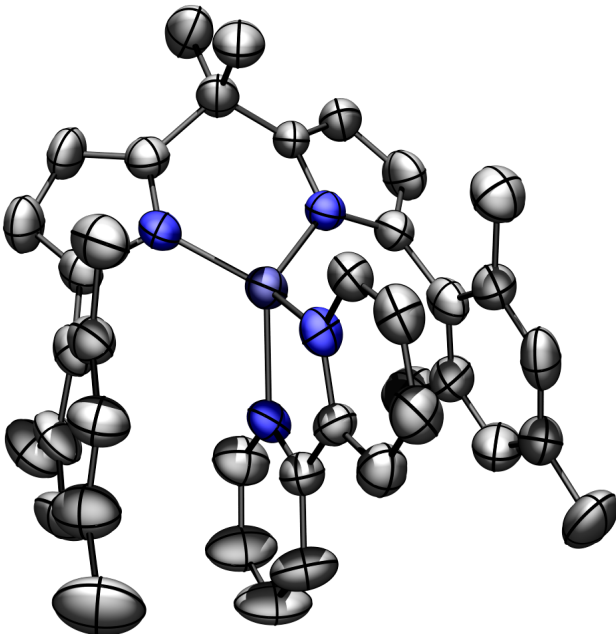
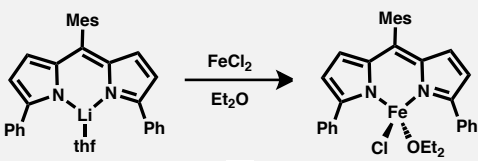
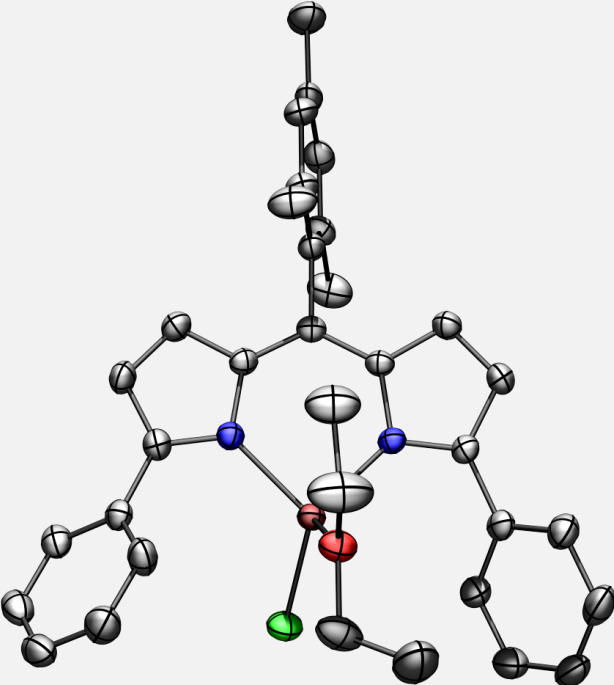
compound/notes	dataset	structure
<p>(dpma)Co(bpy)</p> <p>erk032</p> 		
<p>(^{Ph}dpme)FeCl(OEt₂)</p> <p>bpk001 (erk021)</p> 		

Table A.1. (continued)

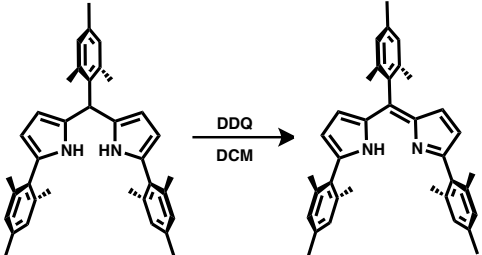
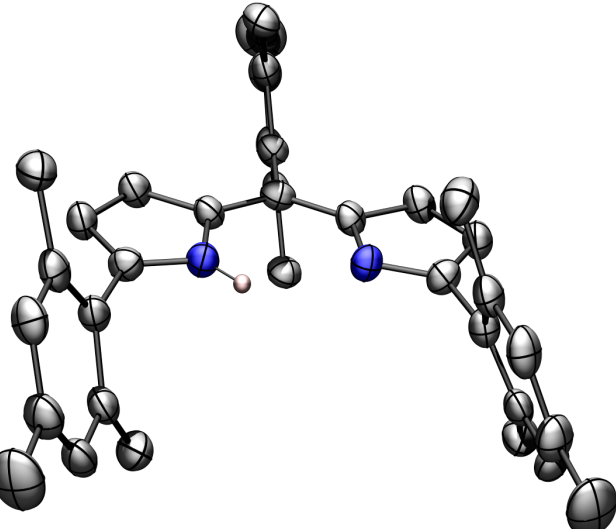
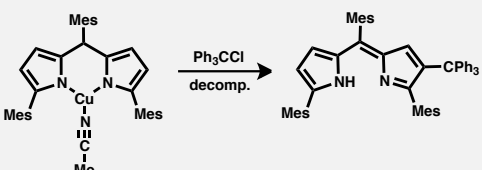
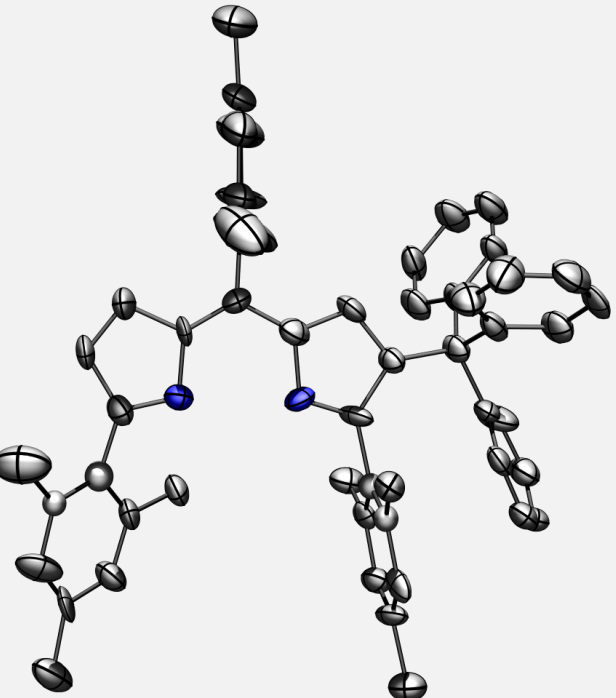
compound/notes	dataset	structure
<p data-bbox="337 300 451 331">^{Mes}dpmeH</p> 	<p data-bbox="630 289 703 321">erk011</p> <p data-bbox="630 321 703 352">erk015</p>	
<p data-bbox="240 888 548 951">2-Ph₃C-^{Mes}dpmeH (poor data – weak diffraction)</p> 	<p data-bbox="630 909 703 940">gae014</p>	

Table A.1. (continued)

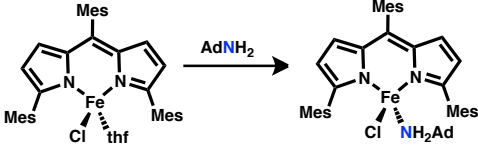
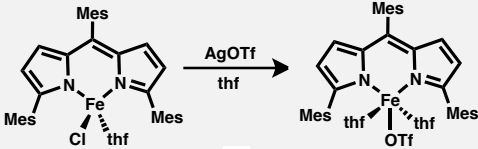
compound/notes	dataset	structure
$(^{\text{Mes}}\text{dpme})\text{FeCl}(\text{NH}_2\text{Ad})$ 	erk029	
$(^{\text{Mes}}\text{dpme})\text{Fe}(\text{OTf})(\text{thf})_2$ 	erk027	

Table A.1. (continued)

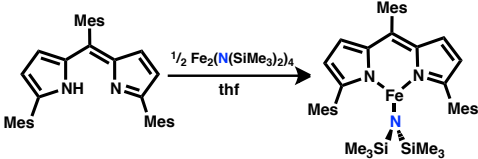
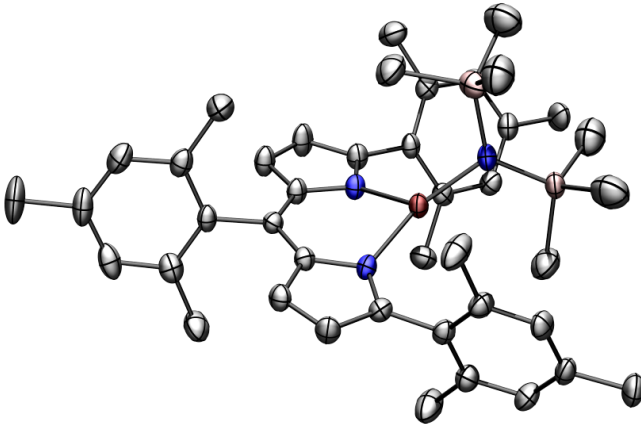
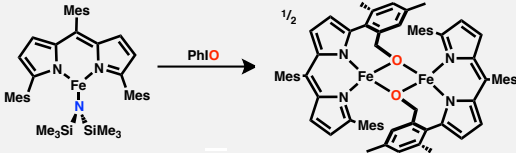
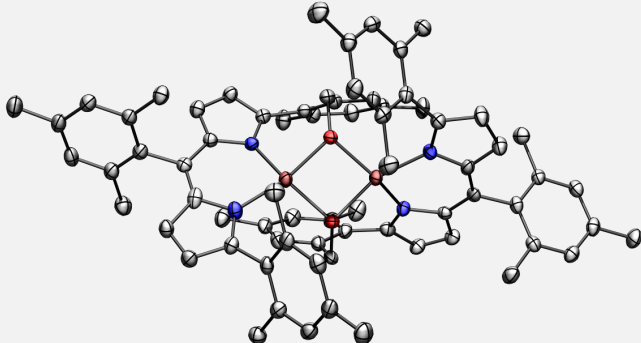
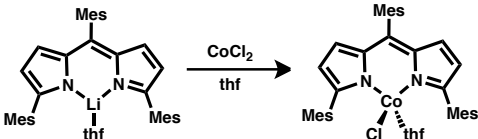
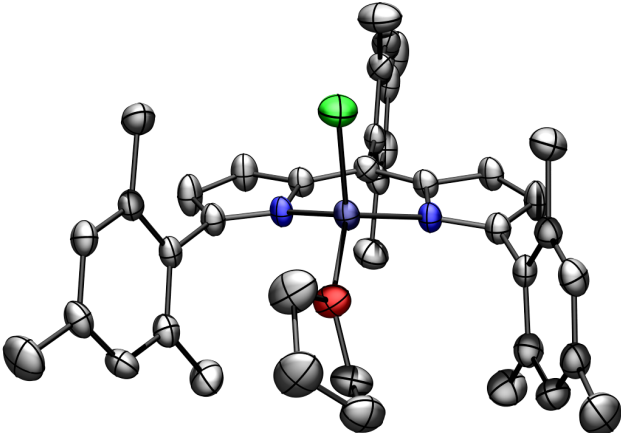
compound/notes	dataset	structure
$(^{\text{Mes}}\text{dpme})\text{Fe}(\text{N}(\text{SiMe}_3)_2)$ 	gae009	
$[(^{\text{Mes}}\text{dpme}-\mu^2\text{-O})\text{Fe}]$ 	gae013	
$(^{\text{Mes}}\text{dpme})\text{CoCl}(\text{thf})$ 	erk014	

Table A.1. (continued)

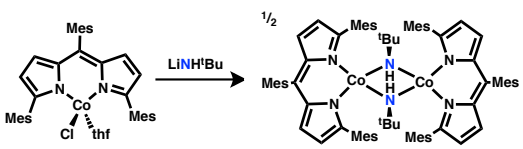
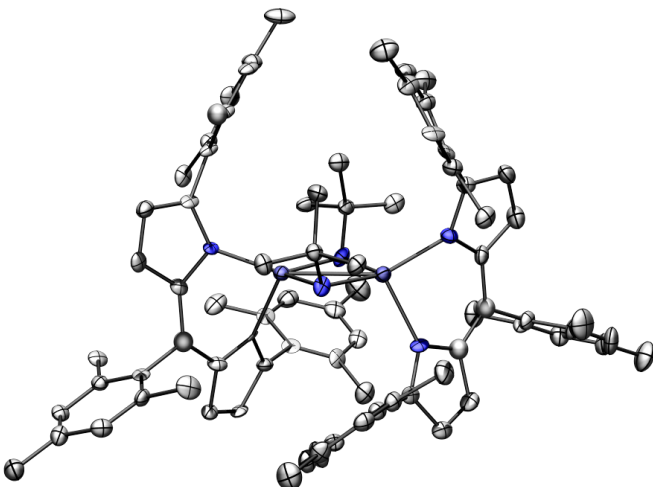
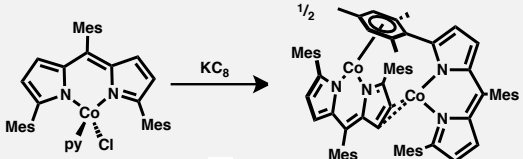
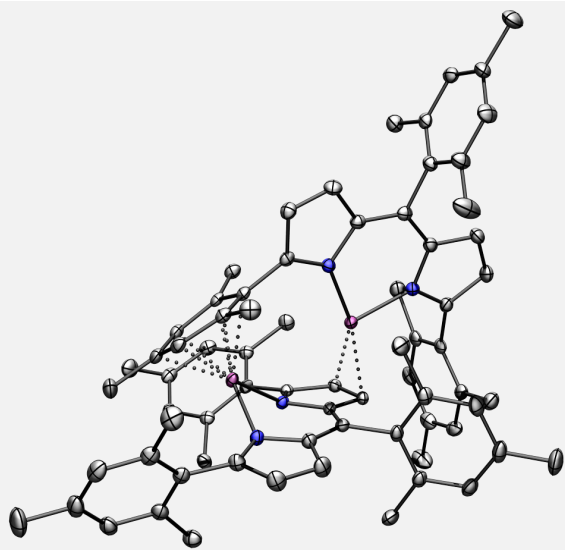
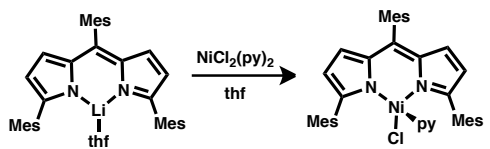
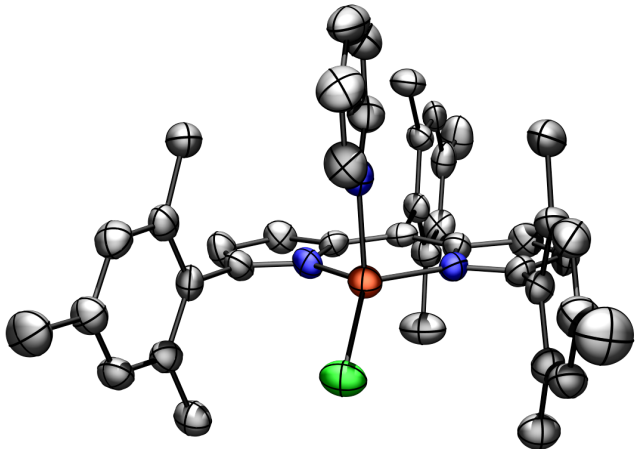
compound/notes	dataset	structure
$[(^{\text{Mes}}\text{dpme})\text{Co}]_2(\mu^2\text{-NH}^t\text{Bu})_2$ 	gae005 (erk036)	
$(^{\text{Mes}}\text{dpme})_2\text{Co}_2$ 	erk082	
$(^{\text{Mes}}\text{dpme})\text{NiCl}(\text{py})$ 	erk016	

Table A.1. (continued)

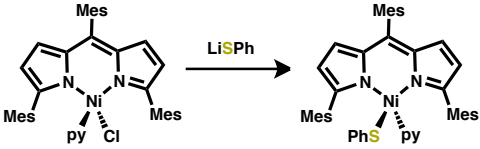
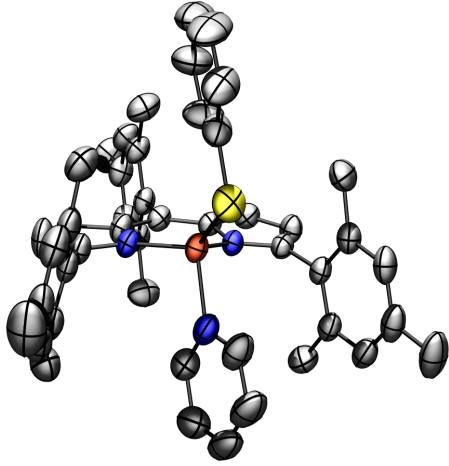
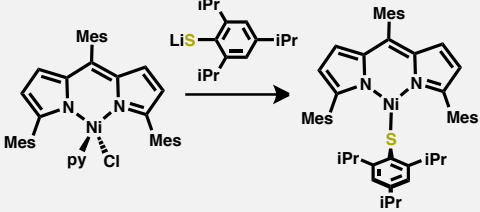
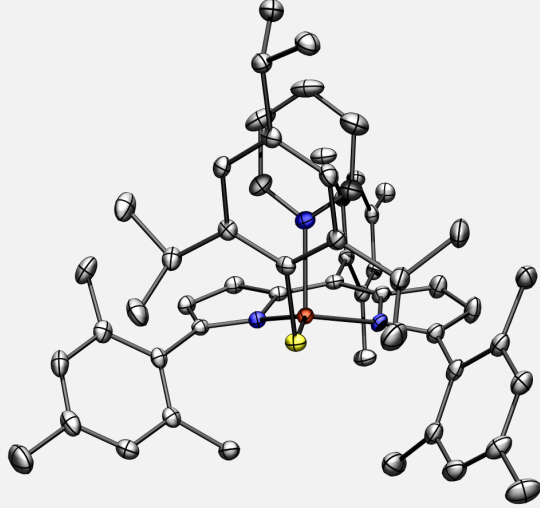
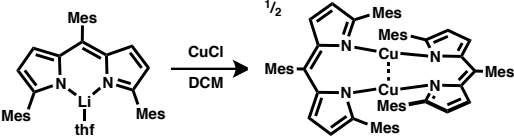
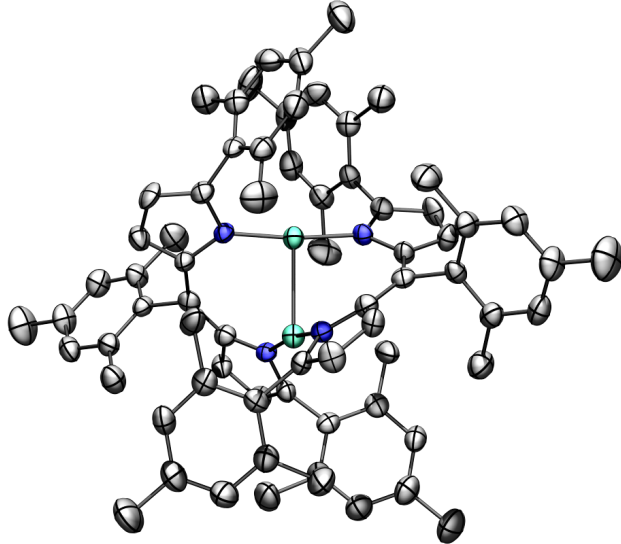
compound/notes	dataset	structure
$(^{\text{Mes}}\text{dpme})\text{Ni}(\text{SPh})(\text{py})$ 	bpk003	
$(^{\text{Mes}}\text{dpme})\text{Ni}(\text{S}(\text{trip}))(\text{py})$ 	bpk004	
$[(^{\text{Mes}}\text{dpme})\text{Cu}]_2$ 	gae002 (erk022)	

Table A.1. (continued)

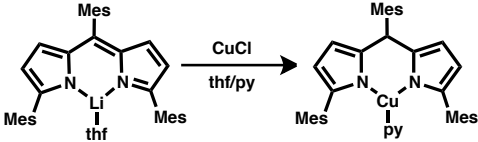
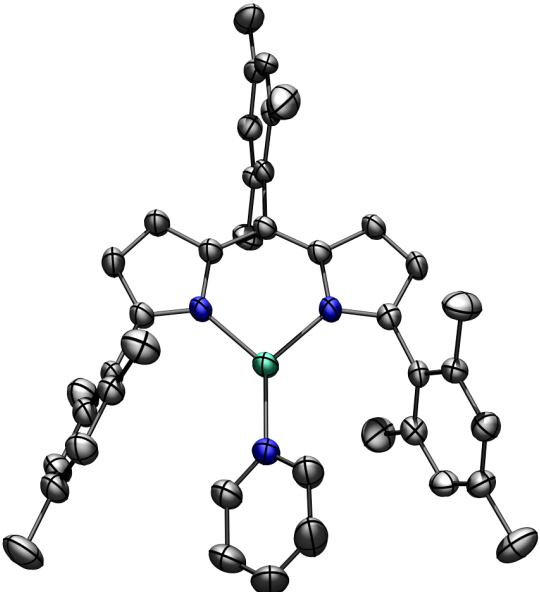
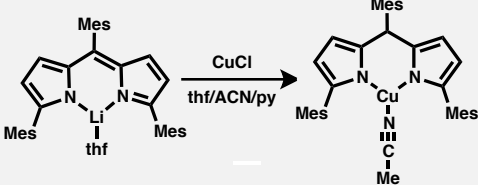
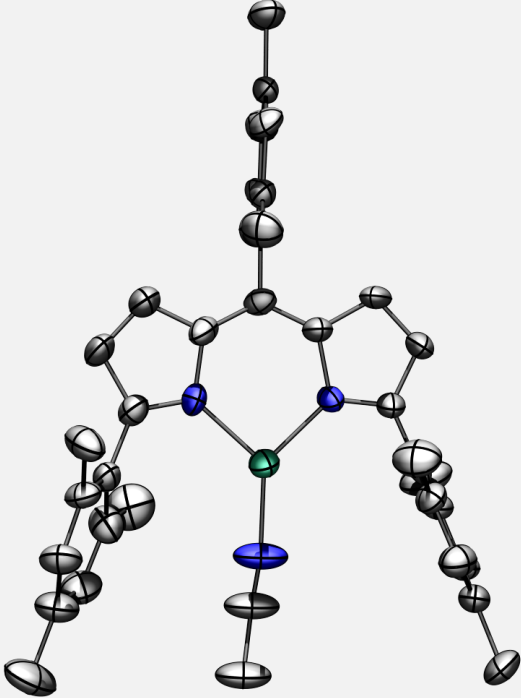
compound/notes	dataset	structure
$(^{\text{Mes}}\text{dpme})\text{Cu}(\text{py})$ 	erk018	
$(^{\text{Mes}}\text{dpme})\text{Cu}(\text{NCMe})$ 	gae001 (erk019) (erk020)	

Table A.1. (continued)

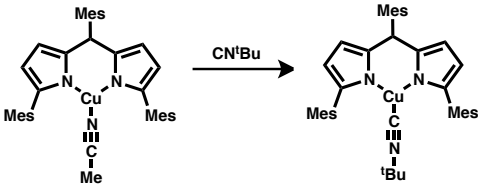
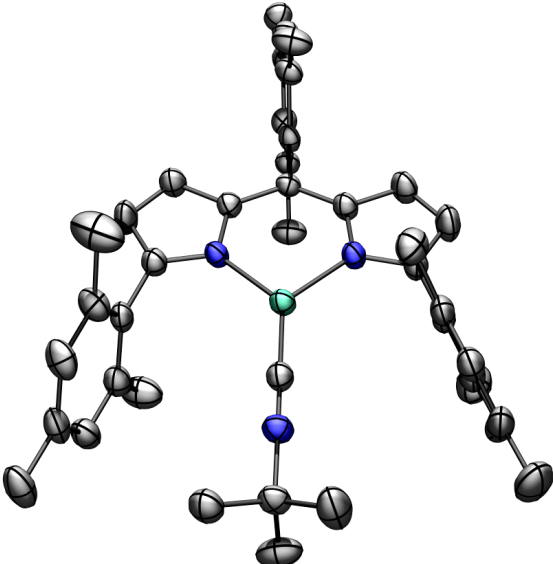
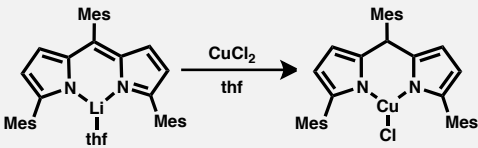
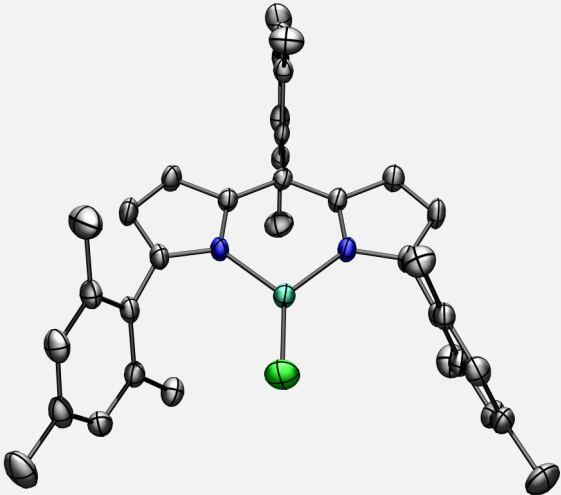
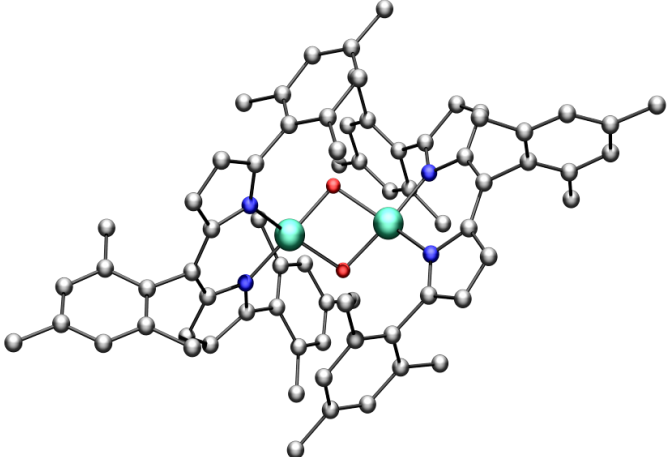
compound/notes	dataset	structure
$(^{\text{Mes}}\text{dpme})\text{Cu}(\text{CN}^t\text{Bu})$ 	gae007	
$(^{\text{Mes}}\text{dpme})\text{CuCl}$ 	gae003 (erk028)	
$[(^{\text{Mes}}\text{dpme})\text{Cu}]_2(\mu^2\text{-OH})_2$ (poor data – weak diffraction)	gae006	

Table A.1. (continued)

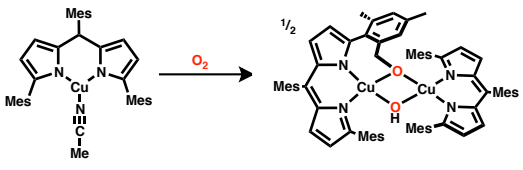
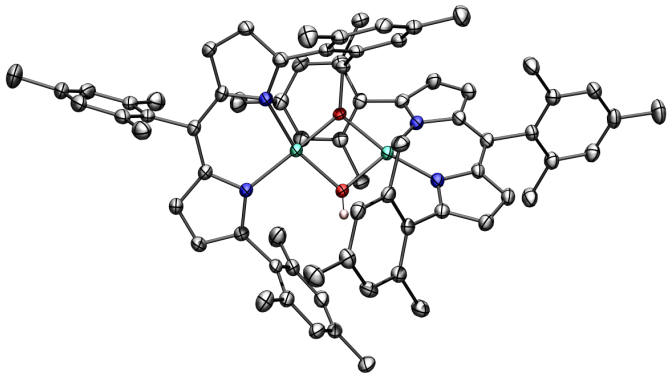
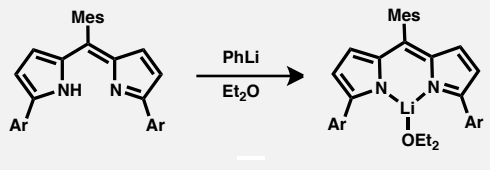
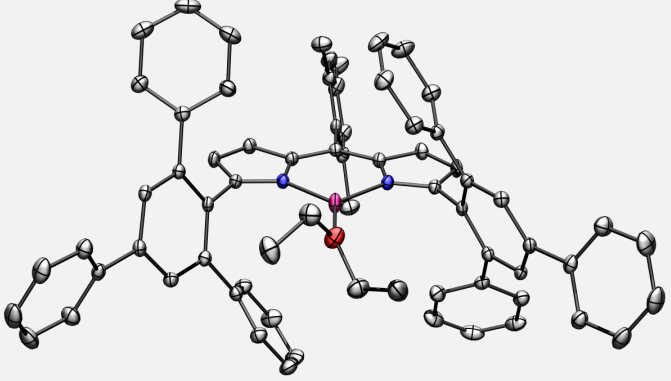
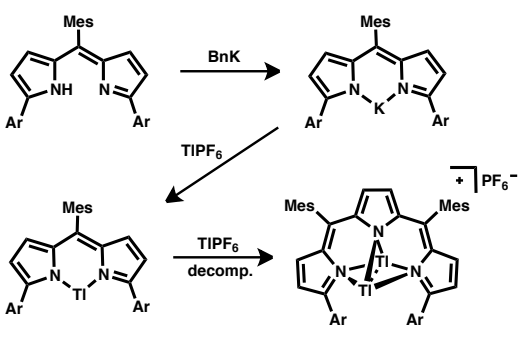
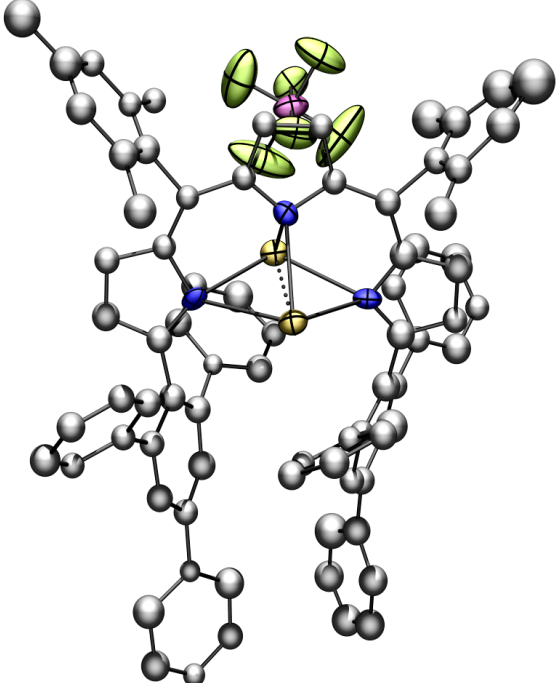
compound/notes	dataset	structure
$(^{\text{Mes}}\text{dpme})(^{\text{Mes}}\text{dpme}-\mu^2\text{-O})\text{Cu}_2(\mu^2\text{-OH})$ 	gae012	
$(^{\text{Ar}}\text{dpme})\text{Li}(\text{OEt}_2)$ 	erk065	
$[\{\text{C}_4\text{H}_2\text{N}-2,5\text{-(CMes-2-C}_4\text{H}_2\text{N-5-Ar)}_2\}\text{Tl}_2][\text{PF}_6]$ (partial data) erk056 	erk056	

Table A.1. (continued)

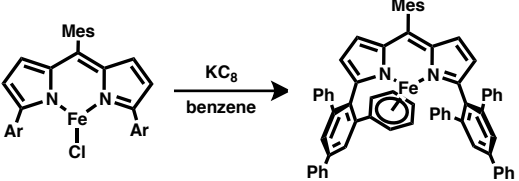
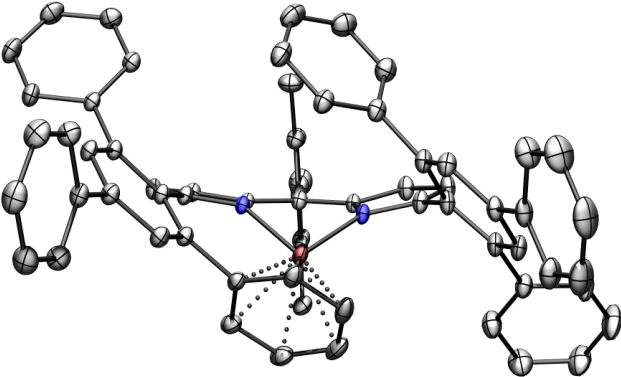
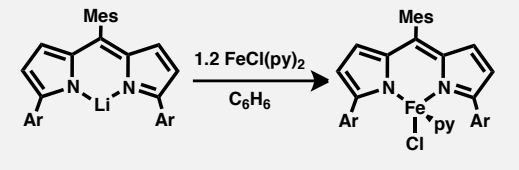
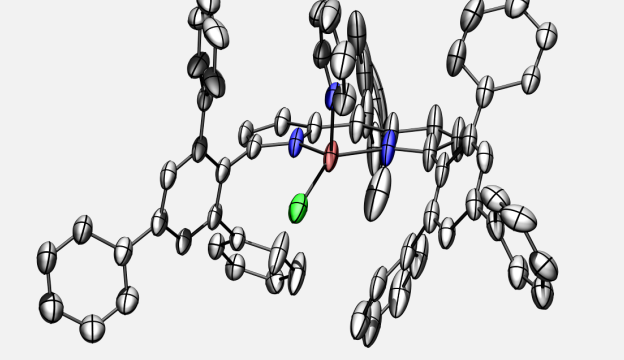
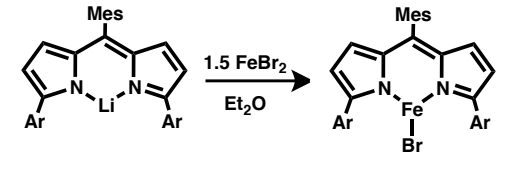
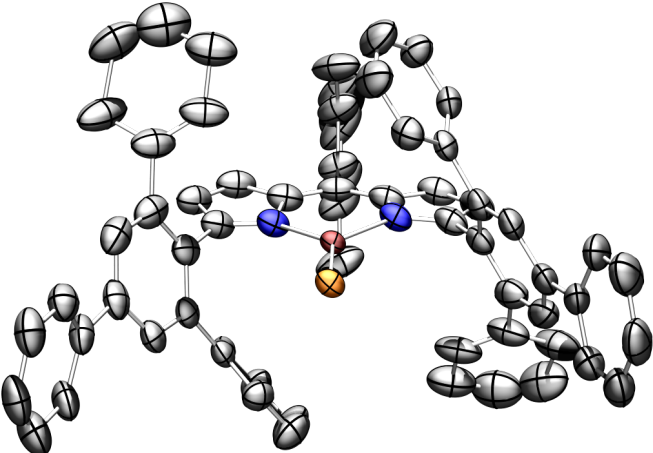
compound/notes	dataset	structure
<p>(^{Ar}dpme)Fe erk103 collected at APS</p> 	<p>erk103 erk057</p>	
<p>(^{Ar}dpme)FeCl(py) (poor data – highly twinned)</p> 	<p>erk061</p>	
<p>(^{Ar}dpme)FeBr erk055</p> 	<p>erk055</p>	

Table A.1. (continued)

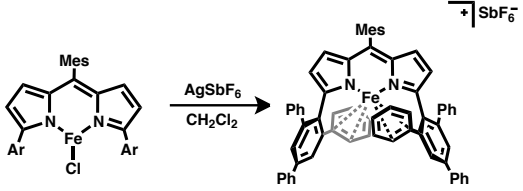
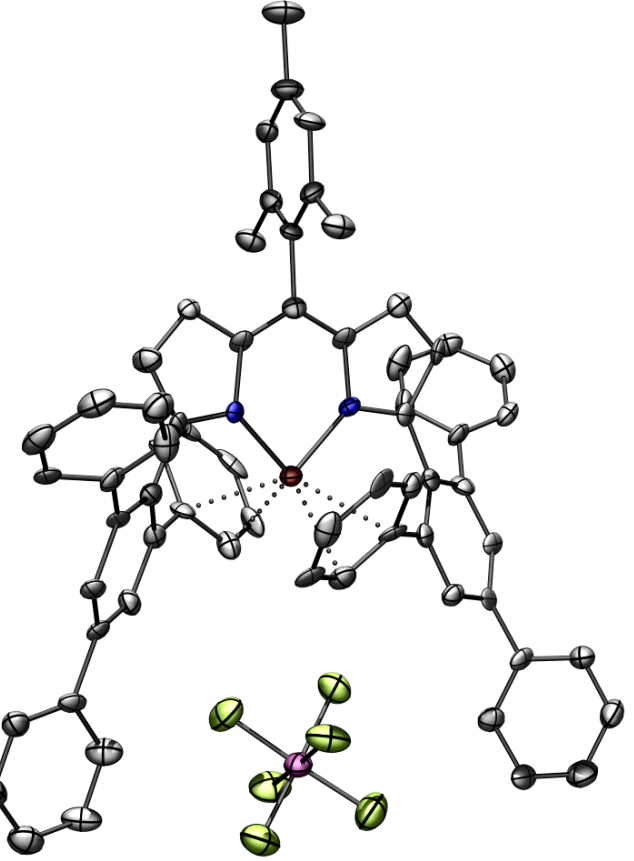
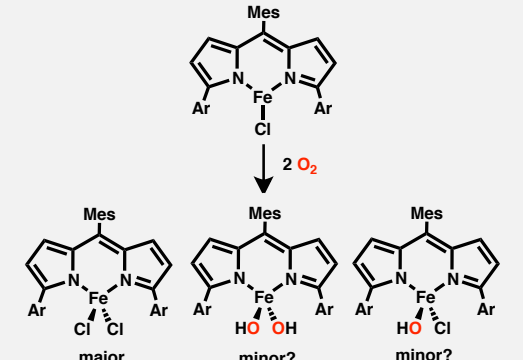
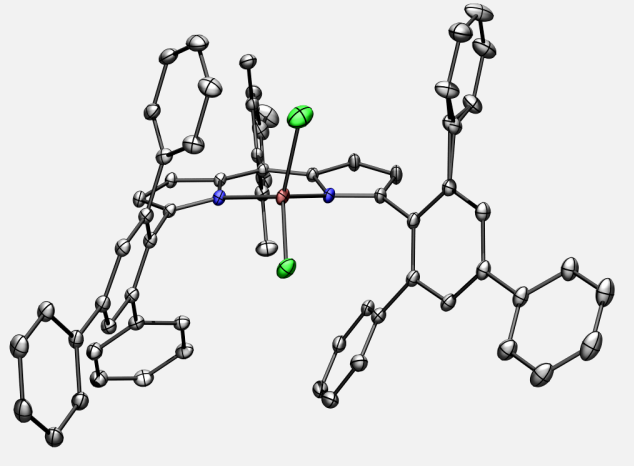
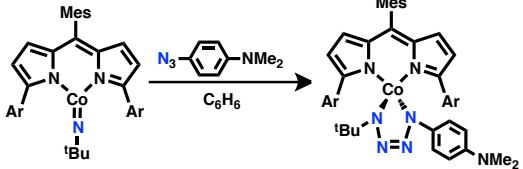
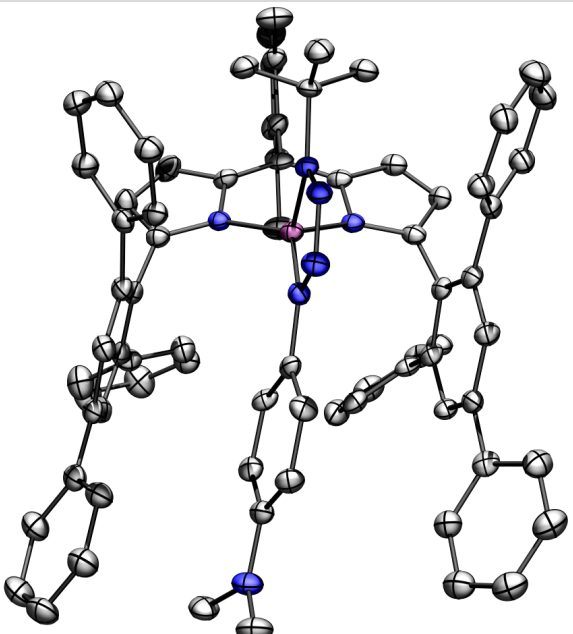
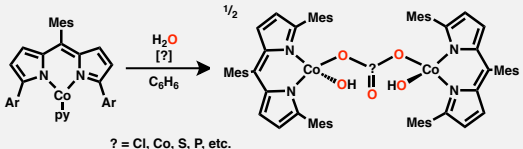
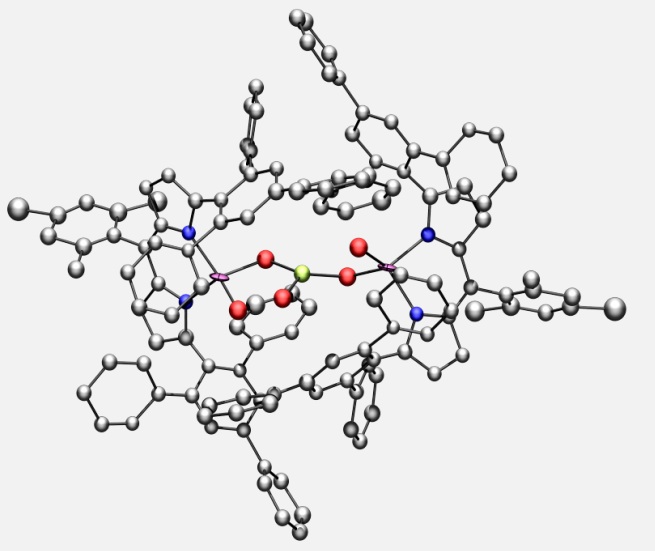
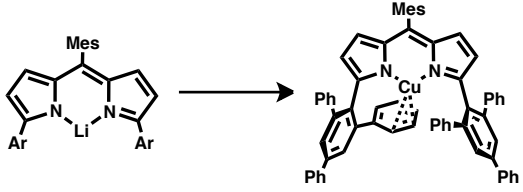
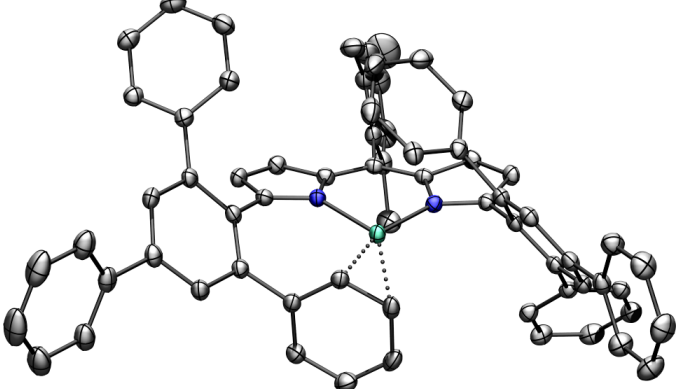
compound/notes	dataset	structure
<p>$[(^{\text{Ar}}\text{dpme})\text{Fe}][\text{SbF}_6]$</p> 	<p>erk052 erk052c</p>	
<p>$(^{\text{Ar}}\text{dpme})\text{FeCl}_2$ (FeCl_2 fragment is disorderd, may be partially $\text{FeCl}(\text{OH})$ and $\text{Fe}(\text{OH})_2$) erk101-collected at APS</p> 	<p>erk101 erk048</p>	

Table A.1. (continued)

compound/notes	dataset	structure
$(^{\text{Ar}}\text{dpme})\text{FeCl}(\text{OH})$ ($\text{FeCl}(\text{OH})$ fragment is disorderd, may be partially FeCl_2 and $\text{Fe}(\text{OH})_2$) erk102 collected at APS erk050	erk102 erk050	
$(^{\text{Ar}}\text{dpme})\text{Fe}(\text{N}_4\text{Ar}^{\text{NMe}_2})$ collected at APS	ek5	
$(^{\text{Ar}}\text{dpme})\text{Co}(\text{N}_4\text{Ad}_2)$	erk069	

Table A.1. (continued)

compound/notes	dataset	structure
<p data-bbox="259 304 527 336">$(^{\text{Ar}}\text{dpme})\text{Co}(\text{N}_4^{\text{tBuAr}^{\text{NMe}_2}})$</p> 	erk080	
<p data-bbox="259 903 552 934">$[(^{\text{Ar}}\text{dpme})\text{Co}(\text{OH})_2](\mu\text{-?O}_3)$</p> <p data-bbox="203 934 609 1155">(weakly diffracting, the identity of the bridging ligand could not be determined, ? may be Cl, Co, S, P or a similar element. The number, position, and linkage of oxygen atoms/hydroxides may also be ambiguous due to disorder/symmetry.)</p> 	erk076	
<p data-bbox="259 1501 454 1533">$(^{\text{Ar}}\text{dpme})\text{Cu}$</p> 	gae015	

EVAN R. KING

59 Faxon Park Road
Quincy, MA 02169

(781) 234-4286
evanking@fas.harvard.edu

EDUCATION

- HARVARD UNIVERSITY, CAMBRIDGE, MA** GPA 3.94/4.0 July 2007 – May 2012
Ph.D. in Chemistry (May 2012)
Advisor: Prof. Theodore A. Betley
Thesis: "Metal-Ligand Multiple Bonds in High-Spin Complexes"
- CORNELL UNIVERSITY, ITHACA, NY** GPA 3.88/4.0 August 2001 - May 2005
B.A. in Chemistry (Summa cum Laude, May 2005)
Advisor: Prof. Paul J. Chirik
Senior Honors Thesis: "Synthesis and Characterization of Indenyl Metallocene Adducts with Divalent Ytterbium"

RESEARCH EXPERIENCE

- HARVARD UNIVERSITY, CAMBRIDGE, MA** July 2007 - Present
Graduate Fellow (Prof. Theodore A. Betley)
- Synthesized and characterized air-sensitive inorganic compounds and catalysts for C–H bond functionalization and small molecule activation.
 - Designed and implemented synthetic and spectroscopic experiments to understand the properties and reactivity patterns of new compounds and catalysts.
 - Performed theoretical calculations for electronic structure determination and comparison to experimental data.
 - Mentored and trained six undergraduate and first-year graduate students to develop synthetic methods and characterization techniques for their independent research projects
- MASSACHUSETTS INSTITUTE OF TECHNOLOGY, CAMBRIDGE, MA** November 2005 - April 2007
Graduate Research Assistant (Prof. Christopher C. Cummins)
- Synthesized and characterized bimetallic complexes as model compounds for water oxidation catalysis.
- CORNELL UNIVERSITY, ITHACA, NY** September 2003 - May 2005
Undergraduate Research Assistant (Prof. Paul J. Chirik)
- Synthesized and characterized air-sensitive lanthanide metal compounds for small molecule activation.
- NORTHEASTERN UNIVERSITY, BOSTON, MA** Summer 2002 & Summer 2003
Undergraduate Research Assistant (Prof. Pamela A. Mabrouk)
- Determined enzyme activity and structural feature changes by Raman spectroscopy under non-cellular conditions.

AWARDS

William Lipscomb Fellowship in Inorganic Chemistry (2011-2012, Harvard University)
Certificate of Distinction for Excellence in Teaching (Spring 2010, Harvard University)
Certificate of Distinction for Excellence in Teaching (Spring 2009, Harvard University)

SKILLS

COMPUTER: Windows, Mac & Unix, MS Office, Adobe Illustrator & Photoshop, IGOR Pro, Java, Chemdraw, X-ray refinement (Bruker AXS, SHELXTL) and X-ray graphics software (ORTEP, Mercury, POV-Ray).

ANALYTICAL TECHNIQUES: NMR spectroscopy, IR & UV-Vis spectroscopy, X-ray crystallography and structure refinement, EPR spectroscopy, SQUID magnetometry, Computational chemistry (DFT, Gaussian)

EVAN R. KING

TEACHING EXPERIENCE

HARVARD UNIVERSITY

Teaching Fellow

2008-2010

Advanced Inorganic Chemistry
Inorganic Chemistry

MASSACHUSETTS INSTITUTE OF TECHNOLOGY

Teaching Assistant

2005-2006

Intro. to Laboratory Chemistry
Principles of Inorganic Chem. I

CORNELL UNIVERSITY

Undergraduate Teaching Assistant

2004-2005

Honors General & Inorganic Chem. I
Honors General & Inorganic Chem. II

PUBLICATIONS

E. R. King, T. A. Betley. "Cobalt Imides Exhibiting Spin Crossover and C-H Bond Activation." *Journal of the American Chemical Society*, **2012**, submitted.

A. R. Fout, D. J. Xiao, Q. Zhao, T. D. Harris, E. R. King, E. V Eames, T. A. Betley. "Synthesis and Characterization of Trinuclear Clusters Spanning Weak-Field to Strong-Field Interactions." *Chemical Science*, **2012**, submitted.

E. R. King, E. T. Hennessy, T. A. Betley. "Catalytic C-H Bond Amination from High-Spin Iron-Imido Complexes." *Journal of the American Chemical Society*, **2011**, 133, 4917-4923.

E. R. King, T. A. Betley. "Unusual Electronic Structure of First Row Transition Metal Complexes Featuring Redox-Active Dipyrrromethane Ligands." *Journal of the American Chemical Society*, **2009**, 131, 14373-14380.

E. R. King, T. A. Betley. "C-H Amination from a Ferrous Dipyrrromethene Complex." *Inorganic Chemistry*, **2009**, 48, 2361-2363.

PRESENTATIONS

"Dipyrrromethene supported low-coordinate high-spin iron complexes and their reactivity as platforms for C-H functionalization via oxidative group transfer" E. R. King, T. A. Betley, *240th American Chemical Society National Meeting*, Boston, MA, August 25, 2010.

"Late metal dipyrrole complexes capable of multi-electron redox processes: Efforts toward C-H functionalization." E. R. King, T. A. Betley, *238th American Chemical Society National Meeting*, Washington, DC, Aug. 16, 2009.

"Late transition metal dipyrrole complexes capable of multi-electron redox and C-H Functionalization." E. R. King, T. A. Betley, *Chemistry and Chemical Biology Graduate Student and Post-doc Seminar Series*, Cambridge, MA, April 10, 2009.

"Synthesis and characterization of low coordinate late first-row transition metal complexes using pyrrole based chelates, and their oxidation chemistry." E. R. King, T. A. Betley, *236th American Chemical Society National Meeting*, Philadelphia, PA, Aug. 17, 2008.

AFFILIATIONS

American Chemical Society (Graduate Student Member since 2005)

Phi Beta Kappa (2005)

National Eagle Scout Association (2001)

REFERENCES

PROF. THEODORE A. BETLEY

Assistant Professor of Chemistry
Harvard University
12 Oxford St., Mallinckrodt 306E
Cambridge, MA 02138
(617) 496-9944
betley@chemistry.harvard.edu

PROF. PAUL J. CHIRIK

Edward S. Sanford Prof. of Chemistry
Princeton University
292 Frick Laboratory
Princeton, NJ 14853
(609) 258-4130
pchirik@princeton.edu

PROF. RICHARD H. HOLM

Higgins Professor of Chemistry
Harvard University
12 Oxford St., Mallinckrodt 306H
Cambridge, MA 02138
(617) 495-0853
holm@chemistry.harvard.edu